Functional Polymers for Lithium Metal Batteries

Submitted in partial fulfillment of the requirements for the degree of

Doctor of Philosophy in

Department of Chemistry

Sipei Li

Carnegie Mellon University

Pittsburgh, PA

December, 2019

Abstract

Lithium metal anode based rechargeable batteries (LMB) are regarded as the most viable alternative to replace state-of-the-art lithium ion batteries (LIB) as they can provide higher-energy-density energy storage. With this year's Nobel Prize in Chemistry being awarded to Akira Yoshino, M. Stanley Whittingham, and John B. Goodenough for their contribution in developing LIBs, even more attention is now drawn to the development of LMBs. Due to the highly reactive nature of metallic lithium and the change with regard to cathode, electrolyte and anode design, the industrial success of LMB has yet to be achieved. Traditionally, in an LMB the role of polymeric components is mostly limited to the role of separators and cathode binders. However, with the continued development of polymer chemistry and its growing number of applications in materials science, it is now recognized that designing and applying functional polymers can greatly improve the practical performance of an LMB.

This thesis describes how various polymer materials could be synthesized and tailored for improving the cycling stability of LMBs. Chapter 1 will systematically discuss the state-of-the-art of various macromolecular approaches to improve each major component of an LMB, namely the electrolyte/separators, anode-electrolyte interface, anode, cathode-electrolyte interface and high-energy-density cathode materials including layered metal oxides and sulfur. Chapter 2 describes the development of two polymer electrolytes with high lithium transference number prepared by atom transfer radical polymerization (ATRP) and anionic ring opening polymerization (ROP). Chapter 3 describes the development of two polymer based artificial solid electrolyte interface (SEI) that can stabilize the lithium deposition on the anode surface during lithium plating. One of the examples uses an organic/inorganic hybrid material prepared by covalently grafting polymers from a solid metal oxide by surface-initiated ATRP. Another one uses a single-ion polymer

discussed in Chapter 2. Chapter 4 discusses the development of a composite lithium metal anode that exhibits flowable properties and is compatible with ceramic solid electrolytes. Chapter 5 discusses how polymeric materials could be used as reactive surfactants to tailor the morphology of lithium metal from plain foils to microparticles and nanoflakes. Finally, a summary with outlook on future directions is provided.

Acknowledgements

First and foremost, I would like to express my most sincere gratitude towards Dr. Krzysztof (Kris) Matyjaszewski for accepting me into his research group. Kris was the reason I chose CMU for my PhD study. In my eyes, Kris is not only my research advisor, but also a role model and a good friend. I full-heartedly thank him for his guidance, encouragement and support during my 5 and a half years here at CMU. I appreciate his wisdom, work ethics, and the trust he put in me, so that I can realize and achieve my potential to the fullest.

I would also like to express my deepest gratitude towards Dr. Jay Whitacre for accepting me into his research group. Jay is one of the nicest people I've met at CMU. I appreciate his friendliness, humor, wisdom, and his super-power of dealing with multiple projects/businesses at the same time. If it was not for Jay's support, I would have not been able to enter the field of battery research.

I've come across many great colleagues during my PhD. In particular, I would like to thank Han Wang, Dr. Saadyah Averick, Zongyu Wang, Rui Yuan, Tong Liu and Dr. Hongkun He. I learnt a great amount of knowledge and experience about batteries and electrochemistry from Han. We are complementary to each other and I couldn't ask for a better partner than Han! When I first entered CMU, the first project I was involved in was inherited from Saadyah. Saadyah is the sincerest person I've met at CMU. Beyond research, I thank Saadayh for his mental support. I would also like to thank Zongyu Wang. He has been my best friend at CMU. I appreciate his selflessness, responsiveness, and reliability. I would also like to thank Rui Yuan, one of my sincerest friends and a great materials scientist. I am grateful to have Tong Liu as my successor in the field of batteries. Our collaboration and dynamics are invaluable. Hongkun and I came from the same research group at Zhejiang University prior than CMU. Hongkun warmly welcomed me

when I first arrived in Pittsburgh. Technically, he is also the first person to lead me into the field of batteries. I am grateful for what he did for me.

I received tremendous help from many other colleagues and collaborators. My committee members, Dr. Subha Das and Dr. Michael Bockstaller provided a different angle of view on my research. Dr. James Spanswick provided countless encouragement and help on my writing. Dr. Tomasz Kowalewski passed me invaluable experience in proposal writing. Dr. Marco Fantin and Dr. Francesca Lorandi provided many helpful suggestions on my proposal writing and paper writing. I would like to thank all the Matyjaszewski Group members and Whitacre Group members for building such creative, supportive, caring and hard-working environments. I would like to thank all my external collaborators, Dr. Yuji Mishina, Maiko Omi, Dr. Konstantinos Verdelis, Lyudmila Lukashova, Leiming Hu, Dr. Venkat Viswanathan, Dr. Vikram Pande, Dr. Alexander Mohamed, Dr. Dominik Konkolewicz, Dr. Shaohua Li, who provided essential help to my research. My gratitude goes to Dr. Rea Freeland, Valerie Bridge, Brenda Chambers, Tim Sager, and Lorna Williams who have always been supportive to me as a PhD student.

Last but not least, I would like to dedicate this dissertation to my family. I would like to thank my Mom Xiaodong Hu and my Dad Yong Li for their unconditional supports. My parents always told me to dream big, be fearless and have fun. They give me all they can so that I would not have to worry about finance. I would like to thank my paternal grandparents Zulong Li and Qiumei Ying for their purest love. I would have never achieved what I have achieved without my family's love and support. This thesis is written in memory of my dearest maternal grandma Jianshan Lu and maternal grandpa Jinhai Hu, who passed away when I was far away from home in the USA. RIP A Bu and A Gong!

Table of Contents

List of Abbreviations

γ	Surface energy of lithium metal
α	Transfer coefficient for lithium redox reaction
^{1}H NMR	Proton nuclear magnetic resonance
AA	Ascorbic acid
AGET ATRP	Activators generated by electron transfer ATRP
ARGET ATRP	Activators regenerated by electron transfer ATRP
ATRP	Atom transfer radical polymerization
BET	Brunauer-Emmett-Teller theory
BiBADA	12-(2-Bromoisobutyramido)dodecanoic acid
BPA	2-Bromo-2-phenylacetic acid
BPAA	α-Bromophenylacetic acid
BPADA	12-(2-Bromo-2-phenylacetamido)dodecanoic acid
$Br^-NOct_4^+$	Tetraoctylammonium bromide
BriBBr	2-Bromoisobutyryl bromide
CE	Coulombic efficiency
CEI	Cathode electrolyte interface
c_{Li+}	Concentration of lithium ion
CNF	Carbon nanofiber
CPE	Composite polymer electrolytes

c_{ref}	Reference concentration defined as 1000 mol/m^3
CTAB	Cetyltrimethyl ammonium bromide
CuAAC	Copper-catalyzed alkyne-azide cycloaddition
D	Salt diffusion coefficient
$Đ$	Molecular weight dispersity
DEC	Diethyl carbonate
DMAP	N,N-dimethylamino pyridine
DMC	Dimethyl carbonate
DME	Dimethoxyethane
DMSO	Dimethyl sulfoxide
DOL	1,3-Dioxolane
DP	Degree of polymerization
DSC	Differential scanning calorimetry
DVB	Divinylbenzene
E_a	Activation energy
EBPA	Ethyl α-bromophenylacetate
EC	Ethylene carbonate
EDC	N-(3-dimethylaminopropyl)-N'-ethylcarbodiimide hydrochloride
EDL	Electric double layer
EGaIn	Eutectic Gallium Indium
EGDMA	Ethylene glycol dimethacrylate

ePPO	Polypropylene elastomer
F	Faraday's constant
FEC	Fluoroethylene carbonate
FIB-SEM	Focused ion beam scanning electron microscope
FRP	Free radical polymerization
G′	Storage modulus
G″	Loss modulus
GA	Gum Arabic
GPE	Glycidyl propargyl ether
HBP	Hyperbranched polymers
HEK293	Human embryonic kidney cells
HF	Hydrofluoric acid
HO	Heterotopic ossification
i	Applied current density
i-Bu_3Al	Trisisobutylaluminum
i_0	Exchange current density at the lithium electrode-electrolyte interface
I^0	Initial current following the voltage step
ICAR ATRP	Initiators for continuous activator regeneration ATRP
I^s	Steady state current measured at the end of the voltage step

J	Current density
LAGP	$Li_{1.5}Al_{l0.5}Ge_{1.5}(PO_4)_3$
LAPS	$Li_{10}GeP_2S_{12}$
LCO	$LiCoO_2$
LCST	Lower critical solution temperature
LFP	$LiFePO_4$
Li-S battery	Lithium-sulfur battery
LIB	Lithium ion battery
LiBOB	Lithium bis(oxalato)borate
LiODFB	Lithium difluoro(oxalato)borate
LiPAA	Lithiated polyacrylic acid
LiPSP	Li polysulfidophosphate
LLZO	$Li_7La_3Zr_2O_{12}$
LLZTO	$Li_{6.4}La_3Zr_{1.4}Ta_{0.6}O_{12}$
LMB	Lithium metal battery
LMCA	Li microparticles (MPs)/carbon nanotube (CNT) composite anode
LMO	$LiMn_2O_4$
LNMO	$Li_{1.2}Ni_{0.2}Mn_{0.6}O_2$
Me_6TREN	Tris(2-dimethylaminoethyl)amine
micro-CT	Micro computed tomography
M_n	Number averaged molecular weight
mPEG	Poly(ethylene glycol) monomethyl ether

MSCP	Multifunctional sulfur-containing polymer
MSEA	2-(Methylsulfinyl)ethyl acrylate
MTEA	2-(Methylthio)ethyl acrylate
MTEMA	2-(Methylthio)ethyl methacrylate
MW	Molecular weight
N-isopropylacrylamide	NIPAM
NASICON	$Na_{1+x}Zr_2Si_xP_{3-x}O_{12}$, $0 < x < 3$
NCA	$LiNi_{0.8}Co_{0.15}Al_{0.05}O_2$
NCM	$LiNi_xCo_yMn_zO_2$ (x+y+z=1)
NCM 111	$LiNi_{1/3}Co_{1/3}Mn_{1/3}O_2$
NCM 523	$LiNi_{0.5}Co_{0.2}Mn_{0.3}O_2$
NCM622	$LiNi_{0.6}Mn_{0.2}Co_{0.2}O_2$
NCM811	$LiNi_{0.8}Co_{0.1}Mn_{0.1}O_2$
NHS	*N*-hydroxysuccinimide
NMP	Nitroxide mediated polymerization
P(SF-DOL)	Poly(vinylsulfonyl fluoride-*ran*-2-vinyl-1,3-dioxolane)
PAM-*g*-GO	Polyacrylamide-grafted graphene oxide
PAN	Polyacrylonitrile
PCEA	Poly (2-chloroethyl acrylate)
PDMS	Polydimethylsiloxane
PEG(M)A	Oligo/poly(ethylene glycol) (meth)acrylate
PEI	Polyethylenimine

PEO	Poly(ethylene oxide)
PEO_X-PC	Poly(ethylene oxide carbonates)
Ph-PTZ	10-Phenylphenothiazine
PI	Polyimide
PIPS	Polymerization-induced phase separation
PMA	Poly(*N*-methyl-malonic amide)
PMDETA	Pentamethyldiethylenetriamine
PPO	Poly(*p*-phenylene oxide)
PSBSE	Pseudo-solid bicontinuous single-ion electrolyte
PTHF	Polytetrahydrofuran
PVP	Polyvinylpyrrolidone
R	Ideal gas constant
R^0	Charge transfer resistance for lithium reduction/oxidation measured by impedance spectroscopy before the voltage step
RAFT	Reversible addition−fragmentation chain-transfer polymerization
RDRP	Reversible-deactivation radical polymerization
rGO	Reduced graphene oxide
rhBMP-2	Recombinant human bone morphogenetic protein-2
RNAi	RNA interference

ROMP	Ring opening methathesis polymerization
RPC	Reactive polymer composite
R^s	Resistance for lithium reduction/oxidation at the end of the voltage step
Runx2	Runt-related transcription factor 2
DB	Degree of branching
SARA ATRP	Supplemental activator and reducing agent ATRP
SBR	Styrene butadiene rubber
SCVP	Self-condensing vinyl polymerization
SEI	Solid electrolyte interface
SEM	Scanning electron microscope
SI-ATRP	Surface-initiated atom transfer radical polymerization
SIPEs	Single-ion polymer electrolytes
siRNA	short interfering RNA
SLMA	Semiliquid lithium metal anode
SPAN	Sulfur−Polyacrylonitrile
SPE	Solid polymer electrolyte
T	Temperature at which the cell is simulated
t	Radius of dendrite tip
t_+	Lithium ion transference number
TEA	Triethylamine

TEM	Transmission electron microscope
T_g	Glass transition temperature
TPMA	Tris(2-pyridylmethyl)amine
V_o	Oxygen vacancy
YSZ	Yttrium stabilized zirconium
β-CD	β-Cyclodextrin
ΔV	DC voltage applied across the cell
η	Complex viscosity
σ	Ionic conductivity

List of Tables

List of Figures

List of Schemes

Prologue

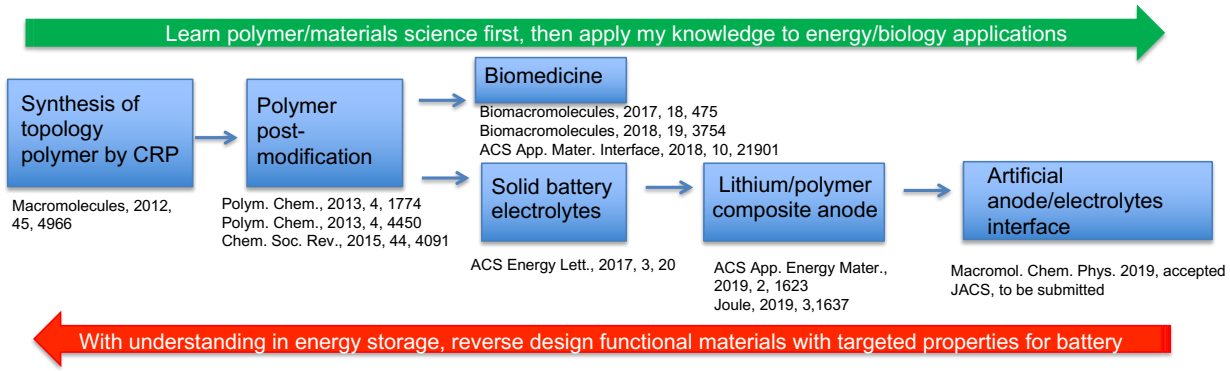

Figure 0. My research trajectory with first-author papers listed.

As listed in Figure 0, I have a unique research trajectory from fundamental polymer chemistry to applications in biomedicine and energy. Before I came to Carnegie Mellon University, I obtained my Master's degree at Zhejiang University, where my research was focused on designing macromolecules with complex topologies and functionalities via advanced polymerization techniques and efficient post-modification chemistries. After I entered CMU, my first project used the knowledge I obtained in synthesizing complex macromolecules to develop biocompatible polymers for bio-related applications such as siRNA delivery or MRI imaging. Through the process, I learnt the philosophy that to harness the specific properties for specific applications one needs first to make tailor-made polymeric materials. Meanwhile, I published three (co)first-author papers related to biomedicine. With this invaluable experience, I later branched out to the field of rechargeable lithium metal batteries where I found my new passion. I realized that polymer chemistry has wide potential in improving the stability of rechargeable batteries, especially lithium metal batteries. However, most battery research groups do not have enough knowledge of polymer chemistry and physics and vice versa is also true for many polymer research groups. As a result, there are tremendous opportunities in bridging these two areas. Here at CMU,

I had the honor to work with the world-famous polymer chemist Dr. Krzysztof Matyjaszewski and world-famous battery scientist Dr. Jay Whitacre. Under their guidance, I started to explore the possibility of applying polymer chemistry, especially controlled radical polymerization, to various aspects of development of a lithium metal battery. In the last three years, I have published four first-author papers and one first-author paper will be submitted very soon, all in the field of lithium metal batteries. In this thesis, I will detail my journey of bridging the fields of polymer science and lithium metal batteries.

Chapter 1. Functional Polymers for Lithium Metal Batteries

1.1. Introduction

With the rapid development of world economics, the over-exploitation of fossil fuels has evidently caused negative impact on the global eco-system. An inevitable consequence is we have to optimize the structure of global energy supply and storage.[1-3] Thus, it has been a worldwide effort to develop renewable/clean energies, such as wind power, hydropower, solar energy, bioenergy, etc.[4-6] Electrochemistry can efficiently convert and store energy without causing serious environmental damage and has the potential to make a major contribution to the implementation of renewable energies. Common electrochemical energy conversion and storage systems include primary batteries, rechargeable batteries, flow batteries, fuel cells, supercapacitors, etc.[7-10] Rechargeable batteries are energy devices that can reversibly convert chemical energy stored in active materials directly into electricity. Due to the extremely high energy efficiency (typically > 90%) compared to a conventional combustion engine (~40%), rechargeable batteries continued to gain attention.[11]

The history of commercial rechargeable batteries dates back to the early 1900's when battery chemistries such as Lead-Acid battery, Ni-Cd battery and Ni-MH battery were commercialized for mobile and stationary applications.[12] Since first commercialized in 1991 by Sony, lithium ion batteries (LIB) continued to gain market success due to several advantages, such as higher energy density, higher discharge voltage, longer cycle life, and a wide working temperature compared to other commonly used battery chemistries.[13] However, the development of lithium ion batteries has hit a bottleneck in recent years. A lithium ion battery with graphite anode and lithiated metal oxide cathode can typically deliver a pack-level energy density less than 300 Wh/Kg, which can barely satisfy the increasing energy requirements of an explosive

technology expansion.[13] Taking electric vehicles (EV) as an example, in order to manufacture an EV to run over 500 miles between charges, a battery pack that can deliver > 500 Wh/Kg is required.[14-16] Compared to the graphite anode used in typical LIBs that only has a theoretical capacity of 375 mAh/g, directly using metallic lithium anode can dramatically improve the cell energy density. This is because lithium metal has the lowest redox potential (-3.04 V vs SHE), high theoretical capacity (3860 mAh/g) and inexpensive market price.[17] Moreover, adopting lithium metal anode allows for the use of a non-lithiated high-energy-density cathode, such as sulfur and oxygen.[18] In pursuit of reliable rechargeable lithium metal batteries (LMB), many governments across the world started their own programs to accelerate research in LMB. For example, the United States established the *Battery500* consortium in 2016, Japan started the *Research and Development Initiative for Scientific Innovation of New Generation Battery (RISING)* project in 2009, China launched the *Made in China 2025* project in 2015, all aiming at pairing a lithium metal anode with high capacity cathode materials for high-energy-density rechargeable LMB.[19]

The success of rechargeable LMB hinges on the functioning of both metallic lithium anode and high-energy cathode materials. Thus, problems associated with both sides of the cell need to be addressed. A typical LMB uses a thin layer of lithium foil anode and aprotic organic liquids as electrolytes. However the surface roughness of lithium metal and its high reactivity towards an organic electrolyte leads to unstable lithium deposition which leads to dendrite formations that can short the battery and cause thermal runaways.[20] When pairing a lithium metal anode with high voltage cathode materials, such as the famous $LiCoO_2$ (LCO) or nickel-doped $LiNiCoMnO_2$ (NMC), the decomposition of the electrolyte in a highly oxidative environment and the structural instability at delithiated stage can quickly lead to capacity loss.[21, 22] A sulfur cathode has high

specific capacity of 1670 mAh/g. However, the implementation of a sulfur cathode suffers from the low active materials loading and the "shuttle effect" which refers to the dissolution of intermediate active materials in electrolytes.[23] Lithium-air (O_2) batteries have an ultra-high theoretical energy density of 3500 Wh/Kg. However, the incompatibility of the lithium electrolytes with oxygen reduction reaction (ORR) and oxygen evolution reaction (OER) has to be solved in order to revive this technique.[18]

Conventionally, in a LIB the use of polymeric materials was mostly limited to the area of inactive binding materials in the cathode, where polymer binders, most commonly polyvinylidene fluoride (PVDF), serve to affix active materials and conductive fillers to aluminum current collectors during charge/discharge.[24] In the last several decades, the development of new polymerization techniques, such as atom transfer radical polymerization (ATRP), reversible addition−fragmentation chain-transfer polymerization (RAFT), nitroxide mediated polymerization (NMP), etc, and modification chemistries has opened up new avenues for creating polymeric materials with controlled molecular weight & dispersity, chain morphology, chemical and physical properties.[25-30] As these two fields - polymer science and battery science - intersect, inspirations and new opportunities arise.[31-35]

Five aspects of battery development need to be considered when building a reliable high-energy-density LMB cell; they are anode, separator/electrolytes, cathode, anode-electrolyte interface (SEI) and cathode-electrolyte interface (CEI) (Figure 1). With the advances of polymer chemistry, roles of polymer materials have expanded to be applicable in all of these aspects. In this Chapter, I will discuss recent advances of applying functional polymers in each of these aspects of an LMB: 1) polymer electrolytes, 2) polymer-based artificial SEI, 3) polymer/Lithium composite anode and 4) application of polymers as functional binders or cathode-electrolyte

interface for high energy cathode materials including nickel-rich layered metal oxides ($LiNi_xCo_yMn_zO_2$ (x+y+z=1), (NMC) and sulfur cathode. The Li-air battery has been thoroughly reviewed and will not be discussed in this thesis.[36, 37]

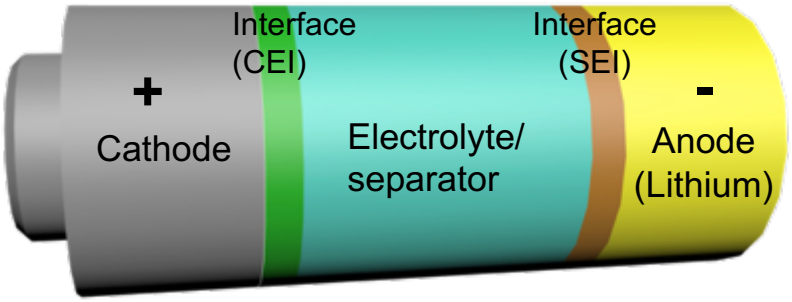

Figure 1. Illustration of five components in a multi-interface lithium metal battery: anode, separator/electrolytes, cathode, anode-electrolyte interface (SEI) and cathode-electrolyte interface (CEI).

1.2. Polymer Electrolytes

Liquid electrolytes show high ionic conductivity σ (1-10 mS/cm) and high wettability with electrodes. However, when used with highly reactive lithium metal, a non-uniform and fragile anode/electrolyte interface, or more often referred to as solid electrolyte interface (SEI), forms on the anode surface, that favors dendrite proliferation and electrolyte depletion. Also liquid electrolytes have minimal mechanical integrity to physically block the dendrite extension and low transference number (t_+), which can also cause formation of concentration gradients that lead to polarization and increased internal resistance, and even salt depletion/precipitation when the cell is cycled at high current densities.[38, 39] The need for enhanced battery safety and higher energy density devices encouraged researchers to focus on solid-state alternatives to conventional liquid electrolytes. Ceramic lithium ion conductors have been widely reported as one of alternatives. For example, garnet type electrolytes $Li_7La_3Zr_2O_{12}$ (LLZO) or NASICON type electrolytes, such as

$Li_{1.5}Al_{l0.5}Ge_{1.5}(PO_4)_3$ (LAGP), $Li_{10}GeP_2S_{12}$ (LAPS), etc., have high ionic conductivity (σ) that is comparable or even higher than the liquid electrolytes.[40] However, most of these electrolytes are not electrochemically stable against metallic lithium. Also the surface roughness and the lithiophobic interface caused a high interfacial resistance that limits the application of this type of electrolytes.[41] In comparison, solid polymer electrolytes (SPEs) provide better interface contact than ceramic electrolytes due to their adaptable/soft nature, although normally with much lower ionic conductivity (σ) and low transference number (t_+). The creation of an SPE with higher σ (>1 × 10^{-1} S/cm at room temperature) and t_+ (>0.8) could potentially provide the most efficient electrolyte system for LMB.

In the late 70s, alkali metal salts dispersed in poly(ethylene oxide) (PEO) were first used as SPEs and their conductivity was correlated to the amorphous phase of PEO.[42] Since then, PEO is the most adopted component of SPEs, mainly because of its relatively low glass transition temperature (T_g ~ -60°C) and the good complexation of Li^+ by ethylene oxide (EO) units.[43] However, PEO has some drawbacks, such as high degree of crystallinity at r.t. (i.e. low conductivity, 10^{-8}-10^{-7} S/cm at r.t.), low mechanical strength, low t_+ (0.1-0.2), poor oxidative stability and vulnerability to hydrogen abstraction.[33, 44] Beyond PEO, other types of polymers were also reported that improved σ and electrochemical stability, such as polyacrylonitrile (PAN),[45] polysulfone,[46] poly(N-methyl-malonic amide) (PMA),[47] poly(ethylene oxide carbonates) (PEO_X-PC),[48] polytetrahydrofuran (PTHF),[49] etc.

It follows that an SPE should: i) chelate Li^+ enough to promote salt dissolution but at the same time allowing Li^+ hopping from coordinating sites; ii) have a high dielectric constant to favor charge separation in the salt; iii) have a low T_g, corresponding to high backbone flexibility and facile segmental motion, resulting in high conductivity; iv) possess good mechanical stability,

which can be achieved by phase separation or crosslinked system, to prevent shortages due to dendrite penetration.[38, 39] Major approaches to improve the properties of SPE include: i) varying polymer architecture, or ii) by introducing inorganic fillers to form composite polymer electrolytes (CPE).[43, 50]

Adjustment of polymer architecture often implies the use of living polymerizations or reversible-deactivation radical polymerization (RDRPs) to precisely control the polymer morphology.[51] In polymer electrolytes based on different architectures, PEO is typically replaced with oligo/poly(ethylene glycol) (meth)acrylate (PEG(M)A) to improve the ionic conductivity, since Li^+ coordinating units are moved to the side chains, which are more flexible than the backbone.[52, 53] Non-linear structure can reduce the crystallinity of the polymer by increasing the free-volume for segmental motions. Non-linear structures such as hyperbranched structures or bottle-brush like structures have been prepared by atom transfer radical polymerization (ATRP) [54] and ring opening metathesis polymerization (ROMP)[53] respectively, that showed improved ionic conductivity, up to three order of magnitude, compared to linear PEO.[55]

Composite polymer electrolytes are SPEs with the addition of inorganic fillers. The presence of fillers typically enhance the ionic conductivity of SPEs.[38, 56] This was explained by considering that the fillers act as crosslinking centers that disrupt the polymer crystallinity, thereby increasing the segmental motion. Meanwhile, the addition of inorganic particles can improve the modulus of the composite materials. Moreover, the inorganic fillers can be ceramic lithium ion conductors, which can introduce a second lithium ion conducting phase. A series of inorganic fillers have been applied, such as Al_2O_3, ZnO, TiO_2, ZrO_2, and other Lewis-acid type metal oxides. For example, Lewis acid-base interactions between Li^+, anions and positively charged oxygen vacancies on yttria stabilized zirconia (YSZ), can favor the salt dissociation and offer new Li^+

conduction paths on the fillers' surface, increasing the ionic conductivity by two order of magnitude.[57] Besides, the morphology and orientation of the nanosized fillers can also affect the enhancement of ionic conductivity. It was found 1D nanowires can provide a channeled Li^+ transport pathway along the surface of 2D nanowires compared to 3D nanoparticles. Cui et al. showed that PAN-based electrolyte with well-aligned ionically conductive LLTO nanowires prepared by electrospinning exhibited one order of magnitude higher room-temperature conductivity than when disordered nanowire or nanoparticles were introduced to the PAN matrix.[58] Polymer chains can also be covalently attached to inorganic fillers. Archer et al. synthesized cross-linked hairy nanoparticles-based electrolytes by first grafting an alkoxy silane terminated oligomeric PEO-OH onto SiO_2 nanoparticles in water. The resulting densely grafted SiO_2-PEO-OH hybrid particles that were used as crosslinker for poly(p-phenylene oxide) (PPO) chains functionalized with isocyanate end groups, achieved a high degree of crosslinking.[59] The pore size could be tuned by changing the volume fraction of nanoparticles. Composite electrolytes obtained by soaking with a liquid electrolyte with membrane pore size <500 nm allowed for smooth Li electrodeposition on Li metal anodes at high current density.

One of the most recent examples of a crossover between polymer science and battery technology is the development of single-ion polymer electrolytes (SIPEs). Conventional SPEs generally have t_+ lower than 0.5 because of their dual-ion conducting character: the motion of Li^+ is coupled to the segmental motion of polymers, and therefore Li^+ ions are less mobile than their anionic counterparts.[60] In contrast, SIPEs have the anions immobilized by the polymer backbone/network so that only lithium ions are freely moving.[61] As a result, SIPE tend to have much higher t_+, typically >0.8. Two questions need to be answered in order to have viable SIPE materials: i) procedures of immobilizing the anions and ii) ways to combat the loss of ionic

conductivity due to strong ionic association. Previously, three types of single-ion polymer electrolytes have been reported: sulfonate-based,[62] acrylate-based,[63] borate-based.[64] These types of SIPEs have low ionic conductivity due to the insufficient ionic dissociation between the lithium ions and electron rich counter ions. Armand et al. recently reported a polystyrene-based SIPE formed by attaching lithium bis(trifluoromethane)sulfonimide ($TFSI^-Li^+$)-like ion pairs onto the p-position of a phenyl group (STFSILi).[65, 66] Due to the bulky structure and dispersed electron density, such lithium ion pairs possess much higher ionic conductivity. An ABA triblock copolymer (polySTFSILi-PEO-polySTFSILi) was prepared with the middle block as PEO block by nitroxide-mediated polymerization (NMP). The TFSI-like bulky anions provided 10 times more improved ionic conductivity (4×10^{-5} S/cm at 90 °C and t_+ of >0.85) while the phase separation due to the immiscibility of the two blocks induced sufficient mechanical strength.[67] The versatile azido-$TFSI^-Li^+$ ion pair was also reported to be clicked onto other backbones as a facile SIPE building block.[68]

A SPE can also be designed to possess advanced mechanical properties. Bao et al. introduced a highly resilient electrolyte composed of a poly(propylene oxide) elastomer (ePPO) obtained from crosslinked Jeffamine precursors and linear diamines to increase the MW between crosslinks, decreasing the modulus while increasing the strain capability of the polymer.[69] (Figure 2a) The ePPO elastomer was mixed with SiO_2 nanoparticles, propylene carbonate plasticizer and LiTFSI to form a highly conductive ($\sigma = 2.5 \times 10^{-4}$ S/cm at r.t.) and resilient (modulus of resilience = 0.32 MJ/m^3). The electrolyte enabled observation of 95% capacity retention after 300 cycles at C/5 and r.t. in Li metal battery with $LiFePO_4$ (LFP) cathode. Another strategy to prepare SPEs with exceptional mechanical properties used the polymerization-induced phase separation (PIPS) approach to polymerize a styrene/divinylbenzene mixture from a PEO macro-RAFT agent in the presence of an ionic liquid that is immiscible with PS and therefore enters the PEO domains.[70]

(Figure 2b) Due to the controlled RAFT polymerization and the cross-linking by divinylbenzene (DVB), a bicontinuous nanostructured membrane was obtained consisting of a mechanically robust crosslinked-PS and a conductive PEO phase. The resulting electrolyte membrane exhibited elasticity modulus approaching 1 GPa and σ > 1 mS/cm at room temperature. Cui et al. adopted a template approach by infusing conductive PEO/LiTFSI phase into a mechanically strong polyimide (PI) film with highly aligned through-film vertical nanochannels. The templated electrolyte is ultrathin (8.6 μm), lightweight, highly flexible and highly conductive (2.3×10^{-4} S/cm at 30 °C). (Figure 2c) All-solid-state lithium-ion batteries fabricated with PI/PEO/LiTFSI solid electrolyte show good cycling performance (200 cycles at C/2 rate) at 60 °C and can withstand abuse tests such as bending, cutting and nail penetration.[71]

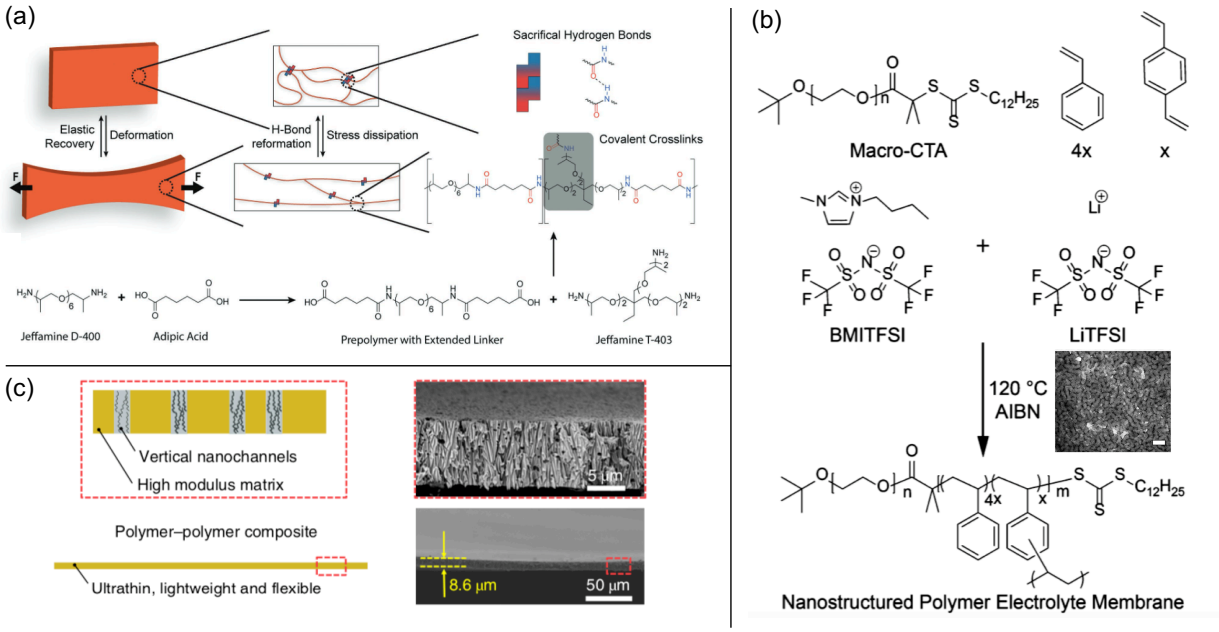

Figure 2. Strategies to prepare SPEs with exceptional mechanical properties: (a) synthesis of a highly resilient polypropylene elastomer.[69] (b) SPE membrane through polymerization-induced phase separation. Inset: TEM image of the bicontinuous membrane, scale bar 100nm.[70] (c) Illustration and SEM images of the ultrathin, flexible SPE with aligned conductive channels.[71]

Polymers can simultaneously act as electrolytes and separators. Due to various challenges in the synthesis of highly conductive and stable SPEs, a great deal of research focuses on engineering the separator membranes to enable stable cycling of LMBs with conventional liquid electrolytes. In this context, Wu et al. substantially improved the properties of conventional polypropylene separators (Celgard) by surface-modifying the membranes with polyacrylamide-grafted graphene oxide (PAM-*g*-GO) 2D molecular brushes, prepared by surface-initiated ATRP (SI-ATRP).[35] (Figure 3a) The GO backbones improved the mechanical strength, while the hairy PAM chains provided a high concentration of functional sites for efficient adhesion and homogeneous distribution of Li^+, resulting in homogeneous and fast Li^+ flux, thanks to the interspaces between the stacked molecular brushes. Li|Li symmetric cells with an ether-based liquid electrolyte and the modified separator showed stable cycling for >2000 cycles at room temperature, even for current density as high as 20 mA/cm^2. Archer et al. reported an in situ formed polymer membrane by using liquid electrolyte precursors 1,3-dioxolane (DOL) that is spontaneously polymerized by cationic ring opening polymerization in the presence of $Al(OTF)_3$. (Figure 3b) The as-formed pseudo-solid interlayer contains polyDOL and unpolymerized free DOL and can retain conformal interfacial contact with all cell components while possessing an ionic conductivity of >1 mS/cm at r.t.. A cell made of lithium foil, polyDOL/DOL electrolyte and high capacity cathode such as sulfur and $LiNi_{0.6}Mn_{0.2}Co_{0.2}O_2$ (NCM622) demonstrated high coulombic efficiency (>99%) and long cycling life (>700 cycles).[72]

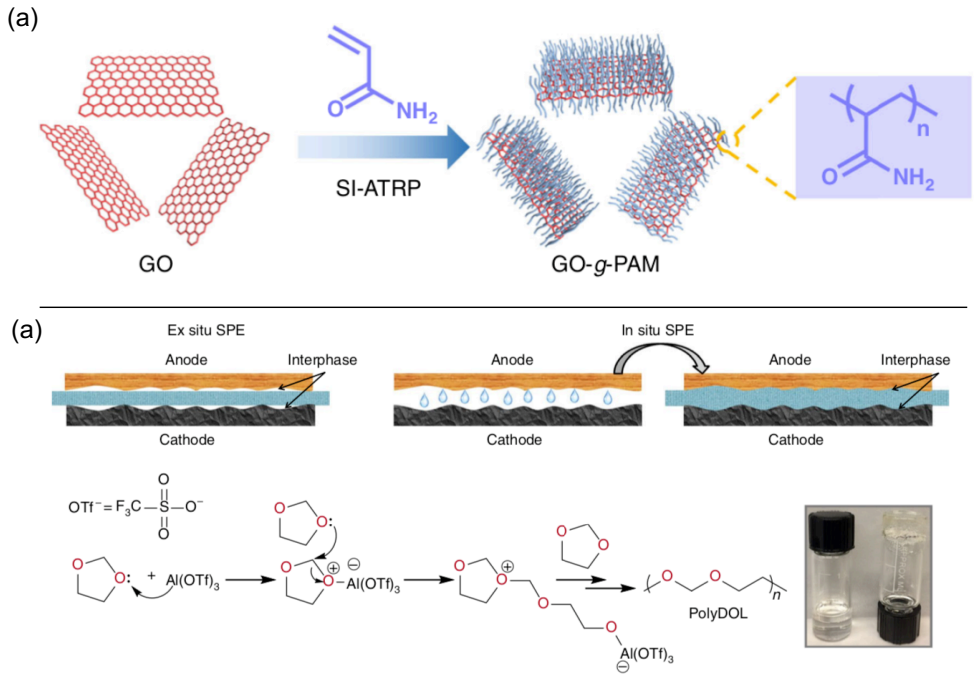

Figure 3. Macromolecular strategies to prepare effective separator layer: (a) Synthesis route to covalently graft hairy PAM from GO by SI-ATRP.[35] (b) mechanism and illustration of in situ formed separator layer by spontaneous cationic ring opening polymerization.[72]

1.3. Artificial Anode/Electrolyte Interface

Due to its high reactivity, lithium metal reacts with most organic electrolytes and forms a passivation layer on the lithium surface to prevent further reactions between lithium and electrolytes. However, this passivation layer is not stable, it is brittle and easy to crack, which can repeat and cause more fresh lithium to be exposed to the electrolyte again as the cycling continues, leading to depletion of both lithium metal and electrolyte, eventually resulting in low coulombic efficiency.[73] This passivation layer, which is electronically insulating and ionically conducting, was named a solid electrolyte interface (SEI) and first introduced by Peled in 1979.[74] The study of SEI was further developed by Peled et al. in 1997 and Aurbach et al. in 1999.[75, 76] Similar to the case of lithium ion batteries with a graphite anode, a dense and intact SEI is necessary to restrict

the electron tunneling and protect additional lithium metal from reacting with the electrolyte. Unfortunately, the exact composition and mechanism of SEI in both LIB and LMB are not clear. Therefore, the SEI is regarded as the most important but least understood component in a rechargeable lithium-based battery. Great efforts have been put into this area to measure and optimize the properties of SEI.[77-78] Since the *in situ* formed SEI in the presence of a conventional liquid electrolyte is not able to suppress formation of lithium dendrites, chemical pretreatment of the lithium metal surface with *ex situ* coating (an artificial SEI) before electrochemical reactions can be an effective strategy to stabilize the interface. Polymers are among one of the most promising choices for preparation of an artificial SEI as it should be flexible, easy to process, ionically conductive and have a low interfacial resistance. The criteria for designing viable artificial SEI include: a) excellent mechanical stability and flexibility, b) good adhesion to the anode and also electrolyte in the case of solid electrolyte, c) high electrical resistance and high cation (of the proper anode) selectivity and permeability, d) high strength, tolerance to expansion and contraction stresses, e) insolubility in the electrolyte and stability over a wide range of operating temperatures and potentials.[40, 79]

In this section, the application of polymer materials and polymer/inorganic composite materials designed as an artificial SEI will be discussed. In order to achieve mechanical stability and flexibility, Guo et al. proposed using a lithiated polyacrylic acid (LiPAA) polymer as a smart SEI layer with high elasticity (Figure 4).[56] LiPAA exhibits high stretchability and can tolerate a strain as high as 582% compared to the initial length. Such high stretchability helped withstand the stress change during lithium plating/stripping. The compact and uniform structure prevented the exposure of lithium metal to the electrolyte. LiPAA polymer also has superior binding abilities due to the high lithiophilicity. Such a design effectively improves the cycle life of a symmetrical

cell up to 700 h under 0.5 mA/cm^2 current density. A smart artificial SEI with self-healing properties could further prevent the structural failure and better compensate for the volume change during lithium plating/stripping. Cui et al. developed polyamides as a self-healing material that is prepared by a condensation reaction between branched oleic acid and diethylene triamine, followed by treating with urea to obtain the final product. Such a method allows for facile tuning of viscoelasticity, healing speed and mechanical strength so that best self-healing properties can be achieved.[80] With the protection of such a self-healing coating, uniform Li deposition was obtained at current density as high as 5 mA/cm^2 and coulombic efficiency as high as 97%.[56]

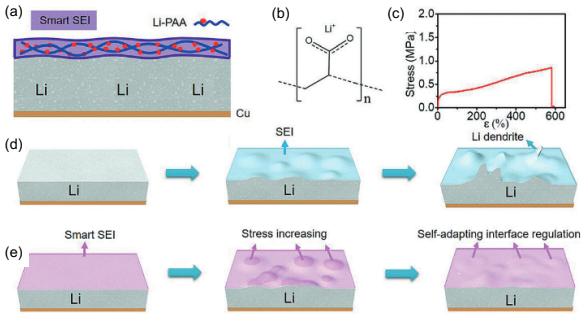

Figure 4. (a) The design of the flexible SEI. (b) Chemical structure of LiPAA SEI. (c) The stress–strain curve of LiPAA gel polymer. (d) The Li dendrites growth process of pristine Li. (e) The flexible SEI decreases the Li dendrite growth through self-adapting interface regulation.[56]

Polydimethylsiloxane (PDMS) based materials exhibit intriguing properties because of its chemical inertness and mechanical flexibility and therefore can be a great building block for artificial SEI. Silly putty, a popular kids' toy, is made of PDMS cross-linked by transient boron-mediated bonds. It can act as an elastic solid when fast deformation happens but also has flowable property when touched gently. The dynamic bond breakage and reformation between polymer chains makes it a smart material, which shows "solid-liquid"-like properties. When this silly putty film is coated on a lithium anode, it improves lithium morphology and cycling ability as a

conformal interface and also inhibits non-uniform Li deposition and dendrite growth.[81] However, PDMS itself is not ionically conductive. Zhu et al. proposed a method to create Li-ion transport pathways on PDMS. Hydrofluoric acid (HF) is employed to create a nanoporous PDMS suitable for Li^+ transport. After HF etching, they obtained nanopores with the size of 40-100 nm. The etching time should be controlled to obtain adequate pore size. Larger pores would result in the direct contact of lithium metal and electrolyte, losing the protection. With this PDMS-modified porous artificial SEI, a cycling coulombic efficiency of 95% was obtained over 200 cycles under 0.5 mA/cm^2. The modified Cu foil with PDMS reaches an average coulombic efficiency 98.2% in 100 cycles at 0.5 mA/cm^2.[82] Helms et al. further examined the influence of SEI porosity on the regulation of Li^+ flux at the anode surface during electrodeposition. It was proven that liquid electrolytes increase their transference number from 0.2 to >0.7 when confined to a porous surface coating with porosity of 0.5-2 nm and can therefore stabilize the electrodeposition of lithium at high capacity.[83] PDMS is also used as a host substrate to create polymer/inorganic hybrid SEIs. Nazar et al. created a PDMS/Li_3PS_4 hybrid membrane that combines the advantage of both PDMS and an otherwise electrochemically unstable ceramic electrolytes Li_3PS_4: i) the compact packing of a Li^+ solid electrolyte phase offers percolated Li^+-conducting channels, ii) PDMS phase provides sufficient elasticity to accommodate the surface roughness/volume change during lithium plating/stripping while preventing direct contact between lithium metal and unstable Li_3PS_4 components, iii) the dense packing also prevents reduction of liquid electrolytes by electrons. Such hybrids SEI resulted in Li plating with 95.8% efficiency for 200 cycles and stable operation in a LTO|Li cell for 2,000 cycles.[84]

The concept of artificial polymer/inorganic hybrids SEI approach has become a trending approach for stabilizing lithium metal. Wang et al. demonstrated an organic/inorganic hybrid SEI

layer which contains Li polysulfidophosphate (LiPSP), poly (2-chloroethyl acrylate) (PCEA), Li sulfides and Li salts. The chlorine-rich polymer poly(2-chloroethyl acrylate) (PCEA) was prepared by free radical polymerization. The LiPSP and PCEA solution were mixed and cross-linked at room temperature under vacuum to form the multifunctional sulfur-containing polymer (MSCP) protective layer. The sulfur-containing polymer can contribute to the formation of organo-(poly)sulfide and inorganic sulfides (e.g., Li_2S/Li_2S_2), which further increases the flexibility of the protective layer to accommodate the volume expansion of lithium metal anodes during the plating/stripping process.[85] Cui et al. prepared an electrochemically stable polymer/nanoparticle hybrid core-shell structure coating by grafting poly(methyl methacrylate) (PMMA) from the surface of silica nanoparticles. The high modulus of 68 GPa of the SiO_2 core is mechanically strong enough to suppress lithium dendrites growth and the PMMA shell helps efficient distribution of the silica nanoparticles and increases the flexibility of the membrane. The synthesis of SiO_2@PMMA core–shell nanocomposites was conducted by emulsion polymerization.[86] They also designed an artificial SEI layer containing Cu_3N nanoparticles (sub-100 nm) in a styrene butadiene rubber (SBR), which has high Li-ion conductivity, high mechanical strength and good flexibility. The Cu_3N nanoparticles can spontaneously react with lithium metal to form Li_3N, one of the fastest Li-ion conductors with ionic conductivity on the order of 10^{-3}-10^{-4} S/cm at room temperature. With the protection of such an artificial SEI, the lithium anode achieved a Coulombic efficiency of 97.4% at 1 mAh/cm^2 over 100 cycles in a Li|Cu half cell.[87] LiF is regarded as one of the key components in a spontaneously formed SEI in a typical lithium ion battery with a graphite anode. It is calculated that the addition of LiF can reduce the activation energy of lithium dendrite growth and therefore lithium deposition tends to form 2D planer structures instead of 3D dendrites.[88, 89] On the other hand, reduced graphene oxide (rGO) has recently been identified as

an effective building block for artificial SEI due to several advantages: i) the organic functional groups on rGO increase the hydrophilicity, ii) excellent mechanical strength prevents dendrite growth, iii) dense packing prevents side reaction between electrons and electrolytes. [35, 90-93] Wang et al. recently demonstrated a molecular-level artificial SEI design using a reactive polymer composite (RPC), which effectively suppresses electrolyte consumption in the formation and maintenance of the SEI. The RPC consists of reactive poly(vinylsulfonyl fluoride-ran-2-vinyl-1,3-dioxolane) (P(SF-DOL)) and rGO nanosheets (Figure 5). The PRC derived SEI was formed in a two-step process. First the RPC layer was attached to the lithium surface by reaction between lithium, sulfonyl fluoride groups and carboxylic acid group from GO nanosheet to form LiF, –SO_2–Li salts and –CO_2–Li salts. Upon cycling, the DOL groups were further reduced to form -O-Li salts. Such a PRC-derived lamellar SEI contains polymeric Li salts embedded with LiF nanoparticles and GO nanosheets and is sufficiently dense to block electrolyte access to the lithium surface. The use of the polymer– inorganic SEI enabled high-efficiency Li deposition and stable cycling of 4 V Li|$LiNi_{0.5}Co_{0.2}Mn_{0.3}O_2$ cells under lean electrolyte (7 μLmA/h), limited Li excess (1.9-fold excess of Li) and high areal capacity loading (3.4 mAh/cm^2).[94]

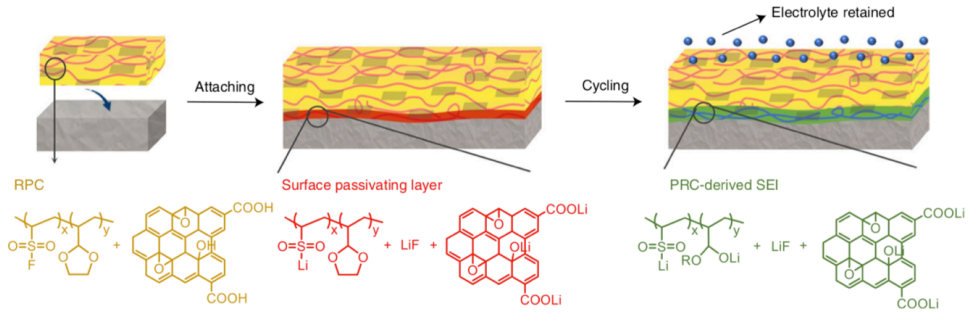

Figure 5. Strategies to construct molecular-level artificial SEI using a reactive polymer composite (RPC).[94]

1.4. Polymer/Lithium Composite Anode

Conventional LMBs use planar lithium foil as the anode. The planar form leaves rather limited space for improving the performance of lithium metal with the exception of the aforementioned SEI approach. Transforming the planar 2D lithium foil to a 3D composite lithium anode has several advantages: i) decreasing the high extent of volume change that otherwise would happen in a "hostless" lithium foil anode; ii) shifting the location of the charge separation process from the anode surface to the entire structure thereby decreasing local current density; iii) lowering the overpotential that would cause extra resistance and voltage loss; iv) allowing functionalities to be added to the 3D scaffold to guide non-dendritic electrodeposition of lithium during charge.[95, 96] Wang et al. developed a 3D crosslinked polyethylenimine (PEI) Li^+-affinity sponge as a lithium metal host by a combination of the self-concentrating and Li^+ pumping features. The strong affinity of Li ions from the 3D PEI sponge can spontaneously concentrate Li^+ in the internal structure rather than in the bulk solution. Meanwhile, interfacial electric double layer (EDL) due to the strong Li^+ affinity promotes the electro-osmosis during Li plating/stripping and therefore overcomes the diffusion-limited current. Such design reduces the concentration polarization, enabling uniform Li^+ distribution and dendrite-free lithium plating/stripping at high current and high deposition capacity (3.8 mAh/cm2) with 99.78% average Coulombic efficiency and practical N/P ratio of 2.[97]

A polymer-based lithium composite anode can also be utilized with solid electrolytes. Solid-state electrolytes are more promising than organic liquid electrolytes in terms of excellent safety in developing lithium-metal anode as well as other high-capacity cathode chemistries, such as sulfur and oxygen.[98] Unfortunately, the high surface roughness of both the anode and solid electrolytes often leads to high interfacial resistance, low areal capacity, and poor power output.

Although coating an inorganic layer, such as silicone, aluminum oxide, or zinc oxide on the surface of lithium can increase the lithiophilicity to certain extent, the repeated volume change will lead to mechanical failures due to rigidity. Consequently, improving the surface contact with wetting agents, such as polymer materials, become a more viable approach compatible with solid electrolytes. Cui et al. solved this problem by creating a tri-layer architecture that is composed of molten lithium metal, layered reduced graphene oxide (rGO) flakes and a flowable PEG interlayer (Figure 6). When a densely packed GO film is put in contact with molten lithium, a "spark reaction" happens that stretches the gap between GO layers. Molten lithium can therefore be sucked into the interlayer via enhanced capillary forces. The remaining surface functionality of rGO transforms the surface of composite anode to become lithiophilic. A flowable PEG/LiTFSI liquid electrolyte is then thermally infused into the gap of the Li/rGO composite. With such tri-layer anode, an all-solid-state lithium metal batteries is constructed with PEG/silica composite electrolyte and LFP as cathode with high–mass loading at 80°C, which exhibits a satisfactory specific capacity even at a rate of 5 C (110 mAh/g) and a capacity retention of 93.6% after 300 cycles at a current density of 3 mA/cm^2.[99]

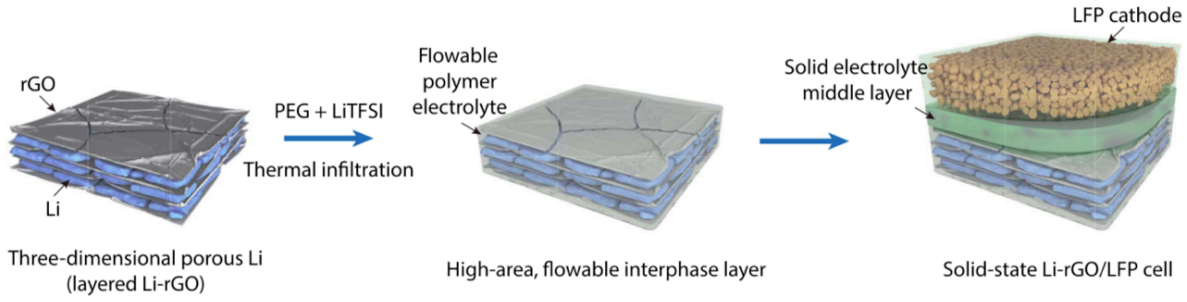

Figure 6. Schematics illustrating the fabrication process of the 3D Li anode with flowable interface for solid-state Li battery.[99]

1.5. Polymers for Preparation of a High Energy Metal Oxide Cathode

Two general options are available as cathode materials when considering LMB at the cell-level, – lithiated layered metal oxide that is also adopted for LIB or non-lithiated high-energy-density cathode materials such as sulfur or oxygen. Adopting the layered metal oxides cathode also has the advantage that the original production infrastructure inherited from LIB industries does not have to change for LMB production. Meanwhile, even an LMB using similar electrolyte and cathode materials can already greatly increase the pack-level energy density as shown in Figure 7.[100] These cathode materials include $LiCoO_2$ (LCO), $LiMn_2O_4$ (LMO), $LiFePO_4$ (LFP), $LiNi_xCo_yMn_zO_2$ (x+y+z=1) (NCM), and $LiNi_{0.8}Co_{0.15}Al_{0.05}O_2$ (NCA). Although LCO was used in the first generation of LIB commercialized by SONY, LCO still holds an edge over other cathode materials in the fields that have a rigid requirement for the voltage platform. However, the high amount of cobalt being used in LCO has urged the industry to seek for a replacement that also has high voltage plateau but with lowered amount of cobalt, that is, a lower-cost nickel-rich cathode materials $LiNi_xCo_yMn_zO_2$ (x+y+z=1) (NCM) or a lithium-rich cathode such as $Li_{1.2}Ni_{0.2}Mn_{0.6}O_2$ (LNMO). There is a variation of NCM, including $LiNi_{1/3}Co_{1/3}Mn_{1/3}O_2$ (NCM 111), $LiNi_{0.5}Co_{0.2}Mn_{0.3}O_2$ (NCM 523), $LiNi_{0.8}Co_{0.1}Mn_{0.1}O_2$ (NCM811), etc. However, as the nickel contents increases, the structural stability decreases in the presence of organic solvent-based electrolytes, which can lead to fast capacity degradation of Li-ion batteries during cycling, especially at high cutoff voltages and/or high temperatures. On the other hand, Li-rich cathode materials still suffer from the challenges of oxygen (O) loss from the lattice during the first charge, side reactions with the electrolyte, and voltage decay during extended cycling.[101] Modifying the surface of cathode electrodes by coating with a conductive polymer, such as polyacrylonitrile (PAN), polypyrrole (PPy), polyaniline (PANI), poly(3,4-ethylenedioxythiophene) (PEDOT), etc,

has been demonstrated as an effective method to mitigate the side reactions and increase the performance of these cathode materials.[102-111] These polymers have good electric conductivity so that when used for coating, they cannot only mitigate the side reaction, but also increase overall conductivity of the composite. More importantly, these polymers are all electrochemically/chemically stable towards oxidation at the cathode potential.

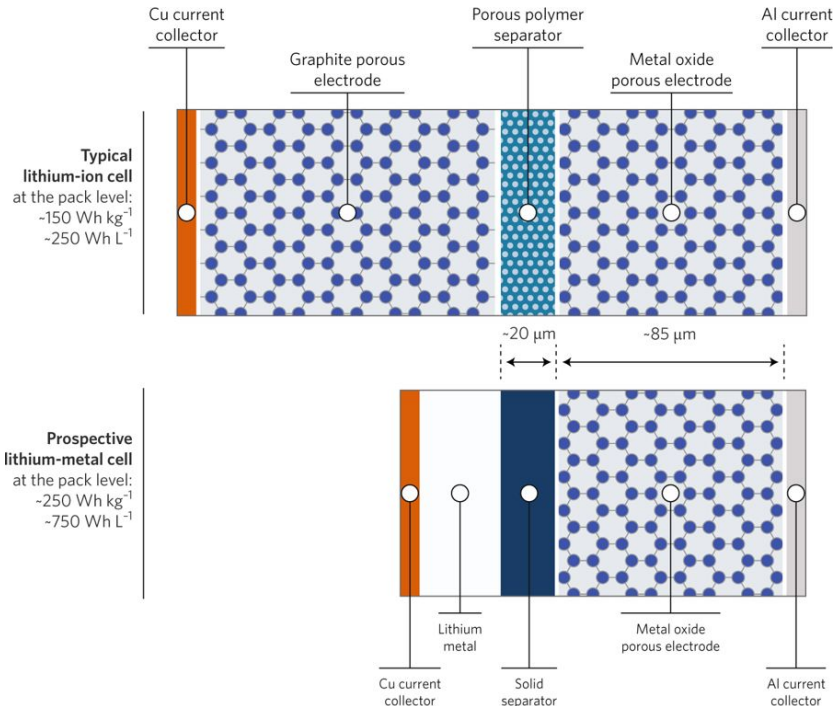

Figure 7. A typical Li-ion cell (top) and one conception of a lithium metal cell (bottom), containing a solid separator, a dense layer of metallic lithium and the same layered metal oxide cathode. The lithium metal cell is in the charged state, with 20% excess lithium. Layer thicknesses are shown to scale. The reduction in volume and mass associated with replacing the graphite electrode with lithium metal is evident.[100]

Wu et al. made the composites of lithium-rich $Li_{1.2}Ni_{0.2}Mn_{0.6}O_2$ and poly(3,4-ethylenedioxythiophene):poly(styrenesulfonate) (PEDOT:PSS) via coprecipitation followed by a wet coating method. The thickness of the polymer coating is 5-20 nm. A composite with an optimal

3 wt % coating exhibits rate capability and cycling properties, with an excellent initial discharge capacity of 286.5 mAh/g at a current density of 0.1 C and a discharge capacity that remained at 146.9 mAh/g at 1 C after 100 cycles.[102] Liu et al. synthesized LiV_3O_8–polyaniline nanocomposites via chemical oxidative polymerization directed by the anionic surfactant sodium dodecyl benzene sulfate. The composite with 12 wt% polyaniline retains a discharge capacity of 204 mAh g^{-1} after 100 cycles and had better rate capability (175 mAh/g at 2 C and 145 mAh/g at 4 C) than the bare LiV_3O_8 in the potential range of 1.5–4.0 V.[103]

The problem with the polymer coating lies in the inhomogeneity of the coating thickness due to the poor control over synthesis conditions, which is addressed further by using better surfactants or advanced synthesis routines. Choi et al. made use of the hydrophobic features of cetyltrimethyl ammonium bromide (CTAB) surfactant and 3,4-ethylenedioxythiophene (PEDOT) monomer in aqueous solution to provide a reasonable driving force to guarantee a uniform coating layer during surface coating with a conductive polymer. [104] In another work by Lu et al, they achieved uniform coating of conducting PANI on the surface of NCM811 by pretreating NCM811 particles with polyvinylpyrrolidone (PVP). Owing to the bonding effect between pyrrolidone rings of PVP and −NH− groups of PANI, the PANI layer could be uniformly anchored on the surface of NCM811, with thickness of 5-7 nm.[105] In another approach developed by Chen et al, instead of using wet-chemistry process, they used a transformative approach using an oxidative chemical vapor deposition technique to build a protective conductive polymer PEDOT skin on layered oxide cathode material. In the solvent-free process, $VOCl_3$ oxidant vapors and the 3,4-ethylenedioxythiophene (EDOT) monomer were simultaneously introduced into a rotary reactor, and then adsorbed onto the NCM111 particle surface (Figure 8). Thereafter, the film polymerized spontaneously via oxidative step-growth polymerization. This novel method successfully builds

the PEDOT skin with uniform thickness on both secondary and primary particles of layered oxide cathode materials. At 0.1 rate, the capacity retention rate over 50 cycles was improved to 76.7%, 85.2%, 96.6% and 95.8% from 67.6%, for bare NCM. At a higher rate 1C, a more remarkable cycling stability enhancement was observed, from 47.7% for bare NCM to 79.1, 83.0, 91.1 and 89.5% after 200 cycles. It is especially noteworthy that the capacity retention rate of 91.1% over 200 cycles at such a high cut-off voltage (4.6 V) and high rate (1 C) is an impressive improvement without using electrolyte additives such as lithium bis(oxalato)borate (LiBOB), lithium difluoro(oxalato)borate (LiODFB) or fluoroethylene carbonate (FEC). The stability results from three effects of the PEDOT skin: (1) suppressing the undesired layered to spinel/rock-salt phase transformation; (2) mitigating intergranular and intragranular mechanical cracking; (3) stabilizing the cathode–electrolyte interface.[106] Such coating techniques can be applied to cathodes with higher energy density, such as layered Ni-rich $LiNi_{0.85}Mn_{0.05}Co_{0.1}O_2$ cathode and Li-rich $Li_{1.2}Mn_{0.54}Ni_{0.13}Co_{0.13}O_2$ cathode.[106]

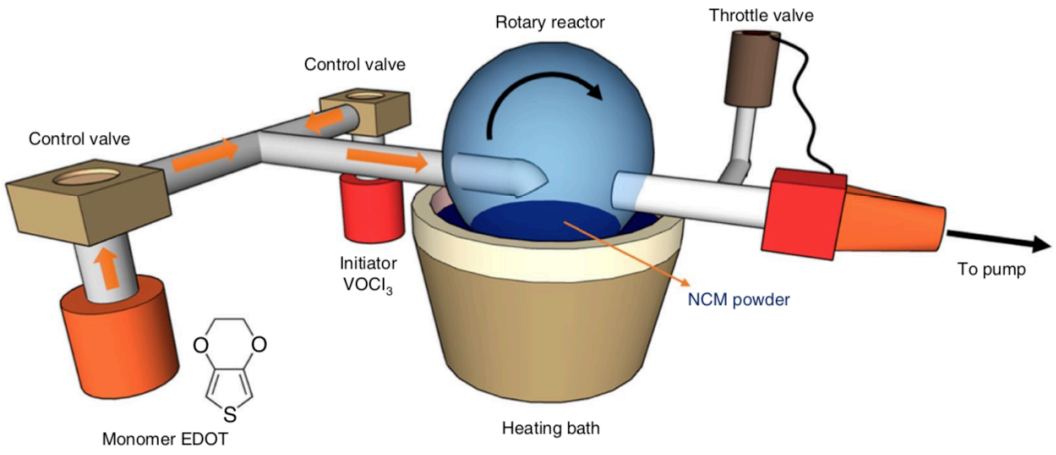

Figure 8. A schematic diagram of the experimental oCVD setup. The oCVD process relies on uniform vapor (oxidant and monomer) adsorption and subsequent in situ polymerization on the NCM particle (secondary/primary) surface.[106]

1.6. Polymers for Next-Generation Sulfur Cathodes

Commercial electrode materials for LIB will soon reach their ceiling in terms of capacity due to the limited number of crystallographic sites naturally available in these compounds for the insertion and extraction of lithium ions. Lithium-Sulfur is the next generation of electrode chemistry with theoretical capacity of 1672 mAh/g. The key problems with the Li-S battery are: i) high resistance of sulfur (~10−30 S/cm) and the intermediate products (i.e., lithium polysulfides Li_2S_x) formed during cycling along with their formidable structural and morphological changes, which can lead to unstable electrochemical contact within sulfur electrodes; ii) Li_2S_x, an intermediate polysulfide product, tends to dissolve in the electrolyte and shuttle between the anode and cathode during cycling, reacting with both the lithium metal anode and the sulfur cathode, i.e., the shuttle effect. In general, polymeric materials are implemented to address the problems with a Li-S battery in two ways: creating a sulfur/polymer composite or a polymer-based cathode/electrolyte interface (CEI).

The general merit for development of a sulfur/polymer composite cathode is to add doped element in order to strengthen the bonding energy between structure and sulfur or intermediate product during cycling, in order to reduce the shuttle effect. Polymers with functional groups, such as PAN, PPy, and PANI show a significant role in improving the performance of a Li-S battery by forming a sulfur/polymer composite. In general, when compared with sulfur/carbon composite, the sulfur/polymer composite has the following advantages: (1) lowered synthesis temperature and simpler synthetic methods; (2) providing a confining effect of the sulfur and intermediate product during cycling by interchain or intrachain bonding; (3) alleviated the volume change of cathode during cycling due to soft nature of the polymer with good resilience. A few strategies exploring sulfur/polymer composite are presented below.[112]

Sulfur−polyacrylonitrile composites (SPAN) was first applied as a cathode in a Li-S battery by Wang et al. in 2003 and they delivered a specific capacity of 1000 mAh/g using a 65% sulfur content in the composite.[113] The structure of SPAN was then further proposed by two groups, Yu et al.[114] and Fanous et al.[115] They both proposed the SPAN structure in which the short -Sx- chains covalently interacted with the dehydrogenated and cyclized PAN backbone. Archer et al. further reported a facile synthesis scheme of a family of SPAN composites that utilize specific interactions with nitrile groups on the polymer backbone and sulfur to promote ring formation and dehydrogenation.[116] Recently, Xie et al. designed a selenium-doped sulfurized polyacrylonitrile cathode which shows excellent electrochemical performance and outstanding compatibility with an ether-based electrolyte. The catalytic amount of Se-doping leads to a higher lithium ion diffusion coefficient and relatively low polarization, resulting in rapid conversion of polysulfide intermediates and fast reaction kinetics, which in turn prevents the dissolution of polysulfide intermediates in ether. It is believed that the solution by rapid and complete conversion from soluble Li_2S_n ($n \leq 4$) to insoluble Li_2S can also be applied in other similar cathodes involving formation of Li_2S_n ($n \leq 4$).[117]

Another application of polymers in Li-S batteries is for the polymer to be at the cathode electrolyte interface (CEI), in addition to the polymer electrolyte described in the previous section. The main advantages of having the polymer interface is to directly block the dissolution and diffusion of polysulfides. [118-124] A few examples have been demonstrated in the past few years. Chiang et al. showed that through multilayer encapsulation of sulfur particles the polysulfide shuttle can be significantly reduced, resulting in a more stable Li–S battery. Sulfur nanoparticles are encapsulated with manganese oxide particles as the inner layer and a layered polypyrrole as the outer layer. The reason for choosing polypyrrole are (1) its porous structure allows electrolyte

uptake; (2) its flexible network supports and contains the inner MnO_2 shell during discharging where the volumetric expansion of sulfur occurs, and (3) its remarkable electronic conductivity improves the bulk conductivity of the electrode and provides electronic charge transfer to the sulfur nanoparticles. SPPyMnO_2 electrode delivers a specific capacity of 1367 mAh/g at C/5 (charge or discharge of two Li in 5 h), corresponding to 81.7% of the theoretical capacity (1672 mAh/g). The bare sulfur electrode on the other hand, only delivers 47% of the theoretical value. Such high utilization in the nanocomposite can be attributed to the higher electrical conductivity of the SPPyMnO_2. Moreover, the double-layer coating delivers coulombic efficiency as high as 98%, when a binder-free electrode is used.[122] Xu et al. prepared a polysulfide-immobilizing polymer to address the shuttling issues. A natural polymer of gum arabic (GA) with precise oxygen-containing functional groups that can induce a strong binding interaction toward lithium polysulfides was deposited onto a conductive support of a carbon nanofiber (CNF) film as a polysulfide shielding interlayer. The as-obtained CNF–GA composite interlayer achieved outstanding performance with a high specific capacity of 880 mA h/g and maintain a specific capacity of 827 mAh/g after 250 cycles under a sulfur loading of 1.1 mg/cm.[123] Manthiram et al. used a similar strategy, but with different chemistries, they employed a thin layer of a polymer with intrinsic nanoporosity (PIN) on a Li^+ conductive solid electrolyte $Li_{1+x}Al_xTi_{2-x}(PO_4)_3$ (LATP), which significantly enhances the ionic interfaces between the electrodes and the solid electrolyte. In the full cell test, the smooth voltage profile and the reasonable discharge–charge voltages reveal that a facile ionic interface was achieved with the assistance of the PIN coating. In terms of long-term recycling stability, for the Li|PIN-LATP|S/C cell, capacity of around 800 mAh/g was maintained after 150 cycles while the Li|Celgard|S/C cell faded quickly starting from the beginning. The origin for the improvement of cycling stability of Li-S cells is the employment of the PIN polymer that prevents the invasion

of polysulfide species to the surface of LATP and maintains an adequate ionic interface contact between the sulfur–carbon composite cathode and the LATP membrane.[119]

1.7. Conclusions

A battery can be regarded as a closed multi-interface system, which includes electrolytes, anode, cathode, anode/electrolyte interface (SEI), cathode/electrolyte interface (CEI), anode/current-collector interface, cathode/current-collector interface, with active materials/electrons shuttling between each interface. By replacing graphite anode in a typical LIB with metallic lithium in an LMB, the interface between anode and electrolyte, or more often referred to as solid electrolyte interface (SEI), becomes much more unstable, with the dendrite issues being the most notable challenge. Due to the attractive high energy density of lithium metal and the resulting practical values, stabilization of the lithium metal anode interface has been regarded as the "holy grail" in the rechargeable battery industry. On the other hand, in order to match the high energy density of lithium metal, new higher-energy-density cathode materials have to be adopted, such as a nickel-rich high-voltage layered metal oxide or a non-lithium-containing sulfur cathode, which further leads to more interfacial problems.

It is obvious from the examples discussed above that functional polymers can be a vital building block for all the aforementioned major components of an LMB. These numerous approaches that have been emerging within recent years clearly represent a new perspective for achieving success with LMBs, that is, applying tailor-made functional polymers with a wide range of mechanical and electrochemical properties as a transient agent to optimize resistance, stability and transport properties at different interfaces in an LMB.

1.8. References

[1] Dresselhaus, M. S.; Thomas, I. L., Alternative energy technologies, *Nature* **2001,** 414, 332.

[2] Sutherland, B. R., Charging up Stationary Energy Storage, *Joule* **2019,** 3, 1.

[3] Nejat, P.; Jomehzadeh, F.; Taheri, M. M.; Gohari, M.; Abd. Majid, M. Z., A global review of energy consumption, CO2 emissions and policy in the residential sector (with an overview of the top ten CO2 emitting countries), *Renewable and Sustainable Energy Reviews* **2015,** 43, 843.

[4] Sovacool, B. K., The intermittency of wind, solar, and renewable electricity generators: Technical barrier or rhetorical excuse?, *Utilities Policy* **2009,** 17, 288.

[5] Zakeri, B.; Syri, S., Electrical energy storage systems: A comparative life cycle cost analysis, *Renewable and Sustainable Energy Reviews* **2015,** 42, 569.

[6] Ragauskas, A. J.; Williams, C. K.; Davison, B. H.; Britovsek, G.; Cairney, J.; Eckert, C. A.; Frederick, W. J.; Hallett, J. P.; Leak, D. J.; Liotta, C. L.; Mielenz, J. R.; Murphy, R.; Templer, R.; Tschaplinski, T., The Path Forward for Biofuels and Biomaterials, *Science* **2006,** 311, 484.

[7] Goodenough, J. B.; Kim, Y., Challenges for Rechargeable Li Batteries, *Chemistry of Materials* **2010,** 22, 587.

[8] Simon, P.; Gogotsi, Y., Materials for electrochemical capacitors, *Nature Materials* **2008,** 7, 845.

[9] Dunn, B.; Kamath, H.; Tarascon, J.-M., Electrical Energy Storage for the Grid: A Battery of Choices, *Science* **2011,** 334, 928.

[10] Winter, M.; Brodd, R. J., What Are Batteries, Fuel Cells, and Supercapacitors?, *Chemical Reviews* **2004,** 104, 4245.

[11] Goodenough, J. B.; Park, K.-S., The Li-Ion Rechargeable Battery: A Perspective, *Journal of the American Chemical Society* **2013,** 135, 1167.

[12] Whittingham, M. S., History, Evolution, and Future Status of Energy Storage, *Proceedings of the IEEE* **2012,** 100, 1518.

[13] Etacheri, V.; Marom, R.; Elazari, R.; Salitra, G.; Aurbach, D., Challenges in the development of advanced Li-ion batteries: a review, *Energy & Environmental Science* **2011,** 4, 3243.

[14] Lu, L.; Han, X.; Li, J.; Hua, J.; Ouyang, M., A review on the key issues for lithium-ion battery management in electric vehicles, *Journal of Power Sources* **2013,** 226, 272.

[15] Franke, T.; Neumann, I.; Bühler, F.; Cocron, P.; Krems, J. F., Experiencing Range in an Electric Vehicle: Understanding Psychological Barriers, *Applied Psychology* **2012,** 61, 368.

[16] Lin, Z.; Liu, T.; Ai, X.; Liang, C., Aligning academia and industry for unified battery performance metrics, *Nature Communications* **2018,** 9, 5262.

[17] Lin, D.; Liu, Y.; Cui, Y., Reviving the lithium metal anode for high-energy batteries, *Nature Nanotechnology* **2017,** 12, 194.

[18] Bruce, P. G.; Freunberger, S. A.; Hardwick, L. J.; Tarascon, J.-M., Li–O2 and Li–S batteries with high energy storage, *Nature Materials* **2011,** 11, 19.

[19] Lu, Y.; Rong, X.; Hu, Y.-S.; Li, H.; Chen, L., Research and development of advanced battery materials in China, *Energy Storage Materials* **2019**.

[20] Tikekar, M. D.; Choudhury, S.; Tu, Z.; Archer, L. A., Design principles for electrolytes and interfaces for stable lithium-metal batteries, *Nature Energy* **2016,** 1, 16114.

[21] Ren, X.; Zou, L.; Cao, X.; Engelhard, M. H.; Liu, W.; Burton, S. D.; Lee, H.; Niu, C.; Matthews, B. E.; Zhu, Z.; Wang, C.; Arey, B. W.; Xiao, J.; Liu, J.; Zhang, J.-G.; Xu, W., Enabling High-Voltage Lithium-Metal Batteries under Practical Conditions, *Joule* **2019,** 3, 1662.

[22] Karayaylali, P.; Tatara, R.; Zhang, Y.; Chan, K.-L.; Yu, Y.; Giordano, L.; Maglia, F.; Jung, R.; Lund, I.; Shao-Horn, Y., Editors' Choice—Coating-Dependent Electrode-Electrolyte Interface

for Ni-Rich Positive Electrodes in Li-Ion Batteries, *Journal of The Electrochemical Society* **2019,** 166, A1022.

[23] Chen, W.; Lei, T.; Wu, C.; Deng, M.; Gong, C.; Hu, K.; Ma, Y.; Dai, L.; Lv, W.; He, W.; Liu, X.; Xiong, J.; Yan, C., Designing Safe Electrolyte Systems for a High-Stability Lithium–Sulfur Battery, *Advanced Energy Materials* **2018,** 8, 1702348.

[24] Li, S.; Mohamed, A. I.; Pande, V.; Wang, H.; Cuthbert, J.; Pan, X.; He, H.; Wang, Z.; Viswanathan, V.; Whitacre, J. F.; Matyjaszewski, K., Single-Ion Homopolymer Electrolytes with High Transference Number Prepared by Click Chemistry and Photoinduced Metal-Free Atom-Transfer Radical Polymerization, *ACS Energy Letters* **2018,** 3, 20.

[25] Matyjaszewski, K., Advanced Materials by Atom Transfer Radical Polymerization, *Advanced Materials* **2018,** 30, 1706441.

[26] Gauthier, M. A.; Gibson, M. I.; Klok, H.-A., Synthesis of Functional Polymers by Post-Polymerization Modification, *Angewandte Chemie International Edition* **2009,** 48, 48.

[27] Zheng, Y.; Li, S.; Weng, Z.; Gao, C., Hyperbranched polymers: advances from synthesis to applications, *Chemical Society Reviews* **2015,** 44, 4091.

[28] Schacher, F. H.; Rupar, P. A.; Manners, I., Functional Block Copolymers: Nanostructured Materials with Emerging Applications, *Angewandte Chemie International Edition* **2012,** 51, 7898.

[29] Novák, P.; Müller, K.; Santhanam, K. S. V.; Haas, O., Electrochemically Active Polymers for Rechargeable Batteries, *Chemical Reviews* **1997,** 97, 207.

[30] Aida, T.; Meijer, E. W.; Stupp, S. I., Functional Supramolecular Polymers, *Science* **2012,** 335, 813.

[31] Choi, S.; Kwon, T.-w.; Coskun, A.; Choi, J. W., Highly elastic binders integrating polyrotaxanes for silicon microparticle anodes in lithium ion batteries, *Science* **2017,** 357, 279.

[32] Zhang, W.; Tu, Z.; Qian, J.; Choudhury, S.; Archer, L. A.; Lu, Y., Design Principles of Functional Polymer Separators for High-Energy, Metal-Based Batteries, *Small* **2018,** 14, 1703001.

[33] Bouchet, R.; Maria, S.; Meziane, R.; Aboulaich, A.; Lienafa, L.; Bonnet, J.-P.; Phan, T. N. T.; Bertin, D.; Gigmes, D.; Devaux, D.; Denoyel, R.; Armand, M., Single-ion BAB triblock copolymers as highly efficient electrolytes for lithium-metal batteries, *Nature Materials* **2013,** 12, 452.

[34] Janoschka, T.; Martin, N.; Martin, U.; Friebe, C.; Morgenstern, S.; Hiller, H.; Hager, M. D.; Schubert, U. S., An aqueous, polymer-based redox-flow battery using non-corrosive, safe, and low-cost materials, *Nature* **2015,** 527, 78.

[35] Li, C.; Liu, S.; Shi, C.; Liang, G.; Lu, Z.; Fu, R.; Wu, D., Two-dimensional molecular brush-functionalized porous bilayer composite separators toward ultrastable high-current density lithium metal anodes, *Nature Communications* **2019,** 10, 1363.

[36] Lu, J.; Li, L.; Park, J.-B.; Sun, Y.-K.; Wu, F.; Amine, K., Aprotic and Aqueous Li–O2 Batteries, *Chemical Reviews* **2014,** 114, 5611.

[37] Christensen, J.; Albertus, P.; Sanchez-Carrera, R. S.; Lohmann, T.; Kozinsky, B.; Liedtke, R.; Ahmed, J.; Kojic, A., A Critical Review of Li/Air Batteries, *Journal of The Electrochemical Society* **2011,** 159, R1.

[38] Xia, S.; Wu, X.; Zhang, Z.; Cui, Y.; Liu, W., Practical challenges and future perspectives of all-solid-state lithium-metal batteries, *Chem* **2018**.

[39] Zhou, D.; Shanmukaraj, D.; Tkacheva, A.; Armand, M.; Wang, G., Polymer Electrolytes for Lithium-Based Batteries: Advances and Prospects, *Chem* **2019**.

[40] Zhang, X.-Q.; Cheng, X.-B.; Zhang, Q., Advances in Interfaces between Li Metal Anode and Electrolyte, *Advanced Materials Interfaces* **2018,** 5, 1701097.

[41] Dudney, N. J., Glass and Ceramic Electrolytes for Lithium and Lithium-Ion Batteries. In *Lithium Batteries: Science and Technology*, Nazri, G.-A.; Pistoia, G., Eds. Springer US: Boston, MA, 2003; pp 624.

[42] Berthier, C.; Gorecki, W.; Minier, M.; Armand, M.; Chabagno, J.; Rigaud, P., Microscopic investigation of ionic conductivity in alkali metal salts-poly (ethylene oxide) adducts, *Solid State Ionics* **1983,** 11, 91.

[43] Mindemark, J.; Lacey, M. J.; Bowden, T.; Brandell, D., Beyond PEO—alternative host materials for Li+-conducting solid polymer electrolytes, *Progress in Polymer Science* **2018,** 81, 114.

[44] Feng, S.; Chen, M.; Giordano, L.; Huang, M.; Zhang, W.; Amanchukwu, C. V.; Anandakathir, R.; Shao-Horn, Y.; Johnson, J. A., Mapping a stable solvent structure landscape for aprotic Li–air battery organic electrolytes, *Journal of Materials Chemistry A* **2017,** 5, 23987.

[45] Choe, H. S.; Carroll, B. G.; Pasquariello, D. M.; Abraham, K. M., Characterization of Some Polyacrylonitrile-Based Electrolytes, *Chemistry of Materials* **1997,** 9, 369.

[46] Sarapas, J. M.; Tew, G. N., Poly(ether–thioethers) by Thiol–Ene Click and Their Oxidized Analogues as Lithium Polymer Electrolytes, *Macromolecules* **2016,** 49, 1154.

[47] Zhou, W.; Wang, Z.; Pu, Y.; Li, Y.; Xin, S.; Li, X.; Chen, J.; Goodenough, J. B., Double-Layer Polymer Electrolyte for High-Voltage All-Solid-State Rechargeable Batteries, *Advanced Materials* **2019,** 31, 1805574.

[48] Meabe, L.; Huynh, T. V.; Lago, N.; Sardon, H.; Li, C.; O'Dell, L. A.; Armand, M.; Forsyth, M.; Mecerreyes, D., Poly (ethylene oxide carbonates) solid polymer electrolytes for lithium batteries, *Electrochimica Acta* **2018,** 264, 367.

[49] Mackanic, D. G.; Michaels, W.; Lee, M.; Feng, D.; Lopez, J.; Qin, J.; Cui, Y.; Bao, Z., Crosslinked poly (tetrahydrofuran) as a loosely coordinating polymer electrolyte, *Advanced Energy Materials* **2018,** 8, 1800703.

[50] Helms, B. A.; Seferos, D. S., Virtual Issue: Designing Polymers for Use in Electrochemical Energy Storage Devices, *Macromolecules* **2019,** 52, 1349.

[51] Shipp, D. A., Reversible-Deactivation Radical Polymerizations, *Polymer Reviews* **2011,** 51, 99.

[52] Bergfelt, A.; Rubatat, L.; Brandell, D.; Bowden, T., Poly (benzyl methacrylate)-poly [(oligo ethylene glycol) methyl ether methacrylate] triblock-copolymers as solid electrolyte for lithium batteries, *Solid State Ionics* **2018,** 321, 55.

[53] Rosenbach, D.; Mödl, N.; Hahn, M.; Petry, J.; Danzer, M. A.; Thelakkat, M., Synthesis and Comparative Studies of Solvent-Free Brush Polymer Electrolytes for Lithium Batteries, *ACS Applied Energy Materials* **2019,** 2, 3373.

[54] Xu, H.; Wang, A.; Liu, X.; Feng, D.; Wang, S.; Chen, J.; An, Y.; Zhang, L., A new fluorine-containing star-branched polymer as electrolyte for all-solid-state lithium-ion batteries, *Polymer* **2018,** 146, 249.

[55] Zhang, Y.; Costantini, N.; Mierzwa, M.; Pakula, T.; Neugebauer, D.; Matyjaszewski, K., Super soft elastomers as ionic conductors, *Polymer* **2004,** 45, 6333.

[56] Li, N.-W.; Shi, Y.; Yin, Y.-X.; Zeng, X.-X.; Li, J.-Y.; Li, C.-J.; Wan, L.-J.; Wen, R.; Guo, Y.-G., A Flexible Solid Electrolyte Interphase Layer for Long-Life Lithium Metal Anodes, *Angewandte Chemie International Edition* **2018,** 57, 1505.

[57] Liu, W.; Lin, D.; Sun, J.; Zhou, G.; Cui, Y., Improved Lithium Ionic Conductivity in Composite Polymer Electrolytes with Oxide-Ion Conducting Nanowires, *ACS Nano* **2016,** 10, 11407.

[58] Liu, W.; Lee, S. W.; Lin, D.; Shi, F.; Wang, S.; Sendek, A. D.; Cui, Y., Enhancing ionic conductivity in composite polymer electrolytes with well-aligned ceramic nanowires, *Nature energy* **2017,** 2, 17035.

[59] Choudhury, S.; Vu, D.; Warren, A.; Tikekar, M. D.; Tu, Z.; Archer, L. A., Confining electrodeposition of metals in structured electrolytes, *Proceedings of the National Academy of Sciences* **2018,** 115, 6620.

[60] Brissot, C.; Rosso, M.; Chazalviel, J.-N.; Lascaud, S., Dendritic growth mechanisms in lithium/polymer cells, *Journal of power sources* **1999,** 81, 925.

[61] Zhang, H.; Li, C.; Piszcz, M.; Coya, E.; Rojo, T.; Rodriguez-Martinez, L. M.; Armand, M.; Zhou, Z., Single lithium-ion conducting solid polymer electrolytes: advances and perspectives, *Chemical Society Reviews* **2017,** 46, 797.

[62] Prosini, P. P.; Banow, B., Composite polyether electrolytes with a poly(styrenesulfonate) lithium salt and Lewis acid type additive, *Electrochimica acta* **2003,** 48, 1899.

[63] Rolland, J.; Poggi, E.; Vlad, A.; Gohy, J.-F., Single-ion diblock copolymers for solid-state polymer electrolytes, *Polymer (Guilford)* **2015,** 68, 344.

[64] Sun, X.-G.; Kerr, J. B., Synthesis and Characterization of Network Single Ion Conductors Based on Comb-Branched Polyepoxide Ethers and Lithium Bis(allylmalonato)borate, *Macromolecules* **2006,** 39, 362.

[65] Bouchet, R.; Maria, S.; Meziane, R.; Aboulaich, A.; Lienafa, L., Single-ion BAB triblock copolymers as highly efficient electrolytes for lithium-metal batteries, *Nat. Mater.* **2013,** 12, 452.

[66] Ma, Q.; Zhang, H.; Zhou, C.; Zheng, L.; Cheng, P.; Nie, J.; Feng, W.; Hu, Y. S.; Li, H.; Huang, X.; Chen, L.; Armand, M.; Zhou, Z., Single Lithium-Ion Conducting Polymer Electrolytes Based on a Super-Delocalized Polyanion, *Angew. Chem. Int. Ed.* **2016,** 55, 2521.

[67] Morris, M. A.; An, H.; Lutkenhaus, J. L.; Epps, T. H., Harnessing the Power of Plastics: Nanostructured Polymer Systems in Lithium-Ion Batteries, *ACS Energy Letters* **2017,** 2, 1919.

[68] Krimalowski, A.; Thelakkat, M., Sequential Co-Click Reactions with Poly(glycidyl propargyl ether) toward Single-Ion Conducting Electrolytes, *Macromolecules* **2019,** 52, 4042.

[69] Lopez, J.; Sun, Y.; Mackanic, D. G.; Lee, M.; Foudeh, A. M.; Song, M. S.; Cui, Y.; Bao, Z., A Dual-Crosslinking Design for Resilient Lithium-Ion Conductors, *Advanced Materials* **2018,** 30, 1804142.

[70] Schulze, M. W.; McIntosh, L. D.; Hillmyer, M. A.; Lodge, T. P., High-modulus, high-conductivity nanostructured polymer electrolyte membranes via polymerization-induced phase separation, *Nano letters* **2013,** 14, 122.

[71] Wan, J.; Xie, J.; Kong, X.; Liu, Z.; Liu, K.; Shi, F.; Pei, A.; Chen, H.; Chen, W.; Chen, J.; Zhang, X.; Zong, L.; Wang, J.; Chen, L.-Q.; Qin, J.; Cui, Y., Ultrathin, flexible, solid polymer composite electrolyte enabled with aligned nanoporous host for lithium batteries, *Nature Nanotechnology* **2019,** 14, 705.

[72] Zhao, Q.; Liu, X. T.; Stalin, S.; Khan, K.; Archer, L. A., Solid-state polymer electrolytes with in-built fast interfacial transport for secondary lithium batteries, *Nature Energy* **2019,** 4, 365.

[73] Yang, C.; Fu, K.; Zhang, Y.; Hitz, E.; Hu, L., Protected Lithium-Metal Anodes in Batteries: From Liquid to Solid, *Advanced Materials* **2017,** 29, 1701169.

[74] Peled, E., The Electrochemical Behavior of Alkali and Alkaline Earth Metals in Nonaqueous Battery Systems—The Solid Electrolyte Interphase Model, *Journal of The Electrochemical Society* **1979,** 126, 2047.

[75] Peled, E.; Golodnitsky, D.; Ardel, G., Advanced Model for Solid Electrolyte Interphase Electrodes in Liquid and Polymer Electrolytes, *Journal of The Electrochemical Society* **1997,** 144, L208.

[76] Aurbach, D.; Markovsky, B.; Levi, M. D.; Levi, E.; Schechter, A.; Moshkovich, M.; Cohen, Y., New insights into the interactions between electrode materials and electrolyte solutions for advanced nonaqueous batteries, *Journal of Power Sources* **1999,** 81-82, 95.

[77] Winter, M., The Solid Electrolyte Interphase – The Most Important and the Least Understood Solid Electrolyte in Rechargeable Li Batteries. In *Zeitschrift für Physikalische Chemie*, 2009; Vol. 223, p 1395.

[78] Verma, P.; Maire, P.; Novák, P., A review of the features and analyses of the solid electrolyte interphase in Li-ion batteries, *Electrochimica Acta* **2010,** 55, 6332.

[79] Peled, E.; Menkin, S., Review—SEI: Past, Present and Future, *Journal of The Electrochemical Society* **2017,** 164, A1703.

[80] Zheng, G.; Wang, C.; Pei, A.; Lopez, J.; Shi, F.; Chen, Z.; Sendek, A. D.; Lee, H.-W.; Lu, Z.; Schneider, H.; Safont-Sempere, M. M.; Chu, S.; Bao, Z.; Cui, Y., High-Performance Lithium Metal Negative Electrode with a Soft and Flowable Polymer Coating, *ACS Energy Letters* **2016,** 1, 1247.

[81] Liu, K.; Pei, A.; Lee, H. R.; Kong, B.; Liu, N.; Lin, D.; Liu, Y.; Liu, C.; Hsu, P.-c.; Bao, Z.; Cui, Y., Lithium Metal Anodes with an Adaptive "Solid-Liquid" Interfacial Protective Layer, *Journal of the American Chemical Society* **2017,** 139, 4815.

[82] Zhu, B.; Jin, Y.; Hu, X.; Zheng, Q.; Zhang, S.; Wang, Q.; Zhu, J., Poly(dimethylsiloxane) Thin Film as a Stable Interfacial Layer for High-Performance Lithium-Metal Battery Anodes, *Advanced Materials* **2017,** 29, 1603755.

[83] Ma, L.; Fu, C.; Li, L.; Mayilvahanan, K. S.; Watkins, T.; Perdue, B. R.; Zavadil, K. R.; Helms, B. A., Nanoporous Polymer Films with a High Cation Transference Number Stabilize Lithium Metal Anodes in Light-Weight Batteries for Electrified Transportation, *Nano Letters* **2019,** 19, 1387.

[84] Pang, Q.; Zhou, L.; Nazar, L. F., Elastic and Li-ion–percolating hybrid membrane stabilizes Li metal plating, *Proceedings of the National Academy of Sciences* **2018,** 115, 12389.

[85] Zhao, Y.; Li, G.; Gao, Y.; Wang, D.; Huang, Q.; Wang, D., Stable Li Metal Anode by a Hybrid Lithium Polysulfidophosphate/Polymer Cross-Linking Film, *ACS Energy Letters* **2019,** 4, 1271.

[86] Liu, W.; Li, W.; Zhuo, D.; Zheng, G.; Lu, Z.; Liu, K.; Cui, Y., Core–Shell Nanoparticle Coating as an Interfacial Layer for Dendrite-Free Lithium Metal Anodes, *ACS Central Science* **2017,** 3, 135.

[87] Liu, Y.; Lin, D.; Yuen, P. Y.; Liu, K.; Xie, J.; Dauskardt, R. H.; Cui, Y., An Artificial Solid Electrolyte Interphase with High Li-Ion Conductivity, Mechanical Strength, and Flexibility for Stable Lithium Metal Anodes, *Advanced Materials* **2017,** 29, 1605531.

[88] Lu, Y.; Tu, Z.; Archer, L. A., Stable lithium electrodeposition in liquid and nanoporous solid electrolytes, *Nature Materials* **2014,** 13, 961.

[89] Wang, H.; Lin, D.; Xie, J.; Liu, Y.; Chen, H.; Li, Y.; Xu, J.; Zhou, G.; Zhang, Z.; Pei, A.; Zhu, Y.; Liu, K.; Wang, K.; Cui, Y., An Interconnected Channel-Like Framework as Host for Lithium Metal Composite Anodes, *Advanced Energy Materials* **2019,** 9, 1802720.

[90] Foroozan, T.; Soto, F. A.; Yurkiv, V.; Sharifi-Asl, S.; Deivanayagam, R.; Huang, Z.; Rojaee, R.; Mashayek, F.; Balbuena, P. B.; Shahbazian-Yassar, R., Synergistic Effect of Graphene Oxide for Impeding the Dendritic Plating of Li, *Advanced Functional Materials* **2018,** 28, 1705917.

[91] Bai, M.; Xie, K.; Yuan, K.; Zhang, K.; Li, N.; Shen, C.; Lai, Y.; Vajtai, R.; Ajayan, P.; Wei, B., A Scalable Approach to Dendrite-Free Lithium Anodes via Spontaneous Reduction of Spray-Coated Graphene Oxide Layers, *Advanced Materials* **2018,** 30, 1801213.

[92] Pu, J.; Li, J.; Shen, Z.; Zhong, C.; Liu, J.; Ma, H.; Zhu, J.; Zhang, H.; Braun, P. V., Interlayer Lithium Plating in Au Nanoparticles Pillared Reduced Graphene Oxide for Lithium Metal Anodes, *Advanced Functional Materials* **2018,** 28, 1804133.

[93] Chen, Y.-T.; Abbas, S. A.; Kaisar, N.; Wu, S. H.; Chen, H.-A.; Boopathi, K. M.; Singh, M.; Fang, J.; Pao, C.-W.; Chu, C.-W., Mitigating Metal Dendrite Formation in Lithium–Sulfur Batteries via Morphology-Tunable Graphene Oxide Interfaces, *ACS Applied Materials & Interfaces* **2019,** 11, 2060.

[94] Gao, Y.; Yan, Z.; Gray, J. L.; He, X.; Wang, D.; Chen, T.; Huang, Q.; Li, Y. C.; Wang, H.; Kim, S. H.; Mallouk, T. E.; Wang, D., Polymer–inorganic solid–electrolyte interphase for stable lithium metal batteries under lean electrolyte conditions, *Nature Materials* **2019,** 18, 384.

[95] Lin, D.; Liu, Y.; Liang, Z.; Lee, H.-W.; Sun, J.; Wang, H.; Yan, K.; Xie, J.; Cui, Y., Layered reduced graphene oxide with nanoscale interlayer gaps as a stable host for lithium metal anodes, *Nature Nanotechnology* **2016,** 11, 626.

[96] Lin, D.; Liu, Y.; Pei, A.; Cui, Y., Nanoscale perspective: Materials designs and understandings in lithium metal anodes, *Nano Research* **2017,** 10, 4003.

[97] Li, G.; Liu, Z.; Huang, Q.; Gao, Y.; Regula, M.; Wang, D.; Chen, L.-Q.; Wang, D., Stable metal battery anodes enabled by polyethylenimine sponge hosts by way of electrokinetic effects, *Nature Energy* **2018,** 3, 1076.

[98] Xia, S.; Wu, X.; Zhang, Z.; Cui, Y.; Liu, W., Practical Challenges and Future Perspectives of All-Solid-State Lithium-Metal Batteries, *Chem* **2019,** 5, 753.

[99] Liu, Y.; Lin, D.; Jin, Y.; Liu, K.; Tao, X.; Zhang, Q.; Zhang, X.; Cui, Y., Transforming from planar to three-dimensional lithium with flowable interphase for solid lithium metal batteries, *Science Advances* **2017,** 3, eaao0713.

[100] Albertus, P.; Babinec, S.; Litzelman, S.; Newman, A., Status and challenges in enabling the lithium metal electrode for high-energy and low-cost rechargeable batteries, *Nature Energy* **2018,** 3, 16.

[101] Wang, L.; Chen, B.; Ma, J.; Cui, G.; Chen, L., Reviving lithium cobalt oxide-based lithium secondary batteries-toward a higher energy density, *Chemical Society Reviews* **2018,** 47, 6505.

[102] Wu, F.; Liu, J. R.; Li, L.; Zhang, X. X.; Luo, R.; Ye, Y. S.; Chen, R. J., Surface Modification of Li-Rich Cathode Materials for Lithium-Ion Batteries with a PEDOT:PSS Conducting Polymer, *Acs Applied Materials & Interfaces* **2016,** 8, 23095.

[103] Gao, X. W.; Wang, J. Z.; Chou, S. L.; Liu, H. K., Synthesis and electrochemical performance of LiV3O8/polyaniline as cathode material for the lithium battery, *J Power Sources* **2012,** 220, 47.

[104] Kwon, Y.; Lee, Y.; Kim, S. O.; Kim, H. S.; Kim, K. J.; Byun, D.; Choi, W., Conducting Polymer Coating on a High-Voltage Cathode Based on Soft Chemistry Approach toward Improving Battery Performance, *Acs Applied Materials & Interfaces* **2018,** 10, 29457.

[105] Gan, Q. M.; Qin, N.; Zhu, Y. H.; Huang, Z. X.; Zhang, F. C.; Gu, S.; Xie, J. W.; Zhang, K. L.; Lu, L.; Lu, Z. G., Polyvinylpyrrolidone-Induced Uniform Surface-Conductive Polymer Coating Endows Ni-Rich LiNi0.8Co0.1Mn0.1O2 with Enhanced Cyclability for Lithium-Ion Batteries, *Acs Applied Materials & Interfaces* **2019,** 11, 12594.

[106] Xu, G. L.; Liu, Q.; Lau, K. K. S.; Liu, Y.; Liu, X.; Gao, H.; Zhou, X. W.; Zhuang, M. H.; Ren, Y.; Li, J. D.; Shao, M. H.; Ouyang, M. G.; Pan, F.; Chen, Z. H.; Amine, K.; Chen, G. H., Building ultraconformal protective layers on both secondary and primary particles of layered lithium transition metal oxide cathodes, *Nature Energy* **2019,** 4, 484.

[107] Dong, H. Y.; Zhang, Y. J.; Zhang, S. Q.; Tang, P. P.; Xiao, X. L.; Ma, M. Y.; Zhang, H. S.; Yin, Y. H.; Wang, D.; Yang, S. T., Improved High Temperature Performance of a Spinel LiNi0.5Mn1.5O4 Cathode for High-Voltage Lithium-Ion Batteries by Surface Modification of a Flexible Conductive Nanolayer, *Acs Omega* **2019,** 4, 185.

[108] Ju, S. H.; Kang, I. S.; Lee, Y. S.; Shin, W. K.; Kim, S.; Shin, K.; Kim, D. W., Improvement of the Cycling Performance of LiNi0.6Co0.2Mn0.2O2 Cathode Active Materials by a Dual-Conductive Polymer Coating, *Acs Applied Materials & Interfaces* **2014,** 6, 2546.

[109] Gao, X. W.; Deng, Y. F.; Wexler, D.; Chen, G. H.; Chou, S. L.; Liu, H. K.; Shi, Z. C.; Wang, J. Z., Improving the electrochemical performance of the LiNi0.5Mn1.5O4 spinel by polypyrrole coating as a cathode material for the lithium-ion battery, *J Mater Chem A* **2015,** 3, 404.

[110] Su, L. S.; Smith, P. M.; Anand, P.; Reeja-Jayan, B., Surface Engineering of a LiMn2O4 Electrode Using Nanoscale Polymer Thin Films via Chemical Vapor Deposition Polymerization, *Acs Applied Materials & Interfaces* **2018,** 10, 27063.

[111] Sun, B.; El Kazzi, M.; Müller, E.; Berg, E. J., Toward high-performance Li (Ni x Co y Mn z) O 2 cathodes: facile fabrication of an artificial polymeric interphase using functional polyacrylates, *J Mater Chem A* **2018,** 6, 17778.

[112] Dong, C. W.; Gao, W.; Jin, B.; Jiang, Q., Advances in Cathode Materials for High-Performance Lithium-Sulfur Batteries, *Iscience* **2018,** 6, 151.

[113] Wang, J. L.; Yang, J.; Xie, J. Y.; Xu, N. X., A novel conductive polymer-sulfur composite cathode material for rechargeable lithium batteries, *Advanced Materials* **2002,** 14, 963.

[114] Yu, X. G.; Xie, J. Y.; Yang, J.; Huang, H. J.; Wang, K.; Wen, Z. S., Lithium storage in conductive sulfur-containing polymers, *J Electroanal Chem* **2004,** 573, 121.

[115] Fanous, J.; Wegner, M.; Grimminger, J.; Andresen, A.; Buchmeiser, M. R., Structure-Related Electrochemistry of Sulfur-Poly(acrylonitrile) Composite Cathode Materials for Rechargeable Lithium Batteries, *Chem Mater* **2011,** 23, 5024.

[116] Wei, S. Y.; Ma, L.; Hendrickson, K. E.; Tu, Z. Y.; Archer, L. A., Metal-Sulfur Battery Cathodes Based on PAN Sulfur Composites, *Journal of the American Chemical Society* **2015,** 137, 12143.

[117] Chen, X.; Peng, L. F.; Wang, L. H.; Yang, J. Q.; Hao, Z. X.; Xiang, J. W.; Yuan, K.; Huang, Y. H.; Shan, B.; Yuan, L. X.; Xie, J., Ether-compatible sulfurized polyacrylonitrile cathode with excellent performance enabled by fast kinetics via selenium doping, *Nat Commun* **2019,** 10.

[118] Lee, J.; Song, J.; Lee, H.; Noh, H.; Kim, Y. J.; Kwon, S. H.; Lee, S. G.; Kim, H. T., A Nanophase-Separated, Quasi-Solid-State Polymeric Single-Ion Conductor: Polysulfide Exclusion for Lithium-Sulfur Batteries, *Acs Energy Lett* **2017,** 2, 1232.

[119] Yu, X. W.; Manthiram, A., Enhanced Interfacial Stability of Hybrid-Electrolyte Lithium-Sulfur Batteries with a Layer of Multifunctional Polymer with Intrinsic Nanoporosity, *Adv Funct Mater* **2019,** 29.

[120] Yao, H. B.; Yan, K.; Li, W. Y.; Zheng, G. Y.; Kong, D. S.; Seh, Z. W.; Narasimhan, V. K.; Liang, Z.; Cui, Y., Improved lithium-sulfur batteries with a conductive coating on the separator to prevent the accumulation of inactive S-related species at the cathode-separator interface, *Energy & Environmental Science* **2014,** 7, 3381.

[121] Zhao, Q.; Zheng, J. X.; Archer, L., Interphases in Lithium-Sulfur Batteries: Toward Deployable Devices with Competitive Energy Density and Stability, *Acs Energy Lett* **2018,** 3, 2104.

[122] Ansari, Y.; Zhang, S.; Wen, B. H.; Fan, F.; Chiang, Y. M., Stabilizing Li-S Battery Through Multilayer Encapsulation of Sulfur, *Adv Energy Mater* **2019,** 9.

[123] Tu, S. B.; Chen, X.; Zhao, X. X.; Cheng, M. R.; Xiong, P. X.; He, Y. W.; Zhang, Q.; Xu, Y., A Polysulfide-Immobilizing Polymer Retards the Shuttling of Polysulfide Intermediates in Lithium-Sulfur Batteries, *Advanced Materials* **2018,** 30.

[124] Xu, H. H.; Wang, S. F.; Manthiram, A., Hybrid Lithium-Sulfur Batteries with an Advanced Gel Cathode and Stabilized Lithium-Metal Anode, *Adv Energy Mater* **2018,** 8.

Chapter 2. Single-ion Polymer Electrolytes

2.1. Preface

Rechargeable batteries with lithium metal anodes are the most viable future technology to provide batteries with higher energy density. However, the low stability of lithium metal anodes under reductive conditions, low transference number and flammability of typical liquid electrolytes lead to high incompatibility with the solid lithium metal. Solid electrolytes are therefore regarded as critical possible replacements of liquid electrolytes. In general, there are two types of solid electrolytes– ceramic Li^+ conductors and polymer electrolytes. Although ceramic Li^+ conductors could have high ionic conductivity and transference number, the difficulty to produce and handle them, as well as the insufficient contact at the anode/electrolyte interface, greatly limited their practicability. In contrast, polymer electrolytes have received great attention as this type of electrolyte can possibly overcome the flaws that have been limiting ceramic electrolytes, especially due to the adaptable nature of polymeric materials. However, typical polymer electrolytes have lower ionic conductivity and lower transference number, and sometimes poor mechanical strength. Therefore, it is highly desirable to find a general synthetic way to create lithium ion conducting polymer electrolytes that feature high transference number, improved ionic conductivity and stability as well as higher mechanical strength.

Bearing these goals in mind, I designed two types of polymer-based electrolytes with high transference number and high ionic conductivity. I designed all of the experiments, performed all of the synthetic experiments and electrochemical tests. Nevertheless, I would like to especially thank Prof. Venkat Viswanathan and Dr. Vikram Pande from Department of Mechanical Engineering at CMU for their contribution in modeling and computation. I would like to thank Han Wang, Julia Cuthbert andZongyu Wang for contribution in materials characterizations,

Hongkun He and Xiangcheng Pan for their contribution in polymer synthesis, Francesca Lorandi for her contribution in paper writing.

These projects resulted in two first-author publication: (1) Sipei Li, Alexander I. Mohamed, Vikram Pande, Han Wang, Julia Cuthbert, Xiangcheng Pan, Hongkun He, Zongyu Wang, Venkatasubramanian Viswanathan, Jay F. Whitacre, Krzysztof Matyjaszewski, "Single-Ion Homopolymer Electrolytes with High Transference Number Prepared by Click Chemistry and Photoinduced Metal-Free Atom-Transfer Radical Polymerization", *ACS Energy Lett.,* **2018,** 3, 20. (impact factor 16.331) and (2) Sipei Li, Francesca Lorandi, Jay F. Whitacre, Krzysztof Matyjaszewski, "Polymer Chemistry for Improving Lithium Metal Anodes", *Macromol. Chem. Phys.*, **2019**, 1900379. This work was supported by the National Science Foundation (DMR 1501324), U.S. Department of Energy, Energy Efficiency and Renewable Energy Vehicle Technologies Office under Award Number DE-EE0007810.

2.2. Single-ion Polymer Electrolyte by Photo-ATRP

2.2.1. Introduction

The urge for higher energy density has driven development of new anode materials, such as silicon and lithium metal.[1, 2] However, adopting such electrodes generates strict safety requirements towards the electrolyte materials,[3, 4] especially regarding the suppression of lithium dendrite formation.[5] Typical electrolytes for lithium ion batteries are dual-ion conductors, with mobile cations and anions that employ combustible organic solvents. This generates a lithium concentration gradient and cell polarization, which can lead to development of lithium dendrites.[6, 7] Once lithium dendrites are formed, they continue to grow until they puncture the battery separator, leading to an internal short circuit and possible thermal runaway of the battery.

Five major approaches have been examined to suppress lithium dendrites growth: formation of an anode surface coating, either formed *in situ*[8] or *ex situ*[5]; incorporation of additives (such as LiF[9]) that stabilize lithium electrodeposition; adoption of solid electrolytes with shear moduli higher than that of the tip of a lithium dendrite (10^9 Pa)[10, 11]; adoption of tortuous, nanoporous separators[12-14]; and adoption of single-ion lithium conductors featuring high transference numbers.[15]

The "single-ion" approach featuring high transference number (t_+) has proven to be one of the most efficient ways to suppress dendrites because it minimizes the concentration gradient near the anode, thereby lowering the driving force for dendrite formation.[16, 17] Typically, there are two types of single-ion lithium conductors, ceramic lithium super ionic conductors and single-ion polymer electrolytes. The single-ion polymer electrolytes are made by covalently immobilizing anions onto the polymeric backbones.[15] Compared to ceramics, polymeric single-ion electrolytes have several advantages such as facile preparation, ability to form thin membranes, tunable mechanical strength, and chemical stability.[18-21] Therefore, extensive efforts have been made to develop single-ion polymer electrolytes with high ionic conductivities and transference numbers.

Currently, four types of single-ion polymer electrolytes have been reported: sulfonate-based,[22, 23] acrylate-based,[24] borate-based,[25-28] and sulfonyl(trifluoromethylsulfonyl)imide-based ($TFSI^-$) polymers[29]. The weak coordination between the bulky $TFSI^-$ anion and lithium ion leads to high lithium conductivity in the electrolytes. Therefore, the fourth type of electrolytes have emerged to be the most promising. Armand *et al.* reported the polystyrene-based single-ion electrolytes by attaching $TFSI^-Li^+$ ion pairs onto the p-position of the phenyl group (STFSILi).[15, 30] An ABA triblock copolymer (polySTFSILi-PEO-polySTFSILi) was prepared with the middle PEO block providing an ionic conductivity of 4×10^{-5} S/cm at 90 °C and t_+ of >0.85.[31] Long et al.

reported an A-BC-A triblock copolymer with randomly copolymerized polyOEGMA-polySTFSILi as the middle block. The polymer showed conductivity of 8 $\times 10^{-6}$ S/cm at 90 °C.[32] Balsara *et al.* prepared blends of PS-b-PEO with poly(octahedral silsesquioxane) (POSS) modified polySTFSILi. The blends system showed ionic conductivity around 10^{-5} S/cm at 90 °C and t_+ of 0.98.[33] However, the polystyrene backbone is unfavorable for lithium conduction and it requires the introduction of either a covalent conductive block of poly(ethylene glycol) (PEO) or a blend with plasticizers to assist lithium conduction.[32-37] Such procedures unavoidably complicate the preparation of electrolytes and the t_+ is usually below 0.93. Also, it still remained a challenge to develop solvent-free single-ion polymer electrolytes with similar ionic conductivity to that of salt-doped non-single-ion polymer electrolytes (>10^{-4} S/cm at 90 °C).[31] Therefore, in order to simplify electrolyte preparation and improve battery performance, it is desirable to develop single-ion homopolymer electrolytes that have higher ionic conductivity (>10^{-4} S/cm at 90 °C) and transference number (>0.93).

Moreover, for electrolytes based on polymeric materials, the control over polymer molecular weight and dispersity ($Đ$) is critical. Reversible deactivation radical polymerizations (RDRP) procedures, including nitroxide-mediated polymerization (NMP),[38] reversible addition-fragmentation chain-transfer (RAFT) polymerization[39] and atom transfer radical polymerization (ATRP) [40, 41] have emerged as convenient techniques for controlled synthesis of functional polymers. Compared to other RDRP methods, ATRP is more advantageous for surface modification and chain-extension. However, the use of ATRP for preparation of single-ion polymer electrolytes remained a challenge and is the subject of this work.

2.2.2. Results and discussion

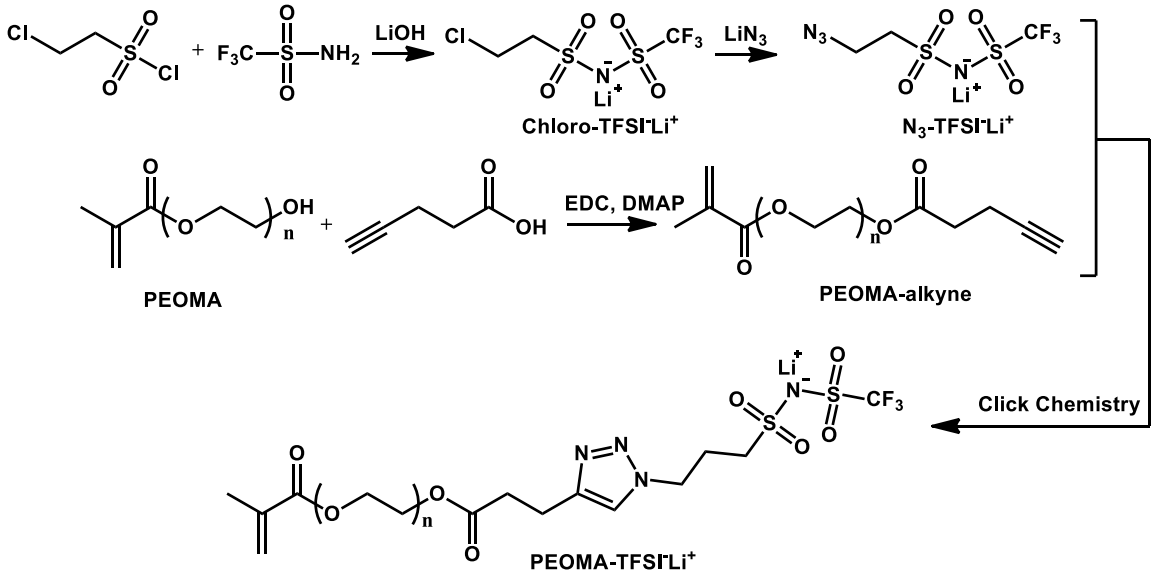

Scheme 1. Synthetic route of PEOMA-TFSI$^-$Li$^+$ macromonomer by click chemistry.

The target of this work was to prepare single-ion homopolymer electrolytes by ATRP, featuring a simplified synthesis of an electrolyte that provided high ionic conductivity, and high transference number. First, a highly conductive PEO-based macromonomer (PEOMA-TFSI$^-$Li$^+$) was prepared based on copper-catalyzed alkyne-azide cycloaddition (CuAAC) reaction shown in Scheme 1.[42-44] Detailed experimental procedures are described in the supplementary information. A hydroxyl-functionalized poly(ethylene glycol) methacrylate (PEOMA) with average molecular weight of 500 was purified as previously reported.[45] The alkyne group was attached by reacting with pentynoic acid. Chloro-TFSI$^-$Li$^+$ was synthesized by condensation between 3-chloropropanesulfonyl chloride and trifluoromethanesulfonamide. The azidation of the chloro-TFSI$^-$Li$^+$ to N_3-TFSI$^-$Li$^+$ was carried out with lithium azide in DMF at 90 ^{o}C. The final product of PEOMA-TFSI$^-$Li$^+$ was synthesized by CuAAC between N_3-TFSI$^-$Li$^+$ and alkyne-functionalized macromonomer PEOMA in the presence of low catalyst amount (0.5 mol% $CuBr_2$).[42, 43]

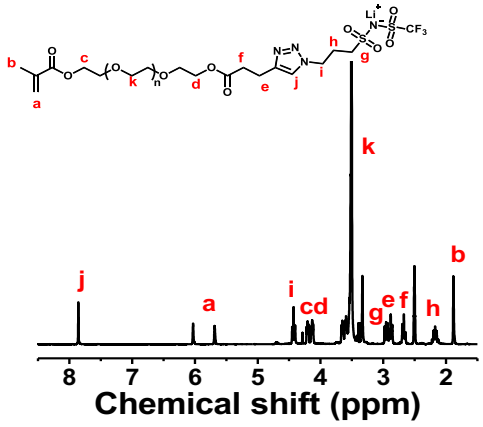

Figure 9. ^{1}H NMR spectrum of the PEOMA-TFSI-Li+

Since the precursor monomer (PEOMA) is actually an oligomer, the monomer has an intrinsic dispersity (*Đ*) ~1.2 (Figure 2c). The average molar ratio of ethylene oxide units (EO) to lithium ions is 10.5/1, which is close to the ideal ratio of EO/Li for high conductivity.[46-48] Residual copper species in the product were removed by passing the product through basic alumina columns. The final product with molecular weight of ~1000 was further washed with lithium carbonate and dialyzed against water for 3 days. Figure 9 shows the proton nuclear magnetic resonance (^{1}H NMR) spectrum of the synthesized macromonomer. Peak **a** (5.6 ~ 6.1 ppm) represents the hydrogen atoms of the double bond. Peak **b** at ~1.8 ppm represents the methyl hydrogen of the methacrylate group. Peak **j** at ~7.9 ppm indicates the formation of triazole ring from cycloaddition. Large multiplet peak **k** at ~3.5 ppm and triplet peak **c** & **d** at ~4.3 ppm are the methylene hydrogen atoms of the EO repeating unit.

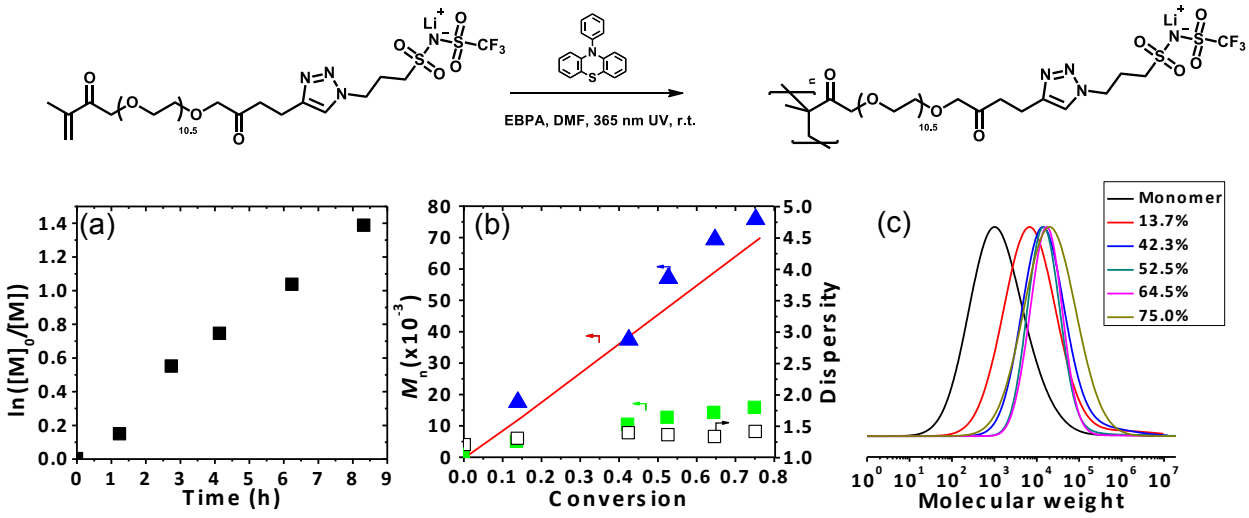

Figure 10. (a) Kinetic plots of ln([M]$_0$/[M]) vs time, (b) plots of Mn×10^{-3} and *Đ* vs conversion. (Blue triangles: Mn from multi-angle light scattering; hollow square: dispersity, Đ) and (c) GPC traces (with DMF containing 50 mM LiBr as eluent and PEO as calibration standards) for metal-free ATRP of PEOMA-TFSI$^-$Li$^+$. Conditions: [PEOMA-TFSI$^-$Li$^+$]$_0$/[EBPA]$_0$/[Ph-PTZ]$_0$ = 100/1/0.1. PEOMA-TFSI$^-$Li$^+$/DMF= 1/3 (w/w), irradiation by 4.9 mW/cm2 UV light.

ATRP is one of the most efficient RDRP techniques to prepare polymers with well controlled molecular weight and dispersity.[40, 49-52] A typical ATRP process involves a copper based catalyst to activate and deactivate propagating chain ends. Several procedures were developed to reduce the concentration of ATRP catalyst, including activator regeneration by electron transfer (ARGET) ATRP,[53] supplemental activator and reducing agent (SARA) ATRP,[54, 55] initiators for continuous activator regeneration (ICAR) ATRP,[53, 56] and *e*-ATRP.[57] Recently, a photoinduced metal-free ATRP using 10-phenylphenothiazine (Ph-PTZ) as an organic photocatalyst was reported.[58-60] The mechanism of photo ATRP is based on an oxidative quenching cycle. First, the ground state PTZ is excited, which then reacts with a dormant alkyl bromide and generates an active propagating chain end. The resulted PTZ$^+$•Br$^-$ deactivates the active center forming dormant

species and returns back to the ground state.[59, 61] This metal-free ATRP technique was applied to the polymerization of a PEOMA-TFSI$^-$Li$^+$ macromonomer. The procedure for the polymerization is described in the supplementary information. The linear semilogarithmic plot (ln([M]$_0$/[M]) vs time) in Figure 10a indicated the steady concentration of active centers during the polymerization. The absolute molecular weight of the polymers was measured by gel permeation chromatography with multi-angle light scattering (GPC-MALS). The M_n values estimated from light scattering (dn/dc = 0.0328) were in good agreement with the theoretical M_n values, indicating high initiating efficiency and highly preserved chain-end functionality throughout the polymerization. GPC traces exhibited a symmetrical narrow Gaussian distribution (Figure 10c), but the dispersity gradually increased at higher conversion. It should be noted that the molecular weight and dispersity measurements were conducted in an eluent phase with 50 mM LiBr in order to screen interactions between ionic species, columns, and solvent.[62]

Table 1. Physical and electrochemical properties of poly(PEOMA-TFSI$^-$Li$^+$)s.

Entry	M_n[a]	$Đ$[a]	DP[a]	T_g (°C)[b]	σ 90 °C (S/cm)[c]	E_a (eV)[c]	t_+[c]
1	1000	1.2	1[d]	-30	1.55×10^{-4}	0.62	0.81
2	7500	1.3	7	-24	1.02×10^{-4}	0.64	0.99
3	14000	1.4	14	-17	4.73×10^{-5}	0.70	0.99
4	29800	1.4	30	-14	2.37×10^{-5}	0.75	0.97

[a] Number-averaged molecular weight (M_n), dispersity ($Đ$) and degree of polymerization (DP) measured from multi-angle light scattering (GPC-MALS);

[b] Glass transition temperature measured from DSC;

[c] Ionic conductivity (σ), activation energy (E_a), and transference number (t_+) measured from EIS.

[d] DP = 1 refers to the macromonomer PEOMA-TFSI$^-$Li$^+$

In order to study the ionic transport properties, polymers with different degrees of polymerization (DP) were prepared by the photoinduced metal-free ATRP. As shown in Figure 11

and Table 1, four samples with different DP were studied, *i.e.*, macromonomer (DP 1), DP 7, DP 14 and DP 30. For PEO-based electrolytes, lowering the crystallinity of the PEO domain was critical to achieve high lithium ion conductivity. Figure 11a comparatively displays the X-ray diffraction (XRD) patterns of the different samples. Two sharp diffraction peaks were observed at ~19° and ~23° for pure PEO with a molecular weight of 10000, indicating the highly crystalline nature of PEO. For the macromonomers and polymers with different DP, the intensity of this peak greatly decreased, suggesting suppressed crystallinity. The lower crystallinity arose from two circumstances: (1) the presence of inorganic content which suppressed the crystallinity of the PEO phase[63] and (2) the brush-like topology (or star-like topology at low DP PEO) which made the compact packing of polymer chains difficult.[64] Ionic conductivities for all polymers versus inverse absolute temperature are presented in Figure 11b in the form of Arrhenius plots. Measurements were carried out from room temperature to 100 °C. All four samples had good ionic conductivity, ranging from 10^{-5} to 10^{-4} S/cm at temperature > 90 °C.[15] Especially, for samples with DP 1 & 7, the ionic conductivity reached over 1×10^{-4} S/cm at 90 °C, which is comparable to salt-doped non-single-ion polymer electrolytes.[31] As DP increased, the ionic conductivity gradually decreased by one order of magnitude.[65] The drop of ionic conductivity with increasing DP could be due to the decrease of long-range mobility of the polymer chains. The differential scanning calorimetry (DSC) analysis consistently proved the mobility decrease, as the glass transition temperature (T_g) increased from ~ -30 °C to ~ -15 °C and the activation energy of ionic conductivity increased from 59.8 KJ/mol to 72.6 KJ/mol, Table 1. Noticeably, when the temperature changed, there was no sharp change in ionic conductivity, which indicated the absence of a melting temperature and a low degree of crystallinity.[15] The similar slope of Arrhenius plot of each sample indicates a similar ion transport mechanism for polymers with different DPs. The electrochemical stability window

was studied using the polymer with DP = 7. Compared to the salt-doped non-single-ion PEO electrolytes, the polymer showed only one redox pair, with a reduction peak below ~1 V vs. Li^+/Li, indicating the anodic stability of the polymer against lithium metal, Figure 11c.

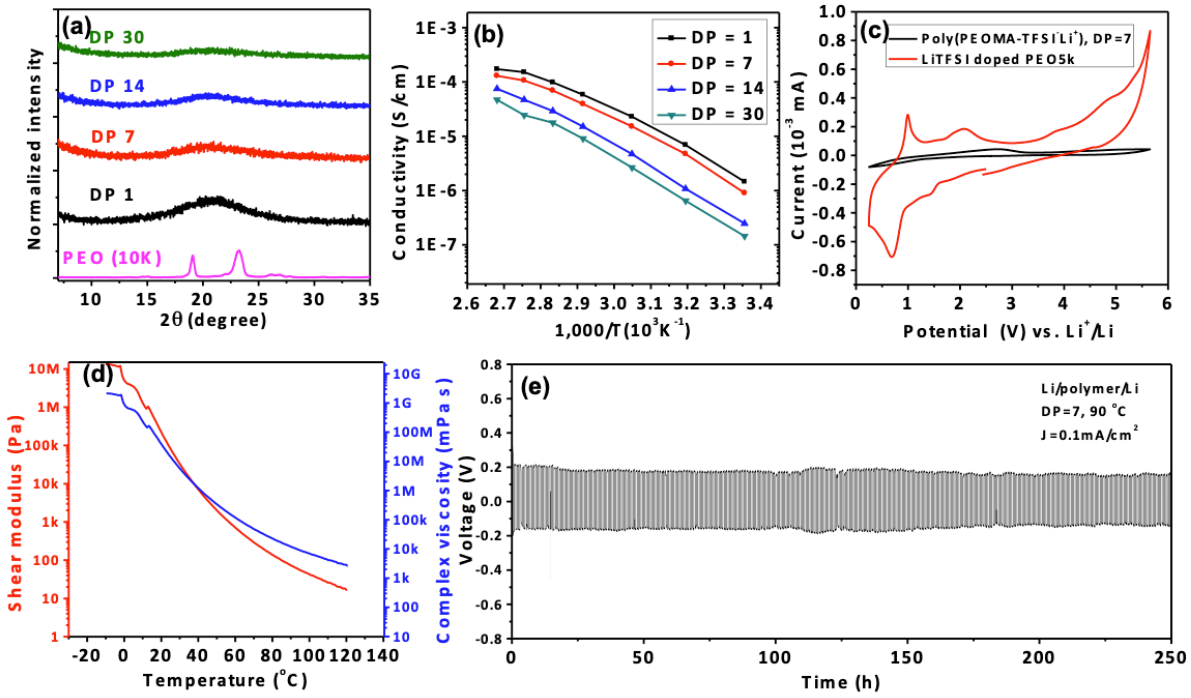

Figure 11. (a) XRD spectra (normalized by weight) and (b) Arrhenius plot of ionic conductivity of poly(PEOMA-$TFSI^-Li^+$) of different DPs; (c) CV curves of poly(PEOMA-$TFSI^-Li^+$) (DP=7, black) and blend of PEO 5K with LiTFSI (red, EO/Li^+ = 10/1) at 0.1 mV/s and r.t.; (d) Shear modulus and complex viscosity of poly(PEOMA-$TFSI^-Li^+$) (DP=7) (e) lithium plating/stripping experiment at J = 0.1 mA/cm^2 90 °C, every cycle lasts 1 hr.

The transference number of lithium ions also reflects the performance of single-ion polymer electrolytes. The transference numbers were determined using a previously reported method.[26] The transference number of 1M $LiPF_6$ in EC/DEC (1:1 v:v) was determined to be 0.31 (supplementary information), consistent with previous reports, indicating the reliability of the

measurements.[66] The monomer had a transference number of 0.82, meaning that the macroanions still had some degree of mobility. Interestingly, all the polymers showed very high transference number, approaching unity; 0.99 for DP 7 and 14, 0.97 for DP 30 respectively. This observation indicates that the lithium ions remained highly delocalized in the non-crystalline PEO domain of the homopolymer. Noticeably, all the single-ion polymers had interfacial resistance around 10^2 KΩ/cm^2, an aspect that needs to be improved for commercial purposes compared to commercial liquid electrolytes. To study the stability of lithium ion transport in the bulk electrolytes, a lithium stripping-plating experiment in a symmetric lithium/polymer/lithium cell was carried out to mimic the operation of charging and discharging in a lithium metal battery.

The poly(PEOMA-TFSI$^-$Li$^+$) (DP=7) was sandwiched in a 250 micron gap between two polished lithium sheet and sealed in a coin cell. Figure 11e shows the time-dependent voltage profile of the cell with the polymer as the electrolytes cycle over 250 h at a constant current density of 0.1 mA/cm^2 and a temperature of 90 ^{o}C. After 290 h, the current density was increased to 0.2 mA/cm^2 and the lithium plating/stripping showed continued stability, Figure 18, for ~100 cycles. Noticeably, due to the brush-liked morphology, the viscoelastic polymer only has a shear modulus of 74 Pa at 90 ^{o}C (Figure 11d). This observation is consistent with a previous report that a high transference number lowers the requirement of mechanical strength for stable electrodeposition of lithium.[67]

A large number of models have been developed to explore the factors responsible for dendrite growth. Bockris *et al*. first developed a kinetic model for zinc electrodeposition in aqueous solutions.[68] Later Monroe *et al*. developed an improved kinetic model to describe the transport factors responsible for lithium dendrite growth in polymer electrolytes and then explored the effects of elastic deformation at the interface.[10, 69] It has been shown by many of the studies

that mechanical properties such as shear modulus, yield strength and fracture toughness play an equally important role to transport properties during electro deposition.[70, 71] Monroe and Newman showed that a polymer modulus of more than twice of that of lithium should lead to stable electro deposition.[10] However most polymers don't have such high shear moduli and their shear moduli can only be increased at the cost of lowering the ionic conductivity. Ahmad *et al.* have recently showed that stable electrodeposition can also be achieved at lower moduli by changing the partial molar volume of lithium in the polymer electrolyte.[11] Tikekar et al. recently developed a combined model, including mechanical and transport properties, and proved that increasing the transport number of the electrolytes results in lowering of the critical modulus required for stable electrodeposition.[66] They show that shear modules of about 100 MPa is sufficient for dendrite suppression. As discussed earlier, the polymers we have formed are very fluid and have moduli of the order of about 1 MPa at r.t. and 100 Pa at 90 ºC. This means that dendrite suppression in these polymers is unlikely to occur due to mechanical properties or via grain boundaries. Hence, in this work we only explore the effect of transport properties. Improving the mechanical properties of these polymers will be done in a future study.

To compare the effect of transport properties on dendrite growth, we employ the kinetic model developed by Monroe *et al.*[68] The model assumes bulk electro neutrality in a defect-free electrolyte and galvanostatic condition to solve for the transient concentration profiles of ions. The transient concentration profiles are used to derive an expression for the current density at the tip of a dendrite of a certain length. The trends remain largely consistent, independent of the choice of the dendrite length. The ratio of the current density at the tip to the current density at the flat electrode surface is a direct measure of the propensity of dendrite growth in an electrolyte and we used this parameter to compare the ability to suppress dendrites for various electrolytes. The

analytical expression for the ratio of current density at the tip to the current density at the electrode is given by:

$$\frac{i_{tip}}{i_{electrode}} = \left(\frac{i_0}{i}\right)\left(\frac{\exp\left(\frac{2\gamma V}{rRT}\right)\exp\left(\frac{\alpha F\eta}{RT}\right) - \exp\left(\frac{-\alpha F\eta}{RT}\right)}{\left(\frac{c_{ref}}{c_{Li^+}}\right)^{\alpha} + \frac{(1-t_+)ri_0\exp\left(\frac{-\alpha F\eta}{RT}\right)}{FDc_{Li^+}}}\right)$$

More details regarding the derivation of the equation and the parameter values are given in the supplementary information. Using this equation, we derived a contour plot to compare the current density at the tip of typical dendrite lengths of 10-100 nm as a function of the diffusion coefficient of lithium ions and transference number for different electrolytes, which is shown in Figure 12. The model predicted that for a defect-free system, there would be significant dendrite suppression by a factor of 3-4 with increasing transference number at constant diffusivities. It is worth highlighting that increasing diffusivities at constant transference number enhances dendrite suppression by a factor of 1.5-2, however, this trend is reversed at very high transference numbers ($t_+ > 0.95$). This observation is consistent with Monroe's work which indicated that at very high transference numbers, the maximum charge passed before shorting happens at very low diffusion coefficients such that we can only observe the decreasing trend of charge passed (increasing trend of tip current ratio) for realistic diffusion coefficients.[69] The model suggests that the synthesized polymers have greater potential to suppress dendrites based on transport properties. An important challenge is to ensure low interfacial impedance at the lithium/polymer electrolyte interface such that high current densities can be supported. To apply our materials to real batteries would be the next goal of our work.

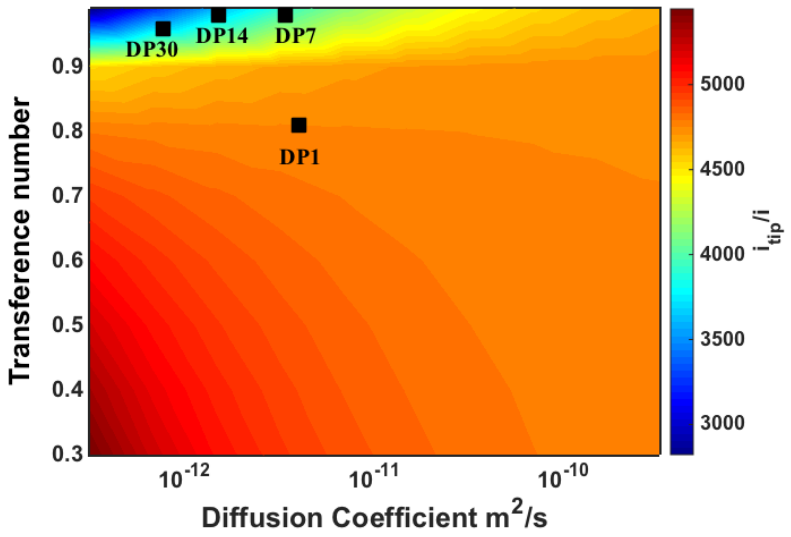

Figure 12. Contour plot showing the propensity of dendrite growth (ratio of tip current to applied current) for electrolytes of different transference numbers and Li^+ diffusion coefficients. The model is evaluated at a temperature of 90 °C and the tip current is calculated using a dendrite of length 10 nm. The black squares represent the polymers synthesized in the current work.

2.2.3. Conclusions

In summary, a new type of single-ion homopolymer electrolyte with high ionic conductivity and high transference number has been synthesized based on click chemistry synthesis of a PEO based macromonomer and photoinduced metal-free ATRP. The homopolymer systems simplified the fabrication of polymer electrolytes, in comparison to block copolymer or polymer blends with plasticizers. The synthetic procedure presents the first case of using ATRP to prepare single-ion polymer electrolytes with good control over molecular weight and dispersity. The polymers had greatly reduced crystallinity due to the combination of homogeneously dispersed lithium ions and the non-linear topology of the polymer electrolyte. As a result, the polymers showed good ionic conductivity (comparable to salt-doped non-single-ion electrolytes)

and high transference number (approaching unity). The clickable ionic precursor N_3-TFSI$^-$Li$^+$ can potentially be attached to various platforms for development of new types of single-ion electrolytes. The polymer with a DP of 7 showed stable lithium plating/stripping cycles for over 300 Hr with current density increasing from 0.1 mA/cm^2 to 0.2 mA/cm^2. The dendrite suppressing capability of the polymers was also predicted by examining the ratio of the current density at the tip to the current density at the flat electrode surface. Therefore, our analysis showed that the polymer with such high transference number should have a high propensity to suppress dendrite growth.

i_0 is the exchange current density at the lithium electrode-electrolyte interface

i is the applied current density

γ is the surface energy of lithium metal

V is the molar volume of lithium metal

α is the transfer coefficient for lithium redox reaction

F is the Faraday's constant

R is the ideal gas constant

T is the temperature at which the cell is simulated

η is the over potential of the lithium reduction reaction at the flat surface

c_{ref} is the reference concentration defined as 1000 mol/m^3

c_{Li^+} is the concentration of lithium ion

t_+ is the transference number of the polymer electrolyte

D is the salt diffusion coefficient

t is the radius of the dendrite tip

2.2.4. Experimental sections and supporting information

Materials. 4-Pentynoic acid (98%) was purchased from GFS Organic Chemicals. Trifluoromethanesulfonamide (95%) was purchased from Oakwood Chemicals. 3-Chloropropanesulfonyl chloride (98%), poly(ethylene glycol) methacrylate (average M_n 500), lithium hydroxide (99.95%), sodium azide (≥99%), N-(3-dimethylaminopropyl)-N'-ethylcarbodiimide hydrochloride (EDC, ≥99%), N,N-dimethylamino pyridine (DMAP, ≥99%), copper bromide (≥99.99%), ascorbic acid, (AA, ≥99%) N,N,N',N'',N'''-pentamethyldiethylenetriamine (PMDETA, 99%), ethyl α-bromophenylacetate (EBPA, 97%) were purchased from Sigma Aldrich. Ph-PTZ was synthesized according to our previous work.[59] All solvents and other chemicals are of reagent quality and were used as received unless special explanation.

Instrumentation. Proton nuclear magnetic resonance (NMR) measurements were performed on a Bruker Avance 300 MHz spectrometer. Molecular weight, molecular weight dispersity ($Đ$) and dn/dc value were determined by combination of gel permeation chromatography and multi-angle light scattering (GPC-MALS). The GPC-MALS used a Waters 515 HPLC pump, Wyatt Optilab refractive index detector, Wyatt DAWN HELEOS-II multi-angle light scattering detector and PSS columns (Styrogel 10^2, 10^3, and 10^5 Å) with 50 °C DMF (50 mM LiBr) solution as eluent phase at flow rate of 1 mL/min. The conductivity was measured by Bio-logic 16-channel VMP-3 multi-channel potentiostat/electrochemical impedance spectrometer at temperature range of r.t. ~ 100 °C. All tested samples were first dried under 90 °C vacuum for 5 days and stored in glove box before use. Temperature dependent shear modulus and complex viscosity was measured by Anton Paar modular compact rheometer MCR 302.

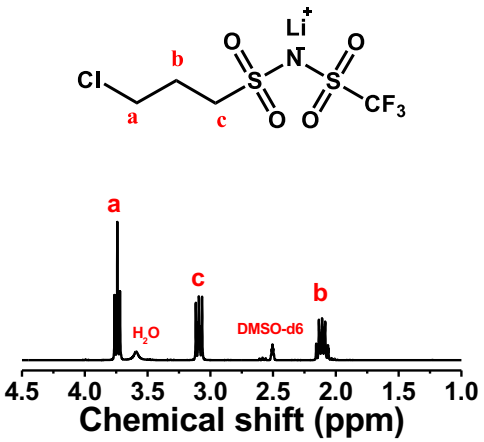

Figure 13. ^{1}H NMR spectrum of 3-chloropropanesulfonyltrifluoromethanesulfonylimide (Cl-TFSI^{-}Li^{+}).

Synthesis of Lithium 3-chloroproanesulfonyltrifluoromethanesulfonylimide (Cl-TFSI^{-}Li^{+}). In a typical procedure, 4.068 g lithium hydroxide (2 equiv.) and 12.627 g trifluoromethanesulfonamide were mixed in 85 mL acetonitrile in a 100 mL round bottom flask deoxygenated by N_2 purge while in an ice bath. 15 g of 3-chloropropanesulfonyl chloride were then injected dropwise into the flask. The reaction was allowed to warm up to room temperature and left to react for 24h. Afterwards, the mixture was filtered to remove insoluble salts and dried under vacuum to yield a pale viscous liquid. The raw material was recrystallized in dichloromethane to give pure white solid, with over ~80% yield. The ^{1}H NMR (300 MHz, DMSO-d_6): δ (ppm) = 3.74 (2H, t, ClCH_2CH$_2$), 3.10 (2H, t, CH$_2$CH_2S(=O)$_2$N), 2.15 (2H, q, ClCH$_2$CH_2)

Synthesis of Lithium 3-azidoproanesulfonyltrifluoromethanesulfonylimide (N$_3$-TFSI^{-}Li^{+}). In a typical procedure, 500 mg Cl-TFSI^{-}Li^{+} (1 equiv.) and 115.7 mg NaN_3 (1.05 equiv.) were mixed in 2 mL DMF in a 10 mL sealed round bottom flask equipped with a stirring bar. The mixture was deoxygenated with a N_2 purge then placed in an oil bath thermostated at 90 ^{o}C. The mixture was allowed to react for 24 h. Afterwards the extra salt was removed by filtration but the

solvent wasn't removed and the solution was directly added to the next step for click chemistry. ^{1}H NMR (300 MHz, DMSO-d_6): δ (ppm) = 3.47 (2H, t, $N_3CH_2CH_2$), 3.02 (2H, t, $CH_2CH_2S(=O)_2N$), 1.91 (2H, q, $N_3CH_2CH_2$).

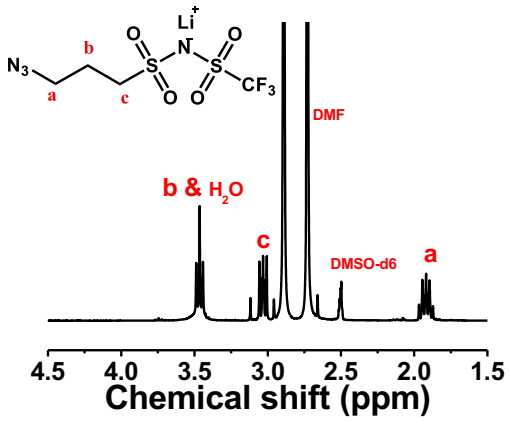

Figure 14. ^{1}H NMR spectrum of 3-azidopropanesulfonyltrifluoromethanesulfonylimide (N_3-TFSI$^-$ Li^+)

Synthesis of alkynyl poly(ethylene glycol) methacrylate (PEOMA-alkyne). Hydroxyl-terminated poly(ethylene glycol) methacrylate (PEOMA-OH) was washed with diphenyl ether and mixture of hexane/chloroform (3/1) to remove dimers. In a typical procedure, 20 g purified hydroxyl-terminated poly(ethylene glycol) methacrylate (1 equiv.), 5.84 g pentynoic acid (1.2 equiv.) and 6.8 g EDC (1.2 equiv.) were mixed in 130 mL dichloromethane in a sealed 500 mL round bottom flask equipped with a stirring bar then the flask was placed in an ice bath. The mixture was deoxygenated by N_2 purge. A solution of 534 mg DMAP (0.12 equiv.) in 3 mL dichloromethane was injected dropwise into the flask. The reaction was then allowed to warm up to room temperature and react for 24 h. The solution was then washed sequentially with 1M HCl solution, saturated sodium bicarbonate and brine (3 times respectively). The organic phase was collected and dehydrated over magnesium sulfate. The final product was obtained after removing

the solvent under vacuum as a light yellow viscous liquid. The ^{1}H NMR is shown below in Figure 15.

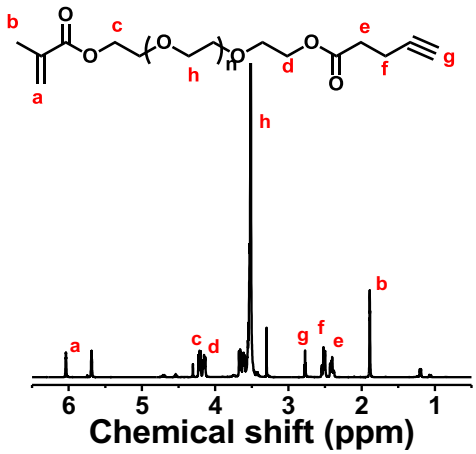

Figure 15. ^{1}H NMR spectrum of alkyne-functionalized poly(ethylene glycol) methacrylate (PEOMA-alkyne).

Click chemistry synthesis of a single-ion monomer PEOMA-TFSI^{-}Li^{+}. In a typical procedure, 3.27 g N3-TFSI^{-}Li^{+} (1 equiv.), 10.2 g PEOMA-alkyne (1.5 equiv.), 12 mg $CuBr_2$ (0.005 equiv.) and 28.1 mg PMDETA (0.015 equiv.) were mixed in 4 mL DMF in a sealed 10 mL Schlenk flask equipped with a stirring bar. The mixture was deoxygenated by 3 freeze-pump-thaw cycles. The flask was allowed to warm up to room temperature and placed in an oil bath thermostated at 50 °C. A deoxygenated solution of 57.2 mg ascorbic acid (0.03 equiv.) in 0.2 mL DMF was injected into the flask under a N_2 purge to initiate the click chemistry by forming the Cu^{I} complex in situ. The reaction was stopped after 72 h and then precipitated by addition to diethyl ether. Then the copper was removed by passing a solution through basic alumina column and ion-exchange resin. The final product was further washed with lithium carbonate and dialyzed against water for 3 days. The wet product was dried by lyophilization. The ^{1}H NMR spectrum was shown in Figure 1 in the main text.

Photo-induced metal-free ATRP of PEOMA-TFSI$^-$Li$^+$. In a typical procedure, 443 mg PEOMA-TFSI$^-$Li$^+$ (100 equiv.), 1.16 mg EBPA (1 equiv.) and 0.13 mg Ph-PTZ (0.1 equiv.) were dissolved in 1.3 mL DMF in a sealed 10 mL Schlenk flask equipped with a stirring bar. The mixture was deoxygenated by 3 cycles of freeze-pump-thaw. The flask was refilled with N_2 and allowed to warm up to room temperature and an initial sample ($t = 0$) was collected by syringe. The reaction was initiated by irradiation with 4.9 mW/cm^2 UV light. Samples were taken periodically to measure conversion via ^{1}H NMR and molecular weights via GPC-MALS.

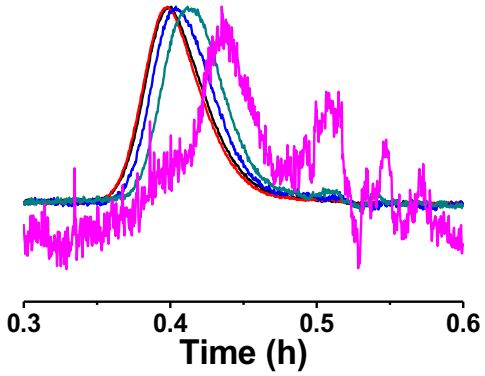

Figure 16. Light scattering data of the same kinetic study in **Figure 10** in the main text. From right to left, signal moved as expectedly. The wavy curve is because the light scattering signal for polymer of low molecular weight is not strong. dn/dc = 0.0328.

Measurement of ionic conductivity. The electrochemical measurements of the ionic conductivities of the polymer electrolytes were carried out using an AC impedance spectroscopic technique. In order to avoid the influence of humidity, the polymer electrolytes were sandwiched in a 2016 coin cell in a glove box with Argon atmosphere , with a level of H_2O and O_2 < 1 ppm. The measurements were performed at temperature ranging from 22 °C to 100 °C. The cell was thermally equilibrated for 30 min at each temperature prior to measurement. The AC impedance

spectra were recorded over the frequency range from 1 to 8 $\times 10^5$ Hz. The values of ionic conductivity were derived from the measured resistance by using the following equation:

$$\sigma = 1/R \times L/A$$

where L (cm) is the thickness of polymer electrolytes in the cell, A (cm^2) is the area of the electrolytes, and R (Ω) is the impedance determined from the Nyquist plot.

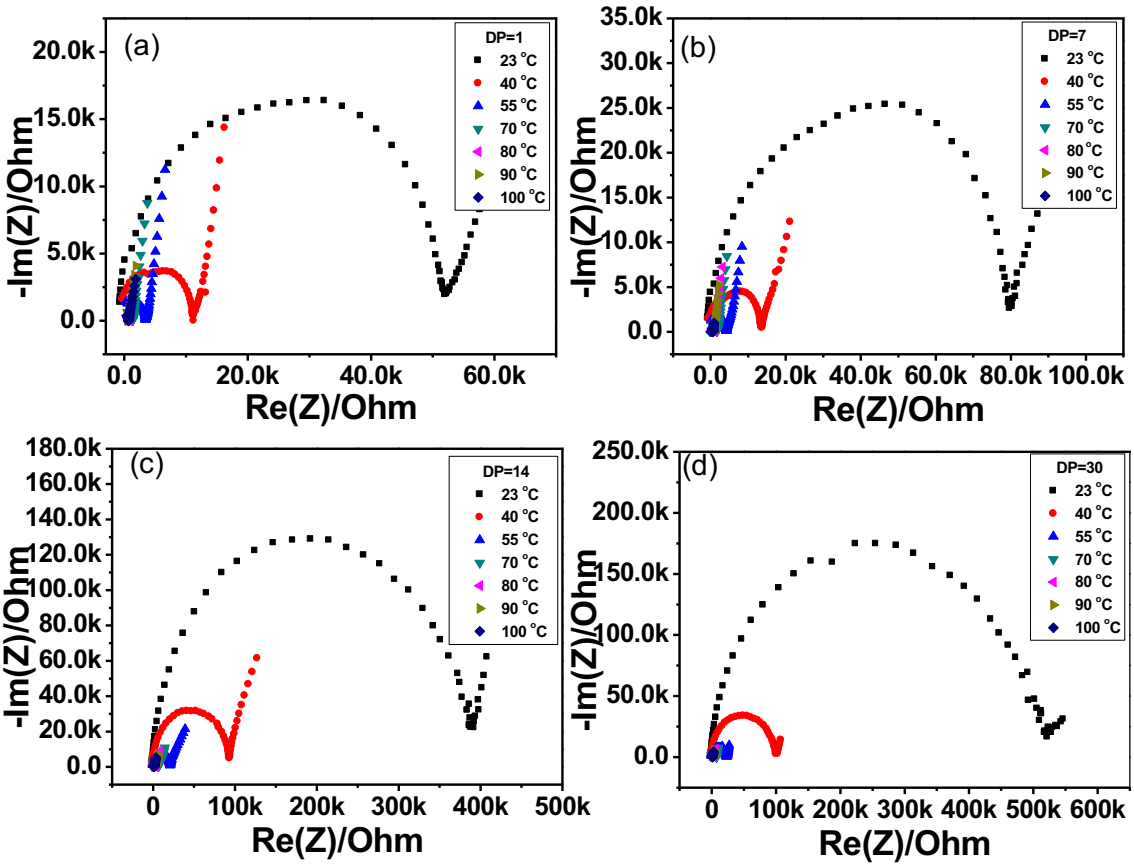

Figure 17. Nyquist plots of polymer electrolytes with different DP. (a) DP =1 (monomer), (b) DP=7, (c) DP=14, (d) DP=30

Measurement of the transference number. The lithium-ion transference number of the polymer electrolytes was obtained by combining AC impedance and DC polarization measurements using a symmetric cell of [Li metal | polymer electrolytes | Li metal] at 60 °C, which

had been described previously.[26] The surface of lithium metal was shaved with a scalpel before use. The cell was assembled in a glove box levels of H_2O and O_2 < 1 ppm). Before measurement, the cell was heated at 60 °C for 1 h in order to obtain good contact, as well as allowing for forming a stable interface, between the electrolytes and electrodes. Then, a DC voltage of 50 mV was applied to the cell until a steady current was obtained, and the initial and steady currents, which flow through the cell, were measured. Simultaneously, the cell was also monitored in the frequency range from 0.01 to 10^6 Hz, by using AC impedance with an oscillation voltage of 20 mV to measure the resistance of the electrolytes and the interface of electrolytes/Li metal electrodes, before and after the DC polarization. The temperature of the cell was accurately controlled at 60 °C.

$$t_+ = \frac{I^s(\Delta V - I^0 R^0)}{I^0(\Delta V - I^s R^s)}$$

The transference numbers were calculated according to the above equation where t_+ is the transference number, ΔV is the DC voltage applied across the cell, I^0 is the initial current following the voltage step, R^0 is the charge transfer resistance for lithium reduction/oxidation measured by impedance spectroscopy before the voltage step, I^s is the steady state current measured at the end of the voltage step, and R^s is the resistance for lithium reduction/oxidation at the end of the voltage step.

Table 2. Measured values for the transference number of electrolytes at 60 °C[a]

Samples	I^0(μA)	I^s(μA)	R^0(KΩ)/cm^2	R^f(KΩ)/cm^2	ΔV(mV)	t_+
DP=1	1.5	1.3	4.95	5.05	50	0.81
DP=7	4.0	3.4	102.8	104.8	50	0.99
DP=14	3.5	2.5	91.7	95.1	50	0.99
DP=30	7.9	7.4	124.6	128.5	50	0.97
1M $LiPF_6$[b]	1.3	0.8	13.3	10.9	50	0.31

[a] diameter of electrode = 1.4 cm. Space of electrode equals 1.6 mm

[b] tested with Celgard separator

.

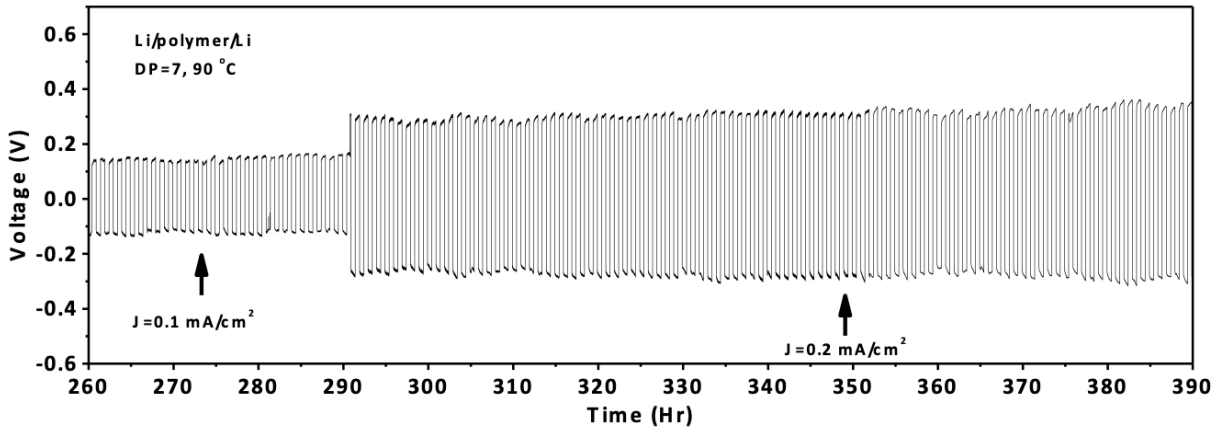

Figure 18. Voltage profile of the continued lithium plating/stripping cycling with a current density increase from 0.1 to 0.2 mA/cm^2 at 90 °C.

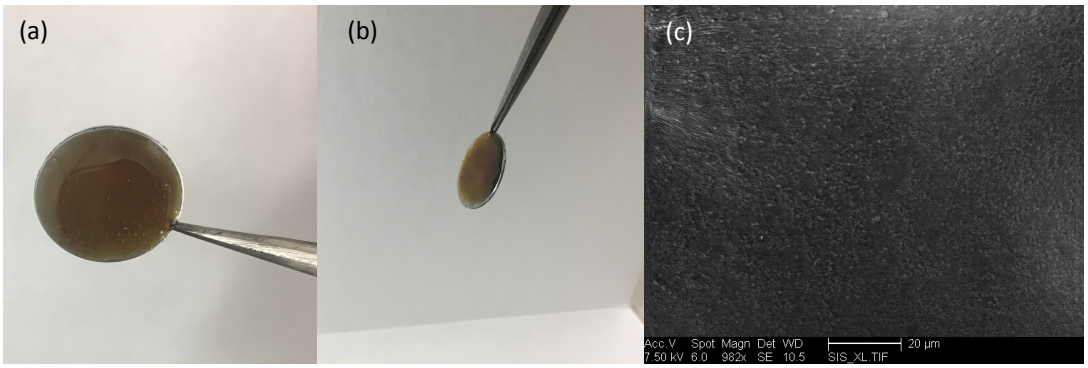

Figure 19. (a)&(b) Macroscopic image of the polymer (DP7) coated on a stainless steel spacer (diameter = 14 mm) ; (c) SEM image of the coated film. (Scale bar=20 micron)

DENDRITE GROWTH MODEL

The model developed by Diggle *et al*.[68] was used to study a dendrite growth rate in the lithium polymer systems. The model first solves for the concentration and potential profiles in a galvanostatically cycled planar cell. The temperature of the cell is assumed to remain constant, the material and transport properties are assumed to be concentration independent and the electrolyte is assumed to be ideal. Now without a supporting electrolyte and assuming local electro neutrality everywhere in the cell, the concentration and potential solutions can be decoupled yielding the following equation:

$$\frac{\partial c}{\partial t} = D\frac{\partial^2 c}{\partial x^2}$$

where c is defined as salt concentration and D is salt diffusion coefficient. This equation is subject to the boundary conditions:

$$i = -\frac{DF}{(1-t_+)}\frac{\partial c}{\partial x}(x=0)$$

$$c(x,0) = c_b$$

$$\frac{1}{L}\int_0^L c(x,t)\,dx = c_b$$

This equation is similar to a standard diffusion equation and heat equation and its solution is well known. The transient concentration solution can be written as:

$$c(x,t) = c_b - \left(\frac{(1-t_+)iL}{DF}\right)\left(-\frac{x}{L}+\frac{1}{2}-4\sum_{k=1}^{\infty}\frac{1}{(2k-1)^2\pi^2}e^{-\frac{(2k-1)^2\pi^2 Dt}{L^2}}\cos\left(\frac{(2k-1)\pi x}{L}\right)\right)$$

We use L = 10 μm, t_+ is the transference number of the polymer electrolyte, D is the salt diffusion coefficient of the polymer electrolyte and c_b is the initial bulk salt concentration, which is 1000 mol/m^3. Once we have solved for the transient concentration as a function of distance in the electrolyte from the lithium metal electrode this result is for a constant current density applied at a flat lithium electrode. Now using Monroe *et al.*'s derivation[69] it is possible to determine the tip current density for dendrites of a given length X at time t. The expression for the tip current density can be written as:

$$i_{tip} = \frac{i_0 \exp\left(\frac{2\gamma V}{rRT}\right)\exp\left(\frac{\alpha F\eta}{RT}\right) - \exp\left(-\frac{\alpha F\eta}{RT}\right)}{\left(\frac{c_{ref}}{c(X,t)}\right)^{\alpha} + \frac{(1-t_+)ri_0}{FDc(X,t)}\exp\left(-\frac{\alpha F\eta}{RT}\right)}$$

The variables used in this expression are:

i_0 is the exchange current density at the lithium electrode-electrolyte interface. We use $i_0 = 30\ \mathrm{A/m^2}$.

γ is the surface energy of lithium metal. Here we use $\gamma = 1.716\ \mathrm{J/m^2}$.

V is the molar volume of lithium metal. $V = 1.3 \times 10^{-5}\ \mathrm{m^3/mol}$.

α is the transfer coefficient for lithium redox reaction and is 0.5

F is the Faraday's constant, F = 96485 C/mol.

R is the ideal gas constant, R = 8.314 J/[mol K]

T is the temperature at which the cell is simulated. We have considered two temperature of operation, 25 and 90 °C (298.15 and 363.15 K) respectively.

η is the overpotential of the lithium reduction reaction at the flat surface and depends on the applied current density *i*, concentration of Li^+ ions near the flat surface (*c(0,t)*) calculated using the expression derived earlier and is solved using the f_{solve} function in MATLAB

$$i = i_0\left(\exp\left(\frac{\alpha F\eta}{RT}\right) - \frac{c(0,t)}{c_b}\left(\exp\left(-\frac{\alpha F\eta}{RT}\right)\right)\right)$$

c(X,t) is the concentration of lithium ion near the tip of dendrite of length *X* and at time *t*.

c_{ref} is a reference concentration and is defined as 1000 mol/m^3 in this case

t_+ is the transference number of the polymer electrolyte and is appropriately chosen for the polymer compounds developed in the experiments.

D is the salt diffusion coefficient and can be defined as: $D = \frac{(z_+ + z_-)D_+D_-}{z_+D_+ + z_-D_-}$ where $z_+ = z_- = 1$ for single charged ions and D_+ and D_- are the diffusion coefficients for the cation and the anion in the polymer electrolyte respectively. D_+ and D_- can be determined from the ionic conductivity and transference number measurements carried out above as follows:

$D_+ = \frac{\sigma t_+ RT}{F^2}$, $D_- = \left(\frac{1}{t_+} - 1\right)D_+$, where σ is the measured ionic conductivity, t_+ is the measured transference number, *R* is the ideal gas constant, *F* is the Faraday's constant and *T* is the temperature of operation of the cell.

r is the radius of the dendrite tip. The value of *r* chosen is such that we consider the maximum dendrite growth rate as carried out by Monroe *et al*. and Diggle *et al.*[68, 69]

We use the calculated i_{tip} and use the ratio $\frac{i_{tip}}{i}$, which is directly proportional deposition rate at the tip versus the flat electrode surface and is a direct measure of dendrite propagation rate. We have evaluated the ratio for various dendrite lengths *X* and at different times t for a range of

transference numbers and diffusion coefficients. However, it was observed that the trend remains the same for different X and t as they only have a small effect on the concentration at the dendrite tip which in turn does not significantly affect i_{tip}. However, the applied current density at the flat electrode, does change the trends significantly as it changes the overpotential for the lithium redox reaction. Figure 20 shows the contour plots for different overpotentials.

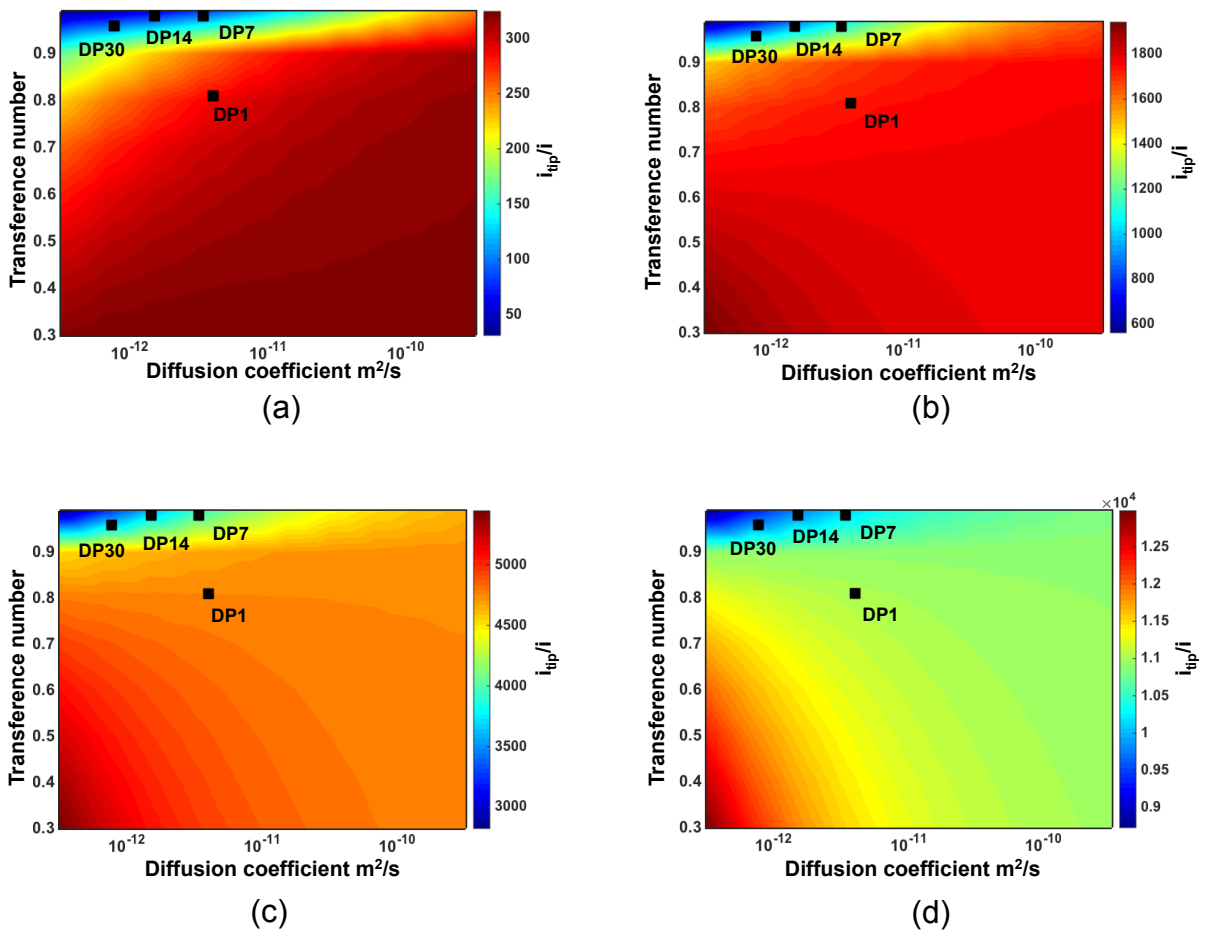

Figure 20. Contour plots showing dendrite growth rate (i_{tip}/i) as a function of diffusion coefficient of lithium and transference number of the polymer electrolyte for different overpotentials (η) i.e. different current densities at flat surface (a) η = 0.01 V, (b) η = 0.05 V, (c) η = 0.1 V, (d) η = 0.15 V at 90 °C.

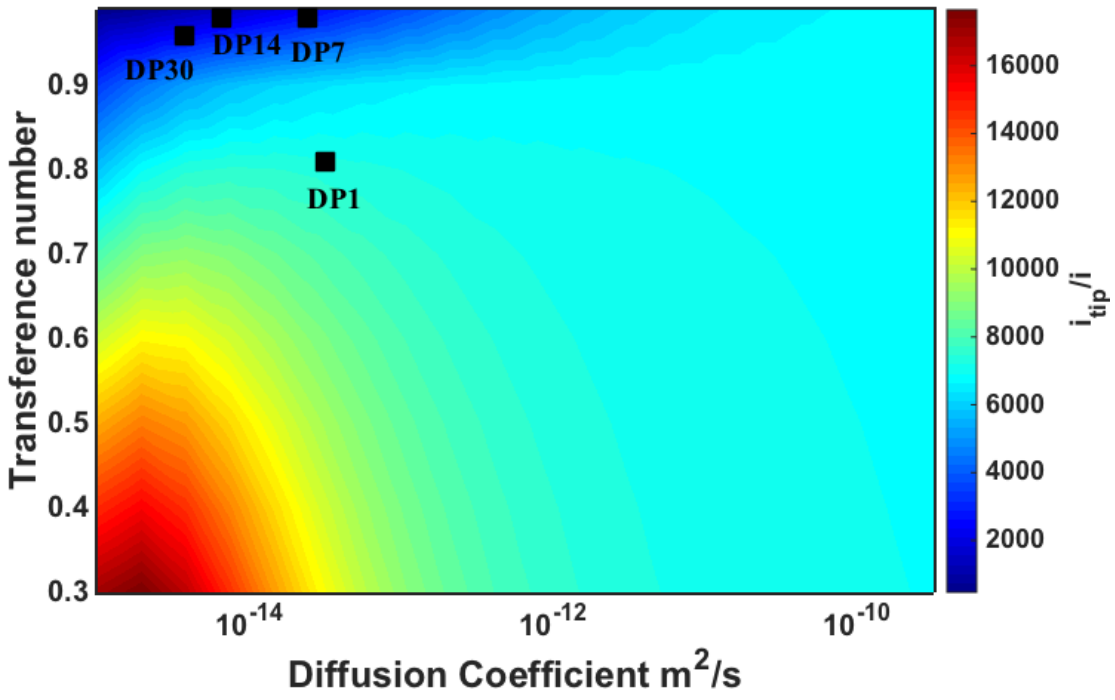

Figure 21. Contour plots showing dendrite growth rate (i_{tip}/i) as a function of diffusion coefficient of lithium and transference number of the polymer electrolyte at room temperature. The black dots show the four polymers in this work.

2.3. Single-ion Polymer Electrolytes Prepared by Anionic ROP

2.3.1. Introduction

Solvent-free polymer electrolytes for rechargeable lithium batteries have received a significant degree of attentions due to their advantages of lower flammability, mechanical flexibility, ease of processing, etc.[72-75] A typical type of non-solvent polymer electrolytes uses a blend of LiTFSI ($Li[(CF_3SO_2)_2N]$) and poly(ethylene oxide) (PEO). In such system, the strong electron withdrawing fluorine atoms and the resonance structures due to the sulfonyl groups in TFSI anions make the lithium ions highly delocalized and can be conveyed through the polyester backbone of PEO.[30] However, the existence of low molecular weight anions will generate a lithium concentration gradients during charge/discharge over the electrodes, causing dendrite growth and battery failure. [76, 77]

One of the best solutions to overcome the development of a concentration gradient is to anchor the counterions onto immobile polymeric structures, forming so-called "single-ion" polymer electrolytes.[78-81] As a result, the immobilized polyanions will prevent the depletion of anions near the anode and thus alleviate the ion gradient.[81-83] So far, several types of single-ion polymeric electrolytes have been reported. Armand et al.[29] synthesized a new type of polymer - LiPSTFSI based on the monomer potassium (4-styrenesulfonyl)(trifluoromethylsulfonyl)imide (STFSIK). A polymer blend of LiPSTFSI/PEO showed conductivity of 10^{-5} S/cm at 70 ^oC. Later, they reported a prototype lithium metal battery consisting of $LiFePO_4$ as cathode based on a triblock copolymer LiPSTFSI-PEO-LiPSTFSI as the electrolyte. The copolymer had a conductivity of 10^{-5} S/cm at 90 ^oC and a transference number of 0.82 at 60 ^oC.[84] Derived from the monomer STFSIK, Zhou et al.[30] reported a more delocalized polymer LiPSsTFSI which had an extra trifluomethylsulfonylimino group in the structure. Blends of LiPSsTFSI/PEO showed

increased ionic conductivity of 10^{-7} ~ 10^{-4} S/cm from r.t. to 90 °C and a transference number of 0.91. Gerbaldi et al.[85] reported a methacrylate type monomer, lithium 1-[3-(methacryloyloxy)propylsulfonyl]-1- (triuoromethanesulfonyl)imide (LiMTFSI). To improve the ionic conductivity, a diblock copolymer of PEO-*b*-polyLiMTFSI was synthesized, which showed comparatively high ionic conductivity (2.3×10^{-6} S/cm and 1.2×10^{-5} S/cm at 25 °C and 55 °C respectively) and a transference number of 0.83. Long et al.[26] reported a single-ion polymer network based on a tetraarylborate polymer, which had a high room temperature conductivity of 2.7×10^{-4} S/cm and a transference number of 0.93. Recently, our group reported preparation of highly conductive single-ion polymer electrolytes based on poly(oligoethylene glycol) methacrylate (polyOEGMA) backbones, by photo-induced Mt-free atom transfer radical polymerization (ATRP)[41, 46, 51, 52, 58, 59, 86-88], which showed high transference number up to 0.99. Most of these single-ion polymer electrolytes were based on a non-conductive carbon-based backbone and had to rely on the PEO phase to transport lithium ions. While a such a backbone can potentially help decrease the crystallinity of the PEO phase, the non-conductive nature of polycarbon backbones can cause phase separation and limit the conductivity. Therefore, it was of great interest to create a single-ion polymer electrolyte based on a PEO backbone.

Herein, a chemically modifiable PEO backbone was synthesized by anionic ring-opening polymerization[89-91] of glycidyl propargyl ether (GPE). An azido lithium salt N_3-TFSI$^-$Li$^+$ was attached onto the backbone by click chemistry[42, 92], giving a single-ion polymer electrolyte polyGPE-TFSI$^-$Li$^+$. The polymer showed a room temperature conductivity of 2.85×10^{-7} S/cm, a 100 °C conductivity of 1.38×10^{-4} S/cm and a transference number of 0.99 at 60 °C. To adjust conductivities, mono-azido PEO (N_3-PEO_{550}) was attached together with N_3-TFSI$^-$Li$^+$ onto the

backbone by click chemistry. At different ratios of N_3-TFSI$^-$Li$^+$ to N_3-PEO$_{550}$, the resulted polymers showed an improvement of conductivity at either r.t. or 100 °C.

2.3.2. Results and discussion

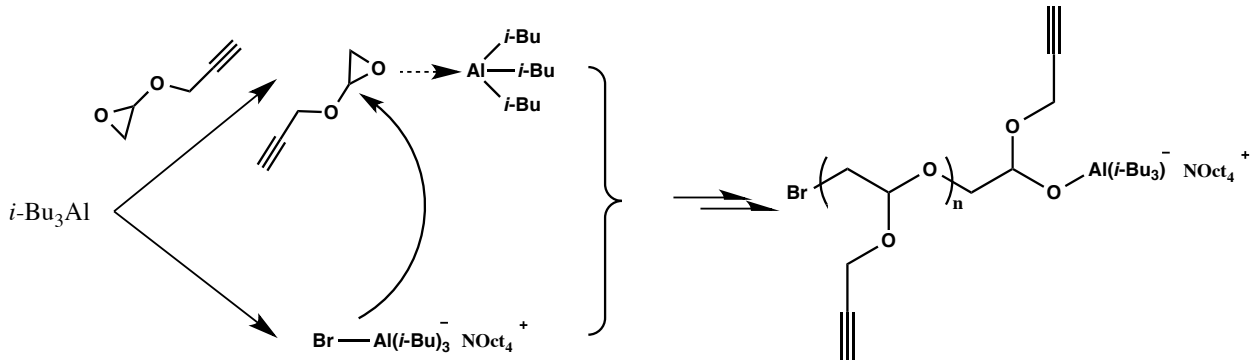

Scheme 2. Reaction mechanism involving monomer activation prior to insertion into the growing "ate" complex.

To synthesize a functionalizable PEO backbone GPE was polymerized by anionic ring-opening polymerization with tetraoctylammonium bromide (Br$^-$NOct$_4^+$) as initiator in the presence of trisisobutylaluminum (*i*-Bu$_3$Al), in anhydrous toluene. The polymerization mechanism involves a monomer activation prior to insertion into a growing "ate" complex, as described in Scheme 2.[89-91] After polymerization, the active chain end was quenched by washing with water. A target degree of polymerization (DP) of 15 was achieved as shown in the GPC trace (Figure 23). ^{1}H NMR spectrum of the synthesized polyGPE in Figure 22 showed the alkyne peak at 2.5 ppm, indicating that the alkyne functionality was well-preserved throughout the polymerization. The molecular weight of polyGPE, analyzed by DMF GPC, was 2,000 with a dispersity of 1.21, indicating good control of polymerization, Figure 23. The N_3-TFSI$^-$Li$^+$ was clicked onto the polyether backbone at complete conversion, giving single-ion polymer electrolytes poly(GPE-TFSI$_{100\%}$) with molecular weight of 3,200 and dispersity of 1.16. To adjust the conductivity, N_3-PEO$_{550}$ short chains were

attached onto the backbone via copper-catalyzed alkyne-azide cycloaddition (CuAAC) click chemistry[92] at two different ratios, 70% N_3-TFSI$^-$Li$^+$/30% N_3-PEO_{550} or 30% N_3-TFSI$^-$Li$^+$/70% N_3-PEO_{550}, Scheme 3. To ensure stoichiometry, the click chemistry was done in two separate steps. First N_3-TFSI$^-$Li$^+$ was added into the reaction with polyGPE and after it was completely consumed an excess amount of N_3-PEO_{550} was added. The final polymers were purified by precipitation in ether. The resulted polymers were termed as poly(GPE-$TFSI_{70\%}$-$PEO_{30\%}$) (M_n= 4,500, dispersity: 1.21) and poly(GPE-$TFSI_{30\%}$-$PEO_{70\%}$) (M_n= 6,600, dispersity: 1.37) respectively.

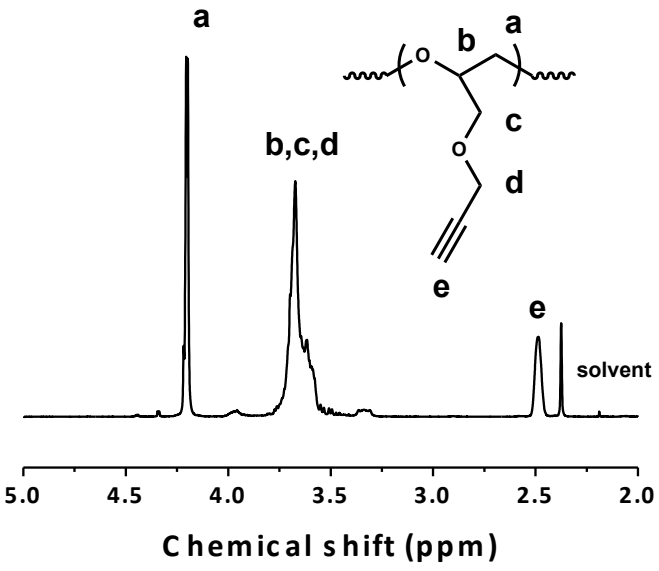

Figure 22. ^{1}H NMR spectrum of polyGPE in $CDCl_3$.

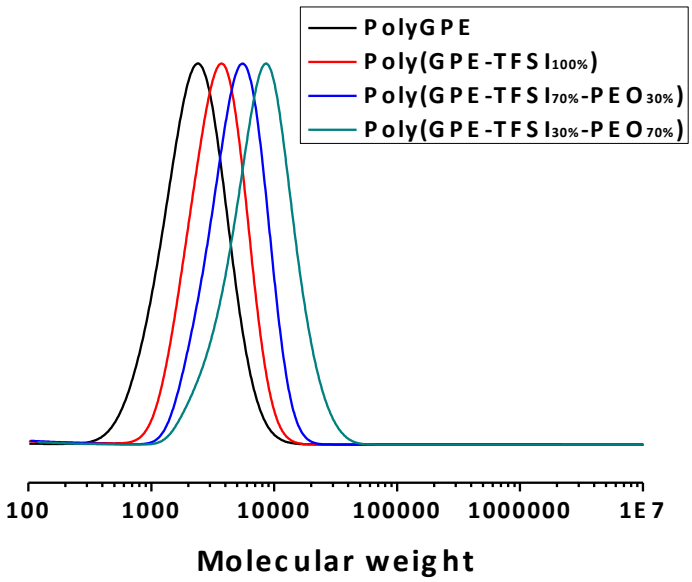

Figure 23. GPC traces of polymer samples.

As shown in Figure 24, as the content of N_3-PEO_{550} increased from 0 to 70% percent, the glass transition temperature (T_g) decreased from -2.4 ºC for poly(GPE-$TFSI_{100\%}$) to -10.0 ºC for poly(GPE-$TFSI_{70\%}$-$PEO_{30\%}$) and -28.0 ºC for poly(GPE-$TFSI_{30\%}$-$PEO_{70\%}$). This could be due to the introduction of short PEO chains onto the backbone that plasticized the polymer matrix and diluted the concentration of inorganic parts. The attachment of short PEO chains also transformed the polymer morphology from a linear shape to a comb-like structure, causing the crystallinity to decrease. As a result, the ionic conductivity was increased, Figure 25. By varying the amount of incorporated short PEO chains, the ionic conductivity could be tuned at both r.t. or high temperature (100 ºC). Based on the chemical structures, poly(GPE-$TFSI_{100\%}$) had a high EO/Li^+ molar ratio of 2/1, poly(GPE-$TFSI_{70\%}$-$PEO_{30\%}$) had a EO/Li^+ ratio of 3.7/1, poly(GPE-$TFSI_{30\%}$-$PEO_{70\%}$) had a EO/Li^+ ratio of 11.3/1. Table 3 and Figure 25d show that adjusting EO/Li^+ ratio and adjusting T_g had different impacts on improving the ionic conductivity at different temperatures. Poly(GPE-$TFSI_{70\%}$-$PEO_{30\%}$) showed similar ionic conductivity (2.90×10^{-7} S/cm) to

poly(GPE-TFSI$_{100\%}$) at r.t., but had much higher conductivity at 100 °C (2.27×10^{-4} S/cm). Comparatively, poly(GPE-TFSI$_{30\%}$-PEO$_{70\%}$) had similar conductivity (1.33×10^{-4} S/cm) to poly(GPE-TFSI$_{100\%}$) at 100 °C, but showed much higher conductivity at r.t (1.03×10^{-6} S/cm). These results suggest that at lower temperature chain-flexibility contributes more to the ionic conductivity than charge carrier concentration while at high temperature, the difference between chain-flexibility becomes less dominant and polymers with higher charge carrier concentrations contributed more to the final ionic conductivity. Therefore, best conductivity performances at different temperatures can be efficiently achieved by tuning the stoichiometry ratio.

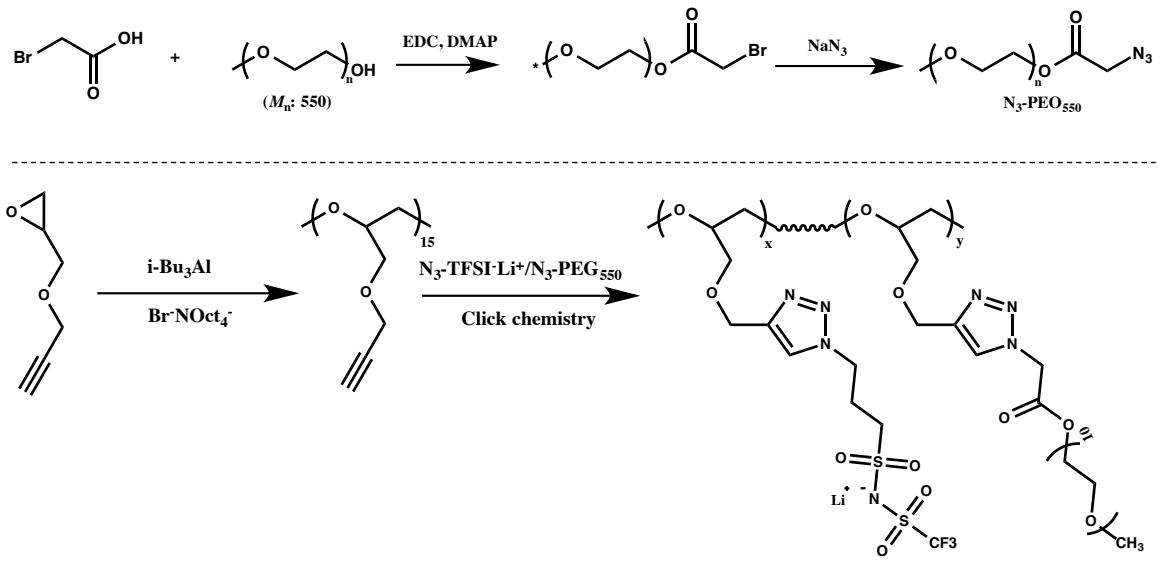

Scheme 3. Synthetic route for polymer electrolytes.

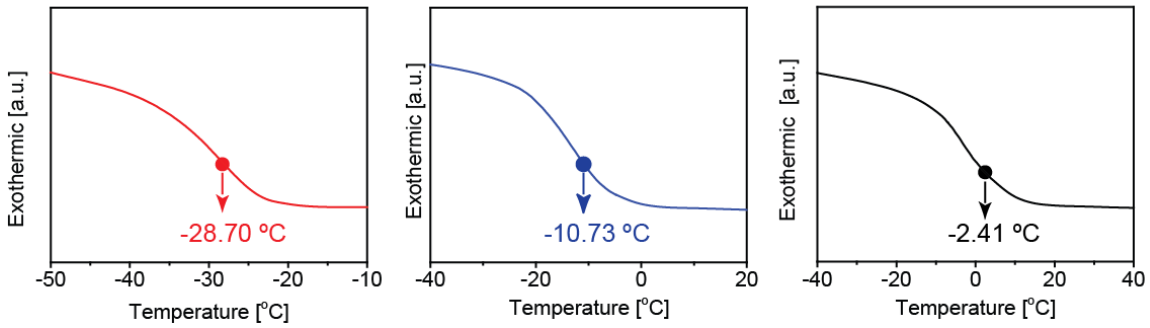

Figure 24. (a) DSC trace of poly(GPE-TFSI$_{30\%}$-PEO$_{70\%}$), (b) DSC trace of poly(GPE-TFSI$_{70\%}$-PEO$_{30\%}$) and (c) DSC trace of poly(GPE-TFSI$_{100\%}$).

The key parameter for single-ion electrolytes is the lithium ion transference number (t_+), which is defined as the fraction of moving lithium ions among all moving ions during charge/discharge.[80] An ideal single-ion electrolyte should have a transference number approaching unity. According to the Chazalviel model, a lithium dendrite is formed due to the anion concentration at the anode and high lithium transference number suppresses the ion concentration gradient at the anode during discharge. Herein, the transference number was investigated according to previous work, as described in supporting information.[26] A liquid electrolyte composed of 1 M $LiPF_6$ in an EC/EDC mix showed a transference number of 0.16 and an electrolyte blend of LiTFSI in PEO (M_n = 10,000, EO/Li^+ = 10/1) showed a transference number of 0.35, which are comparable to previously reported values in the literature.[93] The transference numbers for poly(GPE-TFSI$_{100\%}$), poly(GPE-TFSI$_{70\%}$-PEO$_{30\%}$) and poly(GPE-TFSI$_{30\%}$-PEO$_{70\%}$) were 0.99, 0.97 and 0.98 respectively. This was expected due to the conductive environment of the PEO backbones which made the lithium ions highly delocalized from the bulky TFSI anions.

Table 3. Information of all polymers.

Sample	M_n	$Đ$	T_g (°C)	EO/Li^+	t_+	σ @23 °C (S/cm)	σ @100 °C (S/cm)
PolyGPE	2,000	1.21	-39.5	-	-	-	-
Poly(GPE-$TFSI_{100\%}$)	3,200	1.16	-2.4	2/1	0.99	2.85×10^{-7}	1.38×10^{-4}
Poly(GPE-$TFSI_{70\%}$-$PEO_{30\%}$)	4,500	1.21	-10.0	3.7/1	0.97	2.90×10^{-7}	2.27×10^{-4}
Poly(GPE-$TFSI_{30\%}$-$PEO_{70\%}$)	6,600	1.37	-28.0	11.3/1	0.98	1.03×10^{-6}	1.33×10^{-4}
PEO/LiTFSI	10,000	-	-	10/1	0.35	-	-
1 M $LiPF_6$ in EC/EDC	-	-	-	-	0.31		

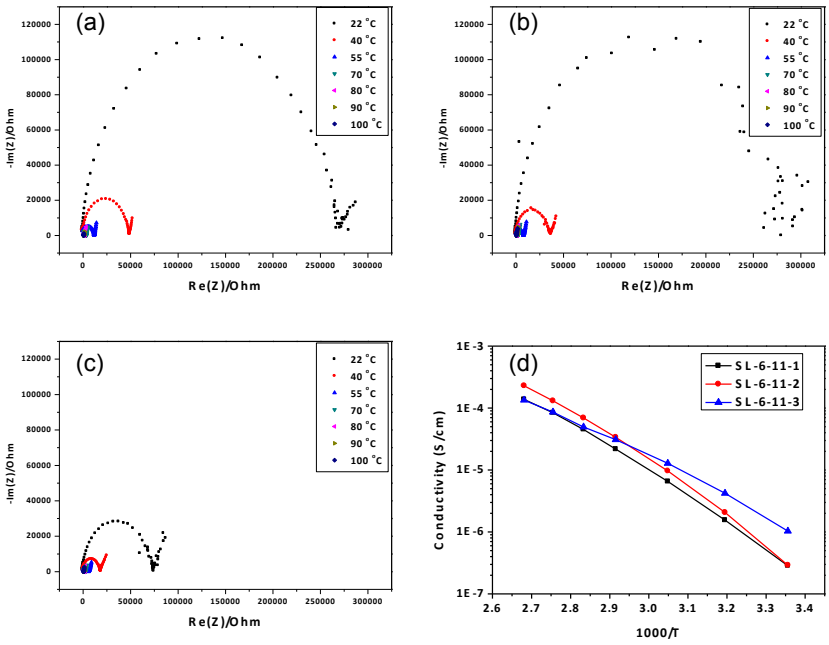

Figure 25. (a) EIS spectrum of poly(GPE-$TFSI_{100\%}$), (b) EIS spectrum of poly(GPE-$TFSI_{70\%}$-$PEO_{30\%}$), (c) EIS spectrum of poly(GPE-$TFSI_{30\%}$-$PEO_{70\%}$) and (d) Nyquist plots of the three polymer samples.

Finally, the electrochemical stability window of the polymers was examined by cyclic voltammetry. The measurements were performed at room temperature between -0.5 V and 5 V (versus Li^+/Li) at a scan rate of 1 mV/s. Poly(GPE-$TFSI_{100\%}$) was stable up to 4 V before oxidation, Figure 26, which was similar to its counterparts based on salt-laden PEO homopolymers.[84] Therefore, the single-ion polymer is applicable for a variety of lithium-ion cathode materials.

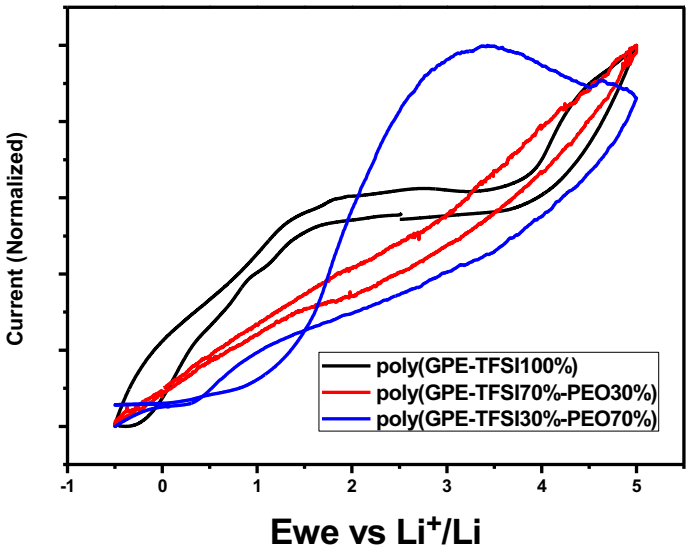

Figure 26. Electrochemical stability window. Voltammogram obtained at 1 mV/s at r.t.

2.3.3. Conclusions

In summary, a series of single-component solvent-free single-ion polymer electrolytes with conductive PEO-like backbones synthesized by anionic ring-opening polymerization and subsequent CuAAC click chemistry were prepared and discussed. The polymers showed high ionic conductivity compared to previously reported single-ion dry polymer electrolytes as well as high transference number. Therefore, one conclusion is that the ionic conductivity was affected by both

concentration of charge carrier and chain-flexibility. The conductivity could be efficiently tuned by adjusting the ratio of N_3-TFSI$^-$Li$^+$/N_3-PEO_{550} to maximize performance at different temperatures. The electrolytes also showed electrochemical stability up to 4 V (versus Li^+/Li). We believe, from a chemical perspective, this work is of great value for designing efficient polymer electrolytes for lithium-metal-based battery technologies.

2.4. Pseudo-Solid Bicontinuous Single-ion Electrolytes

2.4.1. Introduction

The future of electrochemical energy storage hinges on the development of rechargeable batteries that directly utilize the reactive metal as anode materials. Lithium metal anodes possess more than 10 times higher energy capacity than lithium-ion batteries with a graphite anode.[94] However, recharging a lithium metal battery involves the intrinsically unstable electro deposition of lithium. Growth of lithium dendrites, which is associated with the process, presents a major barrier for commercialization of lithium metal batteries, such as Li-S battery, Li-O_2 battery, etc.[95] It is now recognized that the stability of electro deposition is governed by four key properties of an electrolyte: transference number (t_+), ionic conductivity (σ), mechanical strength (G), and the anode surface stability.[67] Current electrolytes very rarely satisfy all these criteria at the same time. For example, commercial small molecule liquid electrolytes have poor mechanical strength, low t_+ (<0.3) and poor surface stability. Mechanical properties and anodic stability can be improved through the use of polymer electrolytes, however at the expense of lowering σ (below 1×10^{-6} S/cm at r.t.) and with no improvement of t_{Li} (<0.3). Finally, while the latter two parameters may be increased by using ceramic electrolytes, those systems are brittle with high interfacial resistance.

In this section, we aimed at creating hybrid electrolytes, which synergize the aforementioned advantages of organic/polymer and inorganic systems and "cancel out" their weaknesses. A templated approach was used. A porous silica template was prepared as a scaffold that can provide mechanical support – reverse sugar template and porous silica template. A single-ion conductive gel polymer phase was infused into the porous inter-connected template, forming a pseudo-solid bicontinuous single-ion electrolyte (PSBSE).

2.4.2. Results and discussions

Monroe and Newman predicted that solid polymer electrolytes with shear modulus (G) around two times that of lithium metal (10^9 Pa) can mechanically block lithium dendrite formation.[10] Silica has a bulk shear modulus of 30 GPa, therefore was selected as the scaffold for PSBSE. A sol-gel approach was used to prepare the porous silica monolith, Figure 27a. The porous SiO_2 scaffold possess two types of pores, 1 μm (Figure 27b&c) and 10 nm (Figure 27d), with a surface area around 250~400 m^2/g, characterized by BET analysis.

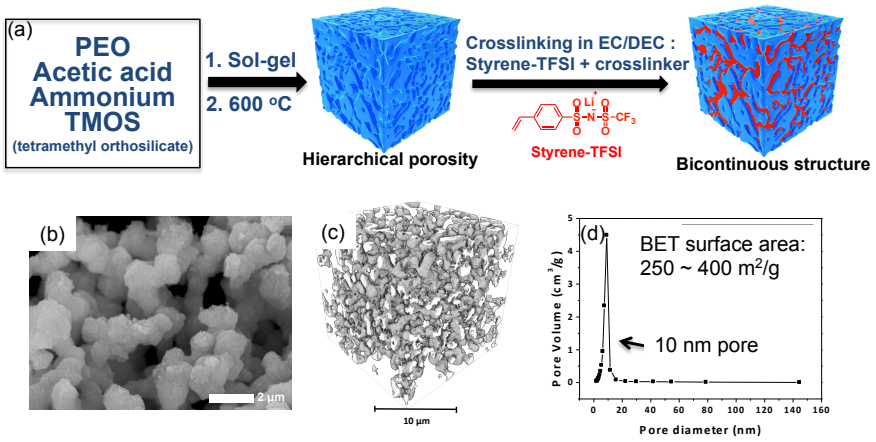

Figure 27. (a) Preparation of PSBSE; (b) SEM image of silica scaffold; (c) Nano-CT image of micron-sized pore; (d) BET nano-sized pore distribution.

Table 4. Comparison between commercial electrolye and PSBSE

Electrolyte	σ (mS/cm)	t_+	Modulus
1 M $LiPF_6$ in EC/DEC	8.0 (r.t.)	0.31	NA
PSBSE	1.5 (r.t.)	0.82	3.5 MPa

The internal conductive phase of PSBSE was created by free radical polymerization (FRP) of an infused solution of styrene-TFSI and crosslinker in EC/DEC, Figure 27a. EIS was used to measure the ionic conductivity and the transference number of the electrolyte. DMA was used to measure the apparent shear modulus, Table 4. As reported in Table 4, PSBSE had a ionic conductivity of 1.5 mS/cm, which is at the same level as a liquid commercial electrolyte at room temperature and a much more improved transference number of 0.82. More importantly, the electrolyte had a high apparent shear modulus of 3.5 MPa compared to the commercial electrolyte, which is in the form of dilute liquid.

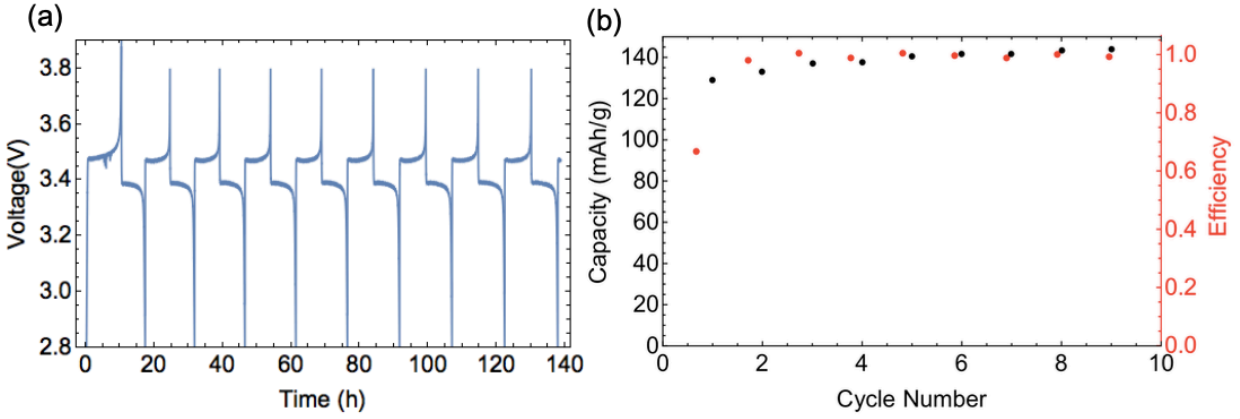

Figure 28. (a) Voltage profile of the lithium metal battery using PSBSE as electrolyte and LFP as cathode. (b) Capacity and Coulumbic efficiency of the first 10 cycles.

To demonstrate that the electrolyte could be cycled in a full battery, the electrolyte was assembled into a 2016 coin cell case with lithium foil as anode and LFP as cathode. The cell was

run at 0.1C. Figure 28a shows the stable voltage profile during the cycling. Figure 28b shows that the cell had a high coulombic efficiency (CE) approaching 100% with a high specific capacity of around 140 mAh/g.

2.4.3. Conclusions

In conclusion, a pseudo-solid bicontinuous single-ion electrolyte (PSBSE) made of a tough silica scaffold and a conductive single-ion phase gel was prepared using a template approach. The PSBSE had unique properties, including high ionic conductivity (1.5 mS/cm at r.t.), high transference number (0.82) and high mechanical strength (3.5 MPa). The electrolyte worked in a full LMB with LFP as cathode at high specific capacity and coulombic efficiency (CE). A broader perspective of this design principle of a pseudo-solid electrolyte will advance the use of functional polymers as electrolyte materials for the development of practical high energy density lithium metal batteries.

2.4.4. Experimental section

Preparation of the porous silica monolith. In a typical procedure, 1.18 g PEO (10,000 Da) was dissolved in 10 mL 0.01 M acetic acid. 4 mL TMOS was dropwise added and stirred in ice bath for 20 min. The resulted homogeneous solution was cast into a mold and allowed to crosslink at 40 ^{o}C for 24 h. The resulting raw monolith was transferred to 0.1 M ammonium solution and boiled at 120 ^{o}C for 9 h. The product was then washed with water and acetone, transferred to tube furnace at calcined at 600 ^{o}C for 4 h.

Synthesis of Styrene-TFSI. The synthesis route for the potassium form of styrene-TFSI is described in Figure 29. In the first step, a 15 g sample of sodium p-vinylbenzenesulfonate is suspended in 70 mL of DMF. The suspension is cooled via ice bath and 30 mL thionyl chloride is added dropwise. The mixture is stirred for 24 h at 25 ^{o}C. Afterwards, the mixture was poured into

ice water and extracted with 100 mL of diethyl ether and dried with $MgSO_4$. After evaporation of the solvent a pale viscous liquid product of the 4-styrene sulfonyl chloride was obtained (yield 70%). In the second step, 8.1 mL of triethylamine (58.1 mmol), 2.89 g of triuoromethylsulfonamide (19.4 mmol) and 9% of DMAP were successively added to 30 mL of dry acetonitrile. The 4-styrene sulfonyl chloride solution was cooled to 0 °C. Then the mixture of triuoromethylsulfonamide was added slowly to this solution and kept under stirring for 16 h. Solvent was removed and the resulting brown solid was dissolved in 50 mL of dichloromethane. This solution was washed with an aqueous solution of $NaHCO_3$ and 1M hydrochloric acid. The potassium form of styrene-TFSI was obtained by neutralization of the acid monomer by a molar excess of K_2CO_3 in water. The resulting suspension was stirred for one hour, filtered and dried to give 4.2 g of a light yellow solid. The lithium ion form was prepared by washing with $LiClO_4$.

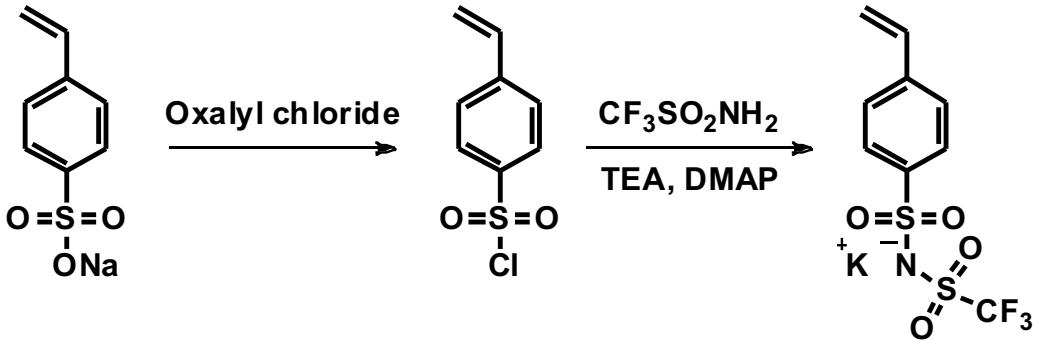

Figure 29. Synthesis route of styrene-TFSI.

Preparation of PSBSE. The silica monolith was immersed in a solution of styrene-TFSI and ethylene glycol dimethacrylate (EGDMA) (3/1) in a mixture of EC and DEC (50 wt%). 10% of AIBN was added and the solution was left to polymerize at 70 °C overnight. The resulted composite was then cut into 20 micron thin film electrolyte for use in a battery.

2.5. References

[1] Bruce, P. G.; Freunberger, S. A.; Hardwick, L. J.; Tarascon, J.-M., Li-O2 and Li-S batteries with high energy storage, *Nat. Mater.* **2012,** 11, 19.

[2] Szczech, J. R.; Jin, S., Nanostructured Silicon for High Capacity Lithium Battery Anodes, *Energy Environ. Sci.* **2011,** 4, 56.

[3] Tarascon, J. M.; Armand, M., Issues and Challenges Facing Rechargeable Lithium Batteries, *Nature* **2001,** 414, 359.

[4] Bhattacharyya, R.; Key, B.; Chen, H.; Best, A. S.; Hollenkamp, A. F., In situ NMR observation of the formation of metallic lithium microstructures in lithium batteries, *Nat. Mater.* **2010,** 9, 504.

[5] Xu, W.; Wang, J.; Ding, F.; Chen, X.; Nasybulin, E.; Zhang, Y.; Zhang, J.-G., Lithium Metal Anodes for Rechargeable Batteries, *Energy Environ. Sci.* **2014,** 7, 513.

[6] Brissot, C.; Rosso, M.; Chazalviel, J. N.; Lascaud, S., In Situ Concentration Cartography in the Neighborhood of Dendrites Growing in Lithium/Polymer-Electrolyte/Lithium Cells, *J. Electrochem. Soc.* **1999,** 146, 4393.

[7] Chang, H. J.; Ilott, A. J.; Trease, N. M.; Mohammadi, M.; Jerschow, A., Correlating Microstructural Lithium Metal Growth with Electrolyte Salt Depletion in Lithium Batteries Using (7)Li MRI, *J. Am. Chem. Soc.* **2015,** 137, 15209.

[8] Xu, K., Nonaqueous Liquid Electrolytes for Lithium-Based Rechargeable Batteries, *Chem. Rev.* **2004,** 104, 4303.

[9] Lu, Y.; Tu, Z.; Archer, L. A., Stable lithium electrodeposition in liquid and nanoporous solid electrolytes, *Nat. Mater.* **2014,** 13, 961.

[10] Monroe, C.; Newman, J., The Impact of Elastic Deformation on Deposition Kinetics at Lithium/Polymer Interfaces, *J. Electrochem. Soc.* **2005,** 152, A396.

[11] Ahmad, Z.; Viswanathan, V., Stability of Electrodeposition at Solid-Solid Interfaces and Implications for Metal Anodes, *Phys. Rev. Lett.* **2017,** 119, 056003.

[12] Tu, Z.; Zachman, M. J.; Choudhury, S.; Wei, S.; Ma, L.; Yang, Y.; Kourkoutis, L. F.; Archer, L. A., Nanoporous Hybrid Electrolytes for High‐Energy Batteries Based on Reactive Metal Anodes, *Adv. Energy Mater.* **2017,** 7, 1602367.

[13] Tu, Z.; Kambe, Y.; Lu, Y.; Archer, L. A., Nanoporous Polymer-Ceramic Composite Electrolytes for Lithium Metal Batteries, *Adv. Energy Mater.* **2014,** 4, 1300654.

[14] Cheng, X. B.; Hou, T. Z.; Zhang, R.; Peng, H. J.; Zhao, C. Z.; Huang, J. Q.; Zhang, Q., Dendrite‐Free Lithium Deposition Induced by Uniformly Distributed Lithium Ions for Efficient Lithium Metal Batteries, *Adv. Mater.* **2016,** 28, 2888.

[15] Bouchet, R.; Maria, S.; Meziane, R.; Aboulaich, A.; Lienafa, L., Single-ion BAB triblock copolymers as highly efficient electrolytes for lithium-metal batteries, *Nat. Mater.* **2013,** 12, 452.

[16] Lu, Y.; Tikekar, M.; Mohanty, R.; Hendrickson, K.; Ma, L.; Archer, L. A., Stable Cycling of Lithium Metal Batteries Using High Transference Number Electrolytes, *Adv. Energy Mater.* **2015,** 5, 1402073.

[17] Diederichsen, K. M.; McShane, E. J.; McCloskey, B. D., The Most Promising Routes to a High Li+ Transference Number Electrolyte for Lithium Ion Batteries, *ACS Energy Lett.* **2017,** 2, 2563.

[18] Zhang, H.; Li, C.; Piszcz, M.; Coya, E.; Rojo, T.; Rodriguez-Martinez, L. M.; Armand, M.; Zhou, Z., Single Lithium-Ion Conducting Solid Polymer Electrolytes: Advances and Perspectives, *Chem. Soc. Rev.* **2017,** 46, 797.

[19] Choi, J.-H.; Ye, Y.; Elabd, Y. A.; Winey, K. I., Network Structure and Strong Microphase Separation for High Ion Conductivity in Polymerized Ionic Liquid Block Copolymers, *Macromolecules* **2013,** 46, 5290.

[20] DeLuca, N. W.; Elabd, Y. A., Polymer electrolyte membranes for the direct methanol fuel cell: A review, *J. Polym. Sci., Part B: Polym. Phys.* **2006,** 44, 2201.

[21] Liang, S.; Chen, Q.; Choi, U. H.; Bartels, J.; Bao, N.; Runt, J.; Colby, R. H., Plasticizing Li single-ion conductors with low-volatility siloxane copolymers and oligomers containing ethylene oxide and cyclic carbonates, *J. Mater. Chem. A* **2015,** 3, 21269.

[22] Prosini, P. P.; Banow, B., Composite polyether electrolytes with a poly(styrenesulfonate) lithium salt and Lewis acid type additive, *Electrochimica acta* **2003,** 48, 1899.

[23] Helen Wang, J.-H.; Colby, R. H., Exploring the role of ion solvation in ethylene oxide based single-ion conducting polyanions and polycations, *Soft Matter* **2013,** 9, 10275.

[24] Rolland, J.; Poggi, E.; Vlad, A.; Gohy, J.-F., Single-ion diblock copolymers for solid-state polymer electrolytes, *Polymer (Guilford)* **2015,** 68, 344.

[25] Liang, S.; Choi, U. H.; Liu, W.; Runt, J.; Colby, R. H., Synthesis and Lithium Ion Conduction of Polysiloxane Single-Ion Conductors Containing Novel Weak-Binding Borates, *Chem. Mater.* **2012,** 24, 2316.

[26] Van Humbeck, J. F.; Aubrey, M. L.; Alsbaiee, A.; Ameloot, R.; Coates, G. W.; Dichtel, W. R.; Long, J. R., Tetraarylborate Polymer Networks as Single-Ion Conducting Solid Electrolytes, *Chem. Sci.* **2015,** 6, 5499.

[27] Sun, X.-G.; Kerr, J. B., Synthesis and Characterization of Network Single Ion Conductors Based on Comb-Branched Polyepoxide Ethers and Lithium Bis(allylmalonato)borate, *Macromolecules* **2006,** 39, 362.

[28] Sun, X.-G.; Kerr, J. B.; Reeder, C. L.; Liu, G.; Han, Y., Network Single Ion Conductors Based on Comb-Branched Polyepoxide Ethers and Lithium Bis(allylmalonato)borate, *Macromolecules* **2004,** 37, 5133.

[29] Meziane, R.; Bonnet, J.-P.; Courty, M.; Djellab, K.; Armand, M., Single-ion polymer electrolytes based on a delocalized polyanion for lithium batteries, *Electrochim. Acta* **2011,** 57, 14.

[30] Ma, Q.; Zhang, H.; Zhou, C.; Zheng, L.; Cheng, P.; Nie, J.; Feng, W.; Hu, Y. S.; Li, H.; Huang, X.; Chen, L.; Armand, M.; Zhou, Z., Single Lithium-Ion Conducting Polymer Electrolytes Based on a Super-Delocalized Polyanion, *Angewandte Chemie International Edition* **2016,** 55, 2521.

[31] Morris, M. A.; An, H.; Lutkenhaus, J. L.; Epps, T. H., Harnessing the Power of Plastics: Nanostructured Polymer Systems in Lithium-Ion Batteries, *ACS Energy Lett.* **2017,** 2, 1919.

[32] Jangu, C.; Savage, A. M.; Zhang, Z.; Schultz, A. R.; Madsen, L. A.; Beyer, F. L.; Long, T. E., Sulfonimide-Containing Triblock Copolymers for Improved Conductivity and Mechanical Performance, *Macromolecules* **2015,** 48, 4520.

[33] Villaluenga, I.; Inceoglu, S.; Jiang, X.; Chen, X. C.; Chintapalli, M.; Wang, D. R.; Devaux, D.; Balsara, N. P., Nanostructured Single-Ion-Conducting Hybrid Electrolytes Based on Salty Nanoparticles and Block Copolymers, *Macromolecules* **2017,** 50, 1998.

[34] Inceoglu, S.; Rojas, A. A.; Devaux, D.; Chen, X. C.; Stone, G. M., Morphology–Conductivity Relationship of Single-Ion-Conducting Block Copolymer Electrolytes for Lithium Batteries, *ACS Macro Lett.* **2014,** 3, 510.

[35] Timachova, K.; Watanabe, H.; Balsara, N. P., Effect of Molecular Weight and Salt Concentration on Ion Transport and the Transference Number in Polymer Electrolytes, *Macromolecules* **2015,** 48, 7882.

[36] Pan, Q.; Chen, Y.; Zhang, Y.; Zeng, D.; Sun, Y.; Cheng, H., A dense transparent polymeric single ion conductor for lithium ion batteries with remarkable long-term stability, *J. Power Sources* **2016,** 336, 75.

[37] Porcarelli, L.; Shaplov, A. S.; Bella, F.; Nair, J. R.; Mecerreyes, D.; Gerbaldi, C., Single-Ion Conducting Polymer Electrolytes for Lithium Metal Polymer Batteries that Operate at Ambient Temperature, *ACS Energy Lett.* **2016,** 1, 678.

[38] Hawker, C. J.; Barclay, G. G.; Orellana, A.; Dao, J.; Devonport, W., Initiating Systems for Nitroxide-Mediated "Living" Free Radical Polymerizations: Synthesis and Evaluation, *Macromolecules* **1996,** 29, 5245.

[39] Moad, G.; Rizzardo, E.; Thang, S. H., Living Radical Polymerization by the RAFT Process, *Aust. J. Chem.* **2005,** 58, 379.

[40] Braunecker, W. A.; Matyjaszewski, K., Controlled/living radical polymerization: Features, developments, and perspectives, *Prog. Polym. Sci.* **2007,** 32, 93.

[41] Matyjaszewski, K., Atom Transfer Radical Polymerization (ATRP): Current Status and Future Perspectives, *Macromolecules* **2012,** 45, 4015.

[42] Moses, J. E.; Moorhouse, A. D., The growing applications of click chemistry, *Chem. Soc. Rev.* **2007,** 36, 1249.

[43] Kolb, H. C.; Finn, M. G.; Sharpless, K. B., Click Chemistry: Diverse Chemical Function from a Few Good Reactions, *Angew. Chem. Int. Ed.* **2001,** 40, 2004.

[44] Golas, P. L.; Matyjaszewski, K., Marrying click chemistry with polymerization: expanding the scope of polymeric materials, *Chem. Soc. Rev.* **2010,** 39, 1338.

[45] Ali, M. M.; Stover, H. D. H., Well-Defined Amphiphilic Thermosensitive Copolymers Based on Poly(ethylene glycol monomethacrylate) and Methyl Methacrylate Prepared by Atom Transfer Radical Polymerization, *Macromolecules* **2004,** 37, 5219.

[46] Zhang, Y.; Costantini, N.; Mierzwa, M.; Pakula, T.; Neugebauer, D.; Matyjaszewski, K., Super Soft Elastomers as Ionic Conductors, *Polymer* **2004,** 45, 6333.

[47] Thelen, J. L.; Inceoglu, S.; Venkatesan, N. R.; Mackay, N. G.; Balsara, N. P., Relationship between Ion Dissociation, Melt Morphology, and Electrochemical Performance of Lithium and Magnesium Single-Ion Conducting Block Copolymers, *Macromolecules* **2016,** 49, 9139.

[48] Chintapalli, M.; Le, T. N. P.; Venkatesan, N. R.; Mackay, N. G.; Rojas, A. A.; Thelen, J. L.; Chen, X. C.; Devaux, D.; Balsara, N. P., Structure and Ionic Conductivity of Polystyrene-block-poly(ethylene oxide) Electrolytes in the High Salt Concentration Limit, *Macromolecules* **2016,** 49, 1770.

[49] Matyjaszewski, K.; Tsarevsky, N. V., Nanostructured functional materials prepared by atom transfer radical polymerization, *Nat. Chem.* **2009,** 1, 276.

[50] Coessens, V.; Pintauer, T.; Matyjaszewski, K., Functional polymers by atom transfer radical polymerization, *Prog. Polym. Sci.* **2001,** 26, 337.

[51] Wang, J.-S.; Matyjaszewski, K., Controlled/"Living" Radical Polymerization. Halogen Atom Transfer Radical Polymerization Promoted by a Cu(I)/Cu(II) Redox Process, *Macromolecules* **1995,** 28, 7901.

[52] Wang, J.-S.; Matyjaszewski, K., Controlled/"living" radical polymerization. atom transfer radical polymerization in the presence of transition-metal complexes, *Journal of the American Chemical Society* **1995,** 117, 5614.

[53] Jakubowski, W.; Matyjaszewski, K., Activators regenerated by electron transfer for atom-transfer radical polymerization of (meth)acrylates and related block copolymers, *Angew. Chem. Int. Ed.* **2006,** 45, 4482.

[54] Konkolewicz, D.; Wang, Y.; Zhong, M.; Krys, P.; Isse, A. A.; Gennaro, A.; Matyjaszewski, K., Reversible-Deactivation Radical Polymerization in the Presence of Metallic Copper. A Critical Assessment of the SARA ATRP and SET-LRP Mechanisms, *Macromolecules* **2013,** 46, 8749.

[55] Konkolewicz, D.; Wang, Y.; Krys, P.; Zhong, M.; Isse, A. A.; Gennaro, A.; Matyjaszewski, K., SARA ATRP or SET-LRP. End of controversy?, *Polym. Chem.* **2014,** 5, 4396.

[56] Matyjaszewski, K.; Jakubowski, W.; Min, K.; Tang, W.; Huang, J., Diminishing catalyst concentration in atom transfer radical polymerization with reducing agents, *Proc. Natl. Acad. Sci.* **2006,** 103, 15309.

[57] Magenau, A. J. D.; Strandwitz, N. C.; Gennaro, A.; Matyjaszewski, K., Electrochemically mediated atom transfer radical polymerization, *Science* **2011,** 332, 81.

[58] Treat, N. J.; Sprafke, H.; Kramer, J. W.; Clark, P. G.; Barton, B. E.; Read de Alaniz, J.; Fors, B. P.; Hawker, C. J., Metal-Free Atom Transfer Radical Polymerization, *J. Am. Chem. Soc.* **2014,** 136, 16096.

[59] Pan, X.; Lamson, M.; Yan, J.; Matyjaszewski, K., Photoinduced Metal-Free Atom Transfer Radical Polymerization of Acrylonitrile, *ACS Macro Letters* **2015,** 4, 192.

[60] Pan, X.; Fang, C.; Fantin, M.; Malhotra, N.; So, W. Y.; Peteanu, L. A.; Isse, A. A.; Gennaro, A.; Liu, P.; Matyjaszewski, K., Mechanism of Photoinduced Metal-Free Atom Transfer Radical Polymerization: Experimental and Computational Studies, *Journal of the American Chemical Society* **2016,** 138, 2411.

[61] Pan, X.; Tasdelen, M. A.; Laun, J.; Junkers, T.; Yagci, Y.; Matyjaszewski, K., Photomediated controlled radical polymerization, *Prog. Polym. Sci.* **2016,** 62, 73.

[62] He, H.; Zhong, M.; Adzima, B.; Luebke, D.; Nulwala, H., A simple and universal gel permeation chromatography technique for precise molecular weight characterization of well-defined poly(ionic liquid)s, *J. Am. Chem. Soc.* **2013,** 135, 4227.

[63] Lin, D.; Liu, W.; Liu, Y.; Lee, H. R.; Hsu, P.-C.; Liu, K.; Cui, Y., High Ionic Conductivity of Composite Solid Polymer Electrolyte via In Situ Synthesis of Monodispersed SiO2 Nanospheres in Poly(ethylene oxide), *Nano Lett.* **2015,** 16, 459.

[64] Yuan, W.; Yuan, J.; Zhang, F.; Xie, X.; Pan, C., Synthesis, Characterization, Crystalline Morphologies, and Hydrophilicity of Brush Copolymers with Double Crystallizable Side Chains, *Macromolecules* **2007,** 40, 9094.

[65] Hu, H.; Yuan, W.; Lu, L.; Zhao, H.; Jia, Z., Low glass transition temperature polymer electrolyte prepared from ionic liquid grafted polyethylene oxide, *J. Polym. Sci. A Polym. Chem.* **2014,** 52, 2104.

[66] Zhao, J.; Wang, L.; He, X.; Wan, C.; Jiang, C., Determination of Lithium-Ion Transference Numbers in LiPF6–PC Solutions Based on Electrochemical Polarization and NMR Measurements, *J. Electrochem. Soc.* **2008,** 155, A292.

[67] Tikekar, M. D.; Archer, L. A.; Koch, D. L., Stabilizing Electrodeposition in Elastic Solid Electrolytes Containing Immobilized Anions, *Sci. Adv.* **2016,** 2, e1600320.

[68] Diggle, J. W.; Despic, A. R.; Bockris, J. O. M., The Mechanism of the Dendritic Electrocrystallization of Zinc, *J. Electrochem. Soc.* **1969,** 116, 1503.

[69] Monroe, C.; Newman, J., Dendrite Growth in Lithium/Polymer Systems: A Propagation Model for Liquid Electrolytes under Galvanostatic Conditions, *J. Electrochem. Soc.* **2003,** 150, A1377.

[70] Barai, P.; Higa, K.; Srinivasan, V., Lithium dendrite growth mechanisms in polymer electrolytes and prevention strategies, *Phys. Chem. Chem. Phys.* **2017,** 19, 20493.

[71] Swamy, T.; Porz, L.; Sheldon, B. W.; Rettenwander, D.; Frömling, T.; Thaman, H.; Berendts, S.; Uecker, R.; Carter, W. C.; Chiang, Y.-M., Mechanism of Lithium Metal Penetration through Inorganic Solid Electrolytes, *Adv. Energy Mater.* **2017,** 7, 1701003.

[72] Armand, M. B., Polymer Electrolytes, *Annual Review of Materials Science* **1986,** 16, 245.

[73] Tarascon, J. M.; Armand, M., Issues and challenges facing rechargeable lithium batteries, *Nature* **2001,** 414, 359.

[74] Di Noto, V.; Lavina, S.; Giffin, G. A.; Negro, E.; Scrosati, B., Polymer electrolytes: Present, past and future, *Electrochimica Acta* **2011,** 57, 4.

[75] Hallinan, D. T.; Balsara, N. P., Polymer Electrolytes, *Annual Review of Materials Research* **2013,** 43, 503.

[76] Shin, J.-H.; Passerini, S., Effect of fillers on the electrochemical and interfacial properties of PEO–LiN(SO2CF2CF3)2 polymer electrolytes, *Electrochimica Acta* **2004,** 49, 1605.

[77] Morita, M.; Fukumasa, T.; Motoda, M.; Tsutsumi, H.; Matsuda, Y.; Takahashi, T.; Ashitaka, H., Polarization Behavior of Lithium Electrode in Solid Electrolytes Consisting of a Poly(Ethylene Oxide)-Grafted Polymer, *Journal of The Electrochemical Society* **1990,** 137, 3401.

[78] Itoh, T.; Mitsuda, Y.; Ebina, T.; Uno, T.; Kubo, M., Solid polymer electrolytes composed of polyanionic lithium salts and polyethers, *Journal of Power Sources* **2009,** 189, 531.

[79] Xu, W.; Sun, X.-G.; Austen Angell, C., Anion-trapping and polyanion electrolytes based on acid-in-chain borate polymers, *Electrochimica Acta* **2003,** 48, 2255.

[80] Mehta, M. A.; Fujinami, T., Li+ Transference Number Enhancement in Polymer Electrolytes by Incorporation of Anion Trapping Boroxine Rings into the Polymer Host, *Chemistry Letters* **1997,** 26, 915.

[81] Chang, H. J.; Ilott, A. J.; Trease, N. M.; Mohammadi, M.; Jerschow, A.; Grey, C. P., Correlating Microstructural Lithium Metal Growth with Electrolyte Salt Depletion in Lithium Batteries Using 7Li MRI, *Journal of the American Chemical Society* **2015,** 137, 15209.

[82] Chazalviel, J. N., Electrochemical aspects of the generation of ramified metallic electrodeposits, *Physical Review A* **1990,** 42, 7355.

[83] Brissot, C.; Rosso, M.; Chazalviel, J. N.; Lascaud, S., In Situ Concentration Cartography in the Neighborhood of Dendrites Growing in Lithium/Polymer - Electrolyte/Lithium Cells, *Journal of The Electrochemical Society* **1999,** 146, 4393.

[84] Bouchet, R.; Maria, S.; Meziane, R.; Aboulaich, A.; Lienafa, L.; Bonnet, J.-P.; Phan, T. N. T.; Bertin, D.; Gigmes, D.; Devaux, D.; Denoyel, R.; Armand, M., Single-ion BAB triblock copolymers as highly efficient electrolytes for lithium-metal batteries, *Nat Mater* **2013,** 12, 452.

[85] Porcarelli, L.; Shaplov, A. S.; Salsamendi, M.; Nair, J. R.; Vygodskii, Y. S.; Mecerreyes, D.; Gerbaldi, C., Single-Ion Block Copoly(ionic liquid)s as Electrolytes for All-Solid State Lithium Batteries, *ACS Applied Materials & Interfaces* **2016,** 8, 10350.

[86] Matyjaszewski, K.; Xia, J. H., Atom transfer radical polymerization, *Chemical reviews* **2001,** 101, 2921.

[87] Matyjaszewski, K.; Tsarevsky, N. V., Macromolecular Engineering by Atom Transfer Radical Polymerization, *J. Am. Chem. Soc.* **2014,** 136, 6513.

[88] Pan, X.; Malhotra, N.; Simakova, A.; Wang, Z.; Konkolewicz, D.; Matyjaszewski, K., Photoinduced Atom Transfer Radical Polymerization with ppm-Level Cu Catalyst by Visible Light in Aqueous Media, *Journal of the American Chemical Society* **2015,** 137, 15430.

[89] Herzberger, J.; Niederer, K.; Pohlit, H.; Seiwert, J.; Worm, M.; Wurm, F. R.; Frey, H., Polymerization of Ethylene Oxide, Propylene Oxide, and Other Alkylene Oxides: Synthesis, Novel Polymer Architectures, and Bioconjugation, *Chemical Reviews* **2016,** 116, 2170.

[90] Carlotti, S.; Desbois, P.; Billouard, C.; Deffieux, A., Reactivity control in anionic polymerization of ethylenic and heterocyclic monomers through formation of 'ate' complexes, *Polymer International* **2006,** 55, 1126.

[91] Rejsek, V.; Sauvanier, D.; Billouard, C.; Desbois, P.; Deffieux, A.; Carlotti, S., Controlled Anionic Homo- and Copolymerization of Ethylene Oxide and Propylene Oxide by Monomer Activation, *Macromolecules* **2007,** 40, 6510.

[92] Kolb, H. C.; Finn, M. G.; Sharpless, K. B., Click Chemistry: Diverse Chemical Function from a Few Good Reactions, *Angewandte Chemie International Edition* **2001,** 40, 2004.

[93] Gorecki, W.; Jeannin, M.; Belorizky, E.; Roux, C.; Armand, M., Physical properties of solid polymer electrolyte PEO(LiTFSI) complexes, *Journal of Physics: Condensed Matter* **1995,** 7, 6823.

[94] Lin, D.; Liu, Y.; Cui, Y., Reviving the lithium metal anode for high-energy batteries, *Nature nanotechnology* **2017,** 12, 194.

[95] Bruce, P. G.; Freunberger, S. A.; Hardwick, L. J.; Tarascon, J.-M., Li-O2 and Li-S batteries with high energy storage, *Nat. Mater.* **2011,** 11, 19.

Chapter 3. Polymer Based Artificial SEIs

3.1. Preface

Although replacing organic liquid electrolytes with solid electrolytes have multiple advantages, that would also mean a complete paradigm shift in terms of manufacturing infrastructure and it is not clear how compatible this would be with existing product lines in which billions of dollars have already been invested in the liquid electrolyte based battery industry. Therefore, if traditional liquid electrolytes can be used to create safe lithium metal batteries, then existing manufacturing facilities can be rapidly deployed for large-scale production.

The unsung hero for the huge success of traditional lithium ion batteries is the spontaneous formation of a solid-electrolyte interface (SEI) that can block the direct contact between electrons and organic electrolytes while providing sufficient regulation of lithium ion flux at the surface of graphite anode. However, the spontaneously formed SEI on a lithium metal anode is intrinsically unstable. This chapter aims to discuss the experimental progress made during my PhD to create a stable artificial SEI that inherits the benefits of natural SEI formed in lithium ion batteries. Two unique types of artificial SEI were developed and are discussed in this Chapter: (1) hybrid SEIs based on hairy nanoparticles prepared by covalently grafting polymers from functional inorganic NPs, and (2) a single-ion polymer SEIs with simplified structure and higher stability prepared by anionic ring opening polymerization. The results confirm that fabricating designed artificial SEIs can improve the cycling stability compared to an unprotected lithium anode.

While I designed all the projects, I would like to acknowledge Dr. Jiajun Yan, Tong Liu, Jacob Flum and Liye Fu for their contribution in materials synthesis. I would like to thank Dr. Sarah Fisco, Leiming Hu, Han Wang and Zongyu Wang for their contribution in materials

characterizations and electrochemical characterizations. I would also like to thank Dr. Francesca Lorandi for her contribution in paper writing.

3.2. A Conformal Artificial Interface Layer Based on Oxygen Vacancy-Rich Hybrids Nanoparticles for Stable Lithium Plating/Stripping

3.2.1. Introduction

Despite the huge market success of lithium ion batteries (LIB), it is economically inevitable to seek for a battery technology beyond LIB that has higher energy density with at least comparable cycling stability.[1] Encouraging advancements have been made in anode, cathode and electrolyte.[2-4] Yet the fundamental part of this quest is widely recognized as enabling the use of lithium metal as anode, having the lowest redox potential (−3.040 V vs. the standard hydrogen electrode) and highest theoretical capacity (3860 mAh/g) among possible anode materials.[5] In a typical LIB, a stable solid electrolyte interface (SEI) layer is spontaneously formed between the graphite anode and organic electrolyte. A stable SEI can prevent the reduction of electrolytes and facilitate the flux and de-solvation of lithium ions, thereby greatly increasing the cycling stability of the anode.[6] Although a lithium metal anode shares the same principle of redox chemistries as a graphite anode, a SEI formed over a lithium metal anode is intrinsically unstable.[7] The compositional inhomogeneity of such SEI layer leads to poor transport of lithium ions, repeated exposure of fresh lithium and consequent electrolyte depletion and formation of detrimental lithium dendrites.[8] As such, it is critical to create on a lithium metal anode a conformal SEI layer that can regulate the lithium ion flux on the anode surface while being mechanically robust and ionically conductive.

Previously, two types of artificial SEI for lithium metal have been extensively explored: a polymer coating and an inorganic coating.[8, 9] Polymer coatings could be easily made by solution

casting or formed *in situ*, and exhibit a certain extent of flexibility/flowability.[10] However, typical polymer coatings possess low ionic conductivity ($<10^{-5}$ S/cm) and poor mechanical strength, especially when swollen by an organic electrolyte. Moreover, due to the low transference number of most polymer materials,[11] they are inefficient at regulating the flux of lithium ions at the anode/electrolyte interface. Conversely, inorganic coatings, such as SiO_2, Al_2O_3, ZnO, etc, have been proposed as an alternative, because of their high shear modulus, functionality, and lithiophilicity.[12] Nevertheless, indistinct and inconsistent coating preparation procedures limit the applicability of inorganic SEI. Moreover, typically brittle inorganic layers cannot withstand the anode volume fluctuation during lithium plating/stripping.[12] Therefore, it is a compelling need to fabricate an inorganic/polymer hybrid SEI that combines advantages of both types of artificial SEI, i.e. facile preparation, high flexibility, ductility, transference number, and ionic conductivity; and overcomes their weakness.

3.2.2. Results and discussion

In this work, we created a class of inorganic/polymer hybrid hairy nanoparticles (NPs) by covalently grafting polyacrylonitrile (PAN) from oxygen vacancy (V_o)-rich yttria stabilized zirconia nanoparticles (YSZ NPs) via surface-initiated atom transfer radical polymerization (SI-ATRP), forming YSZ-*g*-PAN hybrids (Figure 30a) aimed at performing as effective artificial SEIs. PAN was chosen as the grafted polymer due to its wide electrochemical stability window, high ionic conductivity and good membrane forming ability.[13] PAN also has low swellability in typical liquid electrolytes. Meanwhile, the positive surface charges of YSZ NPs can selectively trap the anions, reduce the ion gradient near the anode, and increase the lithium transference number while homogenizing the ion flux during lithium plating.[14] Furthermore, we hypothesized that, compared to non-covalent YSZ/PAN blends, covalently grafted hairy NPs could further improve the

efficiency of the artificial SEI (Figure 30b&c) due to the following rational: (a) the YSZ-*g*-PAN hybrid particles would be much better dispersed in organic solvents than non-covalent blends, resulting in higher membrane homogeneity and higher mechanical integrity; (b) the reduced crystallinity caused by the homogeneous distribution of the inorganic filler and the immobilization of polymer chain end could further increase the ionic conductivity of the artificial SEI; (c) the YSZ-*g*-PAN based artificial SEI would promote more uniform ion transport paths, avoiding uneven lithium deposition typically caused by compositional inhomogeneity.

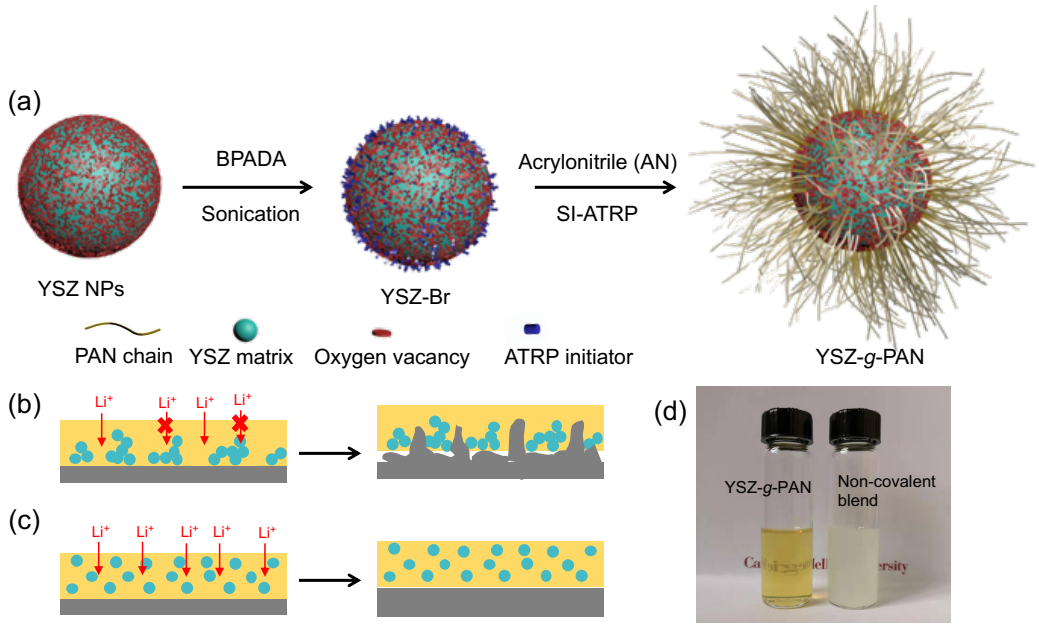

Figure 30. (a) Synthetic route of YSZ-g-PAN hairy nanoparticles. (b) Non-uniform coating prepared from a non-covalent blend of YSZ NPs and PAN/$LiClO_4$ leads to uneven lithium deposition. (c) Uniform hybrid coating using YSZ-g-PAN/$LiClO_4$ leads to dendrite-free lithium deposition. (d) Transparent solution (3 wt%) of YSZ-g-PAN hairy nanoparticles with 24.6 wt% inorganic content dispersed in DMF (left) and opaque dispersion in DMF of non-covalent blend of YSZ NPs and PAN with identical composition (right).

The key to the creation of inorganic/polymer hairy NPs is the availability of a chemical process that allows for tethering of polymer chains to the inorganic components. This process is hampered by chains coupling that typically involves noncovalent coordination, thus being sensitive to minor differences in surface chemical composition and charge. As a result, it remains a challenge to effectively graft polymers from inorganic substrates. Recently, our group reported a fatty-acid derived approach to graft polymer from metals and metal oxides by surface-initiated atom transfer radical polymerization (SI-ATRP).[15, 16] YSZ NPs are a metal oxide, and therefore are suitable for surface-functionalization by the fatty-acid-based tetherable ATRP initiator due to the abundance of surface charges caused by the yttrium doping.[15] However, such initiator, 12-(2-bromoisobutyramido)dodecanoic acid (BiBADA), contains a 2-bromoisobutyramide initiating group, which is far less reactive in ATRP than the acrylonitrile chain end (AN-Br).[17] To overcome this reactivity mismatch, we designed and synthesized a new fatty-acid-like initiator, 12-(2-bromo-2-phenylacetamido)dodecanoic acid (BPADA), that is more compatible with the growing AN-Br chains, Scheme 4. 2-Bromo-2-phenylacetic acid (BPAA) was first activated with *N*-hydroxysuccinimide (NHS) to differentiate its reactivity from the carboxylic group of 12-aminolauric acid. This step was followed by the amidation reaction. To immobilize ATRP initiators onto the surface of YSZ NPs, BPADA and YSZ NPs were sonicated together in the presence of triethylamine (TEA). The material obtained upon sonication could not be fully precipitated from tetrahydrofuran (THF), even at a rotational centrifugal force (RCF) of 4000 G, indicating successful anchoring of organic moieties onto the inorganic surface, thus giving an initiator functionalized YSZ NPs. The macroinitiator was then purified by dialysis against acetone to remove unanchored initiating molecules. SI-ATRP of AN was performed via initiator for continuous activator regeneration (ICAR) ATRP, using 50-200 ppm of a Cu catalyst.[18] Upon

polymerization, the solution was purified by dialysis against dimethylformamide (DMF). A series of hybrid hairy NPs was prepared with inorganic content ranging from 3.0 wt% to 71.1 wt%, Table 5. Figure 30d shows the different solvent dispersity of YSZ NPs with covalently grafted PAN and a non-covalent blend of the same composition. The left picture is a DMF solution of 3 wt% YSZ-g-PAN with 24.6 wt% inorganic content after letting the mixture sit for 6 months. The sample showed a form factor of a transparent solution proving the extremely high dispersibility of such grafted system. In comparison, the right hand picture in Figure 30d is a just prepared opaque dispersion of non-covalent blend of a similar weight fraction of YSZ NPs and PAN. The uniform size distribution of covalently grafted hybrid nanoparticles was further confirmed by dynamic light scattering (DLS) analysis, as shown in Figure 31a. YSZ-*g*-PAN samples with different inorganic content all showed narrow particle distribution in DMF. Specifically, samples with inorganic content of 3.0 wt%, 13.5 wt%, 24.6 wt% and 71.1 wt% respectively had an average size of 265.4 nm, 325.7 nm, 228.7 nm and 204.6 nm, Table 5. The grafted PAN chains were isolated by etching with HF. Polymers molecular weights (MWs) were measured by gel permeation chromatography (GPC). As shown in Figure 31b and Table 5, samples with inorganic content of 3.0 wt%, 13.5 wt%, 24.6 wt% and 71.1 wt% had a MW of 100,000, 136,300, 79,410 and 18,920 respectively. These results proved that the size of the YSZ-*g*-PAN hybrids is correlated to the length of the grafted polymer chains. TEM images of YSZ-*g*-PAN with inorganic content of 13.5 wt%, Figure 34, 24.6 wt% (Figure 31c) and 71.1 wt%, Figure 35, showed uniformly distributed YSZ NPs with little noticeable aggregation. In comparison, a blend of YSZ NPs (24.6 wt%) and PAN showed high degree of particle aggregation, Figure 36. These results prove the advantage of the covalent grafting-from approach that provides uniform NPs distribution in a polymer matrix.[19] The YSZ-*g*-

PAN hybrids showed excellent dispersibility also in dimethylsulfoxide (DMSO), which was subsequently used as solvent for the coating samples.

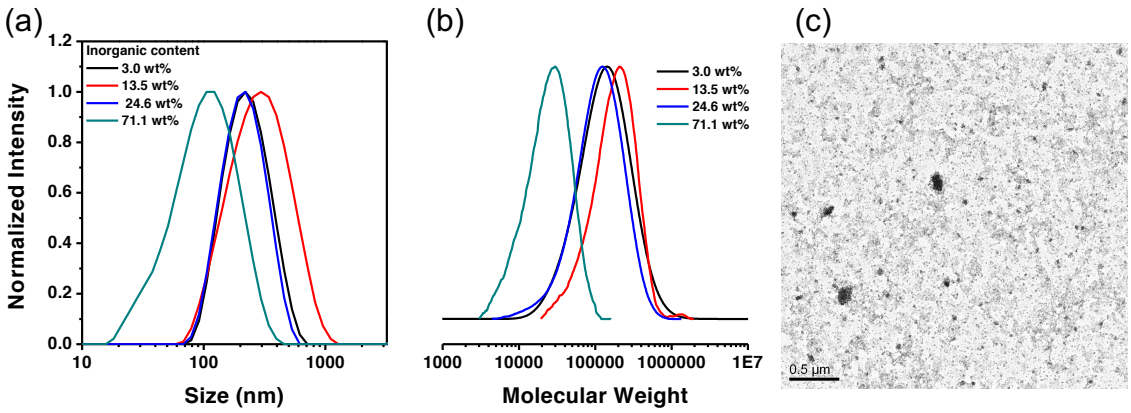

Figure 31. (a) DLS traces of YSZ-g-PAN with different inorganic content, and (b) GPC traces of cleaved PAN chains (b). (c) TEM image of YSZ-g-PAN with 24.6 wt% inorganic content.

The artificial SEI was prepared by drop-casting a DMSO solution containing YSZ-*g*-PAN hairy NPs and $LiClO_4$ onto the surface of fresh lithium chips, Figure 37. Focused ion beam scanning electron microscope (FIB-SEM) was used to study the particle distribution of the artificial SEI. Figure 32a, Figure 38, Figure 39 and Figure 40 show the cross-sections of the artificial SEI. Uniform distributions of YSZ NPs were observed for samples prepared from YSZ-*g*-PAN hairy NPs with inorganic content of 13.5 wt% (Figure 38) and 24.6 wt% (Figure 32a), indicating the homogeneity of the artificial SEI. In comparison, a coating made of YSZ NPs/PAN/$LiClO_4$ non-covalent blends, inorganic content = 24.6 wt%, showed high extent of particle aggregation, Figure 39. Interestingly, the artificial SEI prepared from YSZ-*g*-PAN NPs with 71.1 wt% inorganic content showed aggregations and gyroid-phase-like morphology, Figure 40. Tensile test of the artificial was done using dynamic mechanical analysis (DMA). Membranes made of YSZ-*g*-PAN hairy NPs (inorganic content=24.6 wt%) and $LiClO_4$ and membranes made

of the non-covalent blend with the same composition were tested. As shown in Figure 32b, the non-covalent blend had a higher Young's modulus (0.52 GPa), higher than that of YSZ-g-PAN (0.27 GPa). This is possibly due to the fact that the PAN used for the non-covalent blend was synthesized by initiators for continuous activator regeneration (ICAR) atom transfer radical polymerization (ATRP), with a very narrow molecular weight distribution (M_w/M_n=1.15).[20] However, the artificial SEI based on YSZ-g-PAN hairy NPs showed higher toughness (6.98×10^8 J/m^3) and failure strain (107.2%) than that of the non-covalent blend (4.53×10^8 J/m^3 and). Such higher toughness can be attributed to the higher uniformity of membranes prepared from YSZ-*g*-PAN hairy NPs. Electrochemical impedance spectroscopy (EIS) was used to measure the ionic conductivity of the membranes. Encouragingly, all YSZ-*g*-PAN/$LiClO_4$ with different inorganic contents showed greatly improved ionic conductivity compared to pure PAN/$LiClO_4$ or non-covalent blend of YSZ nanowires, PAN and $LiClO_4$,Figure 32c.[14] Samples with inorganic content of 3.0 wt%, 13.5 wt%, and 24.6 wt% showed room temperature ionic conductivity of 0.29×10^{-4} S/cm, 1.35×10^{-4} S/cm and 1.49×10^{-4} S/cm, respectively, suggesting that even at a relatively low inorganic content the ionic conductivity tends to increase with the content of YSZ NPs. However, at higher inorganic content (71.1 wt%), the room temperature ionic conductivity decreased to 0.65×10^{-4} S/cm, which is likely because of the lower $LiClO_4$ content led to an increased activation energy of ion transport. These results further prove the hypothesized superior properties of YSZ-*g*-PAN hairy NPs.

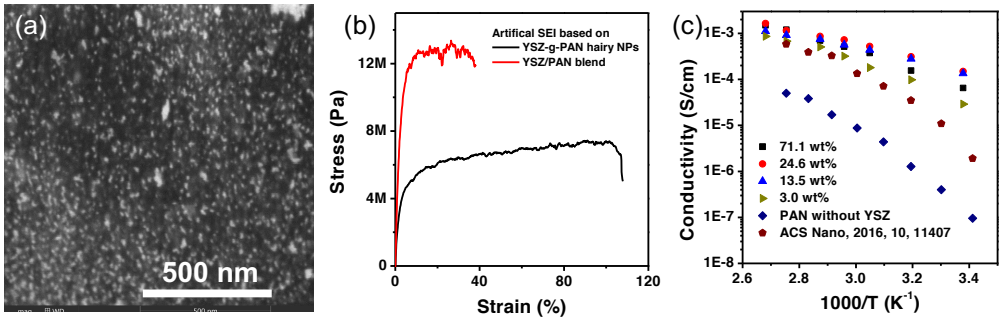

Figure 32. (a) FIB-SEM image of cross-section of the artificial SEI formed using YSZ-g-PAN with inorganic content of 24.6 wt%. (b) Tensile tests of artificial SEI using YSZ-g-PAN with inorganic content of 24.6 wt% and artificial SEI using the non-covalent YSZ/PAN blends of the same composition. (c) Arrhenius plots of ionic conductivity of artificial SEI prepared from YSZ-g-PAN hairy NPs of different inorganic content.

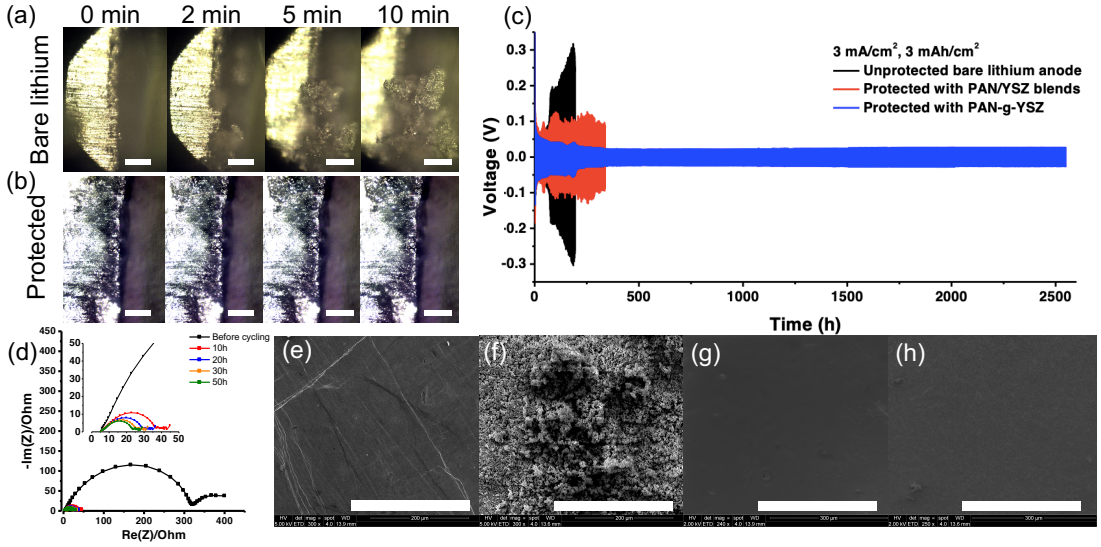

Figure 33. (a) Optical microscope image of the surface of unprotected lithium during lithium deposition at a current density of 5 mA/cm^2 (scale bar=100 micron). (b) Optical microscope image of the surface of lithium protected with artificial SEI using YSZ-g-PAN hairy NPs with 24.6 wt% inorganic content during lithium deposition at a current density of 5 mA/cm^2 (scale bar=100

micron). (c) Symmetric cycling of protected lithium using YSZ-g-PAN hairy NPs with 24.6 wt% inorganic content (blue), YSZ/PAN non-covalent blend (red) and unprotected lithium anode (black) at a current density of 3 mA/cm^2, 1 hour each half step. (d) Cell resistance measured by EIS during the symmetric cycling of lithium protected with artificial SEI using YSZ-g-PAN hairy NPs with 24.6 wt% inorganic content. (e)&(f) SEM images of bare lithium anode before and after cycling at 3 mA/cm^2. Scale bar = 300 micron. (g)&(h) SEM images of lithium anode protected with artificial SEI using YSZ-g-PAN hairy NPs with 24.6 wt% inorganic content before and after cycling at 3 mA/cm^2. Scale bar = 300 micron.

Finally, three types of YSZ-*g*-PAN hybrid hairy NPs with inorganic content of 13.5 wt%, 24.6 wt% and 71.1 wt% were tested as artificial SEIs. An optical microscope was used to detect the surface roughness of the lithium anode in order to demonstrate the effective dendrite suppression of the artificial SEI. A home-made visualization cell was designed for the experiment, Figure 41. Under a current density of 5 mA/cm^2, the formation of mossy lithium dendrites on unprotected lithium was observed after less than 2 min, Figure 33a. In contrast, the surface of lithium anode coated with the artificial SEI remained smooth for over 10 minutes, indicating non-existence of dendrite formation, Figure 33b. To demonstrate the coating benefits on lithium plating/stripping, symmetric cells made of two equivalent lithium anodes, with or without protection of artificial SEI, were assembled and run at a current density of 3 mA/cm^2 with 1 hour for each half step. The cell with unprotected lithium started to polarize immediately and reached about 300 mV overpotential within 200 hours before shortage, Figure 33c. The cell with lithium protected with a non-covalent blend of YSZ NPs/PAN/$LiClO_4$ (24.6 wt%) showed a reduced overpotential, slightly above 100 mV, and longer cycle life, indicating the effectiveness of coating lithium with YSZ NPs added into the polymer matrix. Finally, the lithium protected with the

artificial SEI made from YSZ-*g*-PAN hairy NPs was tested. The artificial SEI with 13.5 wt% inorganic content provided an initial overpotential of about 100 mV. As the cycling proceeded, the voltage decreased and stabilized at about 25 mV for over 350 hours, then the cell eventually shorted, Figure 42. With increasing the inorganic content, the symmetric cycling showed even longer improved cycling stability. The symmetric cell with electrodes coated with artificial SEI having 71.1 wt% inorganic content, lasted for over 2300 hours at 3 mA/cm^2. However, the initial voltage showed certain degree of instability for 250~300 hours, Figure 42. This was possibly due to the relatively high brittleness of the membrane with such high inorganic content, as well as its reduced ionic conductivity. The electrodes protected with artificial SEI made of YSZ-*g*-PAN NPs with 24.6 wt% inorganic content showed the best cycling performance, lasting for over 2500 hours with overpotential of about 20 mV, Figure 33c. This cell also achieved the highest Coulombic efficiency of 99.23%, Table 6, which was measured using a well-established approach.[21] The resistance of cells made of protected or unprotected lithium was measured by electrochemical impedance spectroscopy (EIS) before and after cycling for 50 hours. Compared to the cell with bare lithium, Figure 44, the cell with lithium protected by artificial SEI having 24.6 wt% inorganic content showed lower and more stable resistance both before and after cycling, Figure 33d, in accordance with the lower overpotential shown in Figure 33c. Scanning electron microscopy (SEM) was used to study the surface morphology of electrodes before and after cycling. Figure 33e and Figure 33f showed clear formation of lithium dendrites for lithium without protection of the artificial SEI. In comparison, no dendrite was observed on the surface for lithium protected with artificial SEI, Figure 33g and Figure 33h, proving the efficiency of the protection by YSZ-*g*-PAN artificial SEI.

3.2.3. Conclusions

In conclusion, we have developed a fatty-acid-based ATRP initiator for grafting PAN from *Vo*-rich YSZ NPs with high grafting density by SI-ATRP. The as synthesized YSZ-*g*-PAN hairy NPs with different inorganic contents could be stably dispersed in organic solvents, without observing precipitation for several months. The immobilization of PAN chains on the surface of YSZ NPs greatly reduced the polymer crystallinity, thereby increasing the ionic conductivity of the polymer matrix, while improving its mechanical integrity and membrane-forming ability. The positively charged oxygen vacancy (*Vo*) of the YSZ NPs further reduced the ion gradient near the anode and increased the lithium transference number while homogenizing the ion flux during lithium plating. The aforementioned benefits combined with the easiness of solution drop-casting the SEI led to the facile creation of hybrid artificial SEIs that enabled dendrite-free lithium plating/stripping with Coulombic efficiency as high as 99.23%. The invention of YSZ-*g*-PAN hairy NPs enriched the field of polymer-inorganic hybrid materials and provided new perspectives for the rational design of dendrite-free lithium anodes.

3.2.4. Experimental section and supporting information

Materials and Characterizations.

Materials Acrylonitrile (AN, Sigma-Aldrich, >99%) was purified by passing through a basic alumina column before use. Copper bromide ($CuBr_2$, Aldrich, 99%), hydrofluoric acid (HF, Aldrich, 48%), yttria stabilized zirconia (YSZ, Aldrich, <100 nm, 100 m^2/g), triethylamine (TEA, Alfa Aesar, 99%), azobisisobutyronitrile (AIBN, Aldrich, 98%), tris(2-dimethylaminoethyl)amine (Me_6TREN, Alfa Aesar, 99%), N,N-dimethylformamide (DMF, VWR, 99%), dimethylsulfoxide (DMSO, Fisher, 99.9%), tetrahydrofuran (THF, EMD, 99.9%), anhydrous magnesium sulfate

($MgSO_4$, Fisher), α-bromophenylacetic acid (BPAA, Combi-Blocks, 98%), 1-(3-dimethylaminopropyl)-3-ethylcarbodiimide hydrochloride (EDC, Carbosynth, 97%), N-hydroxysuccinimide (NHS, Sigma-Aldrich, 98%), 12-aminododecanoic acid (TCI, >99%) were used as received.

Nuclear Magnetic Resonance Spectroscopy (NMR) ^1H NMR spectroscopy measurements were performed on a Bruker Advance 300 MHz spectrometer to analyze the final product of BPADA synthesis in $CDCl_3$.

Gel Permeation Chromatography (GPC). Number-average molecular weights (M_n) and molecular weight distributions (MWD) of cleaved PAN chains from PAN-*g*-YSZ samples were determined byGPC. The GPC system used a Waters 515 HPLC pump and a Waters 2414 refractive index detector using Waters columns (Styrogel 102, 103, and 105 Å) with 10 mM LiBr-containing DMF as the eluent at a flow rate of 1 mL/min at 50 °C using linear poly(ethylene oxide) (PEO) based calibrations. Diphenylethylene and toluene were used as internal standards for the system.

Dynamic Light Scattering (DLS). DLS using a Malvern Zetasizer Nano ZS was employed to determine volume-weighted average hydrodynamic radius and distribution of PAN-*g*-YSZ. The particle brushes were suspended in filtered DMF (4.5 μm PTFE filter) at low concentrations.

Transmission Electron Microscopy (TEM). TEM was carried out using a JEOL 2000 EX electron microscope operated at 200 kV. The spatial distribution, radius and inter-particle distances of the YSZ nanoparticles were determined from statistical analysis of the TEM micrographs using ImageJ software.

Tensile Tests. The YSZ-*g*-PAN hairy NPs and YSZ/PAN blend bulk films were tested in the tensile mode by using dynamic mechanical analysis (TA RSA-G2). The film thickness was

comprised between 30 and60 μm. The samples were stretched at a constant tensile rate of 0.001 mm/s at room temperature.

Thermogravimetric Analysis (TGA). TGA with TA Instruments 2950 was used to measure the fraction of YSZ in the hybrids. The data were analyzed with TA Universal Analysis. The heating procedure involved four steps: (1) temperature jump to 120 ºC; (2) hold at 120 ºC for 10 min; (3) ramp up at a rate of 20 ºC/min to 800 ºC; (4) hold for 2 min. The organic content of the samples were normalized to the weight loss between 120 °C and 800 °C. The grafting densities were calculated using the following equation (S1):

$$\sigma_{\mathrm{TGA}} = \frac{(1-f_{\mathrm{YSZ}})N_{\mathrm{A}}A_s}{f_{\mathrm{YSZ}}\,M_n} \qquad \text{(S1)}$$

The value for f_{YSZ} in equation S1 is the inorganic fraction measured by TGA after exclusion of any residual solvent; N_{A} is the Avogadro number; A_{s} is the specific surface area provided by the supplier; M_nH5 is the number average molecular weight of polymer brushes.

Plasma Focus Ion Beam Scanning Electron Microscopy (FIB-SEM) image collection and processing. The instrument used for the milling and imaging was a DualBeam Helios Plasma FIB-SEM (FEI Company, Hillsboro, OR). For the milling process, an ion current of 0.23 nA at 30 kV accelerating voltage was used. The milling distance, or the distance between each slice image, was 4 nm. As for imaging, a through-lens detector (TLD) was used. The working distance was set to be 4 mm, and the electron beam current was 0.34 nA with 5 kV accelerating voltage and 3 μs dwell time. The total time for milling and imaging for each slice was about 3 min.

Electrochemical Testing. For symmetric cell, two lithium chips with diameter of 10 mm was assembled in a 2032 coin cell with 50 μL of 1 M lithium bis(trifluoromethanesulphonyl)imide (LiTFSI) in 1,3-dioxolane (DOL) and 1,2-dimethoxyethane (DME) (1:1 volume ratio) with 1wt% lithium nitrate ($LiNO_3$) as an additive and Celgard 2325 as separators. The cell was cycled at a

current density of 3 mA/cm^2 with areal capacity of 3 mAh/cm^2. For measurement of Coulombic efficiency, the electrolyte used was 1 M lithium bis(trifluoromethanesulphonyl)imide (LiTFSI) in 1,3-dioxolane (DOL) and 1,2-dimethoxyethane (DME) (1/1 volume ratio) with 1 wt% lithium nitrate ($LiNO_3$) as an additive. 50 μL of electrolyte were used in each coin cell to standardize the testing. The batteries were first cycled once between 0 V and 2 V to pretreat the electrodes (no Li deposition). A fixed amount of charge (Q_T = 2 mAh/cm^2) was deposited onto the working electrode and then a smaller portion of the charge (Q_c = 1 mAh/cm^2) was used to cycle Li between working and counter electrodes for *n* cycles. The final stripping charge (Q_S) was stripped away up to 0.5 V.

The average CE over *n* cycles can be calculated using formula (S2)

$$CE_{\text{arg}} = \frac{nQ_C+Q_s}{nQ_C+Q_T} \qquad (2)$$

Synthesis of BPADA. α-Bromophenylacetic acid (BPAA, 4.30 g, 20.0 mmol) and 1-(3-dimethylaminopropyl)-3-ethylcarbodiimide hydrochloride (EDC-HCl, 4.60 g, 24.0 mmol) were mixed in 250 mL of DCM in a 500 mL round bottom flask, followed by addition of N-hydroxysuccinimide (NHS, 0.3 g, 2.0 mmol). The mixture was allowed to react for 30 minutes, then 12-aminododecanoic acid (4.31 g, 20.0 mmol) was added to the flask. The reaction was placed under room temperature and stirred for 17 hours. After completion, the reaction mixture was separated by extraction with dilute HCl solution (pH = 3, 3x) then brine (pH = 3, 3x). The filtrate was then dried with anhydrous $MgSO_4$ and the organic solvent was removed under reduced pressure yielding 5.4 g of BPADA (65% yield). The final compound was analyzed by ^{1}H-NMR: (300 MHz, Chloroform-d) δ 12.04 – 11.95 (s, 1H), 9.82 – 8.63 (s, 1H), 7.60 – 7.35 (m, 5H), 5.45 (s, 1H), 3.42 – 3.24 (m, 2H), 2.35 (t, J = 7.5 Hz, 2H), 1.43 – 1.17 (m, 18H).

Synthesis of YSZ-*g*-PAN hairy NPs. In a typical procedure, 1 g (1.0×10^{20} nm^2) of YSZ were mixed with 0.342 g (0.83 mmol) of BPADA and 116 μL (0.83 mmol) of TEA and dispersed

in 10 mL of THF. The dispersion was sonicated overnight. Consequently, the initiator-functionalized YSZ NPs were unable to fully precipitate from THF even at a rotational centrifugal force (RCF) of 4000 G, indicating successful anchoring of organic moieties onto the inorganic surface. The dispersion was then dialyzed against acetone in three cycles with a MWCO of 10KDa. The solvent was removed under vacuum. To polymerize AN from YSZ, 0.3 g of the initiator-functionalized YSZ were dispersed in a mixture of 2.6 mL (40 mmol) AN and 3.9 mL DMSO. 55 μL (5.0 μmol) of a 20 mg/mL $CuBr_2$ solution in DMF were added. The solution was sonicated overnight to fully disperse the YSZ NPs. Then, 2.5 mg (15 μmol) of recrystallized AIBN and 4.0 mg (15 μmol) of Me_6TREN were added. The reaction was degassed by nitrogen bubbling before heating up to 65 °C. The reaction proceeded for a desired period. The polymerization mixture was then purified by dialysis against DMF in three cycles with a MWCO of 10KDa, resulting in a stable translucent dispersion.

Preparation of artificial SEI on lithium chip. A DMF solution of YSZ-*g*-PAN hairy NPs was evaporated to remove solvent and re-dispersed into DMSO, in which the material still exhibited high dispersity. 70 □L of DMSO solution (total weight percent = 0.5 wt%) containing YSZ-*g*-PAN hairy NPs and $LiClO_4$ (($PAN/LiClO_4$ = 2/1, wt/wt) were drop-casted onto the surface of a lithium chip (diameter = 10 mm). The solvent was left to evaporate at 50 ºC in a glove box (both O_2 and moisture < 0.5 ppm). The coated lithium chip was stored in the glove box for at least 1 week before test.

Scheme 4. Synthesis of 12-(2-bromo-2-phenylacetamido)dodecanoic acid (BPADA)

Table 5. YSZ-g-PAN hybrids synthesized by SI-ATRP.

Entry	Inorganic content (wt%)[a,b]	Inorganic content (vol%)[a,c]	Molecular weight (MW)[d]	MW dispersity[d]	Particle size (nm)[e]	Grafting density (chain/nm^2)
1	3.0	1.36	100,000	1.59	265.3	1.95
2	13.5	6.52	136,300	1.55	325.7	0.29
3	24.6	12.7	79,410	1.73	228.7	0.27
4	71.1	52.3	18,920	1.53	204.6	0.16

[a] measured by TGA

[b] weight percent of YSZ NPs in YSZ-*g*-PAN hairy NPs consisting of YSZ NPs and PAN.

[c] volume percent of YSZ NPs in artificial made of YSZ-*g*-PAN hairy NPs and $LiClO_4$.

[d] measured by GPC with DMF as eluting phase.

[e] measured by DLS

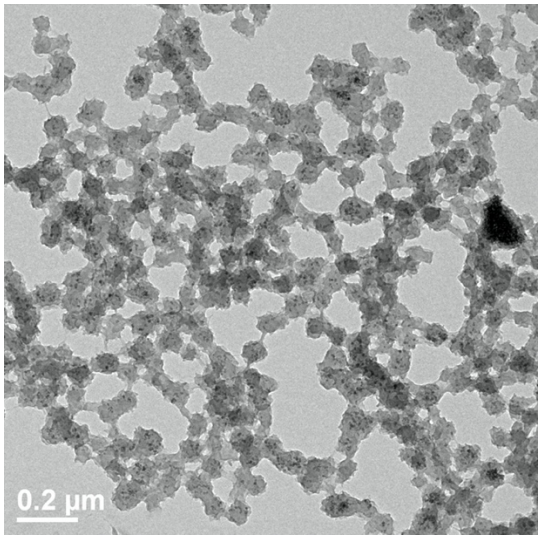

Figure 34. TEM image of YSZ-g-PAN hairy NPs with inorganic content of 13.5 wt%.

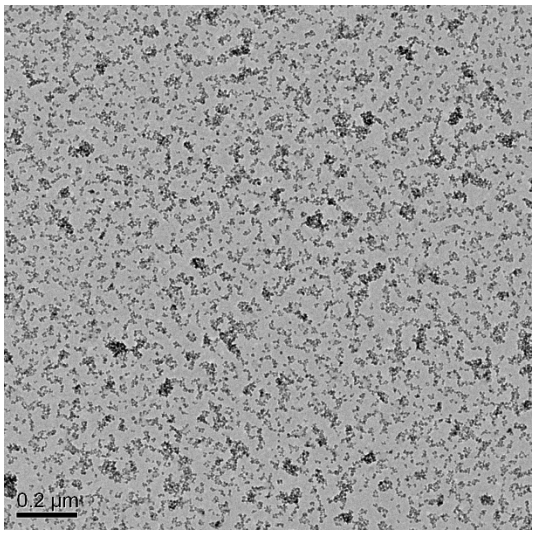

Figure 35. TEM image of YSZ-g-PAN hairy NPs with inorganic content of 71.1 wt%.

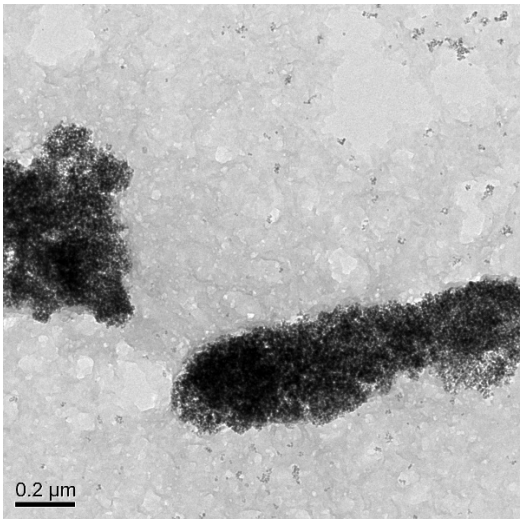

Figure 36. TEM image of non-covalent blend of 24.6 wt% YSZ NPs with PAN.

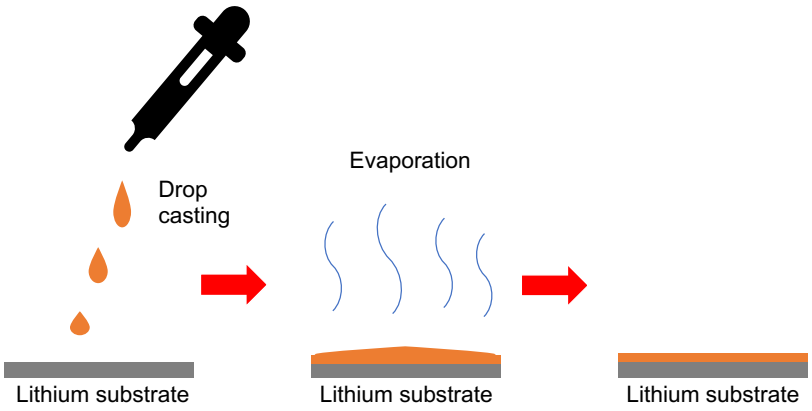

Figure 37. Schematics of preparation of artificial SEI by drop-casting.

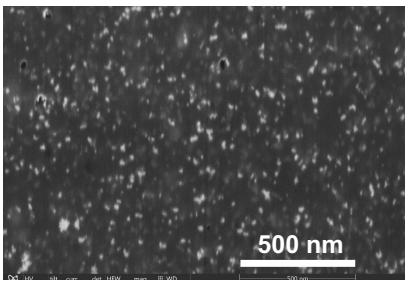

Figure 38. FIB-SEM image of cross-section of formed artificial SEI using YSZ-g-PAN hairy NPs with inorganic content of 13.5 wt%.

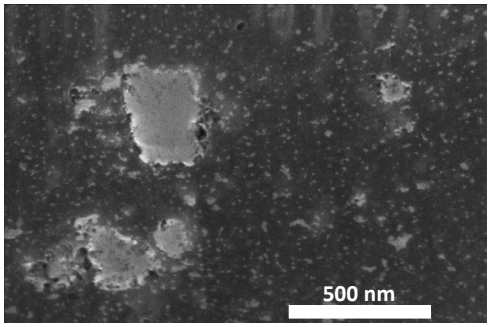

Figure 39. FIB-SEM image of cross-section of formed artificial SEI using a YSZ NPs/PAN non-covalent blend (inorganic content = 24.6 wt%).

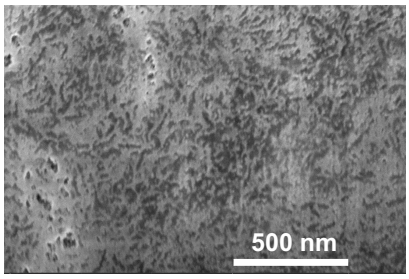

Figure 40. FIB-SEM image of cross-section of formed artificial SEI using YSZ-g-PAN hairy NPs with inorganic content of 71.1 wt%.

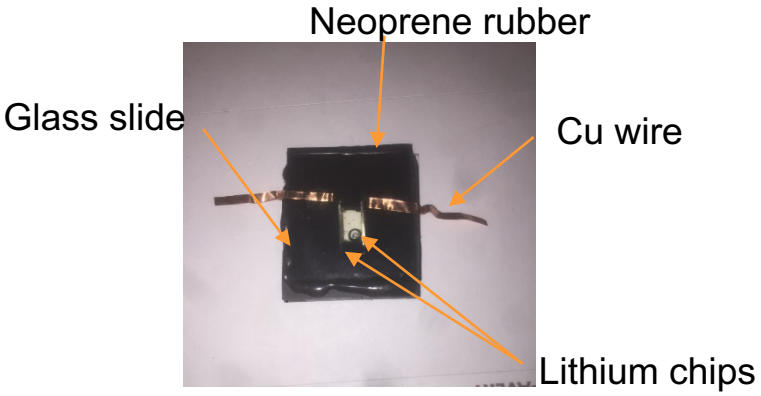

Figure 41. Digital picture of the set-up of home-made visualization cell.

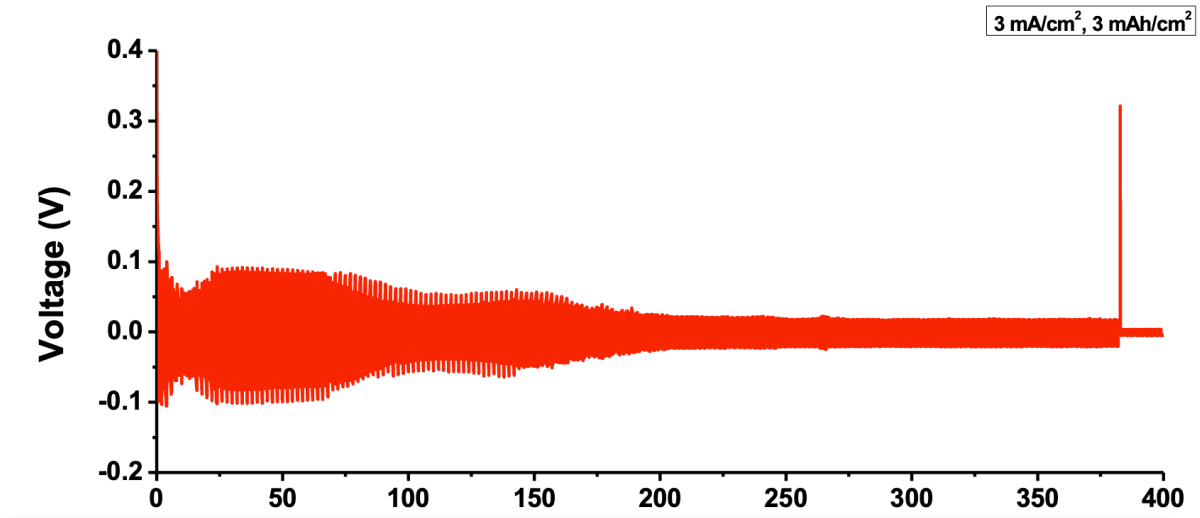

Figure 42. Symmetric cycling of protected lithium using YSZ-g-PAN with 13.5 wt% inorganic content at a current density of 3 mA/cm^2 for 1 hour each half step.

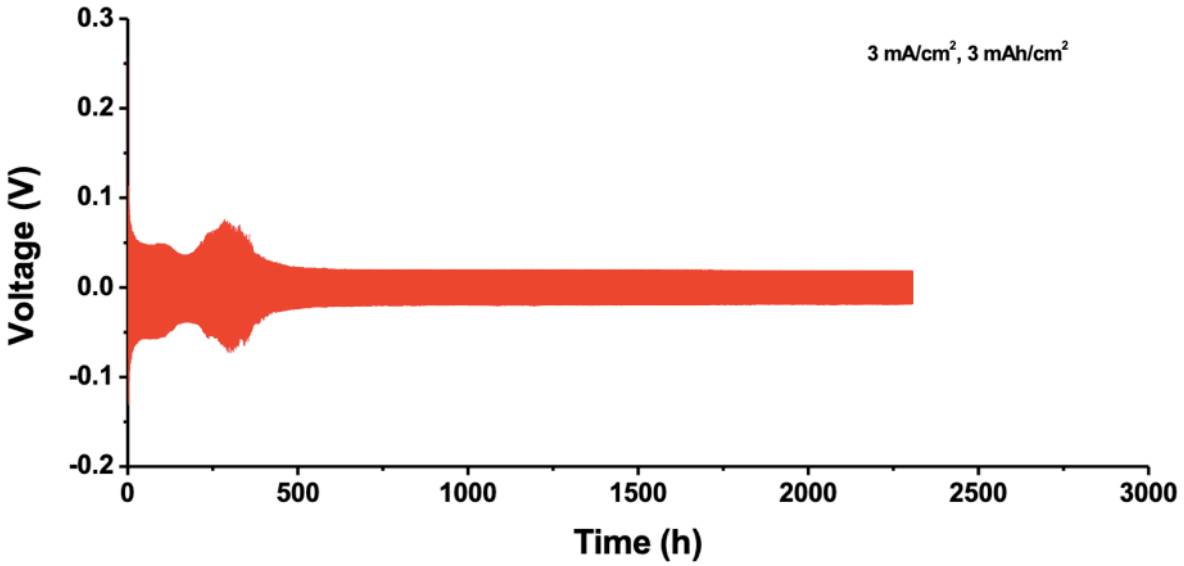

Figure 43. Symmetric cycling of protected lithium using YSZ-g-PAN with 71.1 wt% inorganic content at a current density of 3 mA/cm^2 for 1 hour each half step.

Figure 44. Cell resistance measured by EIS during symmetric cycling of a cell composed of lithium electrodes without protection of artificial SEI.

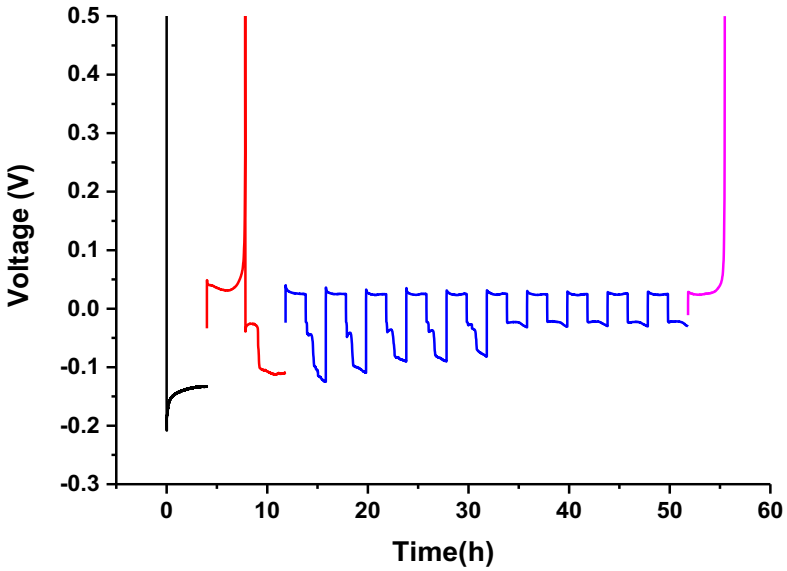

Figure 45. Voltage profile for measuring the Coulombic efficiency (CE) of the electrode protected with artificial SEI using YSZ-g-PAN with 13.5 wt% inorganic content.

Figure 46. Voltage profile for measuring the Coulombic efficiency (CE) of the electrode protected with artificial SEI using YSZ-g-PAN hairy NPs with 24.6 wt% inorganic content.

Figure 47. Voltage profile for measuring the Coulombic efficiency (CE) of the electrode protected with artificial SEI using YSZ-g-PAN NPs with 71.1 wt% inorganic content.

Table 6. Measured Coulombic efficiency (CE) for samples protected with artificial SEI.

Entry	Inorganic content (wt%)	Inorganic content (vol%)	Coulombic efficiency
1	13.5	6.52	98.53
2	24.6	12.7	99.23
3	71.1	52.3	98.55

3.3. PEO-like Single-ion Polymers as Artificial SEIs for Stable Lithium Plating/Stripping

3.3.1. Introduction

Uneven Li plating/stripping cycles on the anode surface cause the breakdown of the stabilizing solid electrolyte interface (SEI), leading to further reactions of lithium with the electrolyte and the formation of lithium dendrites.[22, 23] Once formed, these lithium dendrites continue to grow, causing decreased cycling efficiency and potential safety concerns from internal shorting and thermal runaway. Lithium dendrites are formed primarily as a consequence of unstable electrolyte/anode interface.[23] Typical carbonate based organic electrolytes react with lithium metal under normal operating voltages of the battery.[24, 25] These reactions lead to various insoluble byproducts, which will accumulate on the anode surface forming a passivating SEI. During cycling, the volume of lithium can change drastically due to it being a "hostless" material, causing the brittle SEI to crack: more electrolyte and lithium are then rapidly consumed to re-passivate the interface.[26] Continued breaking and forming of this type of SEI cause the surface to be non-homogenous and promote concentration gradients across the interface.[27, 28] Lithium will

then continue to deposit in these regions with continued cycling, forming dendrites and sections of dead lithium.

SEI stabilization has been one of the major areas of investigation to combat dendrite formation, as the source of their formation is directly addressed. These methods include: high salt concentration in the electrolyte,[29] additives to chemically stabilize the SEI,[30] using Cs or Rb to electrostatically shield dendrite protrusions,[28] atomic layer deposition of metal oxides such as alumina,[31] single ion electrolytes to decrease charging across the lithium surface,[19] and polymer interfaces.[32]

Polymers are promising materials for an artificial interface as they have been shown to be stable against both lithium and organic electrolytes and can adapt to volume changes, unlike many inorganic solid interfaces that are brittle and can crack. Artificial polymeric SEIs were first investigated by Efimov et al. by polymerizing acetylene directly on the surface of lithium metal anodes, decreasing cell impedance as well as showing more stable charge and discharge cycling.[33] Cui et al. introduced dynamic bonding in the polymer through the use of poly(dimethylsiloxane) using boron as a transient crosslinker.[34] The "solid-liquid" interface was able to give good interfacial contact, as well as potentially prevent dendrite formation through the local stiffening of the material when pressure is applied. Polymers can also serve as a matrix for additional additives such as Cu_3N nanoparticles.[35] Nanoparticles of size less than 100 nm were added to a styrene-butadiene rubber matrix to increase the ionic conductivity and stiffness of the interface, while the rubber served as an adaptive layer to maintain integrity of the film without cracking.

Single ion polymers (SIPs) have a high transference number, meaning they will conduct only lithium cations due to anions being anchored to a stationary polymer backbone. Because of this, SIPs can reduce concentration gradients across the electrolyte and at the electrode/electrolyte

interface, in turn making the stripping and plating cycles more stable thereby reducing the growth of dendrites.[36] SIPs typically come in three general classes: anionic groups covalently bonded to the backbone, polymer/inorganic hybrids, and polymers with anion accepting groups.[37] Anionic groups covalently bonded to the backbone have been the most thoroughly studied of these systems, with efforts including: the use of different anions such as sulfonates[38, 39] and trifluoromethanesulfonylimide (TFSI),[36, 40] different polymer architectures such as block copolymers[41, 42] and covalently attaching said polymers to silica[43, 44] or alumina[45] to enhance mechanical properties and reduce crystallinity. Our group has recently synthesized a single ion homopolymer electrolyte of poly(oligo(ethylene oxide) methacrylate lithium sulfonyl(trifluoromethylsulfonyl)imide) prepared through photoinduced metal free atom-transfer radical polymerization, resulting in a high transference number of 0.97-0.99.[11]

However, only a few investigations were carried out using SIPs as an artificial SEI layer, rather than as the electrolyte. Aside from the benefit of better distributing charge along the lithium metal interface to prevent hotspots of dendrite growth, single-ion polymers can also serve to mechanically prevent dendrite formation. Archer et al. used an ionomer with transference numbers reaching 0.88 to create a 20-300 nm thick artificial SEI layer on the surface of lithium, which was able to provide stable cycling at current densities of 3 mA/cm^2 and prevent dendrite formation.[46] Guo et al. developed a lithiated poly(acrylic acid) which acted as a self-adapting interface, acting both to distribute the concentration of anion evenly across the surface as well as to physically prevent dendrites through accommodating volume changes of the lithium during cycling at up to 1 mA/cm^2 current densities.[47] However, most single-ion polymers were based on an ester-based backbone, which were electrochemically unstable against lithium. Besides, the EO (ethylene oxide)/Li ratio was typically low – 10/1. While such low ratio provides the maximum of ionic

conductivity when used as electrolytes, higher lithium contents are needed in order to fight the generation of a lithium concentration gradient when used as a thin layer of artificial SEI. Therefore, it was of interest to create a single-ion polymer with simplified backbone PEO backbone (without ester groups) with a high EO/Li ratio for use as lithium protective artificial SEI.

3.3.2. Results and discussions

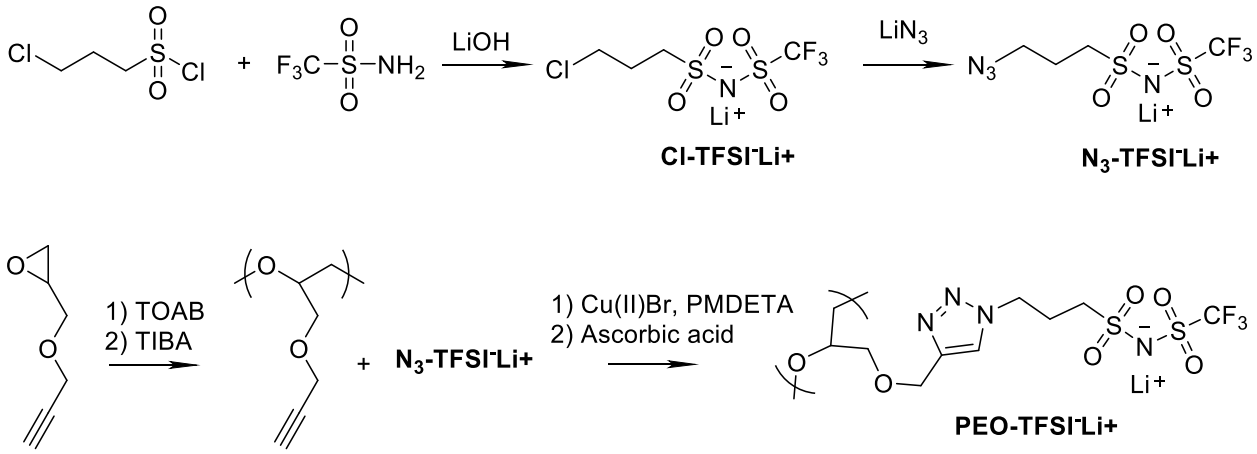

Scheme 5. Synthetic route to PEO-TFSI$^-$Li$^+$.

In this work, a single ion polymer with simplified structure of PEO backbone and high lithium content (EO/Li = 2/1) was created for use as an artificial SEI. Synthesis of the PEO-TFSI$^-$ Li$^+$ is shown in Scheme 5, with detailed experimental procedures given in the supporting information. Synthesis began with anionic ring opening polymerization of propargyl glycidyl ether to form PEO-alkyne using a co-catalyst system of tetraoctylammonium bromide and triisobutylaluminum developed by Deffieux et al[48]. The polymerization mechanism involves a monomer activation prior insertion into a growing "ate" complex as described in Scheme 6.[49-51] A lithium trifluoromethanesulfonimide salt (N_3-TFSI$^-$ Li$^+$) was prepared as previously described by our group through condensation of 3-chloropropanesulfonyl chloride and trifluoromethanesulfonimide in the presence of lithium hydroxide to form Cl-TFSI$^-$ Li$^+$, before being combined with lithium azide at 90˚C to form the targeted salt.[11] The PEO-alkyne and N_3-

TFSI$^-$ Li$^+$ were then clicked through copper mediated azide-alkyne cycloaddition, forming the single ion conducting PEO-TFSI$^-$Li$^+$. Polymers of different molecular weights were synthesized, with molecular weights determined through gel permeation chromatography using a DMF mobile phase containing 50 mM LiBr. Molecular weights and dispersities of samples prepared are shown in Table 7. The complete conversion of the click reaction was confirmed by FTIR analysis with the disappearance of alkyne peaks, Figure 55. Polymers with molecular weights of 74,000 were investigated as artificial SEI prepared by drop-casting on a fresh lithium chip.

Table 7. Properties of PEO-TFSI$^-$Li$^+$ synthesized, including the molecular weights and dispersity

Sample	DP[a]	Pre-Click M_n [b]	$Đ$[b]	Post Click M_n[a]
1	200	20000	1.83	74000
2	150	15200	1.38	47500
3	85	10000	1.48	37000
4	50	6300	1.21	19700
5	15	3000	1.08	11000
6	10	1700	1.22	5300

[a] Degree of polymerization, [b] Number-averaged molecular weight (M_n) and $Đ$ (dispersity) measured from gel permeation chromatography (GPC) using a DMF mobile phase containing 50 mM LiBr at 50 °C

The PEO-TFSI$^-$Li$^+$ described here has several inherent advantages over the polymer SEI systems previously prepared. Esters such as carbonates and acrylates are prone to electrochemical reduction against lithium metal, forming lithium alkyl carbonates ($ROCO_2Li$) among other side products; lowering coulombic efficiency to values less than 80%.[15] Ether linkages such as those in PEO are oxidatively stable at up to 4.5 V versus Li/Li$^+$ and less prone to nucleophilic attack.[52] Because of this electrochemical stability, ethers have been investigated for use in lithium-air batteries. For example, a PEO-lithium triflate solid electrolyte remained stable (as well as the

lithium and carbon electrodes) under operating voltages.[53] Secondly, PEO and TFSI based electrolytes have some of the highest ionic conductivities and transference numbers to date. Bouchet et al. synthesized a BAB triblock copolymer for lithium metal batteries, with the B blocks consisting of poly(styrene trifluoromethanesulfonylimide) and PEO as the A block.[36] Ionic conductivities of 1.3×10^{-5} S/cm and a transference number of 0.85 were obtained, owing to the PEO's ability to solvate and transport lithium ions, while the TFSI anions were only loosely coordinated to lithium allowing it to migrate freely.

To coat the lithium chips, PEO-$TFSI^-Li^+$ was dissolved in DMSO at a concentration of 2 wt%, before being drop cast onto lithium metal chips (16mm in diameter) and dried at 50°C for 24 hours. Two volumes were tested, 0.175 mL and 0.075 mL to determine the necessary thickness to ensure an even coating. Polymer thickness after drying was determined through calculation (assuming an even coating across the lithium chip and a polymer density of 1.3 g/cm^3) to be approximately 8 microns for the 0.175 mL sample, and 3.4 microns for the 0.075 mL sample. SEM images are shown in Figure 48, highlighting the surface morphology of bare lithium in addition to the 0.075 and 0.175 mL samples. As non-homogenous surface morphology is one of the primary causes of the formation lithium dendrites, in order to make an effective artificial interface it must be smoother than that of bare lithium. Both the bare lithium and 3.4 micron thick samples show highly irregular surfaces, with cracks common in the 3.4 micron sample. These cracks and rough areas can serve as sites of concentrated lithium ions, promoting the formation of dendrites. However, the surface of the 8 micron thick sample had no major cracks or holes in the layer, indicating that it could serve as a successful interface. A complete coating was further demonstrated by visualization of the cells after being exposed to air for a short period of time, as shown in Figure 49. The bare lithium and 3.4 micron samples quickly turned a black or gray color,

indicating reaction with nitrogen forming lithium nitride; however the 8 micron sample remained a light orange color indicative of the presence of a polymer coating.

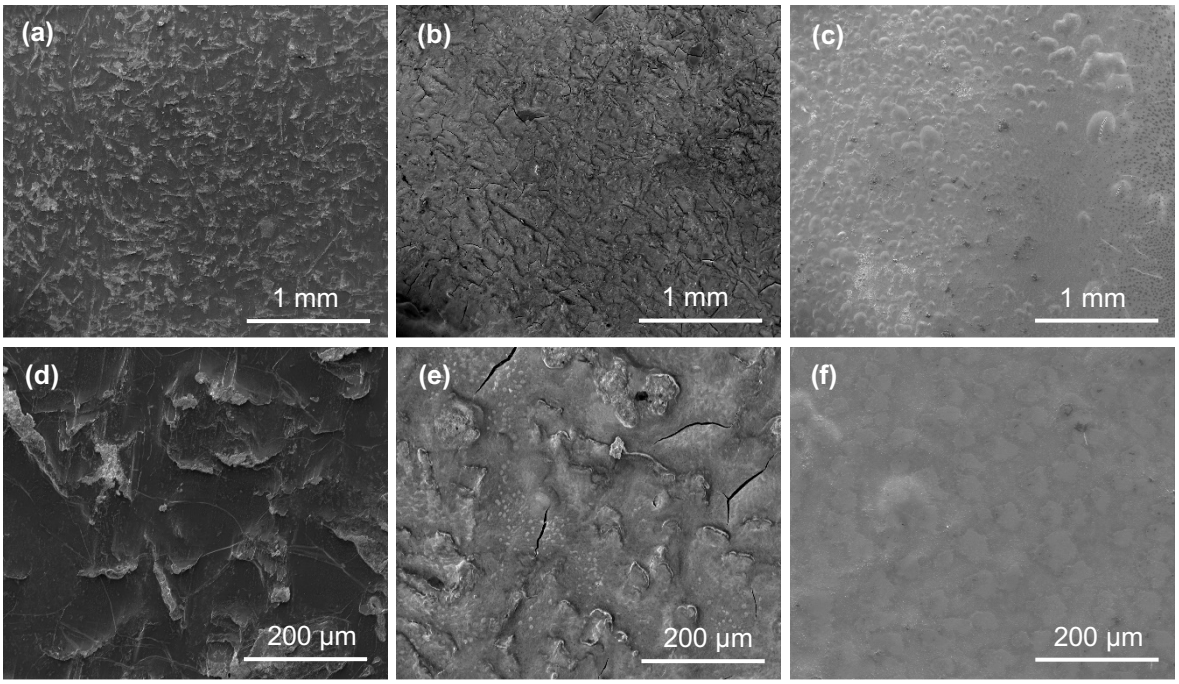

Figure 48. SEM characterization of surface morphology of coated and uncoated lithium. (a) and (d) bare lithium chip. (b) and (e) 3.4 micron thick polymer coating. (c) and (f) 8 micron thick polymer coating.

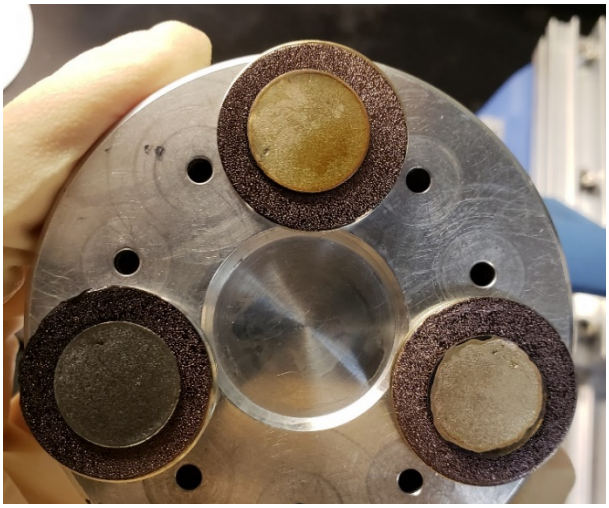

Figure 49. Lithium chips after exposure to air for 5 minutes. uncoated lithium (bottom left), 3.4 micron SIP coating (bottom right), and 8 micron SIP coating (top middle).

Electrochemical tests were conducted in a symmetric Li/Li coin cell using 1 M $LiPF_6$ in an electrolyte solution of 1:1 EC:DMC, with each lithium chip coated on one side with PEO-$TFSI^-$ Li^+ (MW=74,000). Cycling tests were conducted to determine interfacial stability at a current density of 1 mA/cm^2 and 0.5 hour per plating/stripping step, Figure 50a shows the relative cycling performance of bare and coated cells. In the first 20 cycles, bare lithium had highly irregular voltage spikes for both stripping and plating. This behavior is indicative of unstable SEI formation, with spiking caused by breakdown of the SEI and consumption of electrolyte. Figure 50b shows the magnified cycling data of both cells, where the bare lithium potential is a flat plateau with many irregularities, indicating the cell was acting as a resistor and not able to cycle effectively. The SIP coated sample was stable over the entire 350 hours of testing, with an overpotential of only 120 mV for the first 150 cycles before slowly increasing to 200 mV at 350 cycles, which is lower than previous reports of similar artificial SEIs at the same current density of 1 mA/cm^2.[47] The magnified/individual cycles were also highly regular, with no voltage instability. Our PEO-$TFSI^-Li^+$ polymer therefore can facilitate stable cycling at a minimal overpotential, indicating that the polymer is in good contact with the lithium.

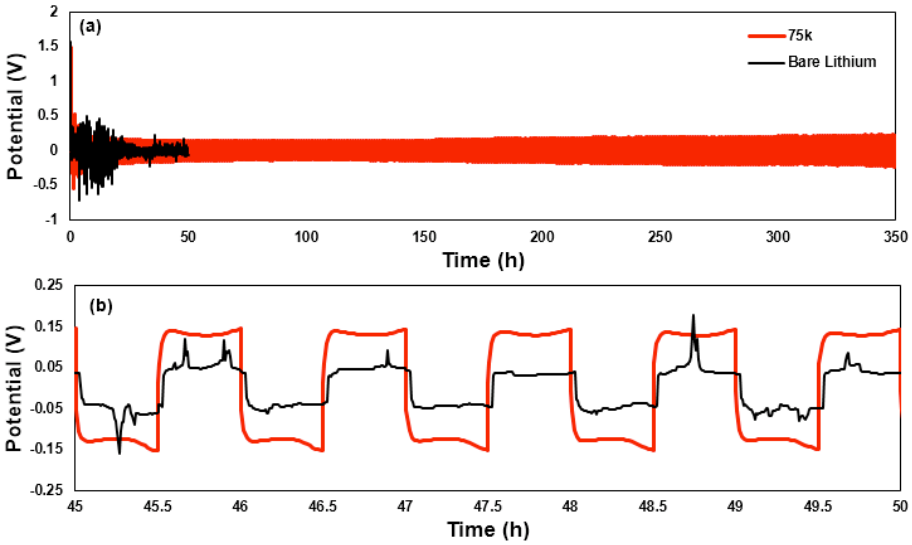

Figure 50. (a) Symmetric cycling data at 1.0 mA/cm^2 for the bare (100 cycles) and coated (350 cycles) symmetrical lithium cells, (b) stripping and plating behavior at 45 to 50 hours.

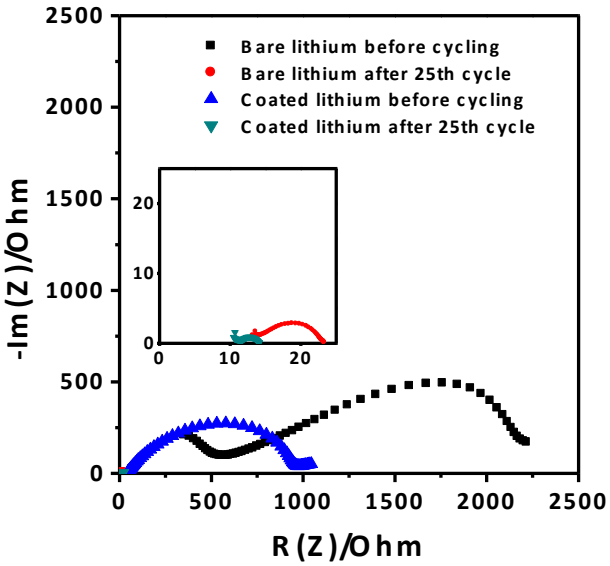

Figure 51. (a) Full EIS data for the coated collected after specified cycles (1 for after the first cycle, etc) and (b) comparison of interfacial resistance between bare and coated lithium after specified cycles.

EIS, electrical impedance spectroscopy was used on cells prepared as previously discussed for cycling in order to determine the effect of the polymer coating on resistance to ionic transport between the lithium and polymer. Impedance was measured before cycling, and after cycling for 25 cycles. The coated sample showed reduced interface resistance compared to the bare lithium chip both before and after cycling, as shown in Figure 51. The key parameter for SIPs is the lithium transference number, which is defined as the fraction of mobile lithium ions among all mobile ions during charge/discharge.[54] An ideal SIP would have a transference number approaching unity, meaning all charge is carried by the lithium cations. The transference number was investigated according to previous work.[55] The transference numbers were calculated according to the equation: $t_+ = \frac{I^s(\Delta V - I^0 R^0)}{I^0(\Delta V - I^s R^s)}$, where t_+ is the transference number, ΔV is the DC voltage applied across the cell, I^0 is the initial current following the voltage step, R^0 is the charge transfer resistance for lithium reduction/oxidation measured by impedance spectroscopy before the voltage step, I^s is the steady state current measured at the end of the voltage step, and R^s is the resistance for lithium reduction/oxidation at the end of the voltage step. The transference number of the PEO-TFSI$^-$Li$^+$ was determined to be 0.98, indicating that lithium ions were highly delocalized throughout the polymer layer due to the minimal interaction with the bound TFSI anion and good conductivity through the PEO matrix. The value of measured parameters is shown Table 8.

3.3.3. Conclusion

In conclusion, a single ion polymer with high transference number, minimal overpotential, and low interfacial resistance has been synthesized for use as an artificial SEI layer in lithium metal batteries. PEO-TFSI$^-$Li$^+$ with a molecular weight of 74,000 was effective at stabilizing lithium stripping and plating cycles at a current density of 1 mA/cm^2 with a minimal overpotential

of 120-200 mV. This minimal increase in interfacial resistance indicates that the polymer is in good contact with the lithium anode and does not hamper the transport of lithium ions. Additionally, the high transference number of 0.98 indicates the PEO-TFSI$^-$Li$^+$ polymer can stabilize the lithium stripping and plating process, allowing for more stable and elongated use of lithium metal batteries.

3.3.4. Experimental section and supporting information

Materials. 3-propanesulfonic acid (98%) was purchased from Combi-Blocks. Trifluoromethanesulfonamide (95%) was purchased from Oakwood Chemicals. Tetraoctylammonium bromide (98%), propargyl glycidyl ether (90%), triisobutylaluminum, copper bromide (99%), L-ascorbic acid, and N,N,N',N",N'''-pentamethyldiethylenetriamine (PMDETA, 99%) were purchased through Sigma Aldrich. Lithium hydroxide (98%) and lithium azide in 40% water were ordered from Acros. Lithium chips were purchased through MTI Corporation. $LiPF_6$ in 1:1 Ethylene carbonate/dimethyl carbonate was purchased from Sigma Aldrich. All solvents were purchased from Fisher Scientific.

Instrumentation. Proton nuclear magnetic resonance (NMR) measurements were performed on a Bruker Avance 500MHz spectrometer. Molecular weight and dispersity were determined through gel permeation chromatography (GPC). Scanning electron microscopy (SEM) was conducted using an FEG-SEM (FEI Quanta 600) under high vacuum with 5keV beam strength. The GPC uses a Waters 515 HPLC pump, a PSS gram 3000 Å and 100 Å column, Waters refractive index detector, and DMF (50mM LiBr) solution as the eluent phase at a 1mL/min flow rate. Electrochemical testing (electrochemical impedance spectroscopy and cycling) were measured using a Biologic VMP3 potentiostat/electrochemical impedance spectrometer.

Ring opening polymerization of propargyl glycidyl ether. In a typical reaction, a 10mL Schlenk flask and magnetic stirrer was dried and allowed to cool under vacuum before being filled with nitrogen. 93 mg of tetraoctylammonium bromide (1 eq), 1 g of propargyl glycidyl ether (50 eq) and 5.00 mL of dry toluene were added. The solution was stirred and degassed for 20 minutes at room temperature, before degassing an additional 15 minutes at 0°C. 90 µL of triisobutylaluminum (2 eq) was added dropwise, and reaction proceeded 24 hours at room temperature. For higher molecular weights, the equivalents of triisobutylaluminum would be increased. The polymer was precipitated in hexane and centrifuged at 3000 rpm for 10 minutes, then dried under vacuum to give PEO-alkyne with ~70% yield. ^{1}H NMR (500MHz, $CDCl_3$): δ (ppm) = 2.49 (1H, s, CH_2CH), 3.60 (1H, q, $OCH(CH_2)_2$), 3.66 (4H, d, OCH_2CH), 4.19 (2H, d, OCH_2CH_3).

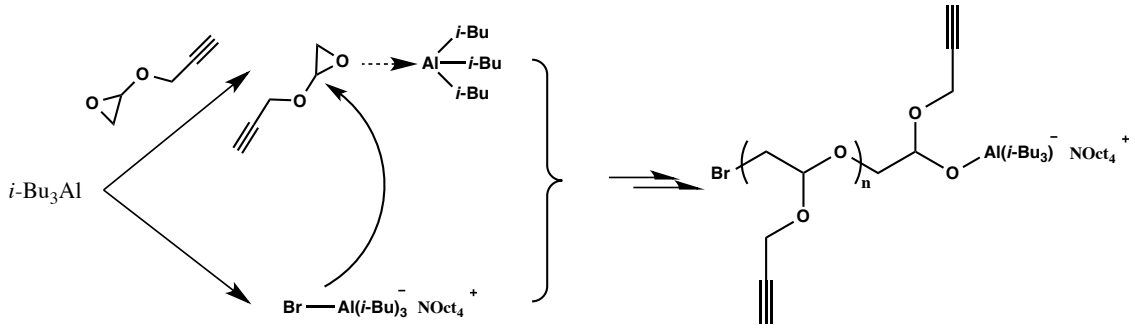

Scheme 6. Polymerization mechanism involving monomer activation prior to insertion into the growing "ate" complex.

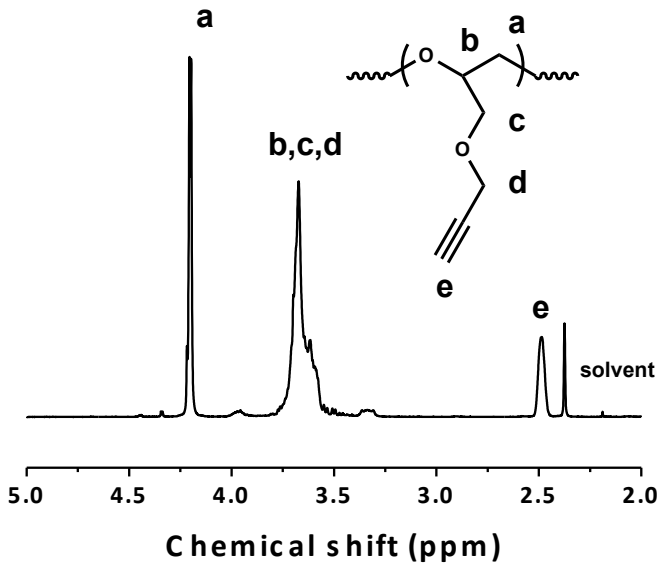

Figure 52. ^{1}H NMR spectrum of PEO-alkyne ($CDCl_3$).

Synthesis of lithium 3-chloropropanesulfonyltrifluoromethanesulfonylimide (Cl-TFSI^{-}Li^{+}). In a typical reaction, 6.736 g of trifluoromethanesulfonamide (1 eq) and 3.792 g of lithium hydroxide (2 eq) were dissolved in 45 mL of acetonitrile in a 100 mL round bottom flask fitted with a stir bar. The solution was purged with nitrogen for 1.5 hours then cooled to 0°C on ice. 8.0 g of 3-chloropropanesulfonyl chloride (1 eq) was added dropwise over 2 hours, then allowed to stir at room temperature for 24 hours. The solution was centrifuged to remove any solids, then dried under vacuum to give a pale orange viscous liquid. The material was recrystallized in dichloromethane to give a white solid with ~80% yield. ^{1}H NMR (500MHz, d_6DMSO): δ (ppm) = 2.10 (2H, quint, $ClCH_2CH_2$), 3.08 (2H, t, $CH_2CH_2S(=O)_2N$), 3.74 (2H, t, $ClCH_2CH_2$)

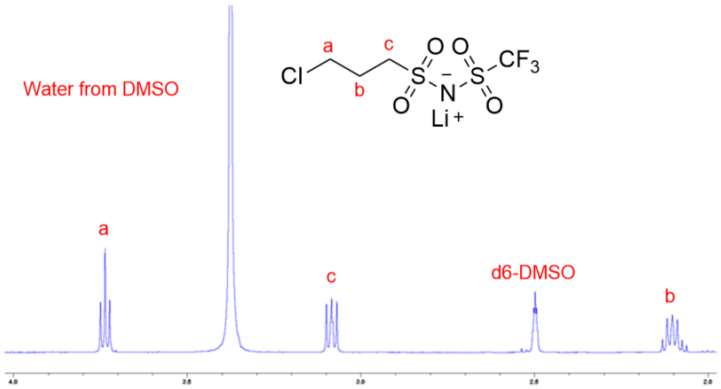

Figure 53. ^{1}H NMR spectrum of 3-chloropropanesulfonyltrifluoromethanesulfonylimide (Cl-TFSI^{-}Li^{+}).

Synthesis of lithium-3azidopropanesulfonyltrifluoromethanesulfonylimide (N_3-TFSI^{-}Li^{+}). 183 mg lithium azide (1.2eq) and 920 mg of Cl-TFSI^{-}Li^{+} (1eq) were dissolved in 5mL of DMF in a 25 mL round bottom flask. The solution was purged with nitrogen before being heated at 90°C for 24 hours. The salt was removed by centrifuge, and the remaining solution was used directly in the click chemistry reaction. ^{1}H NMR (500MHz, d_6DMSO): δ (ppm) = 1.91 (2H, quint, $N_3CH_2CH_2$), 3.02 (2H, t, $CH_2CH_2S(=O)_2N$), 3.45 (2H, t, $N_3CH_2CH_2$)

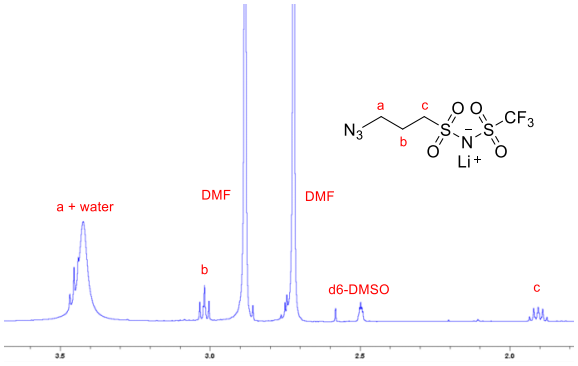

Figure 54. ^{1}H NMR spectrum of 3-azidopropanesulfonyltrifluoromethanesulfonylimide (N_3-TFSI^{-}Li^{+}).

Click reaction to form PEO-TFSI$^-$Li$^+$. In a typical reaction, 250 mg of PEO-alkyne (1 eq), 943 mg of N_3-TFSI$^-$Li$^+$ (1.4 eq), 15 mg of copper (II) bromide (0.03 eq), and 39 mg of PMDETA (.1 eq) were combined in 8mL DMF in a 25 mL round bottom flask and purged with nitrogen. A deoxygenated solution of 79 mg of ascorbic acid (0.2 eq) in 250 µL of DMSO was added under nitrogen. The solution was stirred for 72 hours before precipitation by addition to DCM and dried under vacuum.

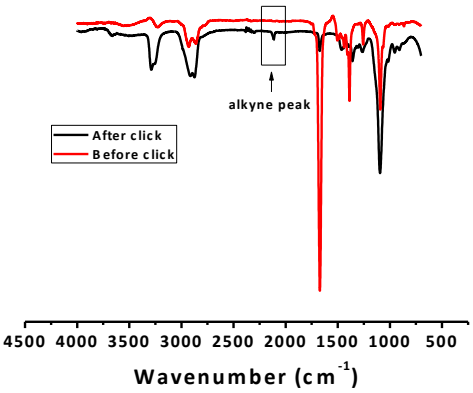

Figure 55. FTIR spectra of polymer before and after click reaction.

Cell preparation and testing. PEO-TFSI$^-$Li$^+$ was dissolved in DMSO at a concentration of 2% by weight. The solution was drop cast in an argon atmosphere, in either 0.175 mL or 0.075 mL amounts, and allowed to dry at 50°C for 24 hours. The coated lithium electrodes were assembled into 2032 coin cells in an argon glovebox, using a hopper spring and 1mm spacer. The separator was 25µm Celguard. Cases were crimped in an MSK-110 hydraulic crimping machine to 750psi. Symmetrical cycling was performed at a current density of ±1.0 mA/cm^2, with each plating/stripping segment lasting 30 minutes. EIS data was collected between 800kHz and 1Hz with a 50mV sinusoidal voltage perturbation.

SEM Sample Preparation. PEO-TFSI$^-$Li$^+$ in DMSO drop cast onto a lithium chips and dried as with other cells. Samples were sputter coated with 2nm of gold before being put into a microscope. A beam strength of 5keV was used in order to ensure the polymer coating was not damaged while imaging.

Measurement of Transference Number. Lithium ion transference number of the PEO-TFSI$^-$Li$^+$ with MW 74,000 was obtained by using AC impedance and DC polarization measurements in a symmetric lithium cell with one lithium electrode coated with polymer and the other bare. A DC potential of 50 mV was applied to the cell, and current was measured until stabilized. The cell resistance was also measured using AC impedance in a frequency range of 0.01 to 10^6 Hz with an oscillation potential of 20mV to measure interfacial resistance. Tests were run at 60 °C.

$$t_+ = \frac{I^s(\Delta V - I^0 R^0)}{I^0(\Delta V - I^s R^s)}$$

The transference numbers were calculated according to the above equation where t_+ is the transference number, ΔV is the DC voltage applied across the cell, I^0 is the initial current following the voltage step, R^0 is the charge transfer resistance for lithium reduction/oxidation measured by impedance spectroscopy before the voltage step, I^s is the steady state current measured at the end of the voltage step, and R^s is the resistance for lithium reduction/oxidation at the end of the voltage step.

Table 8. Measured parameters for calculation of transference number of PEO-TFSI$^-$Li$^+$.

I_0(μA)	I_s(μA)	R^0(KΩ)	R^f(KΩ)	ΔV(mV)	t_+
9.14	9.01	42.91	5.0543.60	50	0.98

3.4. References

[1] Goodenough, J. B.; Park, K.-S., The Li-Ion Rechargeable Battery: A Perspective, *Journal of the American Chemical Society* **2013,** 135, 1167.

[2] Nayak, P. K.; Yang, L.; Brehm, W.; Adelhelm, P., From Lithium-Ion to Sodium-Ion Batteries: Advantages, Challenges, and Surprises, *Angewandte Chemie International Edition* **2018,** 57, 102.

[3] Cano, Z. P.; Banham, D.; Ye, S.; Hintennach, A.; Lu, J.; Fowler, M.; Chen, Z., Batteries and fuel cells for emerging electric vehicle markets, *Nature Energy* **2018,** 3, 279.

[4] Kang, X., Electrolytes and Interphases in Li-Ion Batteries and Beyond, *Chemical reviews.* **2014,** 114, 11503.

[5] Albertus, P.; Babinec, S.; Litzelman, S.; Newman, A., Status and challenges in enabling the lithium metal electrode for high-energy and low-cost rechargeable batteries, *Nature Energy* **2018,** 3, 16.

[6] Martin, W., The Solid Electrolyte Interphase - The Most Important and the Least Understood Solid Electrolyte in Rechargeable Li Batteries, *Zeitschrift für physikalische Chemie.* **2009,** 223, 1395.

[7] Jiang, M.; Xie, Y.; Xu, H.; Jia, J., Developing High-Performance Lithium Metal Anode in Liquid Electrolytes: Challenges and Progress, *Advanced materials.* **2018,** 30.

[8] Tikekar, M. D.; Choudhury, S.; Tu, Z.; Archer, L. A., Design principles for electrolytes and interfaces for stable lithium-metal batteries, *Nature Energy* **2016,** 1, 16114.

[9] Lin, D.; Yuen, P. Y.; Liu, K.; Xie, J., An Artificial Solid Electrolyte Interphase with High Li-Ion Conductivity, Mechanical Strength, and Flexibility for Stable Lithium Metal Anodes, *Advanced materials.* **2017,** 29.

[10] Xia, S.; Wu, X.; Zhang, Z.; Cui, Y.; Liu, W., Practical Challenges and Future Perspectives of All-Solid-State Lithium-Metal Batteries, *Chem* **2019,** 5, 753.

[11] Li, S.; Mohamed, A. I.; Pande, V.; Wang, H.; Cuthbert, J.; Pan, X.; He, H.; Wang, Z.; Viswanathan, V.; Whitacre, J. F.; Matyjaszewski, K., Single-Ion Homopolymer Electrolytes with High Transference Number Prepared by Click Chemistry and Photoinduced Metal-Free Atom-Transfer Radical Polymerization, *ACS Energy Letters* **2018,** 3, 20.

[12] Zhao, C.-Z.; Zhang, Q., Constructing Conformal Interface by Semiliquid Li Metal, *Joule* **2019,** 3, 1575.

[13] Chen-Yang, Y. W.; Chen, H. C.; Lin, F. J.; Chen, C. C., Polyacrylonitrile electrolytes: 1. A novel high-conductivity composite polymer electrolyte based on PAN, LiClO4 and α-Al2O3, *Solid State Ionics* **2002,** 150, 327.

[14] Pan, X.; Fang, C.; Fantin, M.; Malhotra, N.; So, W. Y.; Peteanu, L. A.; Isse, A. A.; Gennaro, A.; Liu, P.; Matyjaszewski, K., Mechanism of Photoinduced Metal-Free Atom Transfer Radical Polymerization: Experimental and Computational Studies, *Journal of the American Chemical Society* **2016,** 138, 2411.

[15] Yan, J.; Pan, X.; Wang, Z.; Lu, Z.; Wang, Y.; Liu, L.; Zhang, J.; Ho, C.; Bockstaller, M. R.; Matyjaszewski, K., A Fatty Acid-Inspired Tetherable Initiator for Surface-Initiated Atom Transfer Radical Polymerization, *Chemistry of Materials* **2017,** 29, 4963.

[16] Yan, J.; Malakooti, M. H.; Lu, Z.; Wang, Z.; Kazem, N.; Pan, C.; Bockstaller, M. R.; Majidi, C.; Matyjaszewski, K., Solution processable liquid metal nanodroplets by surface-initiated atom transfer radical polymerization, *Nature Nanotechnology* **2019,** 14, 684.

[17] Tang, W.; Matyjaszewski, K., Effects of Initiator Structure on Activation Rate Constants in ATRP, *Macromolecules* **2007,** 40, 1858.

[18] Matyjaszewski, K.; Jakubowski, W.; Min, K.; Tang, W.; Huang, J.; Braunecker, W. A.; Tsarevsky, N. V., Diminishing catalyst concentration in atom transfer radical polymerization with reducing agents, *Proceedings of the National Academy of Sciences* **2006,** 103, 15309.

[19] Yan, J.; Bockstaller, M. R.; Matyjaszewski, K., Brush-Modified Materials: Control of Molecular Architecture, Assembly Behavior, Properties and Applications, *Progress in Polymer Science* **2019**, 101180.

[20] Lamson, M.; Kopeć, M.; Ding, H.; Zhong, M.; Matyjaszewski, K., Synthesis of well-defined polyacrylonitrile by ICAR ATRP with low concentrations of catalyst, *Journal of Polymer Science Part A: Polymer Chemistry* **2016,** 54, 1961.

[21] Chen, K.-H.; Sanchez, A. J.; Kazyak, E.; Davis, A. L.; Dasgupta, N. P., Lithium Metal Anodes: Synergistic Effect of 3D Current Collectors and ALD Surface Modification for High Coulombic Efficiency Lithium Metal Anodes (Adv. Energy Mater. 4/2019), *Advanced Energy Materials* **2019,** 9, 1970010.

[22] Li, Z.; Huang, J.; Yann Liaw, B.; Metzler, V.; Zhang, J., A review of lithium deposition in lithium-ion and lithium metal secondary batteries, *Journal of Power Sources* **2014,** 254, 168.

[23] Aurbach, D.; Zinigrad, E.; Cohen, Y.; Teller, H., A short review of failure mechanisms of lithium metal and lithiated graphite anodes in liquid electrolyte solutions, *Solid State Ionics* **2002,** 148, 405.

[24] Aurbach, D.; Markovsky, B.; Levi, M. D.; Levi, E.; Schechter, A.; Moshkovich, M.; Cohen, Y., New insights into the interactions between electrode materials and electrolyte solutions for advanced nonaqueous batteries, *J. Power Sources* **1999,** 81-82, 95.

[25] Aurbach, D.; Zaban, A.; Ein-Eli, Y.; Weissman, I.; Chusid, O.; Markovsky, B.; Levi, M.; Levi, E.; Schechter, A.; Granot, E., Recent studies on the correlation between surface chemistry,

morphology, three-dimensional structures and performance of Li and Li-C intercalation anodes in several important electrolyte systems, *J. Power Sources* **1997,** 68, 91.

[26] Cheng, X.-B.; Zhang, R.; Zhao, C.-Z.; Wei, F.; Zhang, J.-G.; Zhang, Q., A Review of Solid Electrolyte Interphases on Lithium Metal Anode, *Advanced Science* **2016,** 3, 1500213.

[27] Cohen, Y. S.; Cohen, Y.; Aurbach, D., Micromorphological Studies of Lithium Electrodes in Alkyl Carbonate Solutions Using in Situ Atomic Force Microscopy, *J. Phys. Chem. B* **2000,** 104, 12282.

[28] Ding, F.; Xu, W.; Graff, G. L.; Zhang, J.; Sushko, M. L.; Chen, X.; Shao, Y.; Engelhard, M. H.; Nie, Z.; Xiao, J.; Liu, X.; Sushko, P. V.; Liu, J.; Zhang, J.-G., Dendrite-Free Lithium Deposition via Self-Healing Electrostatic Shield Mechanism, *J. Am. Chem. Soc.* **2013,** 135, 4450.

[29] Qian, J.; Henderson, W. A.; Xu, W.; Bhattacharya, P.; Engelhard, M.; Borodin, O.; Zhang, J.-G., High rate and stable cycling of lithium metal anode, *Nat. Commun.* **2015,** 6, 6362.

[30] Miao, R.; Yang, J.; Feng, X.; Jia, H.; Wang, J.; Nuli, Y., Novel dual-salts electrolyte solution for dendrite-free lithium-metal based rechargeable batteries with high cycle reversibility, *J. Power Sources* **2014,** 271, 291.

[31] Kazyak, E.; Wood, K. N.; Dasgupta, N. P., Improved Cycle Life and Stability of Lithium Metal Anodes through Ultrathin Atomic Layer Deposition Surface Treatments, *Chem. Mater.* **2015,** 27, 6457.

[32] Lin, D.; Liu, Y.; Cui, Y., Reviving the lithium metal anode for high-energy batteries, *Nature Nanotechnology* **2017,** 12, 194.

[33] Belov, D. G.; Yarmolenko, O. V.; Peng, A.; Efimov, O. N., Lithium surface protection by polyacetylene in situ polymerization, *Synth. Met.* **2006,** 156, 745.

[34] Liu, K.; Pei, A.; Lee, H. R.; Kong, B.; Liu, N.; Lin, D.; Liu, Y.; Liu, C.; Hsu, P.-c.; Bao, Z.; Cui, Y., Lithium Metal Anodes with an Adaptive "Solid-Liquid" Interfacial Protective Layer, *J. Am. Chem. Soc.* **2017,** 139, 4815.

[35] Liu, Y.; Lin, D.; Yuen, P. Y.; Liu, K.; Xie, J.; Dauskardt, R. H.; Cui, Y., An Artificial Solid Electrolyte Interphase with High Li-Ion Conductivity, Mechanical Strength, and Flexibility for Stable Lithium Metal Anodes, *Adv. Mater.* **2017,** 29, 1605531.

[36] Bouchet, R.; Maria, S.; Meziane, R.; Aboulaich, A.; Lienafa, L.; Bonnet, J.-P.; Phan, T. N. T.; Bertin, D.; Gigmes, D.; Devaux, D.; Denoyel, R.; Armand, M., Single-ion BAB triblock copolymers as highly efficient electrolytes for lithium-metal batteries, *Nature Materials* **2013,** 12, 452.

[37] Jeong, K.; Park, S.; Lee, S.-Y., Revisiting polymeric single lithium-ion conductors as an organic route for all-solid-state lithium ion and metal batteries, *J. Mater. Chem. A* **2019,** 7, 1917.

[38] Park, C. H.; Sun, Y.-K.; Kim, D.-W., Blended polymer electrolytes based on poly(lithium 4-styrene sulfonate) for the rechargeable lithium polymer batteries, *Electrochim. Acta* **2004,** 50, 375.

[39] Ding, Y.; Shen, X.; Zeng, J.; Wang, X.; Peng, L.; Zhang, P.; Zhao, J., Pre-irradiation grafted single lithium-ion conducting polymer electrolyte based on poly(vinylidene fluoride), *Solid State Ionics* **2018,** 323, 16.

[40] Feng, S.; Shi, D.; Liu, F.; Zheng, L.; Nie, J.; Feng, W.; Huang, X.; Armand, M.; Zhou, Z., Single lithium-ion conducting polymer electrolytes based on poly[(4-styrenesulfonyl)(trifluoromethanesulfonyl)imide] anions, *Electrochim. Acta* **2013,** 93, 254.

[41] Morris, M. A.; An, H.; Lutkenhaus, J. L.; Epps, T. H., Harnessing the Power of Plastics: Nanostructured Polymer Systems in Lithium-Ion Batteries, *ACS Energy Lett.* **2017,** 2, 1919.

[42] Jangu, C.; Savage, A. M.; Zhang, Z.; Schultz, A. R.; Madsen, L. A.; Beyer, F. L.; Long, T. E., Sulfonimide-Containing Triblock Copolymers for Improved Conductivity and Mechanical Performance, *Macromolecules* **2015,** 48, 4520.

[43] Porcarelli, L.; Shaplov, A. S.; Salsamendi, M.; Nair, J. R.; Vygodskii, Y. S.; Mecerreyes, D.; Gerbaldi, C., Single-Ion Block Copoly(ionic liquid)s as Electrolytes for All-Solid State Lithium Batteries, *ACS Appl. Mater. Interfaces* **2016,** 8, 10350.

[44] Zhao, H.; Asfour, F.; Fu, Y.; Jia, Z.; Yuan, W.; Bai, Y.; Ling, M.; Hu, H.; Baker, G.; Liu, G., Plasticized Polymer Composite Single-Ion Conductors for Lithium Batteries, *ACS Appl. Mater. Interfaces* **2015,** 7, 19494.

[45] Lago, N.; Garcia-Calvo, O.; Lopez del Amo, J. M.; Rojo, T.; Armand, M., All-Solid-State Lithium-Ion Batteries with Grafted Ceramic Nanoparticles Dispersed in Solid Polymer Electrolytes, *ChemSusChem* **2015,** 8, 3039.

[46] Tu, Z.; Choudhury, S.; Zachman, M. J.; Wei, S.; Zhang, K.; Kourkoutis, L. F.; Archer, L. A., Designing Artificial Solid-Electrolyte Interphases for Single-Ion and High-Efficiency Transport in Batteries, *Joule* **2017,** 1, 394.

[47] Li, N.-W.; Shi, Y.; Yin, Y.-X.; Zeng, X.-X.; Li, J.-Y.; Li, C.-J.; Wan, L.-J.; Wen, R.; Guo, Y.-G., A Flexible Solid Electrolyte Interphase Layer for Long-Life Lithium Metal Anodes, *Angewandte Chemie International Edition* **2018,** 57, 1505.

[48] Labbé, A.; Carlotti, S.; Billouard, C.; Desbois, P.; Deffieux, A., Controlled High-Speed Anionic Polymerization of Propylene Oxide Initiated by Onium Salts in the Presence of Triisobutylaluminum, *Macromolecules* **2007,** 40, 7842.

[49] Herzberger, J.; Niederer, K.; Pohlit, H.; Seiwert, J.; Worm, M.; Wurm, F. R.; Frey, H., Polymerization of Ethylene Oxide, Propylene Oxide, and Other Alkylene Oxides: Synthesis, Novel Polymer Architectures, and Bioconjugation, *Chemical Reviews* **2016,** 116, 2170.

[50] Carlotti, S.; Desbois, P.; Billouard, C.; Deffieux, A., Reactivity control in anionic polymerization of ethylenic and heterocyclic monomers through formation of 'ate' complexes, *Polymer International* **2006,** 55, 1126.

[51] Rejsek, V.; Sauvanier, D.; Billouard, C.; Desbois, P.; Deffieux, A.; Carlotti, S., Controlled Anionic Homo- and Copolymerization of Ethylene Oxide and Propylene Oxide by Monomer Activation, *Macromolecules* **2007,** 40, 6510.

[52] Freunberger, S. A.; Chen, Y.; Drewett, N. E.; Hardwick, L. J.; Bardé, F.; Bruce, P. G., The Lithium–Oxygen Battery with Ether-Based Electrolytes, *Angew. Chem. Int. Ed.* **2011,** 50, 8609.

[53] Croce, F.; Appetecchi, G. B.; Persi, L.; Scrosati, B., Nanocomposite polymer electrolytes for lithium batteries, *Nature* **1998,** 394, 456.

[54] Fujinami, T., Li+ transference number enhancement in polymer electrolytes by incorporation of anion trapping boroxine rings into the polymer host, *Chemistry letters.* **1997**, 915.

[55] Van Humbeck, J. F.; Aubrey, M. L.; Alsbaiee, A.; Ameloot, R.; Coates, G. W.; Dichtel, W. R.; Long, J. R., Tetraarylborate polymer networks as single-ion conducting solid electrolytes, *Chemical Science* **2015,** 6, 5499.

Chapter 4. A Semiliquid Composite Lithium Anode

4.1. Preface

As mentioned in Chapter 1, one hindrance to the future of ceramic electrolytes is their interfacial instability. Garnet type electrolytes have recently emerged to be the most promising choice of electrolytes for solid state ceramic lithium metal batteries due to their electrochemical stability. However, poor surface contact with electrodes due to surface roughness remains a problem.

To tackle this problem, I set out to transform the solid/solid interface in a garnet/lithium interface to a solid/liquid interface by ”lyquefying” the lithium metal. I designed the entire project and would like to especially thank Han Wang for his contribution in this work, which resulted in publication in a *Cell* sister journal *Joule*: Sipei Li, Han Wang, Julia Cuthbert, Tong Liu, Jay F. Whitacre, Krzysztof Matyjaszewski, “A Semiliquid Lithium Metal Anode”, *Joule* **2019**, *3*, 1637-1646. I would like to thank Han Wang, Tong Liu and Julia Cuthbert for contribution in paper writing and materials preparation, characterization.

The microCT work was supported by the NIH S10OD021533 (K. Verdelis, PI), United States, for the purchase of the microCT scanner. Financial support from the NSF (DMR 1501324), United States, is gratefully acknowledged. I would also like to acknowledge use of the Materials Characterization Facility at the Carnegie Mellon University under grant #MCF-677785, United States.

4.2. Introduction

Typical lithium metal based batteries are made of combustible organic liquid based electrolytes and a plain lithium foil.[1-3] The lack of chemical stability of this type of electrolyte against the reactive lithium metal and the dramatic volume change of the metal electrode during

plating/stripping leads to uneven lithium deposition at the interface, which results in dendrite formation. Such dendrite issues can eventually lead to internal shorting which in turn causes thermal runaway and ultimately severe safety issues.[4, 5]

One solution to address these problems, is to replace organic liquid electrolytes with solid ceramic electrolytes that are highly conductive, non-combustible and mechanically tough enough to block penetration of dendrites.[6] However, the interface between lithium and solid electrolytes is known to suffer due to insufficient contact and subsequent high interfacial resistance.[7, 8] As a result, most solid-state batteries cannot run at high or even practically usable current densities.[9] Several novel approaches have been proposed, such as creating a 3D interconnected anolyte layer as a lithium metal matrix,[10] employing polymer/ceramic hybrid electrolytes, introducing new and more robust and stable interfaces,[11-22] or infiltrating polymer into a porous lithium metal based composite with high electrochemical contact surface.[23, 24] Despite some of these promising results, further efforts are still needed to increase lithium loading, reduce the complexity of materials processing, and enhance electrochemical performance while stymieing the formation of destructive dendrites

On the other hand, molten alkali metal electrodes paired with solid electrolytes have been previously proposed as a promising technique for grid-scale energy storage.[24-30] Such a cell design has a liquid/solid interface, that is similar to typical liquid electrolyte-based batteries. Therefore, the interfacial resistance is dramatically lower compared to that of solid/solid interface in a typical solid-state battery.[25] However, the high operating temperature (250~700 ^{o}C) required for such an interface raises concerns about increased rate of corrosion, limited choice of electrolytes, and thus prevents this technique from being used for portable or mobile applications.[25]

Here, a novel class of a semiliquid lithium metal anode (SLMA) based on homogeneous colloidal dispersion of lithium microparticles in a dual-conductive (electronically and ionically) polymer/carbon composite matrix is disclosed and discussed. The SLMA showed liquid-like rheological properties under 25% shear strain even at room temperature. The lithium content of SLMA can reach values as high as 40 vol% with a theoretical volumetric energy density of 800 mAh/mL and a specific capacity of 810 mAh/g. Initially the plating/stripping behavior of the SLMA with a garnet-type ceramic electrolyte separator $Li_{6.4}La_3Zr_{1.4}Ta_{0.6}O_{12}$ (LLZTO) was investigated.[31-34] The liquid form of the SLMA ensured sufficient contact at the anode/electrolyte interface and a low interfacial resistance. Owing to the dual-conductive medium and the much higher surface area of the lithium microparticles as compared to flat lithium foil, the redox process during charge/discharge takes place within the entire volume of the electrode. As such, it strongly reduces the local current density during lithium plating/stripping. At the elevated temperature of 65 ^{o}C, the SLMA showed stable lithium deposition behavior at the current density of 1 mA/cm^2 and areal capacity of 1 mAh/cm^2 with overpotential below 150 mV and almost perfectly planar voltage profile for nearly 400 hours.

4.3. Results and discussion

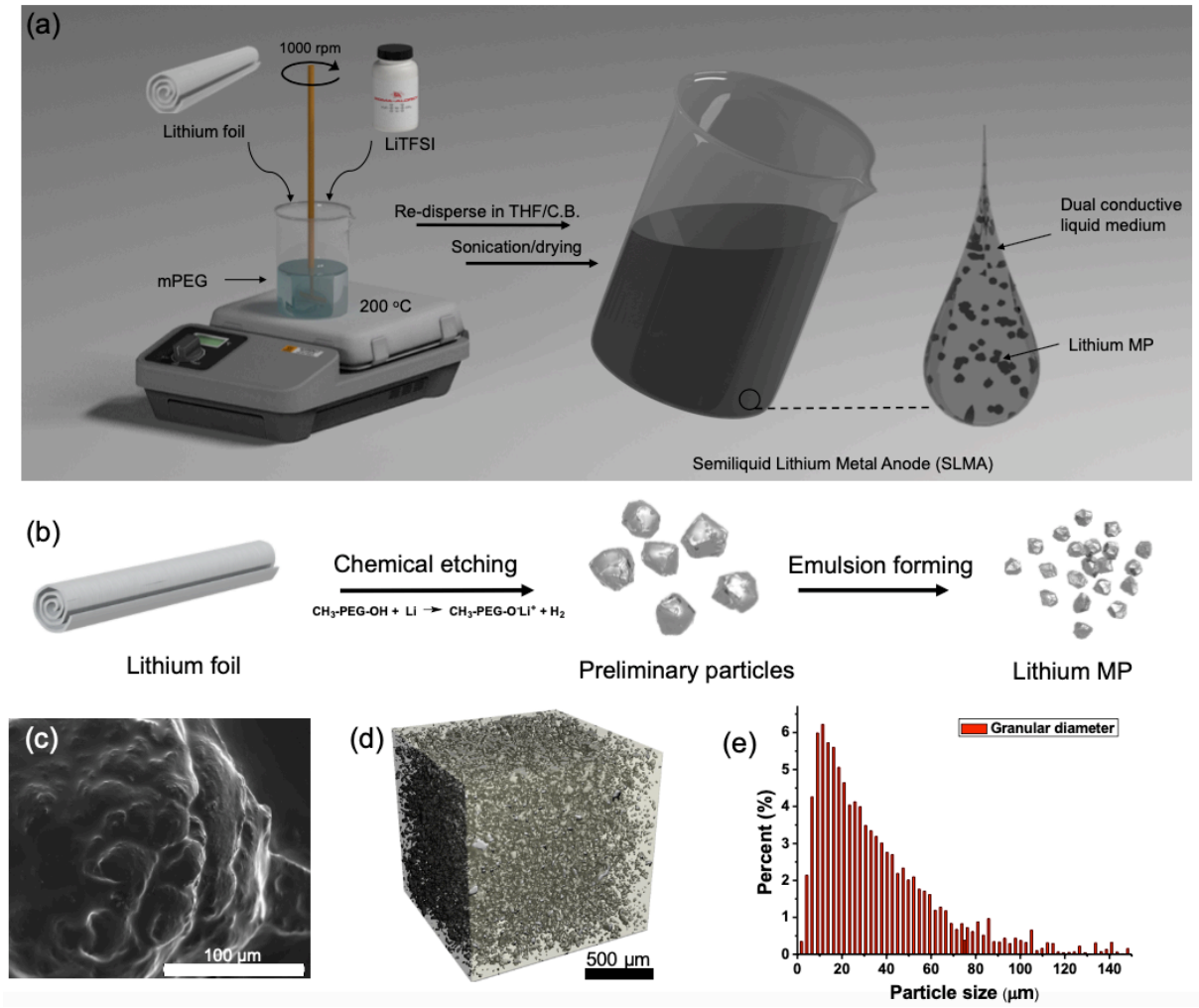

Figure 56. (a) Preparation of SLMA. Lithium foil and LiTFSI were added into a glass vial containing mPEG at 200 °C. The formed emulsion was then redispersed into THF and carbon black was added. After sonication and drying, the SLMA was formed at room temperature. (b) Transformation of lithium particle size during a process of chemical etching and emulsification. (c) SEM image of the formed lithium microparticle dispersed in mPEG (no carbon black added). (d) Micro-CT image showing the internal structure of formed lithium microparticle buried in mPEG (no carbon black added). (e) Distribution of granular thickness of the lithium microparticles dispersed in the polymer matrix.

The SLMA was prepared via a top-down process that involves concurrent emulsification and chemical etching in the presence of a reactive surfactant. The preparation is illustrated in Figure 56. Specifically, lithium chips were added to poly(ethylene glycol) monomethyl ether (MW=750, mPEG) containing lithium bis(trifluoromethanesulfonyl)imide (LiTFSI) (EO/Li=10/1);. The mixture was heated to 200 ºC. At this temperature, the hydroxyl groups from the mPEG quickly react with the lithium metal and the lithium foil was reduced to smaller lithium particles distributed in the polymer matrix. As such, the mPEG acts as a molecular reactive surfactant that facilitates a decrease of lithium particle size to generate lithium microparticles with rather uniform distribution (Figure 56b). In the presence of LiTFSI that helps to stablize the emulsion, a grey emulsion was formed within 5 min of continued mechanical agitation. A colloidal dispersion was formed after the emulsion cooled down. As shown in the SEM image of the as formed colloidal dispersion, Figure 56c, microparticles were evenly dispersed in a polymer medium. Micro-CT was used to visualize the particle distribution in the colloidal dispersion, Figure 56d & e. A dominant distribution of particle size around 10 ~ 60 μm was observed inside the composite. Noticeably, the role of monofunctional hydroxyl groups was crucial as both α,ω-dimethoxy PEG and α,ω-dihydroxy PEG cannot form uniform dispersions. Figure 60 shows the *in situ* micro-CT image of the formed particles in a α,ω-dimethoxy PEG (MW = 250). Due to absence of hydroxyl groups (reactive surfactant), the lithium foil cannot be converted to smaller particles via reaction with hydroxy groups and stabilized by PEG ligands. As such, mere mechanical agitation without chemical etching could not generate uniform/small particle distribution, resulting in a size of lithium particle ca. 100~600 μm. Figure 61 shows the particle distribution in a α,ω-dihydroxy PEG (MW =250). Due to the presence of hydroxyl groups in the polymer, the lithium foil was reduced to smaller particles at an even faster rate than in the case of

mPEG. However, as both of the formed lithiated $–O^-Li^+$ end groups can stabilize the formed particles via ionic interaction at the surface of the particle, the generated $^+Li^-O–PEG–O^-Li^+$ served as an ionic cross-linker and greatly increased the viscosity of the matrix. In about 2 min, the mixture started to gelate and became difficult to stir. As a result, the particles formed can reach 400 μm in diameter. The influence of chain-end functionality of the PEG on the final particle distribution is illustrated in Scheme 7. Besides, the stoichiometry and the agitation time also affect the resulted particle size. With the amount of 16 vol% lithium in the polymer matrix and an elongated agitation time (5 h), sub-micron lithium particles were formed as shown in Figure 62.

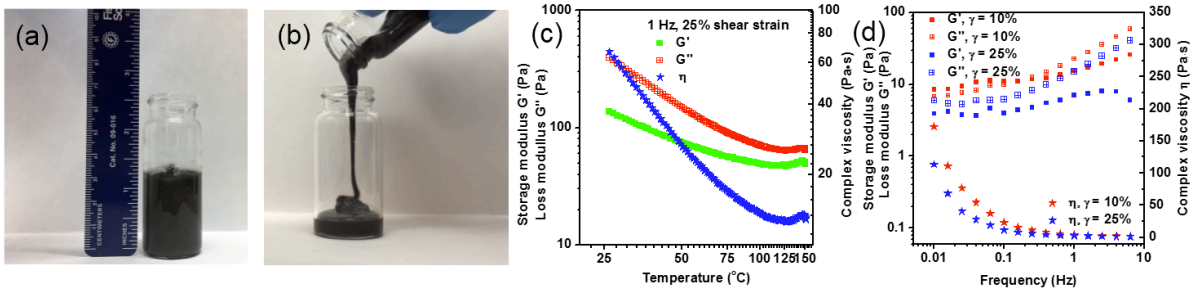

Figure 57. (a) A batch of 15 g of SLMA. (b) Demonstration of the liquid form of the SLMA at 120 °C. (c) Storage modulus (G′), loss modulus (G″) and complex viscosity (η) measured at different temperature at 1 Hz and 25% shear strain. (d) Storage modulus (G′), loss modulus (G″) and complex viscosity (η) measured at different frequency with shear strain (γ) of 10% and 25% at 120 °C.

In addition to the selection of the appropriate polymer, the use of a lithium salt is also critical. Figure 63 shows a mixture formed without the addition of LiTFSI in mPEG. The formed mixture with a lithium content of 25 vol% exhibited a yellowish solid form. To break any possible aggregation of lithium microparticles in the PEG/LiTFSI medium, anhydrous THF was added and the suspension was treated with sonication overnight under argon atmosphere. We also found that sonication helped to improve the surface purity of the lithium particles as the suspension showed

typical metallic luster after sonication, Figure 64. To create a dual (ionic/electronic) conducting medium, 3 wt% of carbon black was added into the suspension and stirred for several hours. THF was then removed by purging with argon flow and the mixture was further dried under vacuum overnight to form the final product SLMA. The synthesis is simple and can readily be scaled up to larger scale. Figure 57a shows a batch of SLMA of 15 grams. Figure 57b shows that the SLMA exhibited liquid behavior and was poured out from the vial at 120 ºC. The rheological properties of the SLMA was further studied by dynamic mechanical analysis (DMA), Figure 57c & d and Figure 65. Figure 57c shows the temperature response (25 ºC to 150 ºC) of storage modulus (G′), loss modulus (G″) and viscosity (η) at 25% shear strain (γ) and frequency of 1 Hz. At this strain rate, the SLMA showed a liquid response throughout the entire temperature range. Figure 57d shows the frequency response (0.01 Hz to 10 Hz) at the shear strain of 10% and 25% at 120 ºC. At 10% shear strain, the SLMA showed solid-to-liquid transition at the frequency of ~0.2 Hz. At 25% shear strain, the SLMA showed a liquid response throughout the entire frequency sweep. The complex shear modulus decreased with the increase of frequency, which indicates a typical non-Newtonian shear-thinning behavior.

The garnet-type lithium-ion conductor is promising due to its high ionic conductivity and broad electrochemical stability window, however, creating a conformally stabile interface between a lithium metal based electrode and solid state electrolyte has been historically difficult.[31-41] To demonstrate the advantage of the SLMA when paired with solid electrolytes, a cell configuration with cubic-phase $Li_{6.4}La_3Zr_{1.4}Ta_{0.6}O_{12}$ (LLZTO) middle layer was assembled and compared with symmetric cell using conventional lithium foil as electrodes. The LLZTO pellets were prepared by a two-step pressing/sintering process without extra surface treatment. The pellet had a thickness of approximately 350 μm and a diameter of 13 mm (Figure 66). The phase content of the electrolyte

pellet was confirmed by XRD to be 100% expected cubic structure, Figure 67. The ionic conductivity of the LLZTO pellet was confirmed by EIS measurement with two sides sputter-coated with copper (Figure 68). The configuration of the symmetric cell is illustrated in Figure 58a & b. In a conventional Li foil/LLZTO/Li foil symmetric cell, due to the high surface roughness of both the lithium metal and the LLZTO, a continuous uniform contact was not possible, resulting in a severely uneven distribution of local current density. In comparison, due to the flowable nature of the SLMA, the contact between electrode and electrolyte is much more uniform and continuous.

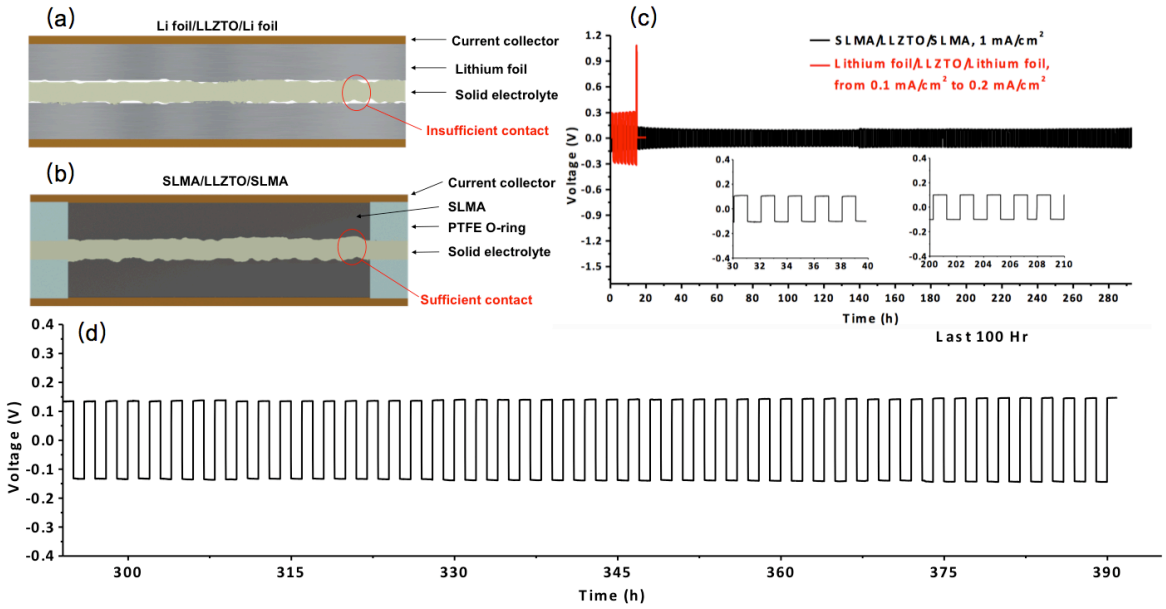

Figure 58. Schematic illustration of (a): a Li foil/LLZTO/Li foil symmetric cell with poor interface contact and (b): a SLMA/LLZTO/SLMA symmetric cell with improved interface contact. (c): Symmetric cycling of SLMA/LLZTO/SLMA at 1 mA/cm^2 and Li foil/LLZTO/Li foil at 0.1 to 0.2 mA/cm^2 at 65 ^{o}C. Half cycle time = 1 h. (d) Zoom in voltage profile of the last 100 h of the symmtric cycling of SLMA/LLZTO/SLMA at 1 mA/cm^2.

To demonstrate the cycling ability of the SLMA, SLMA/LLZTO/SLMA cell was cycled at 0.5 mA/cm^2 (half cycle time = 1 h) at 65 ^{o}C for 150 h. The initial voltage overpotential during

formation cycle was 340 mV and the relatively higher overpotential could be due to the formation of a SEI and stable interfacial contact. Then the overpotential gradually decreased to and stabilized below 50 mV Figure 69. This indicates that an improved and stabilized interface contact formed between the SLMA and the garnet electrolyte, which is also confirmed by EIS in Figure 70. As suggested by the EIS, after first couple of formation cycles, the semicircle at high and middle frequency overlaps, suggesting the interfacial resistance is reduced and stabilized. After the stabilizing formation cycle, the SLMA showed stable voltage profile with almost no hysteresis, which is not short-circuiting in the cell as suggested by the EIS data with semicircle features. In comparison, a Li foil/LLZTO/Li foil symmetric cell was also assembled in the same fixture and was run at 0.1 mA/cm^2 (1 h charge/discharge). Even at this low current density, the initial voltage was as high as over 300 mV at 65 ^{o}C and gradually polarized over time. When the current density increased to 0.2 mA/cm^2 after 14 h, the voltage jumped to over 1000 mV and then quickly shorted, Figure 58c. This indicates that the SLMA system does show dramatic improvement on interfacial stability with solid electrolytes compared to typical lithium anode in a flat metal foil form. Given the cycling performance and the thermal stability of the polymer, 65 ^{o}C is a stable temperature for SLMA. Furthermore, a symmetric cycling at higher current density was also performed at 1.0 mA/cm^2 (half cycle time = 1 h) at 65 ^{o}C. The cycling was performed with 25 cycles of precycling at 0.5 mA/cm^2.

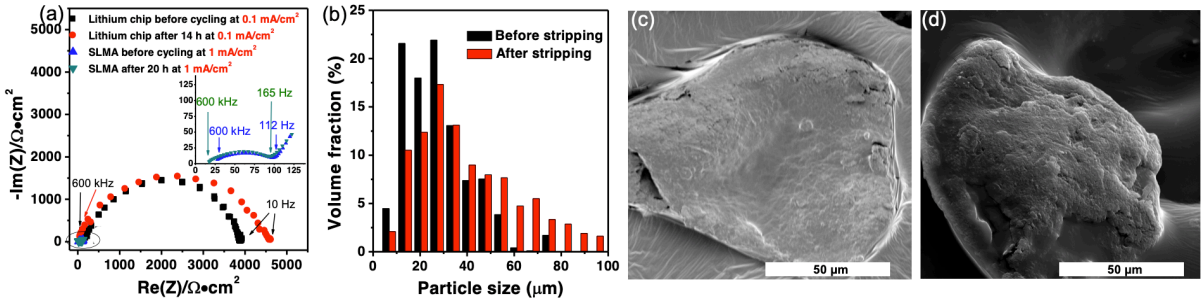

Figure 59. (a) EIS of Li foil/LLZTO/Li foil and EIS of SLMA/LLZTO/SLMA cell before and after cycling. (b) Size distribution of Li MPs dispersed in the polymer medium before and after stripping 9.7 mAh from a thick electrode containing 16.2 mAh of capacity. (c) SEM image of the isolated microparticle before cycling. (d) SEM image of the isolated microparticle after cycling at 1 mA/cm^2.

The SLMA showed ideally stable plating/stripping voltage of ~150 mV without any hysteresis over the long-term cycling, Figure 58c. The inset in Figure 58c also showed an enlarged voltage profile as a function of time. During the cycling, EIS was performed in order to understand the impact of interfacial resistance on the lithium plating/stripping process. For the Li foil/LLZTO/Li foil symmetric cycling, the high overpotential was confirmed by EIS. Although, for the SLMA/LLZTO/SLMA cell, differentiating the interfacial resistance in between three phases (PEO/LiTFSI polymer, Li particle and LLZTO phases) and LLZTO feature in the semicircle at high and middle range frequency is difficult, the diameter of the semicircle is related to the total interfacial resistance of the system. The EIS of Li foil/LLZTO/Li before cycling at 0.1 mA/cm^2 shows a large semicircle and the size of the semicircle increases after cycling at 0.1 mA/cm^2 for 14 h, which could be due to the formation of a destabilized electrode/electrolyte interface, Figure 59a. Whereas, for the SLMA/LLZTO/SLMA cell, before cycling at 1 mA/cm^2 (measured after precycling), the semicircle is one order of magnitude lower than of Li

foil/LLZTO/Li. After 20 h of cycling at 1 mA/cm^2, the impedance remained at the same level, which may suggest a stable interfacial contact, inset of Figure 59a. Due to the dual-conductive medium, the lithium ions are removed from the surface of the microparticles during stripping and are redeposited back to the original microparticles during plating. As a result, the lithium microparticles continue to behave in a "breathing" mode during plating/stripping and the volume change of the electrode can be largely mitigated. Such behavior is also confirmed by the morphology change observed by SEM. In order to further examine the particle "breathing" during cycling, we conducted a deep stripping experiment using a thick electrode with 16.2 mAh total capacity and stripped 9.7 mAh of lithium from one side to the other side, this is equal to ~60% of the lithium content of the electrode. The cell was then disassembled and the SLMA samples before and after stripping were characterized by micro-CT. The particle distributions are shown in Figure 59b and show that after stripping, the percent of smaller particles, with a size lower than 20 micron, decreased whereas the percent of particles larger than 30 microns after stripping increased. The median particle size of the stripped side increased from 27.6 micron to 34 micron. This observation indicates that during the breathing mode, lithium was preferentially stripped from smaller particles. As the lithium particle with higher surface area (larger particles) should have a better chance for the lithium to be plated, the amount of smaller particles should gradually decrease and even disappear after long cycling. Figure 59c shows an isolated lithium microparticles before cycling, which showed a smooth surface. After 20 hours of cycling at 1 mA/cm^2, a layer of lithium was observed to be coated on particles, Figure 59d. Such 3D re-construction of the electrode together with the continuous interfacial contact explains extremely stable lithium plating/stripping behavior, as shown in Figure 58c & d. In order to achieve further improvement of cycling, one future direction will be to create a SLMA with improved particle distribution.

In Figure 72a, we compared the cycling capacities and current densities of the Li metal-based anodes based from surface-modified garnet type solid-state electrolytes and lithium anodes.[10, 35-43] Due to the poor contact and the dramatic volume change at the anode–electrolyte interface during cycling, the previously reported solid-state Li anodes with ceramic electrolytes were mostly limited to low capacities per cycle (<0.5 mAh/cm^2) and small current densities (<0.2 mA/cm^2). Our work showed dramatically improved areal capacity and current density as compared to some of the most representative previous systems that operate below the melting point of lithium metal. Also, we compared cumulative capacity cycled of the cells in terms of mAh/cm^2 in these systems. Our work showed much longer cycling life-span, Figure 72b. This comparison suggests that for systems with the SLMA as an anode, no surface-modification is needed for the solid electrolyte, which greatly simplifies the preparation of solid state electrolytes and also decreases the preparation cost. One critical measure of practicability is the percentage of the capacity that is cyclable. Table 9 compares the "depth" of cycling in this work to previous reports that use either garnet type electrolytes or commercial liquid electrolytes. In a practical cell, the capacity of anode and cathode should be balanced, meaning that typically >40% of the lithium in an anode should be accessed. A full cell with SLMA under practical conditions with deeper cycling of the anode will be explored in a future.

4.4. Conclusion

We have demonstrated a completely novel approach for large-scale preparation of lithium metal/polymer composite electrodes (SLMA). This new class of electrode materials exhibited liquid-like behavior that is similar to molten state lithium metal but can operate at a much lower temperature of 65 ^{o}C. The material preparation is based on emulsification using a reactive polymer surfactant, which results in a stable colloidal dispersion of uniform lithium microparticles in a

polymer matrix. With up to 40 vol% lithium content, the SLMA has a volumetric capacity of 800 mAh/mL. When integrated with a garnet-type electrolyte in a symmetric cycling fixture, the cell showed extremely stable voltage profile with ~150 mV overpotential and almost no hysteresis at 1 mA/cm^2 with 1 h half cycle time at 65 ^{o}C for nearly 400 hours. Such a stable voltage profile is due to several unique factors of the SLMA: 1) the reversed liquid/solid (electrode/electrolyte) interface provided very good contact; 2) electron/ion charge transfer that occurred evenly across the entire 3D structure of the dual-conductive medium; 3) the adaptable polymeric medium greatly mitigated the local volume change during lithium plating/stripping; 4) the SLMA provided enhanced electrochemical stability against solid electrolytes.

The methodology presented in this study could be further extended to other metal-based rechargeable battery systems, such as sodium metal batteries, potassium metal batteries, etc. Due to the high electrochemical stability of the SLMA, the system could be applied to many solid electrolytes without extra surface treatment. As a result, the production cost could be greatly reduced. The methodology may also have larger impact on practical applications such as next-generation electric vehicles that require a capacity of 500 Wh/Kg and wearable devices which require high flexibility of the electrode materials. The simplicity of material preparation procedure may potentially be suitable for large-scale production and may have bridged the gap between portable devices that use lithium ion batteries and grid-scale energy storage that uses molten metal batteries.

4.5. Experimental section and supporting information

Preparation of semiliquid lithium metal anode (SLMA). The fabrication process was carried out in an argon-filled glove box with sub-ppm (parts per million) O_2 and H_2O levels. In a typical procedure, 7.0 g of α–methoxy-ω-hydroxy poly(ethylene glycol) (MW=750, mPEG) was

mixed with 4.56 g of lithium bis(trifluoromethanesulfonyl)imide (LiTFSI) in a 50 mL round bottom flask equipped with a stirring bar and then heated at 200 ºC to form a transparent liquid. 3.24 g of lithium metal was cut into small pieces (average size ~ 1 cm) and added to the mPEG/LiTFSI mixture. The mixture was stirred at 1000 rpm on a heated stirring plate. The size of the lithium chips was reduced to sub millimeter particles after the first 2 min, after reacting with the hydroxy groups present on the mPEG. Within 5 min, a grey homogeneous emulsion was formed. The mixture was stirred for another 10 min. Then the mixture was cooled down to room temperature and 20 mL of anhydrous THF was added into the flask. 444 mg of carbon black was then added to the suspension which was placed in a sonication bath for overnight. Afterwards, the suspension was heated at 90 ºC to evaporate the THF. After overnight drying under vacuum, a black liquid-like metal/polymer colloidal composite was formed as the final product.

Preparation of LLZTO solid electrolytes. Ta-doped LLZO (LLZTO) powder was purchased from MSE Supplies LLC. The LLZOT powder was kept in an argon-filled glovebox. LLZTO powder was cold-pressed into a 13 mm die and transferred to a tube furnace. The cold-pressed LLZTO pellet was then sintered at 1050 ºC for 10 h with 10 ºC/min heating and cooling rate under dry flow air. After sintering, the LLZTO pellet was immediately transferred into a glovebox for further use.

Assembly of the coin cell and electrochemical tests. 2032-type coin cells (MTI) were assembled to study the electrochemical performance of SLMA. The set-up of the coin cell is shown in Figure 58. First, a stacked PTFE O-rings with 0.25 mm thickness and 8 mm inner diameter were placed on both sides of the LLZTO pellet. Then, the open space inside the PTFE O-ring was filled with SLMA on both sides, followed by the spacer and a wave spring which were finally pressed to the coin cell. Then the coin cell was transferred to an oven at 65 ºC. All the electrochemical

tests, including symmetric cycling and EIS, were performed at 65 ºC and were conducted utilizing a Bio Logic VMP3 Multi-Channel Potential/Electrochemical Impedance Spectrometer. The symmetric cycling of SLMA was carried out with charge and discharge time of 1 hour without rest between the steps. For EIS test of the coin cell, measurements were taken after the coin cell was rested for 3 h. The data were collected between 600 kHz and 10 mHz by applying a 10 mV sinusoidal voltage perturbation.

Materials and characterizations. Poly(ethylene glycol) monomethyl ether (mPEG, MW=750 and MW=350), dihydroxy oligomeric ethylene glycol (dihydroxy PEG, MW=200), dimethoxy oligomeric ethylene glycol (dimethoxy PEG, MW=250), anhydrous tetrahydrofuan (THF) (>99.9%) were purchased from Sigma-Aldrich. Lithium bis(trifluoromethanesulfonyl)imide (LiTFSI) (>98%) was purchased from TCI America. Lithium chips (99.9%) and garnet type LLZTO powder were purchased from MTI corporation. SUPER P™ carbon blacks were purchased from MatWeb. X-ray diffraction (XRD) patterns of commercial LLZTO powder and LLZTO pellet were characterized on a PANalytical X'pert diffractometer with a Cu Kα radiation with scan range from $8 - 70^{o}$ 2θ. The Scanning Electron Microscopy (SEM) was performed on Philips XL30. Mechanical properties were assessed using an Anton Paar MCR-302 Rheometer fitted with a parallel plate tool with diameter D = 25 mm. The samples were subjected to periodic torsional shearing between two the parallel plates. The frequency sweeps were carried out at 120°C at a constant applied shear strain of 0.1% (γ) over a frequency range 0.001~100 Hz. 3D distribution of lithium mircoparticles in the polymeric medium were analyzed by microcomputed tomography (microCT) imaging using a Scanco μCT 50 (Scanco Medical, Brüttisellen, Switzerland) ex vivo microCT scanner with a 6.8 μm voxel resolution, 45KVp beam energy, 133 μA intensity, 0.36 degrees rotation step (180 degrees angular range) and

an exposure of 800ms per view. Specimens were packed in standardized plastic holders provided by the manufacturer by dripping molten state composite at elevated temperature. 3D volumes were generated automatically from raw files and calibrated using the Scanco software. microCT 3D morphometry and densitometry (DECwindows Motif 1.6, Scanco Medical) software was used for viewing and quantitative evaluation of images, as well as generation of 3D renderings of scanned specimen volumes. Particle diameter distribution within the measured sample were evaluated, calculated in 3D mode by the morphometry package of the software and after segmentation of lithium microparticles from the rest polymeric denser phase using a 196 grayscale value.

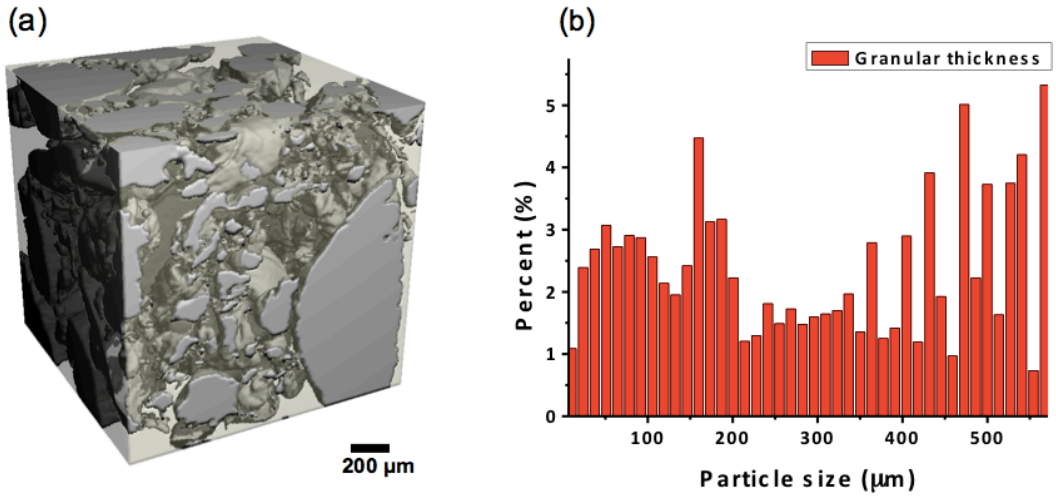

Figure 60. Micro-CT image showing the internal size distribution of lithium particles generated in a dimethoxy PEG medium.

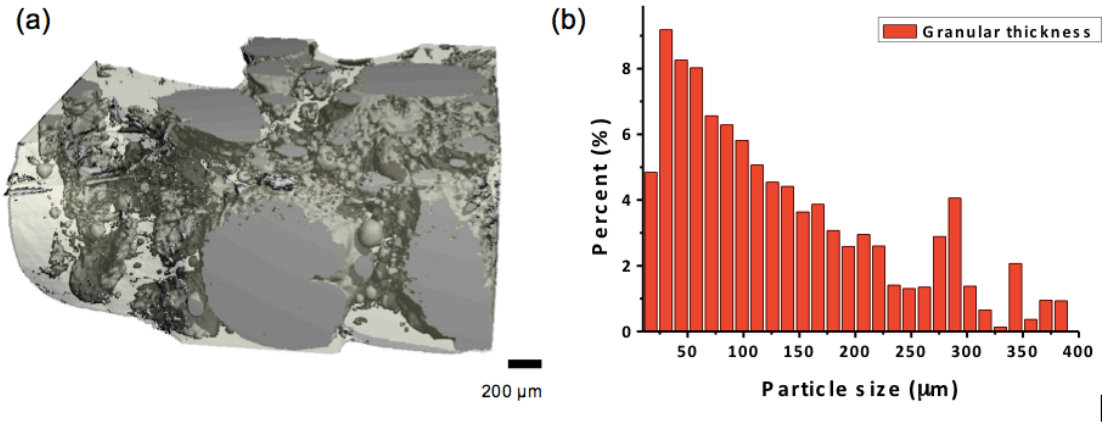

Figure 61. Micro-CT image showing the internal size distribution of lithium particles generated in a dihydroxy PEG medium.

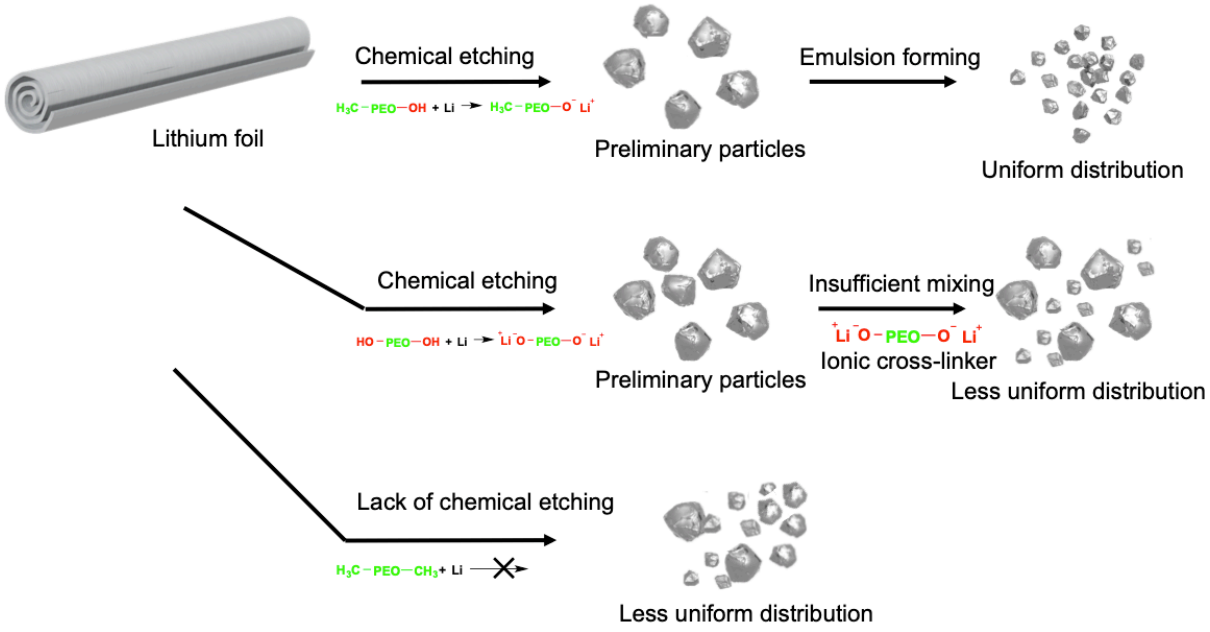

Scheme 7. Illustration of mechanism of particle formation at 200 °C with PEG with different chain end functionalities.

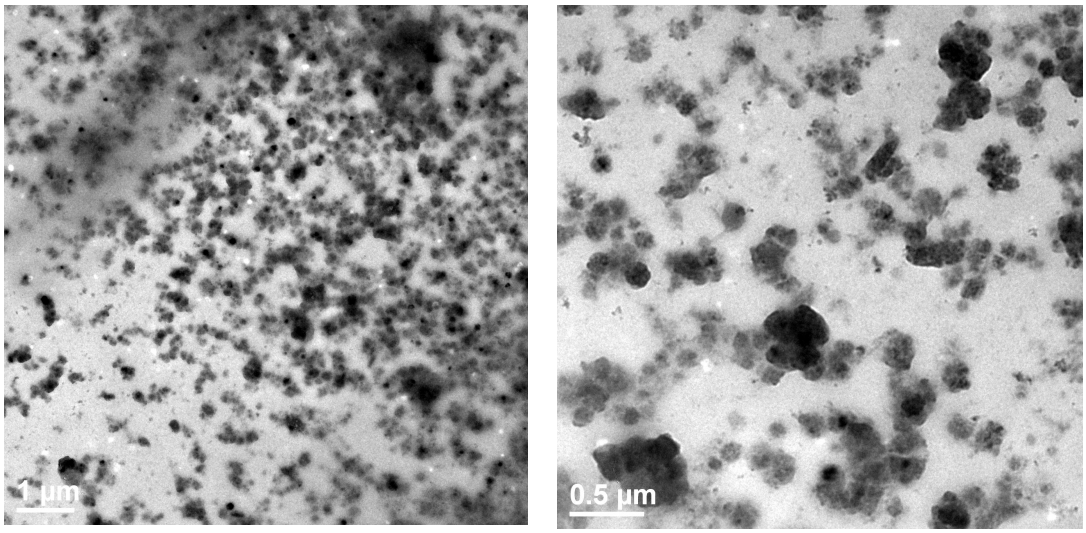

Figure 62. TEM image of sub-micron lithium metal particles formed with 16 vol% feed amount and elongated agitation time (5 h).

Figure 63. Lithium/mPEG composite prepared without the addition of LiTFSI. V(Li)/V(PEO)=1/3. The sampled showed low homogeneity and a solid-like form.

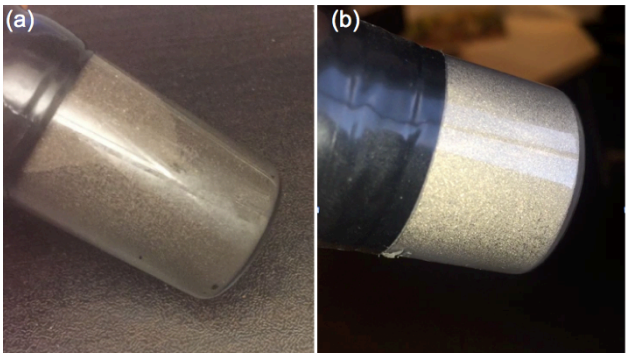

Figure 64. (a) Lithium microparticles/polymer composite redispersed in THF before sonication. (b) Lithium microparticles/polymer composite redispersed in THF after sonicating, showing a metallic luster under light.

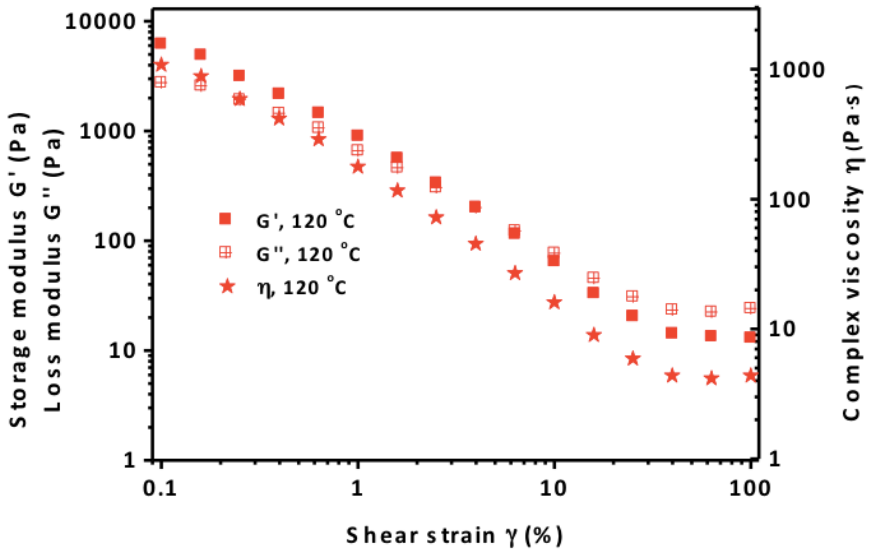

Figure 65. Rheological property of SLMA. Storage modulus (G'), loss modulus (G'') and complex viscosity at different shear strain at 120 ºC and 1 Hz.

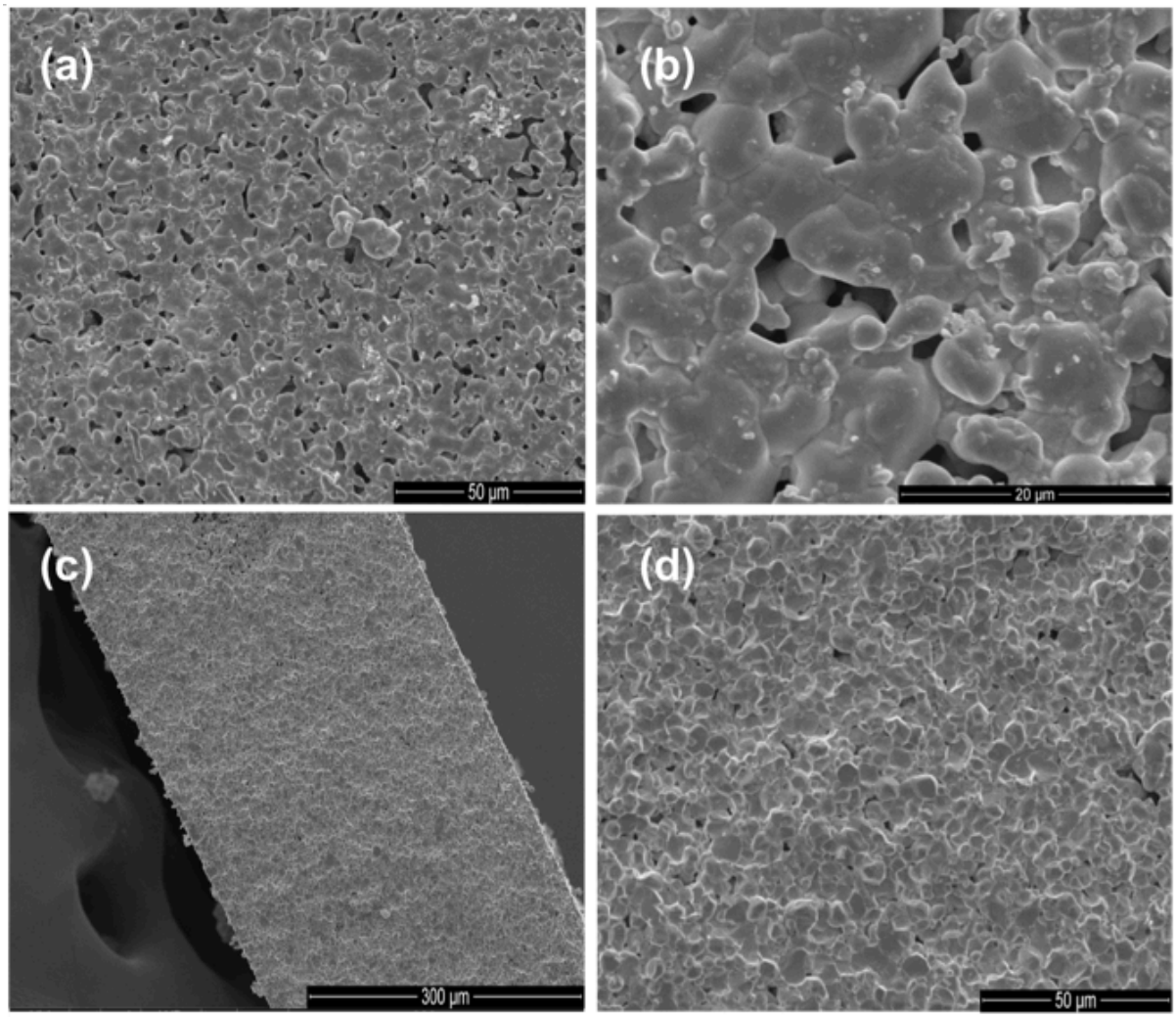

Figure 66. SEM of (a) surface of LLZTO pellet, (b) zoom-in image of surface LLZTO pellet, (c) cross-section image of LLZTO pellet and (d) zoom-in image of cross-section of LLZTO pellet.

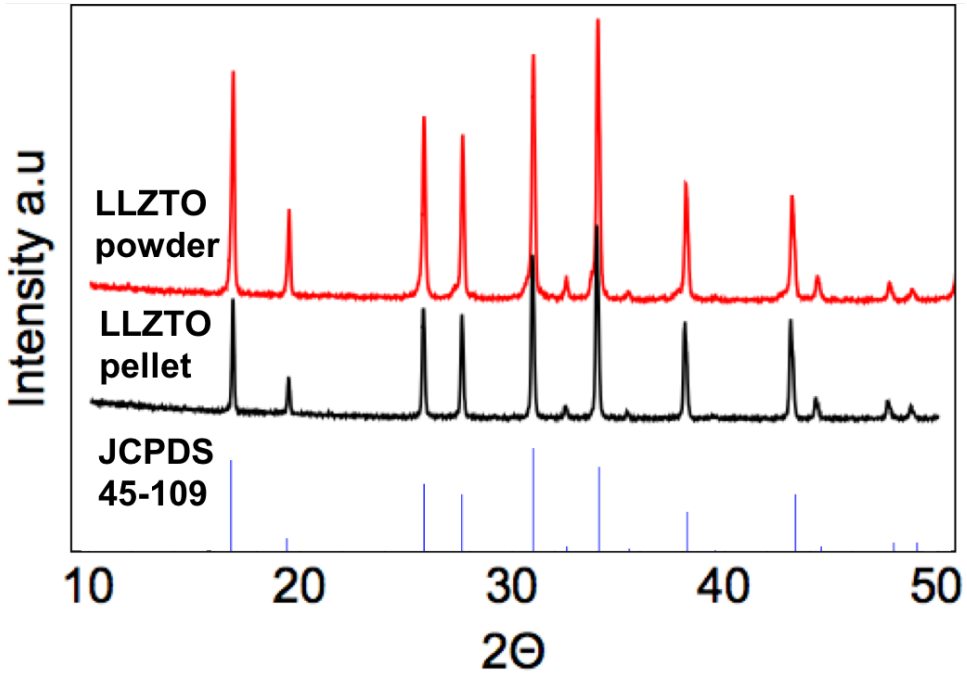

Figure 67. XRD pattern of purchased LLZTO powder and sintered LLZTO pellet.

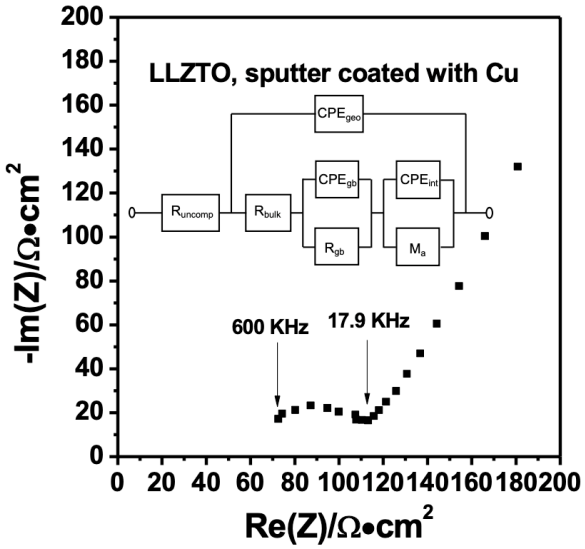

Figure 68. EIS of LLZTO with two sides sputter-coated with Copper measured at 65 oC. (Pellet thickness: 500 micron) R and CPE refer to the resistance and constant phase element, respectively. The subscripts "uncomp", "geo", "bulk", "gb", and "int", represent uncompensated, geometric dimensions, bulk, grain boundary, and interfacial phenomena related to surface roughness and the

nonideality of the copper electrodes, respectively. Ma refers to anomalous mass diffusion. The ionic conductivity was estimated to be 0.8 mS/cm according to J. Am. Ceram. Soc., 98 [4] 1209–1214 (2015).

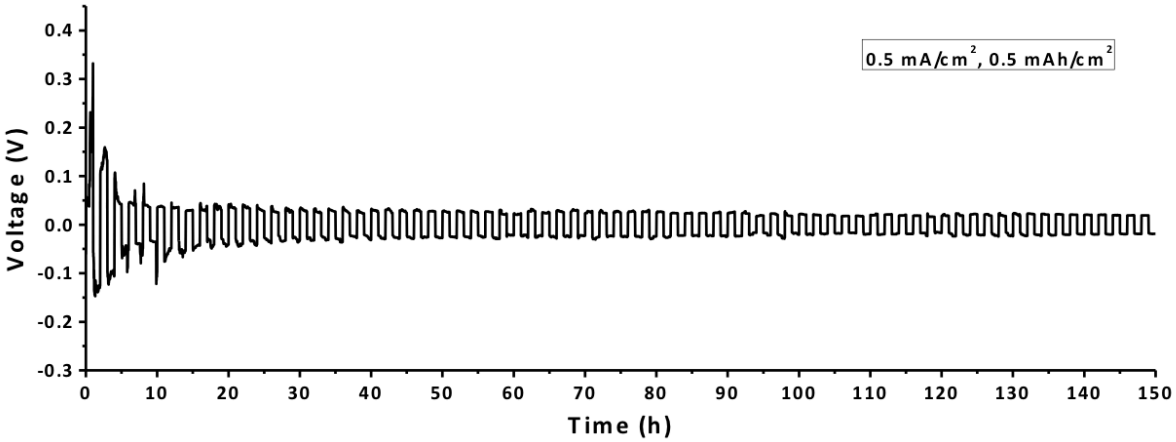

Figure 69. Symmetric cycling of SLMA/LLZTO/SLMA at 0.5 mA/cm^2 (1h charge/discharge) at 65 ^{o}C for 150 h.

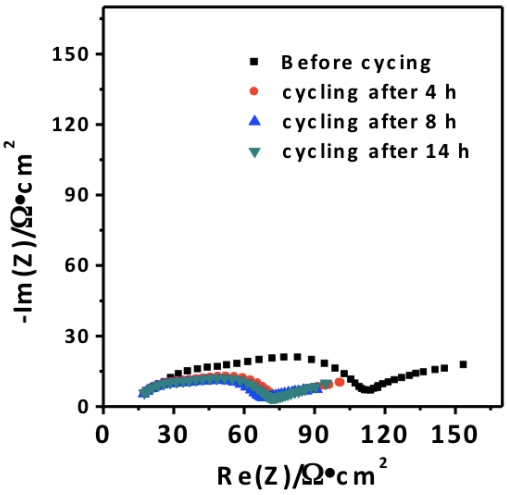

Figure 70. EIS of symmetric cycling of SLMA/LLZTO/SLMA at 0.5 mA/cm^2 and 0.5 mAh/cm^2 at 65 ^{o}C for 150 h.

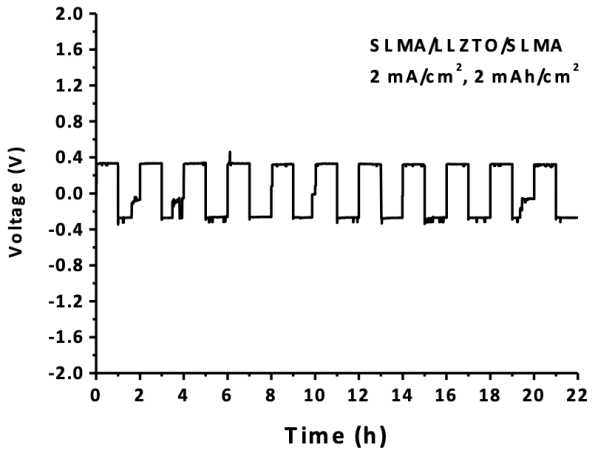

Figure 71. Symmetric cycling of SLMA/LLZTO/SLMA at 2 mA/cm^2 (1 h charge/discharge).

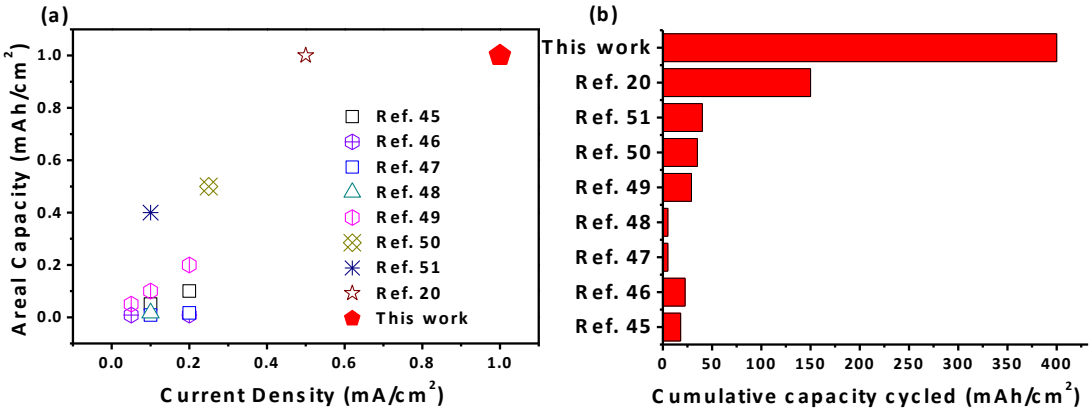

Figure 72. (a) Comparison of the cycling areal capacity and current density of SLMA anodes reported herein with previous reports that use lithium anodes and surface-modified garnet type electrolytes. (b) Comparison of the cumulative capacity cycled in this work with previous reports.

Table 9. Comparison of theoretical areal capacity, current density, cycled areal capacity and cumulative capacity.

Reference	Journal	Li content	Theoretical areal capacity (mAh/cm^2)	Current density (mA/cm^2)	Cycled areal capacity (mAh/cm^2)	Cumulative capacity (mAh/cm^2)
Our work		40 vol%	9	1	1	407
Ref 52	*Adv. Mater.*, **2019**	50 wt%	15.45	0.3	0.15	75
Ref 20	*PNAS*, **2018**	50 vol%	5.15~15	0.5	1	150
Ref. 45	*Nat. Mater.*, **2017**	100%	41.2	0.2	0.1	18
Ref. 46	*JACS*, **2016**	Unknown	Unknown	0.05~0.2	0.008~0.016	11
Ref. 47	*Sci. Adv.*, **2017**	100%	> 37	0.1 ~ 0.2	0.008~0.016	5
Ref. 48	*Nano Lett.*, **2017**	100%	30.9	0.1	0.016	4.7
Ref 53	*Angew. Chem.*, **2017**	100%	35.02	0.1	0.008	4
Ref. 34	*Nat. Nanotech.*, **2016**	Unknown	10.9	1	1	222

4.6. References

[1] Xu, K., Nonaqueous liquid electrolytes for lithium-based rechargeable batteries, *Chemical reviews* **2004,** 104, 4303.

[2] Lu, Y.; Tu, Z.; Archer, L. A., Stable lithium electrodeposition in liquid and nanoporous solid electrolytes, *Nature Materials* **2014,** 13, 961.

[3] Li, N.-W.; Shi, Y.; Yin, Y.-X.; Zeng, X.-X.; Li, J.-Y.; Li, C.-J.; Wan, L.-J.; Wen, R.; Guo, Y.-G., A Flexible Solid Electrolyte Interphase Layer for Long-Life Lithium Metal Anodes, *Angew. Chem. Int. Ed.* **2017,** 57, 1505.

[4] Xu, W.; Wang, J.; Ding, F.; Chen, X.; Nasybulin, E.; Zhang, Y.; Zhang, J.-G., Lithium metal anodes for rechargeable batteries, *Energy & Environmental Science* **2014,** 7, 513.

[5] Lin, D.; Liu, Y.; Cui, Y., Reviving the lithium metal anode for high-energy batteries, *Nature nanotechnology* **2017,** 12, 194.

[6] Zhou, G.; Li, F.; Cheng, H.-M., Progress in flexible lithium batteries and future prospects, *Energy & environmental science* **2014,** 7, 1307.

[7] Goodenough, J. B.; Kim, Y., Challenges for Rechargeable Li Batteries, *Chem. Mater.* **2010,** 22, 587.

[8] Cheng, X.-B.; Zhang, R.; Zhao, C.-Z.; Wei, F.; Zhang, J.-G., A Review of Solid Electrolyte Interphases on Lithium Metal Anode, *Advanced science* **2016,** 3, 1500213.

[9] Varzi, A.; Raccichini, R.; Passerini, S.; Scrosati, B., Challenges and prospects of the role of solid electrolytes in the revitalization of lithium metal batteries, *Journal of Materials Chemistry A* **2016,** 4, 17251.

[10] Yang, C.; Zhang, L.; Liu, B.; Xu, S.; Hamann, T.; McOwen, D.; Dai, J.; Luo, W.; Gong, Y.; Wachsman, E. D.; Hu, L., Continuous plating/stripping behavior of solid-state lithium metal anode in a 3D ion-conductive framework, *Proc. Nat. Acad. Sci.* **2018,** 115, 3770.

[11] Tao, X.; Liu, Y.; Liu, W.; Zhou, G.; Zhao, J.; Lin, D.; Zu, C.; Sheng, O.; Zhang, W.; Lee, H.-W.; Cui, Y., Solid-State Lithium–Sulfur Batteries Operated at 37 °C with Composites of Nanostructured Li7La3Zr2O12/Carbon Foam and Polymer, *Nano Letters* **2017,** 17, 2967.

[12] Duan, H.; Yin, Y.-X.; Shi, Y.; Wang, P.-F.; Zhang, X.-D.; Yang, C.-P.; Shi, J.-L.; Wen, R.; Guo, Y.-G.; Wan, L.-J., Dendrite-Free Li-Metal Battery Enabled by a Thin Asymmetric Solid Electrolyte with Engineered Layers, *Journal of the American Chemical Society* **2018,** 140, 82.

[13] Fu, K.; Gong, Y.; Dai, J.; Gong, A.; Han, X.; Yao, Y.; Wang, C.; Wang, Y.; Chen, Y.; Yan, C.; Li, Y.; Wachsman, E. D.; Hu, L., Flexible, solid-state, ion-conducting membrane with 3D garnet nanofiber networks for lithium batteries, *Proceedings of the National Academy of Sciences* **2016,** 113, 7094.

[14] Chen, L.; Li, Y.; Li, S.-P.; Fan, L.-Z.; Nan, C.-W.; Goodenough, J. B., PEO/garnet composite electrolytes for solid-state lithium batteries: From "ceramic-in-polymer" to "polymer-in-ceramic", *Nano Energy* **2018,** 46, 176.

[15] Li, S.; Mohamed, A. I.; Pande, V.; Wang, H.; Cuthbert, J.; Pan, X.; He, H.; Wang, Z.; Viswanathan, V.; Whitacre, J. F.; Matyjaszewski, K., Single-Ion Homopolymer Electrolytes with High Transference Number Prepared by Click Chemistry and Photoinduced Metal-Free Atom-Transfer Radical Polymerization, *ACS Energy Letters* **2018,** 3, 20.

[16] Dirlam, P. T.; Glass, R. S.; Char, K.; Pyun, J., The use of polymers in Li-S batteries: A review, *Journal of Polymer Science Part A: Polymer Chemistry* **2017,** 55, 1635.

[17] Choudhury, S.; Vu, D.; Warren, A.; Tikekar, M. D.; Tu, Z.; Archer, L. A., Confining electrodeposition of metals in structured electrolytes, *Proceedings of the National Academy of Sciences* **2018,** 115, 6620.

[18] Stalin, S.; Choudhury, S.; Zhang, K.; Archer, L. A., Multifunctional Cross-Linked Polymeric Membranes for Safe, High-Performance Lithium Batteries, *Chemistry of Materials* **2018,** 30, 2058.

[19] Villaluenga, I.; Wujcik, K. H.; Tong, W.; Devaux, D.; Wong, D. H. C.; DeSimone, J. M.; Balsara, N. P., Compliant glass–polymer hybrid single ion-conducting electrolytes for lithium batteries, *Proceedings of the National Academy of Sciences* **2016,** 113, 52.

[20] Pang, Q.; Zhou, L.; Nazar, L. F., Elastic and Li-ion–percolating hybrid membrane stabilizes Li metal plating, *Proceedings of the National Academy of Sciences* **2018,** 115, 12389.

[21] Dong, W.; Zeng, X.-X.; Zhang, X.-D.; Li, J.-Y.; Shi, J.-L.; Xiao, Y.; Shi, Y.; Wen, R.; Yin, Y.-X.; Wang, T.-s.; Wang, C.-R.; Guo, Y.-G., Gradiently Polymerized Solid Electrolyte Meets with Micro-/Nanostructured Cathode Array, *ACS Applied Materials & Interfaces* **2018,** 10, 18005.

[22] Zeng, X.-X.; Yin, Y.-X.; Shi, Y.; Zhang, X.-D.; Yao, H.-R.; Wen, R.; Wu, X.-W.; Guo, Y.-G., Lithiation-Derived Repellent toward Lithium Anode Safeguard in Quasi-solid Batteries, *Chem* **2018,** 4, 298.

[23] Liu, Y.; Lin, D.; Jin, Y.; Liu, K.; Tao, X.; Zhang, Q.; Zhang, X.; Cui, Y., Transforming from planar to three-dimensional lithium with flowable interphase for solid lithium metal batteries, *Science Advances* **2017,** 3.

[24] Lin, D.; Liu, Y.; Liang, Z.; Lee, H.-W.; Sun, J.; Wang, H.; Yan, K.; Xie, J.; Cui, Y., Layered reduced graphene oxide with nanoscale interlayer gaps as a stable host for lithium metal anodes, *Nature Nanotechnology* **2016,** 11, 626.

[25] Jin, Y.; Liu, K.; Lang, J.; Zhuo, D.; Huang, Z.; Wang, C.-a.; Wu, H.; Cui, Y., An intermediate temperature garnet-type solid electrolyte-based molten lithium battery for grid energy storage, *Nature Energy* **2018**.

[26] Shimotake, H.; Rogers, G. L.; Cairns, E. J., Secondary Cells with Lithium Anodes and Immobilized Fused-Salt Electrolytes, *Industrial & Engineering Chemistry Process Design and Development* **1969,** 8, 51.

[27] Kim, H.; Boysen, D. A.; Ouchi, T.; Sadoway, D. R., Calcium–bismuth electrodes for large-scale energy storage (liquid metal batteries), *Journal of Power Sources* **2013,** 241, 239.

[28] Bradwell, D. J.; Kim, H.; Sirk, A. H. C.; Sadoway, D. R., Magnesium–Antimony Liquid Metal Battery for Stationary Energy Storage, *Journal of the American Chemical Society* **2012,** 134, 1895.

[29] Wang, K.; Jiang, K.; Chung, B.; Ouchi, T.; Burke, P. J.; Boysen, D. A.; Bradwell, D. J.; Kim, H.; Muecke, U.; Sadoway, D. R., Lithium–antimony–lead liquid metal battery for grid-level energy storage, *Nature* **2014,** 514, 348.

[30] Ning, X.; Phadke, S.; Chung, B.; Yin, H.; Burke, P.; Sadoway, D. R., Self-healing Li–Bi liquid metal battery for grid-scale energy storage, *Journal of Power Sources* **2015,** 275, 370.

[31] Fergus, J. W., Ceramic and polymeric solid electrolytes for lithium-ion batteries, *Journal of Power Sources* **2010,** 195, 4554.

[32] Deng, Z.; Mo, Y.; Ong, S. P., Computational studies of solid-state alkali conduction in rechargeable alkali-ion batteries, *Npg Asia Materials* **2016,** 8, e254.

[33] Yu, S.; Schmidt, R. D.; Garcia-Mendez, R.; Herbert, E.; Dudney, N. J.; Wolfenstine, J. B.; Sakamoto, J.; Siegel, D. J., Elastic Properties of the Solid Electrolyte Li7La3Zr2O12 (LLZO), *Chemistry of Materials* **2016,** 28, 197.

[34] Tan, J.; Tiwari, A., Synthesis of Cubic Phase Li7La3Zr2O12 Electrolyte for Solid-State Lithium-Ion Batteries, *Electrochemical and Solid-State Letters* **2011,** 15, A37.

[35] Han, X.; Gong, Y.; Fu, K.; He, X.; Hitz, G. T.; Dai, J.; Pearse, A.; Liu, B.; Wang, H.; Rubloff, G.; Mo, Y.; Thangadurai, V.; Wachsman, E. D.; Hu, L., Negating interfacial impedance in garnet-based solid-state Li metal batteries, *Nature Materials* **2016,** 16, 572.

[36] Luo, W.; Gong, Y.; Zhu, Y.; Fu, K. K.; Dai, J.; Lacey, S. D.; Wang, C.; Liu, B.; Han, X.; Mo, Y.; Wachsman, E. D.; Hu, L., Transition from Superlithiophobicity to Superlithiophilicity of Garnet Solid-State Electrolyte, *Journal of the American Chemical Society* **2016,** 138, 12258.

[37] Fu, K.; Gong, Y.; Liu, B.; Zhu, Y.; Xu, S.; Yao, Y.; Luo, W.; Wang, C.; Lacey, S. D.; Dai, J.; Chen, Y.; Mo, Y.; Wachsman, E.; Hu, L., Toward garnet electrolyte–based Li metal batteries: An ultrathin, highly effective, artificial solid-state electrolyte/metallic Li interface, *Science Advances* **2017,** 3.

[38] Wang, C.; Gong, Y.; Liu, B.; Fu, K.; Yao, Y.; Hitz, E.; Li, Y.; Dai, J.; Xu, S.; Luo, W.; Wachsman, E. D.; Hu, L., Conformal, Nanoscale ZnO Surface Modification of Garnet-Based Solid-State Electrolyte for Lithium Metal Anodes, *Nano Letters* **2017,** 17, 565.

[39] Li, Y.; Zhou, W.; Chen, X.; Lü, X.; Cui, Z.; Xin, S.; Xue, L.; Jia, Q.; Goodenough, J. B., Mastering the interface for advanced all-solid-state lithium rechargeable batteries, *Proceedings of the National Academy of Sciences* **2016,** 113, 13313.

[40] Tsai, C.-L.; Roddatis, V.; Chandran, C. V.; Ma, Q.; Uhlenbruck, S.; Bram, M.; Heitjans, P.; Guillon, O., Li7La3Zr2O12 Interface Modification for Li Dendrite Prevention, *ACS Applied Materials & Interfaces* **2016,** 8, 10617.

[41] Sharafi, A.; Kazyak, E.; Davis, A. L.; Yu, S.; Thompson, T.; Siegel, D. J.; Dasgupta, N. P.; Sakamoto, J., Surface Chemistry Mechanism of Ultra-Low Interfacial Resistance in the Solid-State Electrolyte Li7La3Zr2O12, *Chemistry of Materials* **2017,** 29, 7961.

[42] Duan, J.; Wu, W.; Nolan, A. M.; Wang, T.; Wen, J.; Hu, C.; Mo, Y.; Luo, W.; Huang, Y., Lithium–Graphite Paste: An Interface Compatible Anode for Solid-State Batteries, *Adv. Mater.* **2019,** 31, 1807243.

[43] Fu, K.; Gong, Y.; Fu, Z.; Xie, H.; Yao, Y.; Liu, B.; Carter, M.; Wachsman, E.; Hu, L., Transient Behavior of the Metal Interface in Lithium Metal–Garnet Batteries, *Angew. Chem. Int. Ed.* **2017,** 56, 14942.

Chapter 5. Tuning the Lithium Metal Morphology

5.1. Preface

A typical lithium metal anode is only a mere piece of lithium metal foil. This results in a limited amount of work on the modification of the lithium metal anode, although the lithium metal anode is the heart of a rechargeable lithium metal battery.

I designed a novel approach to the development of a lithium metal anode by using a polymer surfactant and physical alteration to transform the foil form of a lithium metal anode to two types of powder forms: a microparticle-form and a nanoflake-form. Transforming the electrode structure from a plain foil to stacked micro/nano particles has several advantages: (1) the porous structure enhances the active surface area, thereby decreasing the local current density; (2) the cavities can alleviate the volume change during cycling; (3) the powder form allows for a well-controlled mass-loading, which is essential when balancing mass of cathode and anode during cell assembly; (4) the powder form also allows easy blending with functional additives; e.g. polymer binder, conductive filler, to further improve cell performance. Therefore, a lithium metal anode made of such powder form outperforms a traditional lithium metal battery in multiple aspects. The fabrication of the two forms of lithium powder will be discussed in section 5.2 and 5.3 respectively.

I designed the whole projects which resulted in one publication in a top energy related journal: Sipei Li, Han Wang, Wei Wu, Francesca Lorandi, Jay F. Whitacre, Krzysztof Matyjaszewski, "Solvent-Processed Metallic Lithium Microparticles for Lithium Metal Batteries", *ACS Appl. Energy Mater.* **2019**, *2*, 1623-1628. I would like to thank my Francesca Lorandi for her contribution in materials preparation and paper writing, Wei Wu for his contribution in electrode preparation and Han Wang for his contribution in electrochemical characterization and paper

writing. Financial support from National Science Foundation (Grant DMR 1501324) is acknowledged.

5.2. Solvent-Processed Metallic Lithium Microparticles for Lithium Metal Batteries

5.2.1. Introduction

Conventional Li metal anodes are in the form of a plain foil. However, the dramatic volume change at the foil surface during cycling and the high reactivity of Li metal against organic electrolytes can easily cause formation of dendrites, leading to poor Coulombic efficiency and eventual cell failure.[1, 2] Many attempts have been made to improve the cycling efficiency and stability,[3-10] however, further efforts are still needed in terms of materials processing, cell assembly and cost-effectiveness.

Transforming the electrode structure from a plain foil to stacked microparticles has several advantages: (1) the porous structure enhances the active surface area, thereby decreasing the local current density; (2) the cavities can alleviate the volume change during cycling; (3) the powder form allows for a well-controlled mass-loading, which is essential when balancing mass of cathode and anode during cell assembly; (4) the powder form also allows easy blending with functional additives; e.g. polymer binder, conductive filler, to further improve cell performance, (5) finally, microparticles are usually easier to prepare than nanoparticles and therefore more applicable for the industrial purposes. As such, microparticle-based materials systems have been successfully used in many challenging electrode systems, with the silicon particle-based anode being a notable example,[11] along with several others such as a metallic magnesium anode,[12] or a metallic bismuth anode.[13]

However, the preparation of metallic lithium microparticles (Li MPs) has been barely investigated and the preparation details were not fully disclosed.[14-16] Commercial sources of Li

MPs are not common. Therefore, it is of significant academic and industrial interest to develop a method for the large-scale and relatively safe preparation of Li MPs.

5.2.2. Results and discussions

We report a facile top-down approach for preparing Li MPs that involves the use of reactive polymer surfactant and the use of such Li MPs as a proof-of-concept for preparation of a Li MPs/carbon nanotube (CNT) composite anode (LMCA). The LMCA showed clearly improved electrochemical performance vs. a plain Li foil anode in both symmetric cycling and in a full cell test.

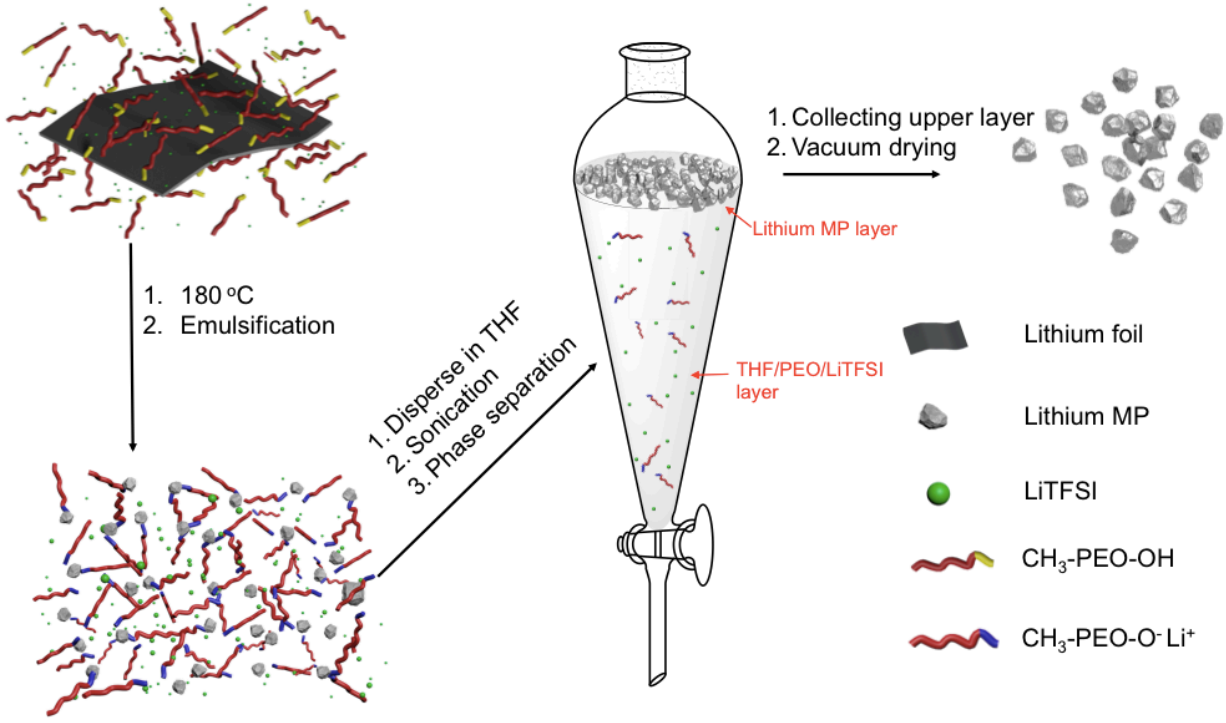

Scheme 8. Preparation of lithium microparticles.

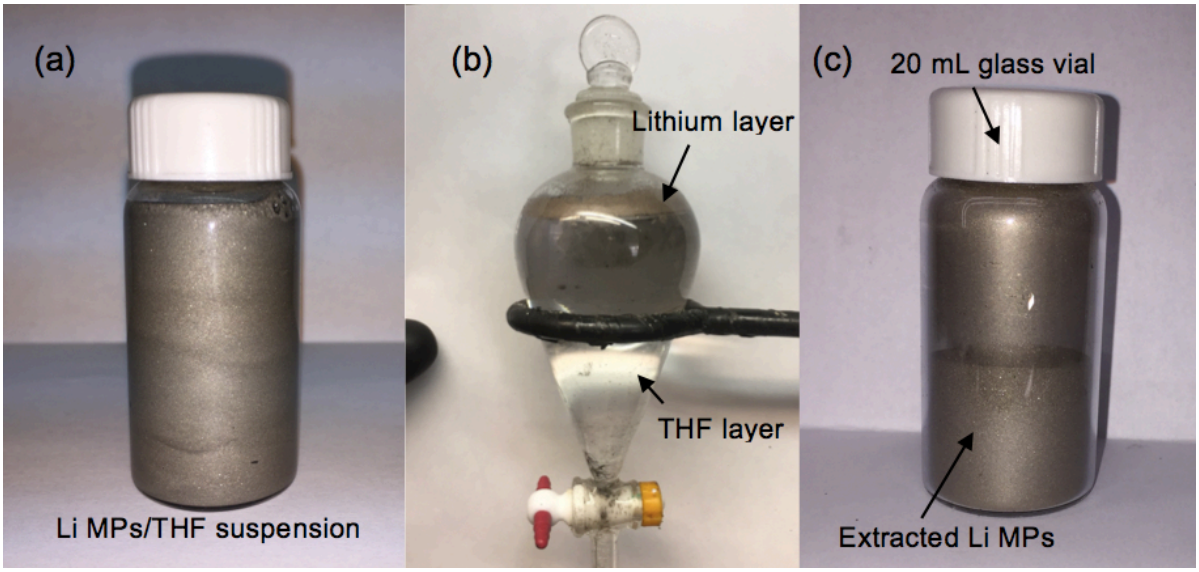

Figure 73. (a) Suspension of Li MPs in THF/mPEG/LiTFSI solution after sonication. (b) Spontaneous separation of Li MPs in a separatory funnel. (c) 1.5 g of extracted Li MPs in a 20 mL glass vial.

The preparation of Li microparticles is illustrated in scheme 8. Li foils were added into a glass vial containing a transparent polymer liquid that consisted of poly(ethylene glycol) monomethyl ether (MW=750, mPEG) and lithium bis(trifluoromethanesulfonyl)imide (LiTFSI) and heated at 180 °C. The Li foil formed smaller pieces by the chemical etching between the hydroxy groups of mPEG and the lithium metal. The lithium metal started to melt at this temperature and then the smaller particles formed a greyish emulsion in the presence of an added lithium salt and end-group-lithiated PEG within 10 min with a shearing speed of 800 RPM. In this procedure the mPEG serves as a reactive surfactant and the presence of LiTFSI helps to stabilize the emulsion. The hydroxy groups of the monofunctional mPEG reacted with metallic Li, thus accelerating the melting process of the lithium metal and enabling the use of substantially lower shearing forces compared to previous reports.[14, 15, 17, 18] Due to the protecting effect of the polymer chains, no corrosion of glass vials from molten lithium was observed. Therefore, a customized

mixing vessel is no longer needed. The agitation was stopped after 15 minutes of agitation, and the reaction mixture was allowed to cool down to room temperature to form a uniform colloidal dispersion. Anhydrous tetrahydrofuran (THF) was added and the mixture was sonicated overnight. The sonication not only broke down particle aggregates but also helped to clean the surface of the Li MPs by mechanically removing surface impurities resulting from side reactions that occurred at high temperature. After sonication a Li MP/THF suspension was formed, Figure 73a. Since the density of lithium (0.56 g/cm^3) is lower than THF (0.89 g/cm^3) a phase separation step was adopted to extract the Li MPs. The suspension of Li MP/THF was transferred to a separatory funnel and an extra amount of anhydrous THF was added. The suspension was kept still and after 30 min and two separate layers formed, Figure 73b. The top greyish layer consisted of floating Li MPs and the bottom layer was a solution of PEG/LiTFSI in THF with some insoluble impurities. The bottom layer was removed, whereas the upper layer was left to dry under vacuum to yield greyish powders with metallic luster, indicative of the high purity Li. Due to the high reactivity towards ambient air, further efforts were still needed to create a transferring device for quantifying the surface purity of the Li MPs. Figure 73c shows 1.5 g of prepared Li MP contained in a 20 mL glass vials. Interestingly, the Li MP cannot form compact packing and only 1.5 g of Li MP filled almost half the volume of the 20 mL vial. The mono chain-end functionality of the reactive surfactant is crucial. The as-prepared Li MP using mPEG has an approximate particle size around 30~60 μm, Figure 74a & b. In contrast, Li particles prepared by using dihydroxy PEG, Figure 77, or dimethoxy PEG, Figure 78, both showed larger particle size (even > 1 mm) and much broader size distribution. This is because dihydroxy PEG can serve as a cross-linker between MP and inhibits the stirring of the mixture. For dimethoxy PEG, the lack of chemical etching resulted in a much slower and insufficient process of emulsification. A solvent-processed approach to prepare lithium

MPs with polymeric reactive surfactant greatly reduced the requirement of specialized instruments, making the preparation significantly easier and safer as compared to previously reported approach.

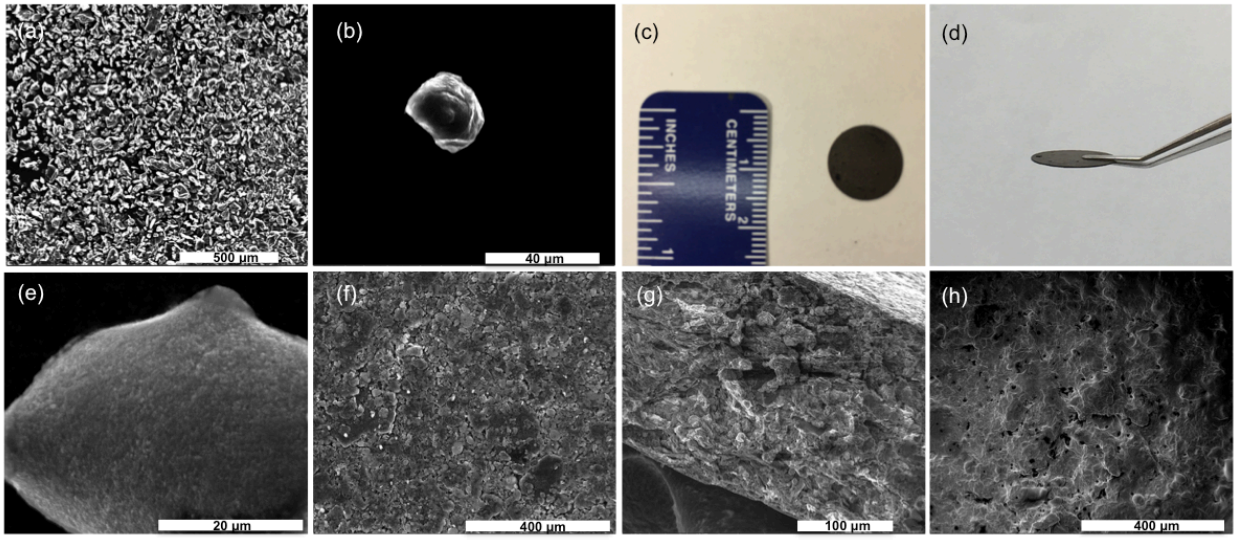

Figure 74. (a)&(b) SEM images of as-prepared Li MPs. (c)&(d) Digital photos of LMCA pellet. (e) SEM image of Li MPs mixed with CNT, (f) surface of LMCA pellet, (g) cross-section of LMCA pellet before symmetric cycling and (h) surface of LMCA pellet after symmetric cycling at 0.5 mA/cm^2 for 350 h.

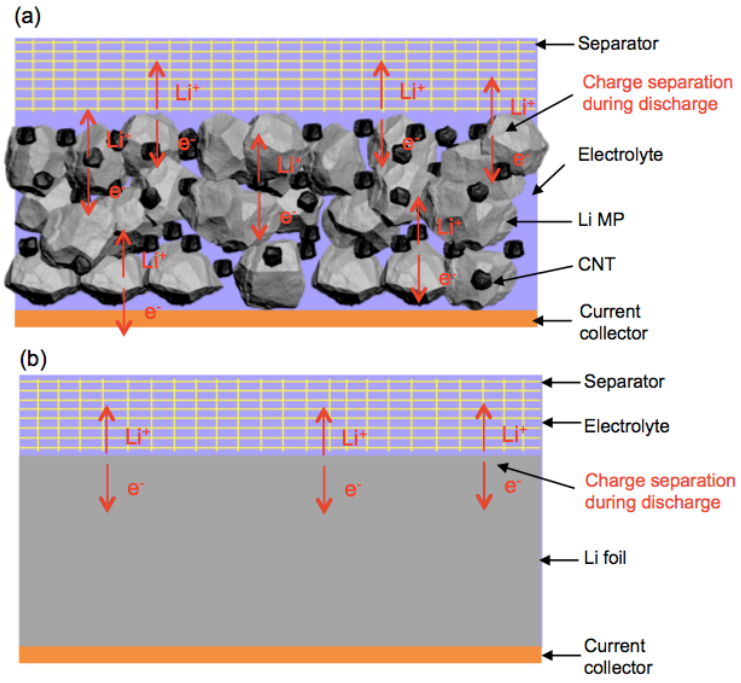

Scheme 9. Half-cell configuration of LMCA (a) and Li foil anode (b) with liquid electrolyte.

A proof-of-concept Li MPs/CNT composite anode (LMCA) was prepared. Because of the powder form of the Li MPs, the mass loading and fabrication of the electrode could be easily controlled. 80 wt% Li MP was precisely weighed and evenly mixed with 20 wt% CNT in a DAC-150 Speedmixer. The mixed powder was then pressed into a pellet with a thickness of 220 μm and a diameter of 13 mm, Figure 74c & d. After mixing, CNTs were uniformly coated on the Li MP surface, Figure 74e. SEM images of the surface and cross-section of the pellet confirmed the porous internal structure of the LMCA anode, Figure 74f & g. To study the plating/stripping behavior of LMCA, two symmetric cells using either LMCA or Li foil as electrode were assembled, respectively in a 2032-type coin cell case with 1 M LiPF6 in EC/DEC as electrolyte with a Celgard separator. Figure 75a shows the symmetric cycling of the two cells both at 0.5 mA/cm^2 current density, with 1 h charging/discharging time. Under this current density, the initial voltage of LMCA cell was 40 mV while that of Li foil cell was over 160 mV. This was in

agreement with the impedance spectra of the two cells measured before cycling, Figure 75b. The LMCA cell showed much lower resistance, as suggested by the smaller semicircle in the high-frequency range. During long-term charge/discharge cycle testing, the LMCA cell showed a highly stable and consistent voltage profile for the first 260 hours. Insets in Figure 75a show the enlarged voltage profile of LMCA cell at hour 50 and hour 250 during the test. At both points, the overpotential was 40 mV, identical to the initial value. The cell slightly polarized by 2~3 mV after 300 h. In contrast, the lithium foil anode cell has an initial overpotential of 120 mV. The voltage profile was also more asymmetric and spiky. The voltage increased to a high of 200 mV after 130 h. and the cell eventually shorted after 130 h, likely due to internal shorts in the form of Li dendrites. The improved cycling stability is also confirmed by impedance spectra measured after 100 h of cycling. For the Li foil cell, the interface resistance increased by almost 100 $\Omega \bullet cm^2$ while the LMCA cell increased only 5 $\Omega \bullet cm^2$, Figure 75c. This higher cycling stability of LMCA is due to two factors: (1) the 3D porous internal structure of LMCA and higher electrolyte/electrode contact area lead to lower local current density[19] and reduce the chances of dendrite formation towards the counter-electrode direction;[20] (2) the 3D structure ensured that the charge transfer takes place across the whole volume and greatly limits the local volume change during plating/stripping (Scheme 9).[3, 21, 22] Figure 74h shows that after cycling, the porous structure was preserved, but the surface became rougher. Symmetric cycling data at higher current densities (1 mA/cm^2, 2 mA/cm^3 and 3 mA/cm^2) are illustrated in Figure 80 and Figure 81, which also show reduced overpotential in comparison with plain lithium foil. Due to the increased surface area, the contribution of side reactions of lithium with the electrolytes might increase. In order to prevent these side reactions, future work will focus on creating a stable SEI at the surface of individual particles as well as introducing binding materials to prevent the detachment of dead lithium from

the electrode. The effect of adding different conductive fillers such as commercially inexpensive carbon black, graphene and copper powder will be investigated. Especially, due to the unique mechanical integrity, multiple forms and lithiophilicity, it has been demonstrated the addition of graphene can help to prevent dendrite growth,[23, 24] stabilize scalable lithium loading[25] and improve electrode mechanical properties[26]. Another challenge will be to reduce the thickness of the electrode in order to improve the device energy and power density as well as to balance the anode/cathode weight. However, thinner electrodes may introduce more device design challenges as the % of volume change experienced during charging/discharge will increase; we continue to investigate this matter.

To further investigate functionality in a full cell, a LCMA anode pellet was paired with $LiFePO_4$ (LFP) cathode and compared to a lithium foil anode with the same cathode. The details of cathode preparation and cell assembly are described in the supporting information. Both long-term cycling and rate performance were tested. The capacity was calculated per gram of cathode. As shown in Figure 76, at 0.5 mA/cm^2 current density, LMCA/LFP full cell showed 112 mAh/g discharge capacity in the first cycle and 111 mAh/g discharge capacity after 100 cycles, indicating less than 1% capacity loss after 100 cycles. The periodic change of capacity is due to the fluctuation of room temperature. The Li foil/ LFP full cell achieved only 104 mAh/g discharge capacity in the first cycle and 92 mAh/g discharge capacity after 100 cycles, equating to over 10% capacity loss. Moreover, in a rate performance test (Figure 76b), the LMCA/LFP also showed notable improvement over Li foil/LFP. The Li foil cell showed a discharge capacity of 132, 125, 105, 90 and 58 mAh/g at rate of 0.1, 0.2, 0.5, 1 and 2 C respectively, whereas the discharge capacity for the LMCA cell was 141, 132, 117, 100 and 76 mAh/g at 0.1, 0.2, 0.5,1 and 2 C. Also the LMCA showed higher first cycle round trip Coulombic efficiency than lithium foil (Figure 83). The

capacity difference is also supported by the voltage profile comparison at different current densities in Figure 76c&d. Compared to the Li foil/LFP full cell at all current densities, the voltage plateau of LMCA/LFP cell was lower during charge and higher during discharge, indicating that higher voltage could be harnessed in a LMCA anode than Li foil anode. These results suggest that, LMCA/LFP full cell has much better cycling stability than the Li foil/LFP full cell. Noticeably, in the future, the cathode preparation will be optimized in order to achieve even higher specific capacity.

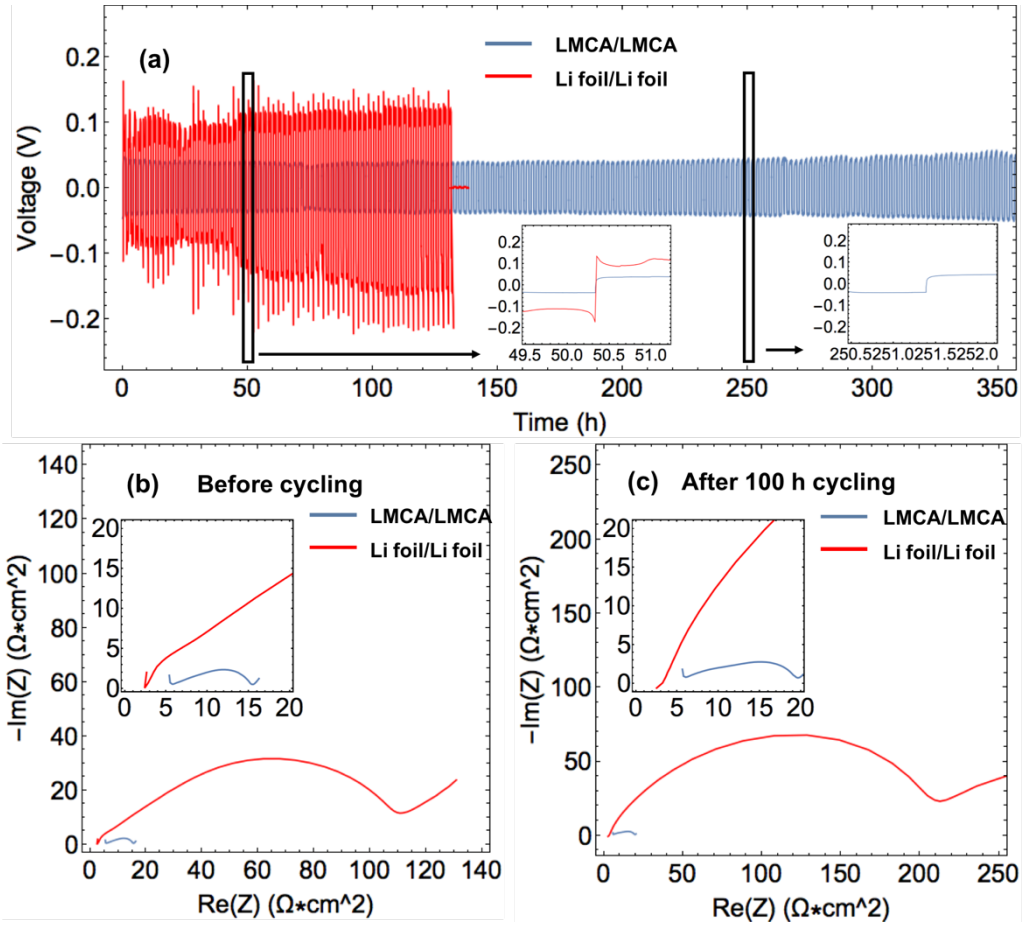

Figure 75. (a) Symmetric cycling data of LMCA/LCMA and Li foil/Li foil cells at 0.5 mA/cm^2 current density with 1 h charging/discharging times. The inset plots show the voltage profiles of LMCA/LCMA cell after 50 h and 200 h cycling. (b). EIS results of LMCA/LMCA cell and Li

foil/Li foil cell at 0.5 mA/cm^2 before cycling. (c) EIS results of LMCA/LMCA cell and Li foil/Li foil cell after 100 h of cycling at 0.5 mA/cm^2 (Left: high frequency; Right: low frequency).

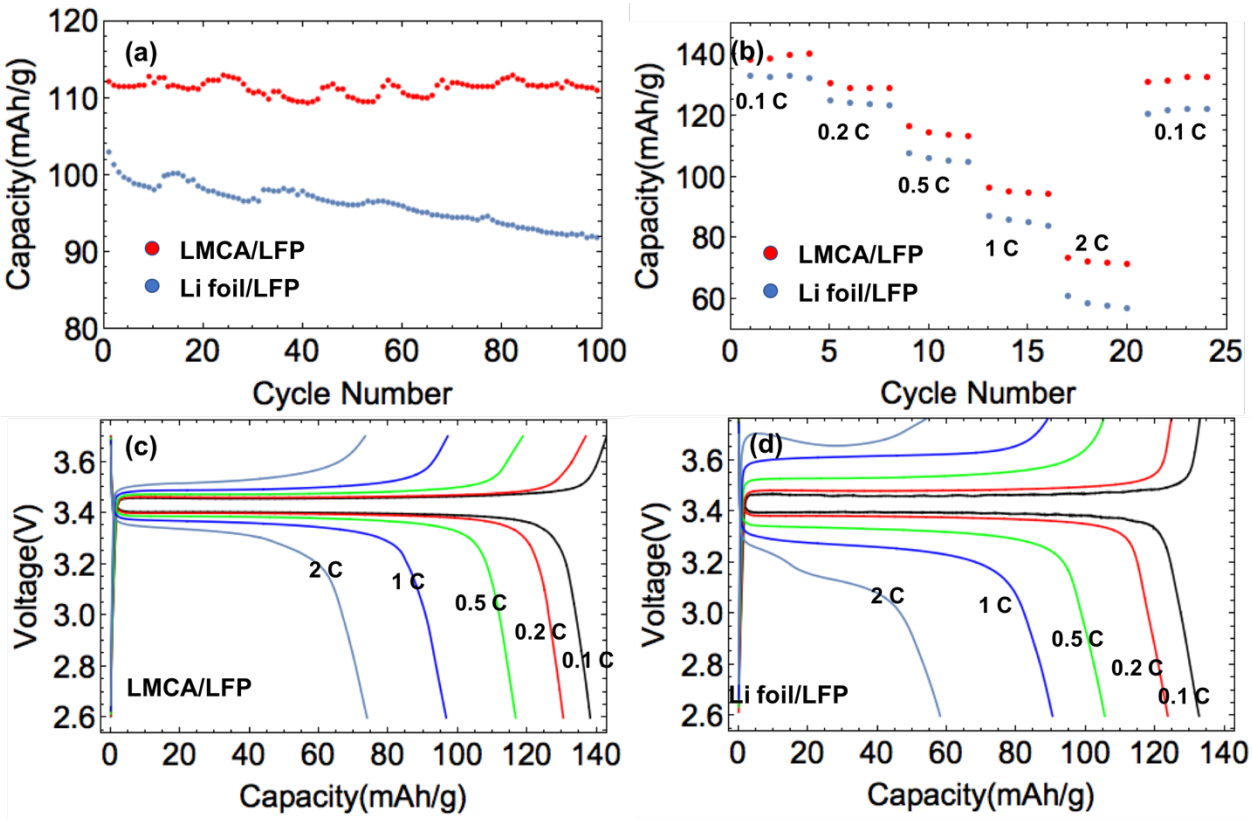

Figure 76. (a) Long-term cycling of LMCA/LFP full cell and Li foil/LFP full cell at 0.5 mA/cm^2 current density with 2.6 V and 3.8 V voltage cut-off. (b) Rate capability test of LMCA/LFP full cell and Li foil/LFP full cells at different current density with 2.6 V and 3.8 V voltage cut-off. (c) Voltage profile of LMCA/LFP cell under different current density. (d) Voltage profile of Li foil/LFP cell at different current density. (Capacity calculated per gram of cathode)

5.2.3. Conclusion

In conclusion, this work reports a facile method for the preparation and extraction of a large amount of Li microparticles (Li MPs) by a solvent-processing procedure. Compared to previous

approaches, such a solvent-processed approach with reactive-surfactant is safer, much more user-friendly for typical laboratories and can be easily reproduced and scaled up. A powder form allows for the preparation of composite anodes with functional fillers, such as conductive carbon, at room temperature, avoiding possible safety issues if the procedure was carried out at temperatures above the melting point of lithium. A proof-of-concept composite anode based on Li MPs was prepared. Both symmetric cell and full cell cycling tests proved the advantages of using Li MPs based anode as compared to a typical Li foil anode. Given both the academic and industrial interest in Li microparticles, the proposed procedure has great commercial potential in the field of electrode materials and electrolytes for LMB. Furthermore, we envisioned that this methodology for preparing low melting point metallic microparticles could be extended to other alkaline metal anodes systems, such as metallic sodium and potassium.

5.2.4. Experimental section and supporting information

Materials and characterizations. Poly(ethylene glycol) monomethyl ether (mPEG, MW=750 and MW=350), dihydroxy oligomeric ethylene glycol (dihydroxy PEG, MW=200), dimethoxy oligomeric ethylene glycol (dimethoxy PEG, MW=250), anhydrous tetrahydrofuran (THF) (>99.9%) were purchased from Sigma-Aldrich. Lithium bis(trifluoromethanesulfonyl)imide (LiTFSI) (>98%) was purchased from TCI America. Lithium chips (99.9%), a 13 mm stainless steel die, and $LiFePO_4$ (LFP) powder were purchased from MTI. Carbon nanotubes (CNTs)-based Conductive Additives for Lithium Ion Battery (outside diameter (d_{50}): 50-80 nm, length: 10-15 μm) were purchased from US Research Nanomaterials Inc. TIMCAL Graphite & Carbon Super P® Conductive Carbon Black was purchased from MatWeb.

Scanning electron microscopy (SEM) was performed on a Philips XL30 scanning electron microscope.

Preparation of Li MPs. The whole fabrication process was carried out in an argon-filled glove box with sub-ppm (parts per million) O_2 and H_2O levels. In a typical procedure, 0.6 g of mPEG (MW=750) was mixed with 0.39 g LiTFSI (EO/Li = 10/1) in a 20 mL glass vial equipped with a stirring bar and heated at about 180 ^oC to give a transparent liquid. Then 0.264 g lithium metal were preliminarily cut into small pieces (average size ~ 1 cm^2) and added into the mPEG/LiTFSI mixture. The mixture was stirred at 800 RPM on a hot plate for 10-15 min. After the mixture was cooled down to room temperature, 10 mL of anhydrous THF were added to the vial. The suspension was put in a sonication bath for 10 hours. After that, the suspension was added to ~100 mL THF and transferred to a separatory funnel. After 30 min, two layers formed. The upper layer containing Li MPs was collected and dried under vacuum to give pure Li MPs with a metallic luster, with an average yield of 90%.

Fabrication of LMCA electrode. The Li MPs and CNT were weighed, to provide a mixture with a mass ratio 4:1. The mixture was transferred to a plastic container. Then, the container was sealed and put in a DAC-150 Speedmixer. The mixer was run at 3000 RPM for 1 min and left to rest for another 1 min. The mixing process was repeated 3 times to give a homogeneous black powder. After mixing, the powder was transferred to a 13 mm stainless steel die and pressed into a pellet under a pressure of 250 psi.

Assembly of coin cell and electrochemical test. All electrochemical tests, including symmetric cycling, full-cell test and electrochemical impedance spectroscopy (EIS), were performed at 25 ^oC in a Bio Logic VMP3 Multi-Channel Potential/Electrochemical Impedance Spectrometer, 2032-type coin cells were used. The separator from Celgard with 25 μm thickness

was used. Commercial electrolyte (1 M $LiPF_6$ in 1:1 ethylene carbonate (EC): diethyl carbonate (DEC)) was used. Two pieces of LMCA pellet with 13 mm diameter were used for symmetric cycling. The symmetric cell was cycled at 0.5 mA/cm^2 current density, at 25 ^{o}C. For the full-cell test, the LFP electrode was prepared by spray-drying. The LFP, carbon black and poly(vinylidene fluoride) (PVDF) powder were weighed to provide a weight ratio of 7:2:1 and the mixture was gradually added to N-methyl-2-pyrrolidone (NMP). The slurry was stirred for 30 min and sonicated for 30 min. Then the mixture was sprayed onto an aluminum foil, attached to the hot plate. After the spray-drying, the aluminum foil was then transferred into a vacuum oven at 80 ^{o}C and dried overnight. For both long-term cycling and rate performance test, the LMCA/LFP cells were run with constant charge and discharge current under the same voltage cut-off between 2.6 V and 3.7 V. For long term cycling, the LMCA/LFP full cell was cycled at a current density of 0.5 mA/cm^2 for 100 cycles, at 25 ^{o}C. The applied current for the LMCA/LFP full cell was calculated by the diameter of the LMCA electrode. For rate performance test, the LMCA/LFP full cell was cycled at current densities of 0.1, 0.2, 0.5, 1 and 0.1 mA/cm^2 (5 cycles for each current density). The capacity was calculated per gram of cathode. Measurements for the EIS were taken after the coin cell was rested for 3 h. The data was collected between 600 kHz and 100 mHz by applying a 10 mV sinusoidal voltage perturbation. The same tests with identical parameters were applied to the Li foil/Li foil symmetric cell, and Li foil/LFP full cell.

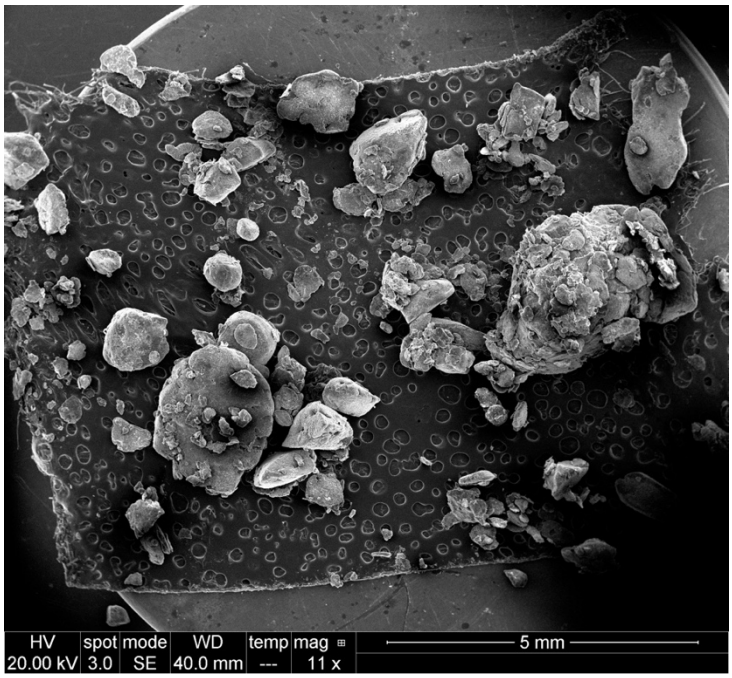

Figure 77. SEM image of lithium particles prepared from dihydroxy PEG.

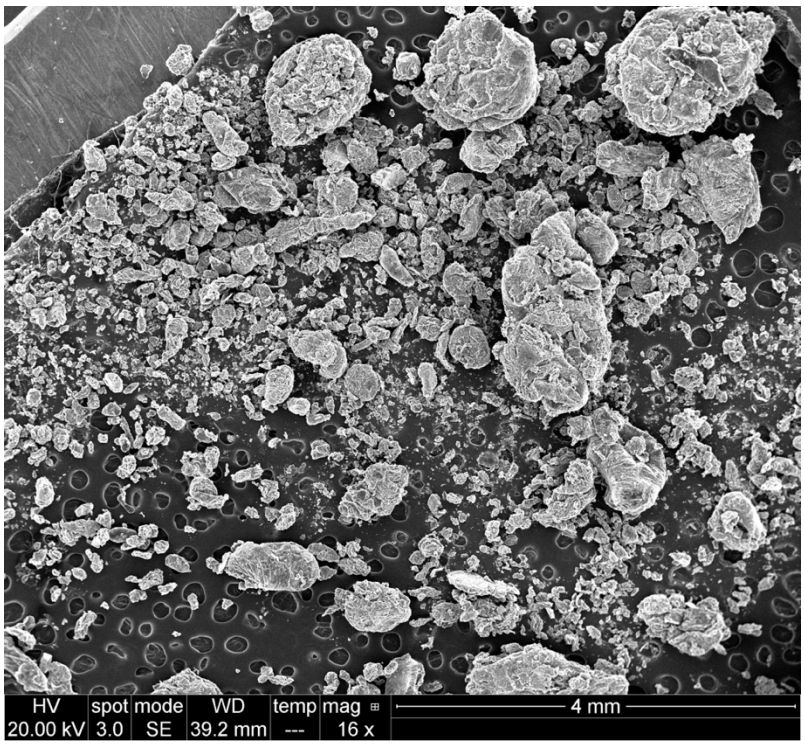

Figure 78. SEM image of lithium particles prepared from dimethoxy PEG.

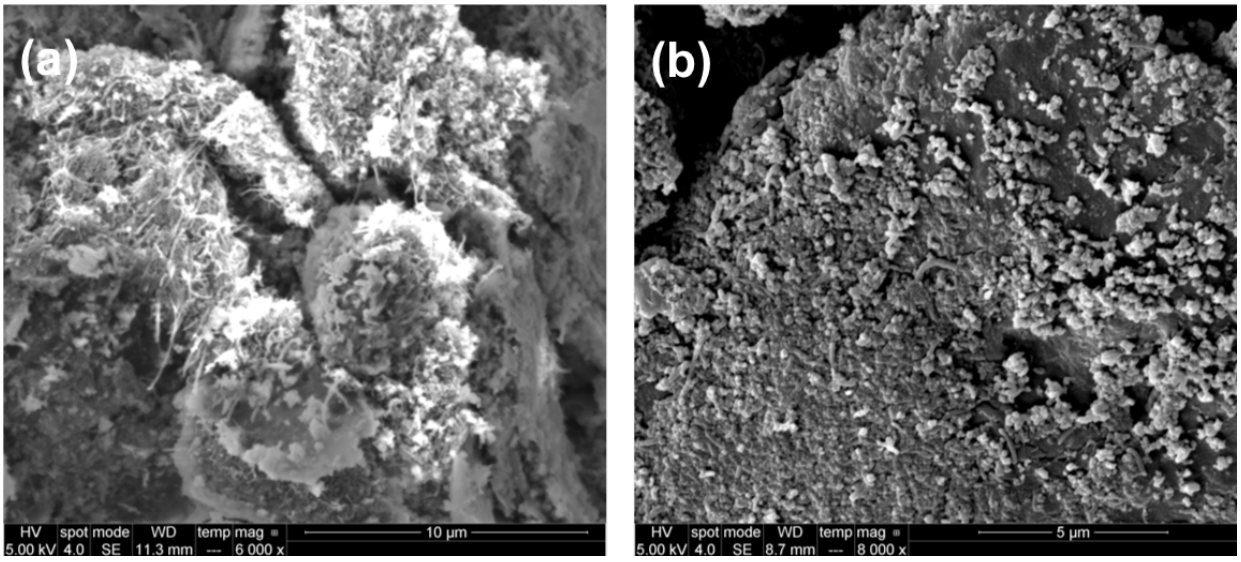

Figure 79. SEM images of (a) cross-section of LMCA pellet and (b) surface of LMCA pellet.

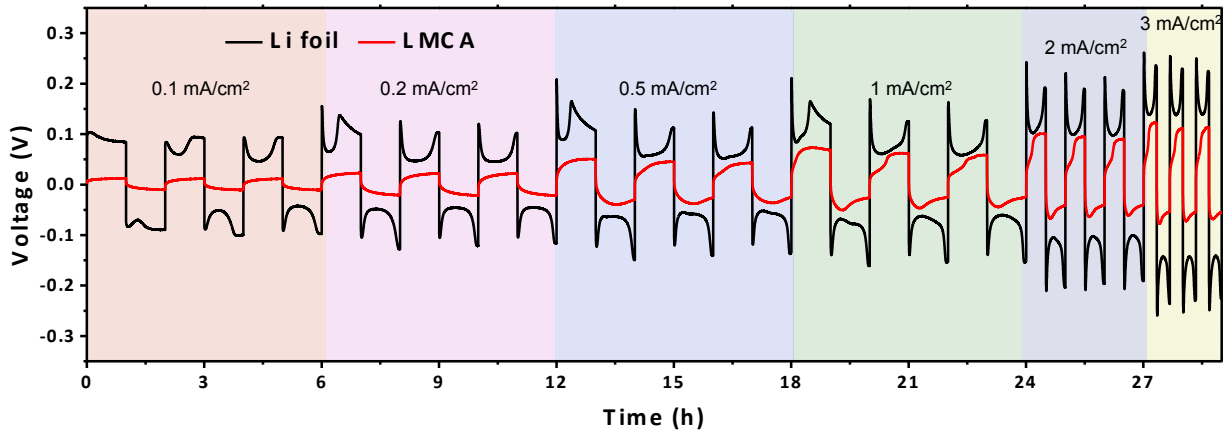

Figure 80. Symmetric cycling comparison of LMCA/LMCA and Li foil/Li foil. For cycling at 0.1, 0.2 0.5 and 1 mA/cm^2, each step is 1 hour. For 2 mA/cm^2, each step is 30 min and for 3 mA/cm^2 each step is 20 min.

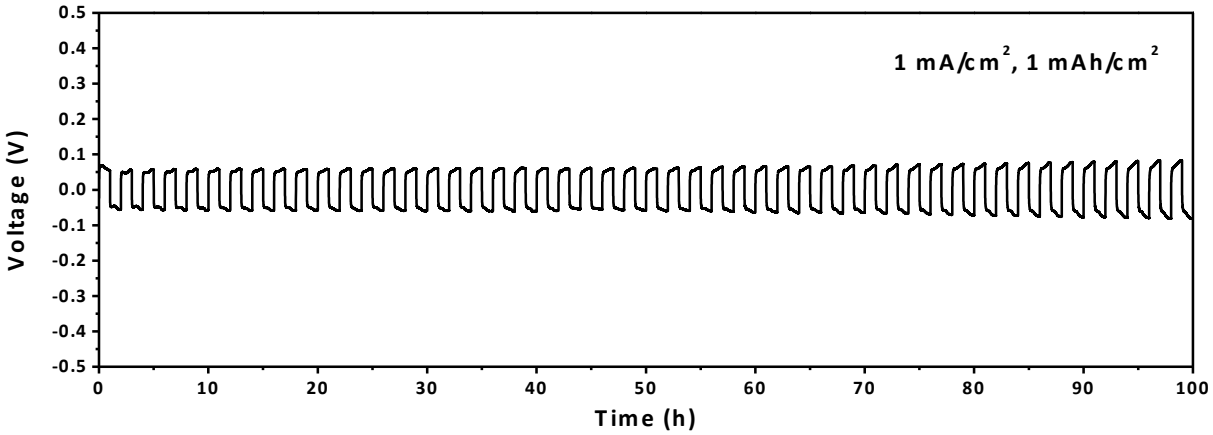

Figure 81. Symmetric cycling of LMCA/LMCA at 1 mA/cm^2 with 1 hour at each step.

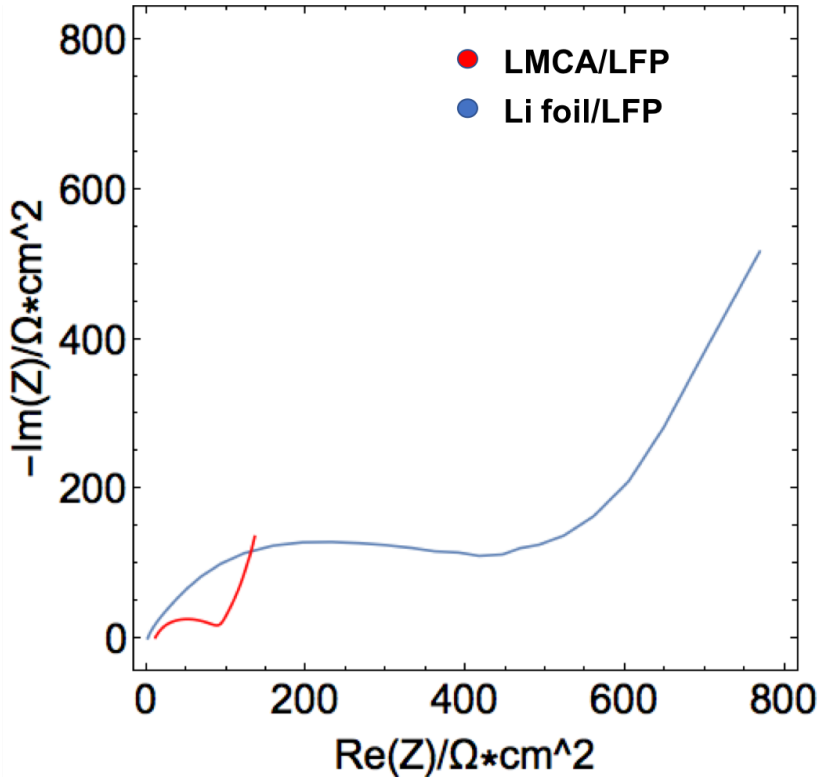

Figure 82. EIS of LMCA/LFP and Li foil/LFP full cell before rate performance test.

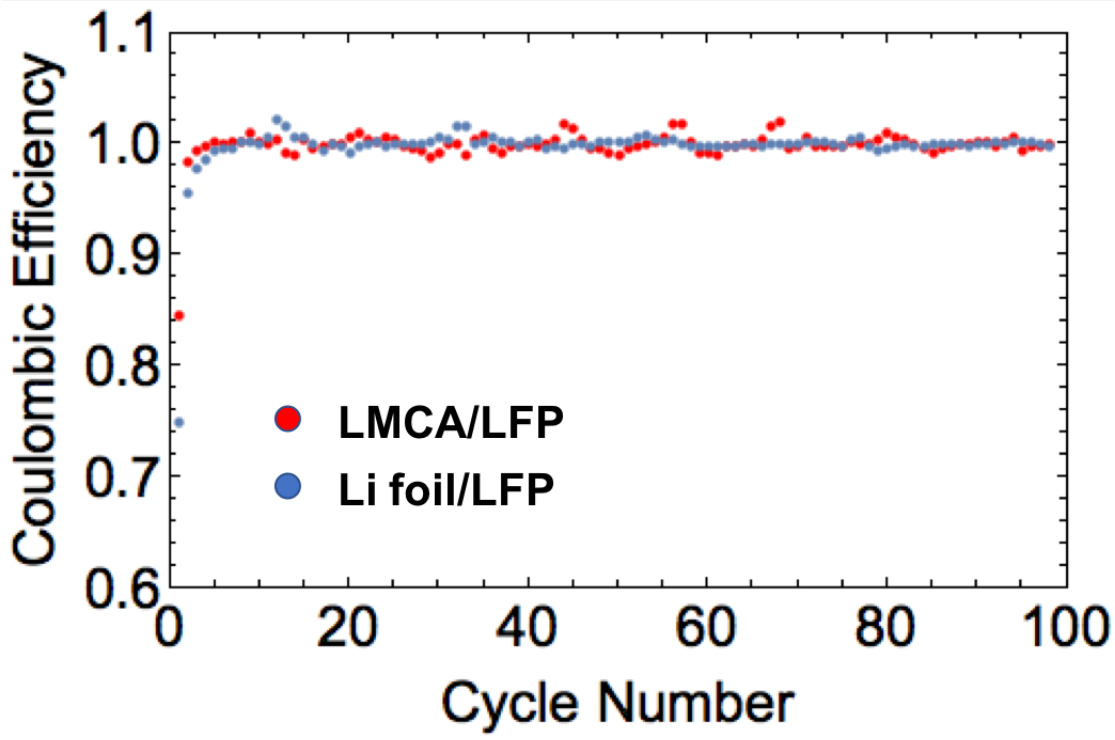

Figure 83. Coulombic efficiency of LMCA/LFP and Li foil/LFP full cells running under a current density of 0.5 mA/cm^2 for long-term cycling test.

5.3. Preparation of Lithium Nanoflakes by a Physical Wet-Milling Approach

5.3.1. Introduction

As introduced in section 5.2, one of the major benefits of reducing the size of lithium from millimeter-level plain foil to micron-level particles is to increase the contact surface area. Therefore, it would be even more interesting to reduce the size of lithium from a micron level to the nanometer level, at least in one dimension. Typically, there are two procedures employed for the preparation of inorganic nanostructures, the bottom-up and the top-down approaches.[27] A bottom-up synthesis method implies that the nanostructures are synthesized by stacking atoms onto each other, which gives rise to crystal planes, which further stack onto each other, resulting in the synthesis of nanostructures. However, due to the high reactivity of metallic lithium, it is extremely

difficult to apply the bottom-up approach for the preparation of lithium nanostructures. Not to mention the complication of achieving high product purity and materials for a scalable procedure. A top-down synthesis method implies that the nanostructures are synthesized by reducing the size of inorganics from a larger dimension. A top-down approach can thus be viewed as an approach where the building blocks are removed from the substrate to form the nanostructure. In this section, a wet-milling based top-down approach will be introduced to prepare lithium nanoflakes (Li NFs) with high purity. Composite lithium/carbon anodes were prepared with varied composition. Compared to LMCA, the nanoflakes based lithium composite anode showed further reduced overpotential during cycling.

5.3.2. Results and discussions

The first attempt to prepare lithium nanostructures was a modification of the approach of preparing Li MPs that is discussed in section 5.2. It was found that by increasing the agitation time and reducing the feeding amount of lithium, the particle size of resulting lithium could be further decreased to submicron level. As shown in Figure 84, by increasing the agitation time to 1 hour while reducing the feed amount of lithium to 10 vol%, sub-micron size lithium could be prepared. However, the yield of lithium was very low due to the increased extent of side-reactions and the difficulties of extracting sub-micron size lithium due to enhanced Brownian motion. Furthermore, the purity of the nanoparticles was low as the collected particles had no metallic luster and a brown color. We suspected that the elongated reaction time caused unwanted side reactions and therefore the application of higher agitation force without increasing the agitation time could increase the purity and yield of lithium NPs.

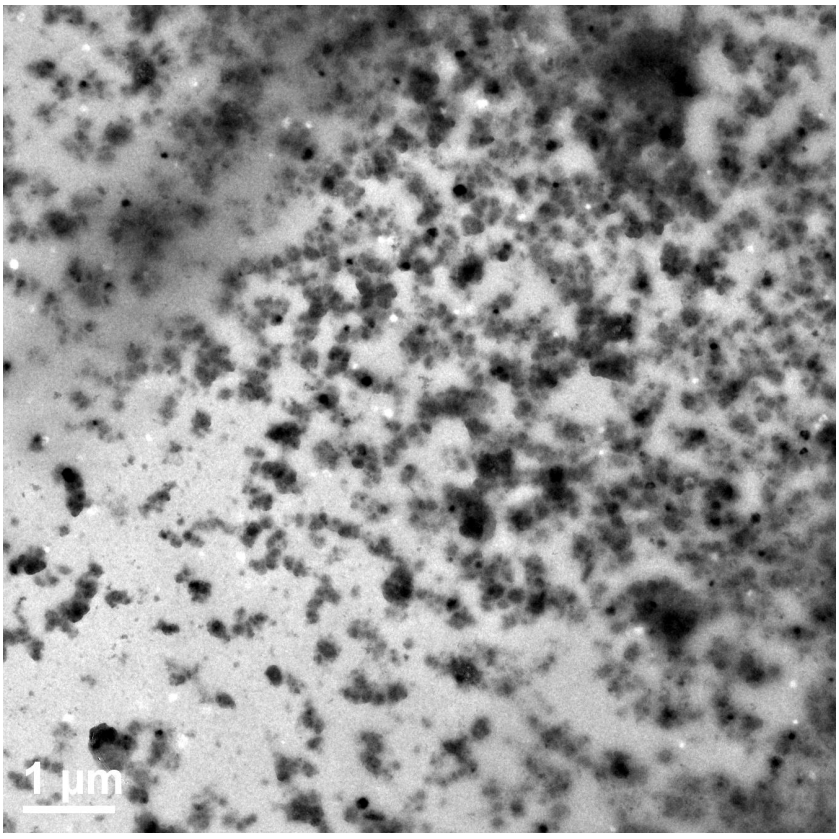

Figure 84. TEM image of sub-micron lithium particles prepared by increasing the agitation time to 1 hour while reducing the amount of fed lithium to 10 vol%.

Alternatively, in order to lower level of the side reactions that occurred at high temperature (>180 ^{o}C), a physical wet-milling approach was adopted for preparing lithium nanostructures with high purity. Similar to a regular ball-milling approach, where particle size is grinded down by collapsing the substrate with a grinding media, Li MPs prepared from section 5.2 were re-dispersed in THF and stirred slowly in the presence of a small magnetic stirring bar. The dispersion of Li MPs into THF served to avoid aggregation of the lithium MPs when flattened into macroscopic lithium sheets. As a result, the Li MPs were all flattened into smaller flakes with thickness at the sub-micron level. Moreover, the wet-milling served as a polishing process and the surface purity

of the lithium was further improved (Figure 85). As shown in Figure 86, the Li NFs had sub-micron thickness with micron-level width.

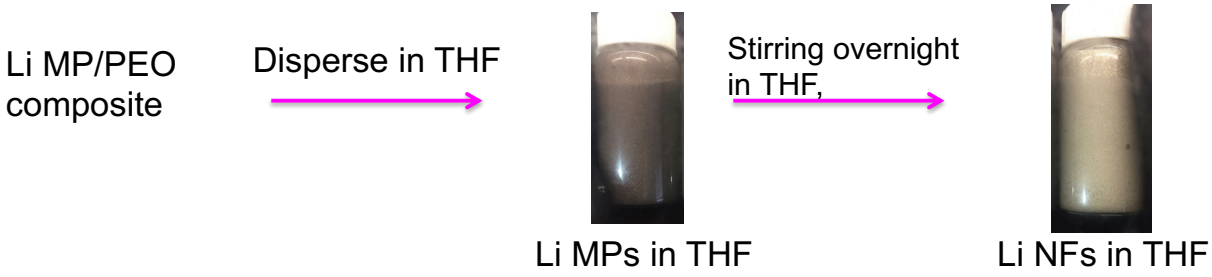

Figure 85. Wet-milling approach to prepare lithium nanoflakes (Li NFs) with improved purity.

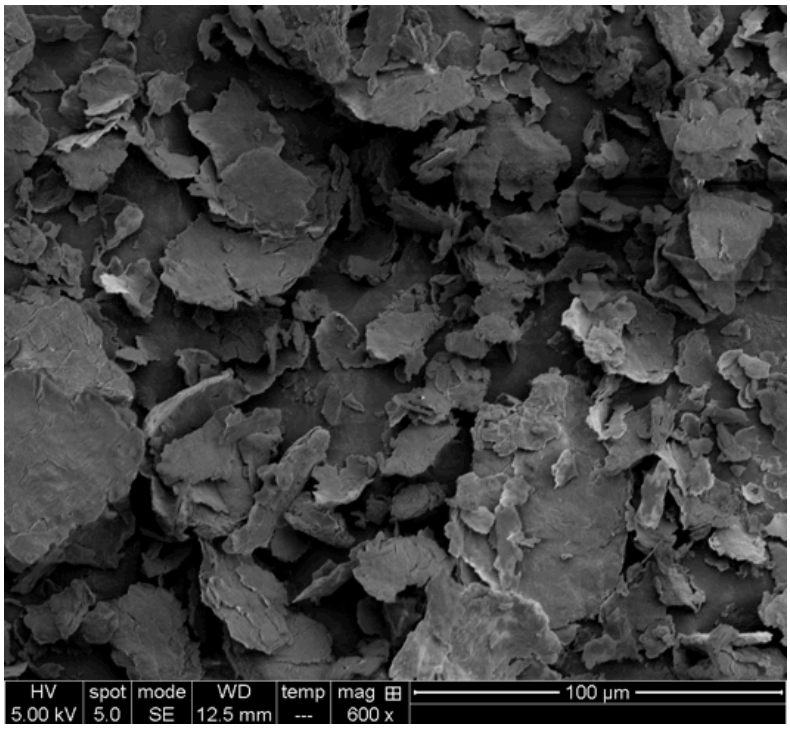

Figure 86. SEM image of prepared Li NFs with sub-micron thickness.

A composite anode made of Li NFs and 20 wt% carbon black was prepared using a similar approach to the method described in section 5.2, Figure 87. For comparison, a composite anode made of Li MPs with the same amount of carbon were also prepared. Symmetric cells using both type of composite anodes were assembled in 2032 coin cell cases, using 1 M $LiPF_6$ in EC/DEC

electrolyte, and run at 0.5 mA/cm^2. As shown in Figure 88, the Li NFs-based composite anode showed even lower overpotential. We believe this is because since one dimension of the lithium particles was reduced to a sub-micron size, the contact surface area was improved. Together with the fact that the lithium NFs have higher surface purity, internal cell resistance was decreased, leading to the overpotential drop.

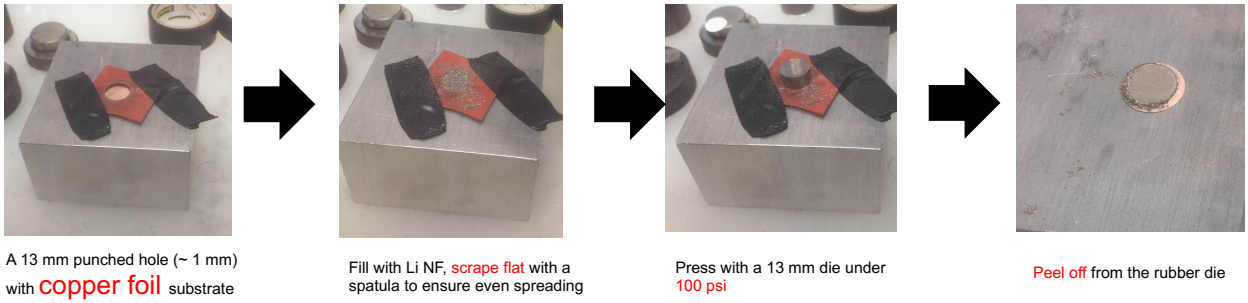

Figure 87. Preparation of the Li NFs/carbon composite anode.

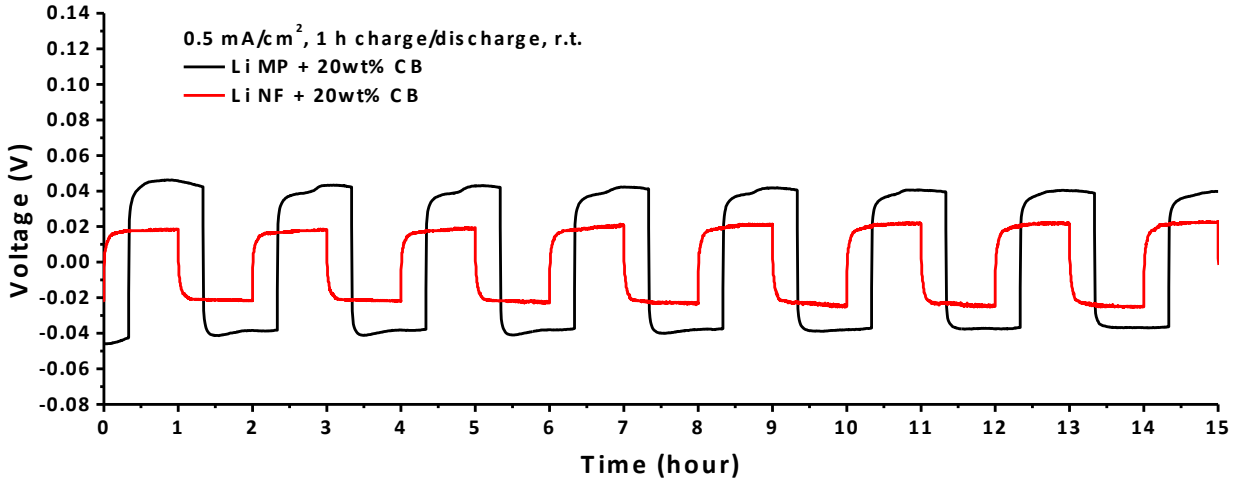

Figure 88. Symmetric cycling voltage profiles of composite anodes using Li NFs (red) and Li MPs (black) as lithium source. Cells run at 0.5 mA/cm^2, 1 hour each half step.

5.3.3. Conclusion

In conclusion, a physical wet-milling approach was developed to further tune the morphology of lithium particles from micron-size particles to nanoflakes with sub-micron thickness. The Li NFs had improved surface area and higher surface purity. As a result, a composite anode prepared from Li NFs showed an even further decrease in cycling overpotential. Moreover, due to the unique 2D morphology of Li NFs, we expect it to have the potential of building a mortar & brick structure with unusual mechanical properties.

5.4. References

[1] Li, N.-W.; Shi, Y.; Yin, Y.-X.; Zeng, X.-X.; Li, J.-Y.; Li, C.-J.; Wan, L.-J.; Wen, R.; Guo, Y.-G., A Flexible Solid Electrolyte Interphase Layer for Long-Life Lithium Metal Anodes, *Angewandte Chemie International Edition* **2018,** 57, 1505.

[2] Xu, X.; Wang, S.; Wang, H.; Hu, C.; Jin, Y.; Liu, J.; Yan, H., Recent progresses in the suppression method based on the growth mechanism of lithium dendrite, *Journal of Energy Chemistry* **2018,** 27, 513.

[3] Lin, D.; Liu, Y.; Liang, Z.; Lee, H.-W.; Sun, J.; Wang, H.; Yan, K.; Xie, J.; Cui, Y., Layered reduced graphene oxide with nanoscale interlayer gaps as a stable host for lithium metal anodes, *Nature Nanotechnology* **2016,** 11, 626.

[4] Tu, Z.; Nath, P.; Lu, Y.; Tikekar, M. D.; Archer, L. A., Nanostructured Electrolytes for Stable Lithium Electrodeposition in Secondary Batteries, *Acc. Chem. Res.* **2015,** 48, 2947.

[5] Li, S.; Mohamed, A. I.; Pande, V.; Wang, H.; Cuthbert, J.; Pan, X.; He, H.; Wang, Z.; Viswanathan, V.; Whitacre, J. F.; Matyjaszewski, K., Single-Ion Homopolymer Electrolytes with High Transference Number Prepared by Click Chemistry and Photoinduced Metal-Free Atom-Transfer Radical Polymerization, *ACS Energy Letters* **2018,** 3, 20.

[6] Wong, D. H. C.; Thelen, J. L.; Fu, Y.; Devaux, D.; Pandya, A. A.; Battaglia, V. S.; Balsara, N. P.; DeSimone, J. M., Nonflammable perfluoropolyether-based electrolytes for lithium batteries, *Proc. Nat. Acad. Sci.* **2014,** 111, 3327.

[7] Zhang, R.; Cheng, X.-B.; Zhao, C.-Z.; Peng, H.-J.; Shi, J.-L.; Huang, J.-Q.; Wang, J.; Wei, F.; Zhang, Q., Conductive Nanostructured Scaffolds Render Low Local Current Density to Inhibit Lithium Dendrite Growth, *Adv. Mater.* **2016,** 28, 2155.

[8] Duan, H.; Zhang, J.; Chen, X.; Zhang, X.-D.; Li, J.-Y.; Huang, L.-B.; Zhang, X.; Shi, J.-L.; Yin, Y.-X.; Zhang, Q.; Guo, Y.-G.; Jiang, L.; Wan, L.-J., Uniform Nucleation of Lithium in 3D Current Collectors via Bromide Intermediates for Stable Cycling Lithium Metal Batteries, *J. Am. Chem. Soc.* **2018,** 140, 18051.

[9] Yuan, Y.; Wu, F.; Bai, Y.; Li, Y.; Chen, G.; Wang, Z.; Wu, C., Regulating Li deposition by constructing LiF-rich host for dendrite-free lithium metal anode, *Energy Storage Materials* **2019,** 16, 411.

[10] Shen, X.; Cheng, X.; Shi, P.; Huang, J.; Zhang, X.; Yan, C.; Li, T.; Zhang, Q., Lithium–matrix composite anode protected by a solid electrolyte layer for stable lithium metal batteries, *Journal of Energy Chemistry* **2019,** 37, 29.

[11] Wang, C.; Wu, H.; Chen, Z.; McDowell, M. T.; Cui, Y.; Bao, Z., Self-healing chemistry enables the stable operation of silicon microparticle anodes for high-energy lithium-ion batteries, *Nat. Chem.* **2013,** 5, 1042.

[12] Son, S.-B.; Gao, T.; Harvey, S. P.; Steirer, K. X.; Stokes, A.; Norman, A.; Wang, C.; Cresce, A.; Xu, K.; Ban, C., An artificial interphase enables reversible magnesium chemistry in carbonate electrolytes, *Nat. Chem.* **2018,** 10, 532.

[13] Huang, J.; Lin, X.; Tan, H.; Zhang, B., Bismuth Microparticles as Advanced Anodes for Potassium-Ion Battery, *Adv. Energy Mater.* **2018,** 8, 1703496.

[14] Hong, S.-T.; Kim, J.-S.; Lim, S.-J.; Yoon, W. Y., Surface characterization of emulsified lithium powder electrode, *Electrochim. Acta* **2004,** 50, 535.

[15] Seong, I. W.; Hong, C. H.; Kim, B. K.; Yoon, W. Y., The effects of current density and amount of discharge on dendrite formation in the lithium powder anode electrode, *J. Power Sources* **2008,** 178, 769.

[16] Heine, J.; Krüger, S.; Hartnig, C.; Wietelmann, U.; Winter, M.; Bieker, P., Coated Lithium Powder (CLiP) Electrodes for Lithium-Metal Batteries, *Adv. Energy Mater.* **2014,** 4, 1300815.

[17] Kim, J. S.; Yoon, W. Y., Improvement in lithium cycling efficiency by using lithium powder anode, *Electrochim. Acta* **2004,** 50, 531.

[18] Shim, J.; Lee, J. W.; Bae, K. Y.; Kim, H. J.; Yoon, W. Y.; Lee, J.-C., Dendrite Suppression by Synergistic Combination of Solid Polymer Electrolyte Crosslinked with Natural Terpenes and Lithium-Powder Anode for Lithium-Metal Batteries, *ChemSusChem* **2017,** 10, 2274.

[19] Lin, D.; Zhao, J.; Sun, J.; Yao, H.; Liu, Y.; Yan, K.; Cui, Y., Three-dimensional stable lithium metal anode with nanoscale lithium islands embedded in ionically conductive solid matrix, *Proc. Nat. Acad. Sci.* **2017,** 114, 4613.

[20] Cheng, X.-B.; Zhang, R.; Zhao, C.-Z.; Zhang, Q., Toward Safe Lithium Metal Anode in Rechargeable Batteries: A Review, *Chem. Rev.* **2017,** 117, 10403.

[21] Chi, S.-S.; Liu, Y.; Song, W.-L.; Fan, L.-Z.; Zhang, Q., Prestoring Lithium into Stable 3D Nickel Foam Host as Dendrite-Free Lithium Metal Anode, *Adv. Funct. Mater.* **2017,** 27, 1700348.

[22] Kim, J.-S.; Yoon, W.-Y.; Kim, B.-K., Morphological differences between lithium powder and lithium foil electrode during discharge/charge, *J. Power Sources* **2006,** 163, 258.

[23] Hwang, J.-Y.; Park, S.-J.; Yoon, C. S.; Sun, Y.-K., Customizing a Li–metal battery that survives practical operating conditions for electric vehicle applications, *Energy & Environmental Science* **2019,** 12, 2174.

[24] Wang, A.; Zhang, X.; Yang, Y.-W.; Huang, J.; Liu, X.; Luo, J., Horizontal Centripetal Plating in the Patterned Voids of Li/Graphene Composites for Stable Lithium-Metal Anodes, *Chem* **2018,** 4, 2192.

[25] Liu, S.; Wang, A.; Li, Q.; Wu, J.; Chiou, K.; Huang, J.; Luo, J., Crumpled Graphene Balls Stabilized Dendrite-free Lithium Metal Anodes, *Joule* **2018,** 2, 184.

[26] Wang, A.; Tang, S.; Kong, D.; Liu, S.; Chiou, K.; Zhi, L.; Huang, J.; Xia, Y.-Y.; Luo, J., Bending-Tolerant Anodes for Lithium-Metal Batteries, *Adv. Mater.* **2018,** 30, 1703891.

[27] Biswas, A.; Bayer, I. S.; Biris, A. S.; Wang, T.; Dervishi, E.; Faupel, F., Advances in top–down and bottom–up surface nanofabrication: Techniques, applications & future prospects, *Adv. Colloid Interface Sci.* **2012,** 170, 2.

Chapter 6. Conclusions

6.1. General

The 2019 Nobel Prize in Chemistry was awarded to honor the development of lithium ion batteries. With the current graphite-anode based lithium ion batteries approaching their theoretical energy limit, the development of a lithium metal anode has been considered critical for the preparation of the next-generation lithium-based higher-energy rechargeable batteries,[1] because it delivers a higher theoretical specific capacity, 3860 mAh g^{-1} vs. 372 mAh g^{-1} for a conventional graphite anode, and has extremely low electrochemical redox potential, −3.04 V vs. SHE.[2] A state-of-the-art LIB equipped with graphite anode and NCM cathode has an energy density of 350 Wh/Kg. By replacing the graphite anode with lithium metal, the energy density could reach over 500 Wh/Kg, which is sufficient to power an electric vehicle for over 500 miles before a second full charge.[3] Furthermore, when paring a non-lithiated high-energy cathode, such as sulfur or O_2, with lithium metal, the energy density could be further increased to 800 Wh/Kg, completely revolutionizing the current field of energy storage.[2]

It remains a challenge to achieve a cycling stability for a lithium metal anode as high as in the case of a graphite anode. Traditionally, polymeric materials in a LIB are mostly used as non-reactive binder materials. However, recent advances in polymer chemistry have given polymer materials new “lives” in all aspects of an LMB, i.e., electrodes (cathode and anode), electrolyte and electrode/electrolyte interfaces (cathode-side and anode-side).

The first part of the thesis (Chapter 1) explained why and where the challenges are for the success of lithium metal batteries and introduces how polymer materials could be applied in the five aforementioned aspects of LMBs.

The second part of the thesis (Chapters 2 and Chapter 3) discusses how synthetic polymers could be used as a conductive layer for the stabilization of the anode interface. Chapter 2 emphasizes the importance of development and maintenance of a high transference number (t_+) in an electrolyte for LMBs. Two examples were given regarding how high transference number could be easily achieved through the selection and use of synthetic polymers. Polymers with tailor-made composition, morphology and functionality were achieved via combination of advanced polymerizations and modification chemistries, such as atom transfer radical polymerization (ATRP), ring opening polymerization (ROP) and copper-catalyzed alkyne-azide cycloaddition (CuAAC). Chapter 3 focused on the significance of a "mysterious" part of LMBs – the solid electrolyte interface (SEI). A spontaneously formed SEIs on lithium metal are brittle, inhomogeneous, and low in ionic conductivity, therefore will be repeatedly broken during battery cycling, exposing fresh lithium to further parasitic side reactions. Two types of polymeric materials were discussed for their application as artificial SEIs for a lithium metal anode, including an oxygen vacancies-rich YSZ/PAN hybrid material and a high-MW single-ion conducting polymer with simplified PEO-like backbone. Lithium anodes protected with these polymeric materials showed clearly improved cycling performance compared to lithium metal anodes without protection.

The third part of the thesis (Chapter 4 and Chapter 5) discusses the use of low MW monohydroxyl polyethylene glycol (mPEG) as reactive agent for the preparation of composite lithium anodes. Chapter 4 provided details on a simple approach to create liquid-like lithium composite anodes by dispersing *in situ* generated lithium microparticles in an electronically and ionically conductive liquid polymer composite. The flowing composite can work as an extremely stable anode with a solid ceramic electrolyte due to the generation of sufficient contact at the

anode/electrolyte interface. The methodology presented in this chapter complements the broader interest of developing safe high-energy-density solid-state rechargeable alkaline metal batteries. Chapter 5 described the use of mPEG as a reactive surfactant to taper down the size of typical millimeter-level lithium foil to micron-size lithium particles (Li MPs) and sub-micron lithium nanoflakes (Li NFs). Transforming lithium foils to microparticles or nanoflakes has several notable advantages including: (1) the porous structure can reduce the local current density and alleviate the volume change during cycling; (2) the powder form allows for a well-controlled mass-loading and easy blending with functional additives (e.g. polymer binder, conductive filler).

6.2. Outlook

The novel applications of advanced polymer materials for LMBs presented in this thesis confirm that functional polymers can be a vital building block for all the major components of an LMB. The numerous approaches that have been emerging within recent years illustrate a new perspective for achieving high performance practical LMBs: the application of tailor-made functional polymers with a wide range of mechanical and electrochemical properties to optimize resistance, stability and transport properties at the different interfaces in LMBs.

Advanced polymer materials for LMBs are typically engineered to accomplish specific tasks and are tested in combination with conventional battery materials and standard setups. Instead, a more integrated strategy is required to achieve practical polymer-based LMBs. For instance, single-ion conducting polymer electrolytes should be used together with a polymer coated Li metal or a flowable polymer/Li composite anode in order to achieve better wettability of the electrode material. The integration of different polymer-based parts is expected to introduce new challenges but also provide better understanding of interfacial phenomena.

Looking ahead, one would hope to eliminate the interfaces, meaning that there will be no/limited barriers for mass transport between cathode and anode. In order to achieve this, the polymer should be covalently grafted/attached by chemical bonds rather than simply blended/mixed with inorganic components. It is reasonable to expect that in the near future polymers will be grafted directly from lithium metal foil or particles. This will likely result in efficient prevention of dead lithium formation and better ionic transport between binding polymers and Li, particularly in a 3D form. Moreover, we previously demonstrated that grafting polymers from metallic EGaIn (Eutectic Gallium Indium) particles can reduce the melting point of the metal alloy.[4] Therefore, grafting polymers from lithium metal could greatly enhance the flexibility of the composite anode as well as its adaptability to solid electrolytes.

6.3. References

[1] Tarascon, J. M.; Armand, M., Issues and challenges facing rechargeable lithium batteries, *Nature* **2001,** 414, 359.

[2] Lin, D.; Liu, Y.; Cui, Y., Reviving the lithium metal anode for high-energy batteries, *Nature Nanotechnology* **2017,** 12, 194.

[3] Hwang, J.-Y.; Park, S.-J.; Yoon, C. S.; Sun, Y.-K., Customizing a Li–metal battery that survives practical operating conditions for electric vehicle applications, *Energy & Environmental Science* **2019,** 12, 2174.

[4] Yan, J.; Malakooti, M. H.; Lu, Z.; Wang, Z.; Kazem, N.; Pan, C.; Bockstaller, M. R.; Majidi, C.; Matyjaszewski, K., Solution processable liquid metal nanodroplets by surface-initiated atom transfer radical polymerization, *Nature Nanotechnology* **2019,** 14, 684.

6.4. List of publications

First-author publications:

1. **Li, S.**; Liu, T.; Yan, J.; Flum, J.; Wang, Z.; Fu, L.; Hu, L.; Lorandi, F.; Wang, H.; Yuan, R.; Whitacre; J.; Matyjaszewski, K., A Conformal Artificial Interface Layer Based on Oxygen Vacancy-Rich Hybrids Nanoparticles for Stable Lithium Plating/Stripping. **2019**, to be submitted.
2. **Li, S.**; Lorandi, F.; Whitacre, J.; Matyjaszewski, K., Polymer Chemistry for Improving Lithium Metal Anodes. *Macromol. Chem. Physic.* **2019**, DOI: 10.1002/macp.201900379.
3. **Li, S.**; Wang, H.; Cuthbert, J.; Liu, T.; Whitacre, J.; Matyjaszewski, K., A Semiliquid Lithium Metal Anode. *Joule* **2019**, DOI: 10.1016/j.joule.2019.05.022.
4. **Li, S.**; Wang, H.; Wu, W.; Lorandi, F.; Whitacre, J.; Matyjaszewski, K., Solvent-Processed Metallic Lithium Microparticles for Lithium Metal Batteries. *ACS Appl. Energy Mater.* **2019**, DOI: 10.1021/acsaem.9b00107.
5. Yan, J.; **Li. S.**; Cartieri, F.; Wang, Z.; Hitchens, T.; Leonardo, J.; Averick, S.; Matyjaszewski, K., Iron Oxide Nanoparticles with Grafted Polymeric Analogue of Dimethyl Sulfoxide as Potential Magnetic Resonance Imaging Contrast Agents. *ACS Appl. Mater. Inter*. **2018**, DOI: 10.1021/acsami.8b06416. (Joint first author)
6. **Li. S.**; Omi, M.; Cartieri, F.; Konkolewicz, D., Mao, Gao, H.; Averick, S.; Mishina, Y.; Matyjaszewski, K., Cationic Hyperbranched Polymers with Biocompatible Shells for siRNA Delivery. *Biomacromolecules* **2018**, DOI: 10.1021/acs.biomac.8b00902.
7. **Li. S.**; Mohamed, A.; Pande, V.; Wang, H.; Cuthbert, J.; Pan, X.; He, H.; Wang, Z.; Viswanathan, V.; Whitacre, J.; Matyjaszewski, K., Single-Ion Homopolymer Electrolytes with High Transference Number Prepared by Click Chemistry and Photoinduced Metal-

Free Atom-Transfer Radical Polymerization. *ACS Energy Lett.* **2017**, DOI: 10.1021/acsenergylett.7b00999.

8. **Li, S.**; Chung, H. S.; Simakova, A.; Wang, Z.; Park, S.; Fu, L.; Cohen-Karni, D.; Averick S.; Matyjaszewski, K.; Biocompatible Polymeric Analogues of DMSO Prepared by Atom Transfer Radical Polymerization. *Biomacromolecules*, **2017**, DOI: 10.1021/acs.biomac.6b01553.
9. **Li, S.**; Zheng, Y.; Zhu, Z.; Gao, C., Hyperbranched Polymers: Advances from Synthesis to Applications. *Chem. Soc. Rev.* **2015**, DOI: 10.1039/C4CS00528G. (Prior to CMU)
10. **Li. S.**; Gao, C., Dendritic Molecular Brushes: Synthesis via Sequential RAFT Polymerization and Cage Effect for Fluorophores. *Polym. Chem.* **2013**, DOI: 10.1039/C3PY00546A. (Prior to CMU)
11. **Li, S.**; Han, J.; Gao, C., High-Density and Hetero-Functional Group Engineering of Segmented Hyperbranched Polymers via Click Chemistry. *Polym. Chem.* **2013**, DOI: 10.1039/C2PY20951A. (Prior to CMU)
12. **Li, S.**; Han, J.; Tang, A.; Gao, C., Water-Soluble and Clickable Segmented Hyperbranched Polymers for Multifunctionalization and Novel Architecture Construction. *Macromolecules* **2012**, DOI: 10.1021/ma300718d. (Prior to CMU)

<u>Non-first-author publications:</u>

1. Wang, Z.; Fantin, F., Sobieski, J., Wang, Z.; Yan, J.; Lee, J.; Liu, T., **Li, S.**; Olszewski, M., Bockstaller, M. R.; Matyjaszewski, K., Pushing the Limit: Synthesis of SiO2-g-PMMA/PS Particle Brushes via ATRP with Very Low Concentration of Functionalized SiO2–Br Nanoparticles. *Macromolecules* **2019**, DOI: 10.1021/acs.macromol.9b01973.
2. Wang Z.; Liu, T.; Lin, K. S.; **Li, S.**; Yan, J.; Olszewski, M.; Sobieski J.; Pietrasik, J.;

Bockstaller, M. R.; Matyjaszewski, K.; Synthesis of Ultra-high Molecular Weight SiO2-g-PMMA Particle Brushes. *J. Inorg. Organomet. Polym. Mater.* **2019**, DOI: 10.1007/s10904-019-01289-8.

3. Rui, Y.; Wang, H.; Sung, M.; Damodaran, K.; Gottlieb, E.; Kopec, M.; Eckhart, K.; **Li, S.**; Whitacre, J.; Matyjaszewski, K.; Kowalewski, T., Well-Defined N/S Co-Doped Nanocarbons from Sulfurized PAN-b-PBA Block Copolymers: Structure and Supercapacitor Performance. *ACS Appl. Mater. Inter.* **2019**, DOI: 10.1021/acsanm.9b00340.
4. Brezinski, W.; Karayilan, M.; Clary, K.; Pavlopoulos, N.; **Li, S.**; Fu, F.; Matyjaszewski, K.; Evans, D.; Glass, R.; Lichtenberger, D.; Pyun, J., [FeFe]-Hydrogenase Mimetic Metallopolymers with Enhanced Catalytic Activity for Hydrogen Production in Water. *Angew. Chem. Int. Ed. Engl.***2018**, DOI: 10.1002/anie.201804661.
5. Wang, G.; Schmitt, M.; Wang, Z. Lee, B.; Pan, X.; Fu, L.; Yan, J.; **Li, S.**; Xie, G.; Bockstaller, M.; Matyjaszewski, K., Polymerization-Induced Self-Assembly (PISA) Using ICAR ATRP at Low Catalyst Concentration. *Macromolecules*, **2016**, DOI: 10.1021/acs.macromol.6b01966.
6. He, H.; Averick, S.; Mandal, P.; Ding, H.; **Li, S.**; Gelb, J.; Kotwal, N.; Merkle, A.; Litster, S.; Matyjaszewski, K., Multifunctional Hydrogels with Reversible 3D Ordered Macroporous Structures. *Adv. Sci.* **2015**, DOI: 10.1002/advs.201500069.
7. Han, J.; Zheng, Y.; Zheng, S.; **Li, S.**; Hu, T.; Tang, A.; Gao, C., Water Soluble Octa-Functionalized POSS: All-Click Chemistry Synthesis and Efficient Host–Guest Encapsulation. *Chem. Commun.* **2014**, DOI: 10.1039/C4CC01956C. (Prior to CMU)
8. Han, J.; Zheng, Y.; Zhao, B.; **Li, S.**; Zhang, Y.; Gao, C.; Sequentially Hetero-functional,

Topological Polymers by Step-growth Thiol-yne Approach. *Sci. Rep.* **2014**, DOI: 10.1038/srep04387. (Prior to CMU)

Appendix A. Biocompatible Polymeric Analogue of DMSO Prepared by ATRP

A.1. Preface

Before I entered CMU, I obtained my Master's degree in Zhejiang University where I studied the synthesis and functionalization of hyperbranched polymers. When I entered the PhD program of the Department of Chemistry at CMU, I continued my research in polymer synthesis and I first focused on bio related applications. My background in polymer chemistry laid foundation for my later branching out to applying polymer science in energy related areas especially lithium metal batteries.

In this Chapter, I will present one of my earliest work on developing a super-water-soluble biocompatible polymer and its non-linear topologies. This work resulted in a first-author publication in *Biomacromolecules* - Sipei Li, Hee Sung Chung, Antonina Simakova, Zongyu Wang, Sangwoo Park, Liye Fu, Devora Cohen-Karni, Saadyah Averick, Krzysztof Matyjaszewski, "Biocompatible Polymeric Analogues of DMSO Prepared by Atom Transfer Radical Polymerization", *Biomacromolecules* **2017**, *18*, 182475-482. I would like to thank Hee Sung Chuang, Antonina Simakova and Sangwoo Park for their contributions in polymer synthesis. I would like to thank Zongyu Wang and Liye Fu for their contributions in polymer characterizations. I would like to thank Devora Cohen-Karni and Saadyah Averick for biocompatibility test. I would like to thank the National Institutes of Health R01DE020843 and the NSF (DMR 1501324) for the financial support.

A.2. Introduction

Biocompatible polymers are used in a wide range of therapeutic applications, including drug delivery,[1] siRNA delivery,[2] gene delivery,[3] vaccination,[4] and tissue engineering.[5]

Poly(ethylene glycol) (PEG) is among the most widely used polymers in biomedical applications due to its hydrophilicity, water-solubility and chemical stability of the ether groups. Its neutral charge prevents interactions with negatively charged cell membranes, or opsonins that enhance phagocytosis and polymer clearance.[6] In addition PEGylated species can circulate longer in the bloodstream.[7] However, the conjugation of mono-functional PEG to bio-relevant molecules may result in the formation of heterogeneous products due to the presence of bi-functional PEG impurities.[7] Low molecular weight PEG may aggregate at elevated temperatures due to its lower critical solution temperature (LCST). In addition, it has been recently reported that the immunogenicity of PEG may result in inefficient drug delivery and severe immune reactions.[7] These limitations have motivated studies on the preparation and evaluation of other types of water-soluble, biocompatible polymers, with diverse chemistry to replace PEG. Poly(2-oxazoline)s, also synthesized by ring-opening polymerization, are potential alternatives to PEG. However, depending on substituents, they may exhibit limited solubility in water.[8]

It is interesting to explore synthesis of biocompatible polymers by reversible deactivation radical polymerizations (RDRP) procedures, such as atom transfer radical polymerization (ATRP),[9, 10] reversible addition-fragmentation chain transfer (RAFT) polymerization,[11] and nitroxide-mediated polymerization (NMP).[12] RDRP procedures were already employed to prepare some PEG-alternatives, such as poly(oligo(ethylene oxide) methyl ether methacrylate),[13, 14] polycarboxybetaines,[15] polyacrylamides,[16] polyvinylpyrrolidone.[17] Recently, several procedures were developed to reduce the concentration of ATRP catalyst required to control the polymerization, including activator regeneration by electron transfer (ARGET) ATRP,[18] supplemental activator and reducing agent (SARA) ATRP,[19, 20] initiators for continuous activator regeneration (ICAR) ATRP,[21] photoATRP[22, 23] and *e*-ATRP.[24] These systems have also been

successfully applied to aqueous media.[22] Polymers with various architectures, such as hyperbranched polymers, [25] star polymers,[26, 27] nanogels[28] and with other topologies,[29, 30] have been prepared under such conditions.

Previously, the synthesis of polymers based on sulfur-containing monomers, disulfide dimethacrylate,[13, 14, 29] 2-(methylthio)ethyl acrylate (MTEA) and 2-(methylthio)ethyl methacrylate (MTEMA)[31] were reported. MTE(M)A was also converted to tertiary sulfonium species stable in an aqueous environment. Diblock copolymers of PEG with sulfonium segments were biocompatible up to 50 μg/mL. They also efficiently formed polyplexes with siRNA for gene knockdown.[31]

Dimethyl sulfoxide (DMSO) is a neutral uncharged molecule used as a transdermal delivery enhancer,[32] polymerase chain reaction inhibitor,[33] cryoprotectant,[34] and in veterinary medicine.[35] The biocompatibility of DMSO is largely due to the presence of the polar aprotic methyl sulfoxide group.[32] Inspired by these unique properties of DMSO, we aimed to synthesize a polymeric analogue of DMSO by ATRP that possesses similar properties of high water-solubility and low cytotoxicity, in addition to the absence of a LCST.[36-38] In this paper, the polymeric analogue of DMSO was prepared by oxidation of well-defined poly(2-(methylthio)ethyl acrylate) (polyMTEA) and also directly from the sulfoxide containing monomer, 2-(methylsulfinyl)ethyl acrylate (MSEA), formed via oxidation of MTEA. Well-defined linear polyMSEA with low dispersity (<1.3) was synthesized by ARGET ATRP in the presence of 100 ppm copper catalyst. In addition, two well-defined star polymers[39, 40] were prepared, one using a "core-first" approach with a biodegradable β-cyclodextrin core and the other one by an "arm-first" approach with divinyl benzene as crosslinker. The LCST of pure polyMSEA, ca. 140 ^{o}C, was estimated from the solution aggregation points of copolymers of MSEA and NIPAM with different compositions. The

cytotoxicity of neutral water-soluble linear and star-shaped polyMSEAs was evaluated using human embryonic kidney cells (HEK 293) at concentrations up to 3 mg/mL. This new family of biomacromolecules could potentially be replacement of established PEGylation approach in a wide range of biological applications.

A.3. Results and discussion

The synthetic route for MSEA is shown in Scheme 10. The monomer 2-(methylthio)ethyl acrylate (MTEA) was synthesized by an EDC catalyzed esterification procedure detailed in the previous work.[31] The sulfoxide containing monomer 2-(methylsulfinyl)ethyl acrylate (MSEA) was then prepared by oxidation with 1.1 equiv. of hydrogen peroxide in an aqueous solution. The hydrogen peroxide solution was injected into MTEA (liquid state) at feed rate of 50 μL/min in order to avoid potential side reactions caused by heat release. The oxidization was complete and no further oxidation to sulfone occurred, as confirmed by the absence of the NMR peaks of methine protons next to a sulfone group at ~3.6 ppm.[41]

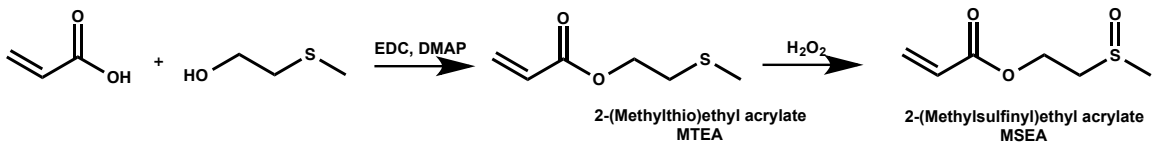

Scheme 10. Synthesis of MTEA and MSEA monomers

The ^{1}H NMR spectrum of MSEA in DMSO-d_6 is shown in Figure 89. The peak integration ratio of **a**/**b**/**a'**/**c**/**d**/**e** equals 1.00/0.98/1.01/2.04/2.06/3.02 confirming the high purity of the synthesized monomer. The **c** protons and **d** protons split into two peaks due to two prochiral carbons next to a chiral sulfur atom. The peak splitting of **c** protons is less pronounced as they are farther from the chiral sulfur than the **d** protons. The DMSO-d_6 peak is located at 2.5 ppm and is negligible due to high concentration of the compound.

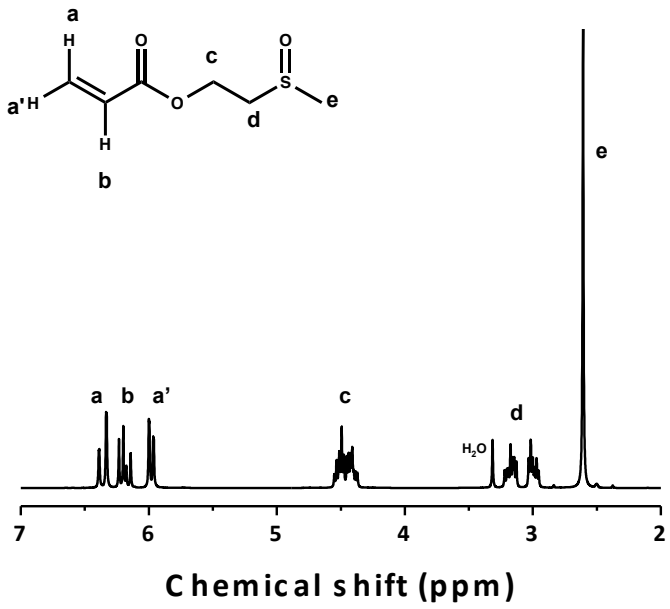

Figure 89. ^{1}H NMR spectrum of MSEA.

Free radical polymerization (FRP) of MSEA was previously reported.[42, 43] Herein, MSEA was polymerized by ATRP using relatively low amounts of copper (1,000 or 100 ppm). The ATRP rate depends on the relative ratio of [Cu^{I}-L]/[X-Cu^{II}-L], rather than the absolute amount of copper species (Equation 1). [44]

$$R_{\mathrm{p}} = k_{\mathrm{p}}[\mathrm{M}][\mathrm{P}_{\mathrm{n}}^{*}] = k_{\mathrm{p}}K_{\mathrm{ATRP}}\left(\frac{[\mathrm{P_nX}][\mathrm{Cu^I{-}L}][\mathrm{M}]}{[\mathrm{X{-}Cu^{II}{-}L}]}\right) \quad (1)$$

In the polymerization with 1,000 ppm Cu^{II}, the reducing agent was added at the beginning of the polymerization (following the AGET procedure),[45] whereas in the reaction with 100 ppm Cu^{II}, the reducing agent was added slowly over 5 h to ensure that some Cu^{II} deactivator complex was present throughout the polymerization (ARGET ATRP).[18] The semilogarithmic plot for ARGET system indicated the steady concentration of active centers during the polymerizations but in AGET some deviation was observed, Figure 90a.[46]

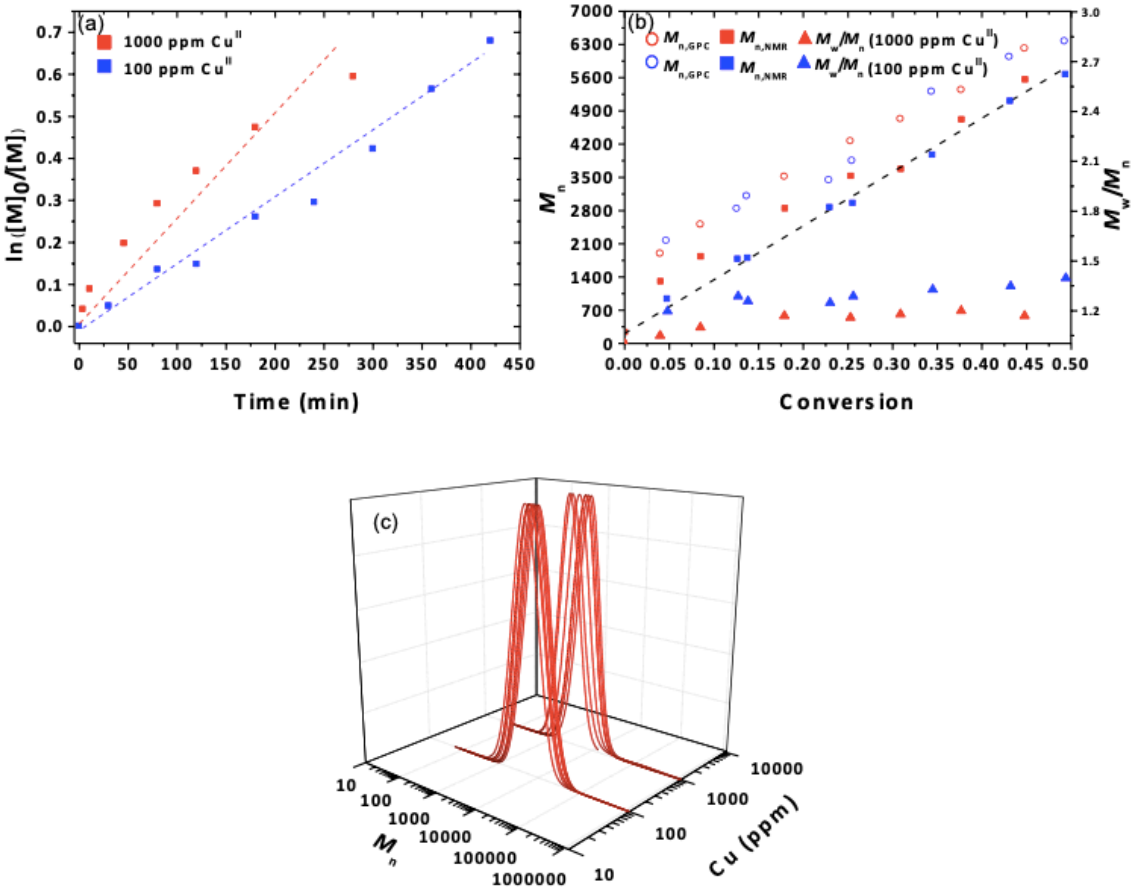

Figure 90. (a) Kinetic plots of ln([M]0/[M]) vs time, (b) plots of M_n and M_w/M_n vs conversion and (c) GPC trace for ATRP of MSEA. AGET conditions: $[MSEA]_0/[EBiB]_0/[CuBr_2]_0/[TPMA]_0/[AA]_0$ = 70/1/0.07/0.15/0.7, 35 ºC. ARGET conditions: $[MSEA]_0$/ $[EBiB]_0/[CuCl_2]_0/[TPMA]_0/[AA]_0$ = 70/1/0.007/0.015/0.14 (AA added over 5 h), 35 ºC. (AA: ascorbic acid)

The M_n values estimated from GPC based on linear PMMA standards were slightly higher than the theoretical values, which could be due to either incomplete initiation or the difference in hydrodynamic volume between the GPC calibration standards (PMMA) and polyMSEA, Figure 90b. GPC traces exhibited a symmetrical narrow Gaussian distribution throughout the polymerization Figure 90c. M_n values were also calculated from ^{1}H NMR for each kinetic point,

according to Equation 2, where $\delta_{5.99}$ represents the integration area of one of the vinyl hydrogen atoms, $\delta_{4.52}$ represents the integration area of methylene peaks next to the ester group in monomer and polymer and $\delta_{1.16}$ represents the integration area of methyl groups of EBiB. Figure 91a. M_{MSEA} is the molar mass of monomer MSEA, M_{EBiB} is the molar mass of initiator EBiB.

$$M_{\mathrm{n,NMR}} = \frac{3\times(\frac{\delta_{4.52}}{2}-\delta_{5.99})}{\delta_{1.16}} \times M_{\mathrm{MSEA}} + M_{\mathrm{EBiB}} \qquad (2)$$

The good agreement between the theoretical values and the $M_{\mathrm{n,NMR}}$ in Figure 90b indicated efficient initiation. In Figure 91b, the chain-end functionality was observed for an isolated polyMSEA sample prepared by AGET ATRP with 1,000 ppm Cu^{II} . The sample was collected at 35% conversion with $M_{\mathrm{n,\ NMR}}$ of 4,000 and $M_{\mathrm{w}}/M_{\mathrm{n}}$ of 1.20. Peak **a** exhibited a triplet shape associated with a quartet-like **c**. Peak **d** split into doublet-like shape due to the chirality of the sulfoxide groups and polymer tacticity. The ratio of integration areas of **a/d** (1.00/0.27) was close to 3/1, indicating a good preservation of the chain-end functionality. The dispersity of the polymer prepared with 1,000 ppm Cu^{II} reaction remained well below 1.2 during the polymerization, while the dispersity of the polymer prepared with 100 ppm Cu^{II} reaction was higher, 1.25 at 13.7% conversion, 1.32 at 34.4% conversion and 1.34 at 43.1% conversion, Figure 90b. The increased dispersity can be attributed to the presence of a lower amount of deactivator (Cu^{II}). As shown in Equation 3, a decrease of [X-Cu^{II}-L] can increase the value of M_w/M_n.

$$\frac{M_{\mathrm{w}}}{M_{\mathrm{n}}} = 1 + \frac{1}{\mathrm{DP_n}} + \left(\frac{k_{\mathrm{p}}[\mathrm{P_nX}]}{k_{\mathrm{deact}}[\mathrm{X-Cu^{II}-L}]}\right)\left(\frac{2}{\mathrm{p}} - 1\right) \qquad (3)$$

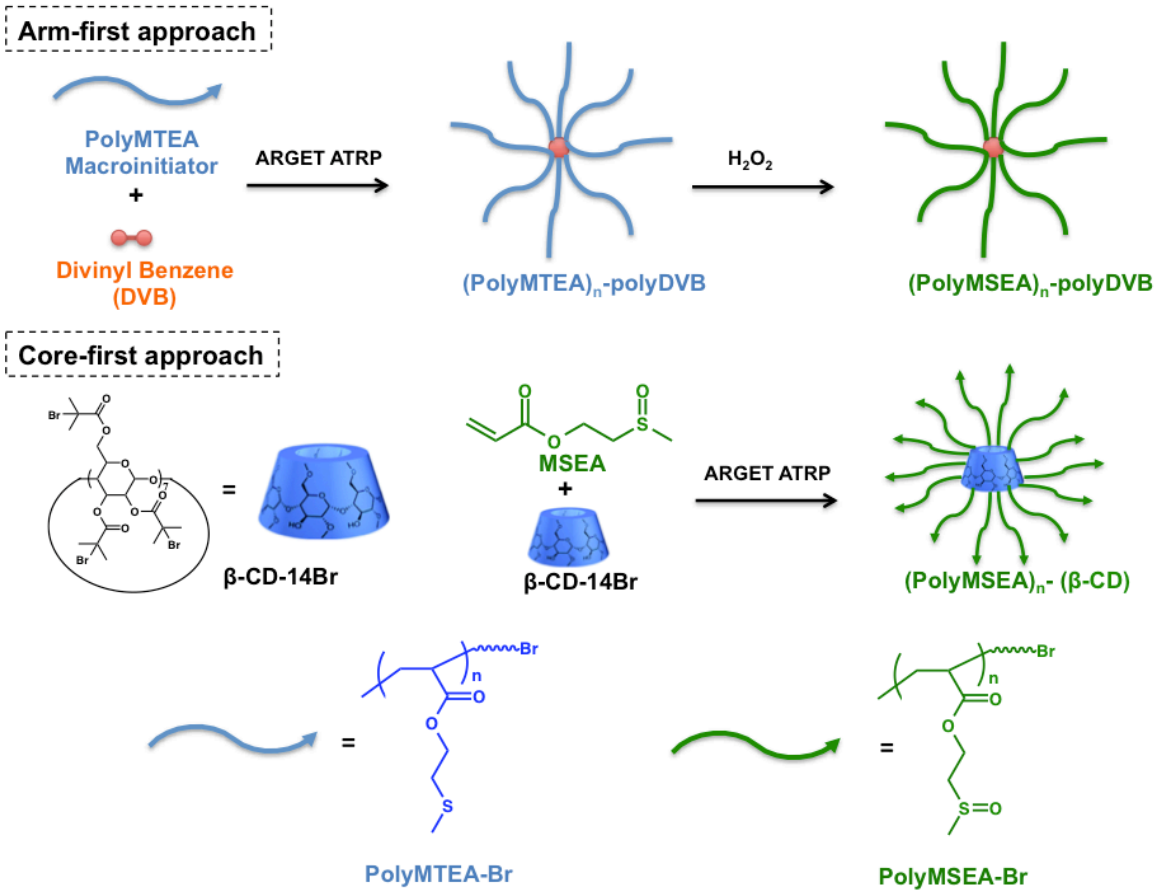

Scheme 11. Synthesis of star polymer (polyMSEA)$_n$-polyDVB by the "arm-first" approach and (polyMSEA)$_n$-(β-CD) by the "core-first" approach.

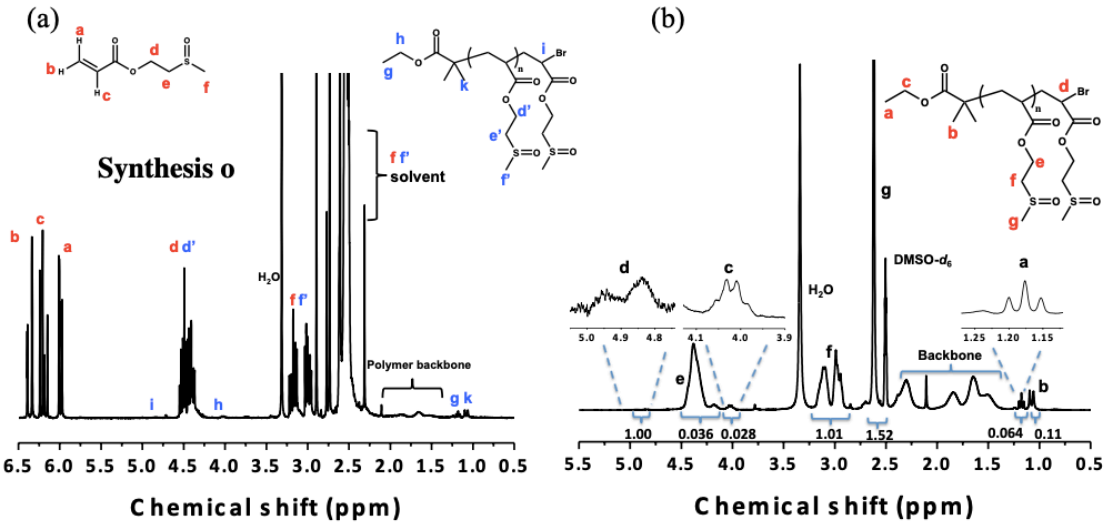

Figure 91. Example of ^{1}H NMR spectrum for calculation of $M_{n,NMR}$. (Samples collected during polymerization by syringe and diluted in DMSO-d_6) (a) and ^{1}H NMR spectrum of an isolated polyMSEA with a preserved chain-end functionality (b).

Synthesis of star polymer. Two types of sulfoxide-containing star polymers (polyMSEA)$_n$-polyDVB and (polyMSEA)$_n$-(β-CD) were synthesized by "arm-first" approach and "core-first" approach, respectively. The synthetic routes are shown in Scheme 11.

In the "arm-first" the polyMTEA macromonomer was synthesized by ARGET ATRP in acetone, according to previous work.[31] The kinetic plots are shown in Figure 98. A polyMTEA polymer with M_n = 2,900 and dispersity of 1.24 was used as the macroinitiator for the synthesis of a sulfide-containing star polymer (polyMTEA)$_n$-polyDVB. The (polyMTEA)$_n$-polyDVB was prepared by ARGET ATRP with Sn(EH)$_2$ as reducing agent and divinyl benzene (DVB) as crosslinker.[47]

As shown in Figure 99, the macroinitiator peak gradually decreased over time as the polymerization proceeded, and a new peak at higher molecular weight gradually formed and shifted to the region of higher molecular weights. The reaction was stopped at conversion 91.4%

and the star polymer was purified by precipitation and dialysis. The purified $(polyMTEA)_n$-polyDVB star polymer showed a unimodal peak with a molecular weight of M_n = 10,200 according to calibration with linear PMMA standards and M_n = 30,500 as measured by static light scattering method, Figure 92.

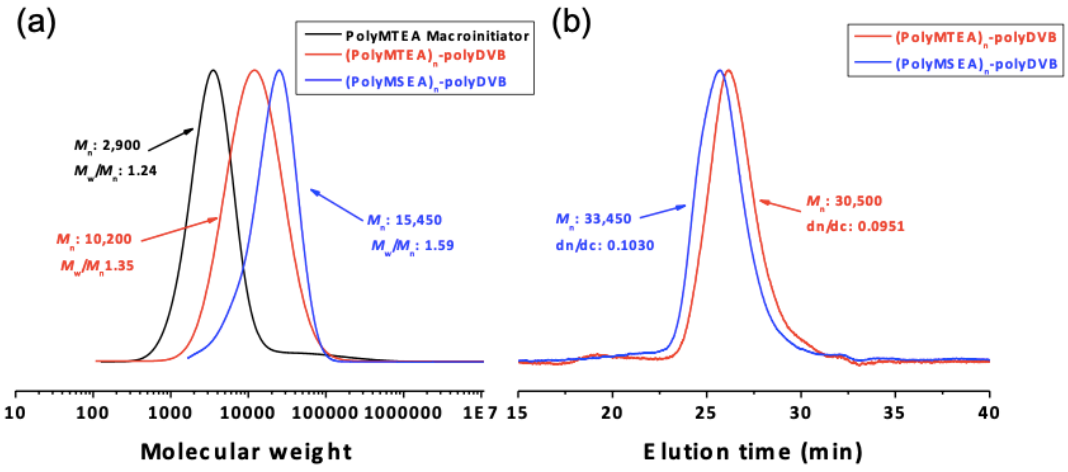

Figure 92. (a) dRI GPC traces of macroinitiator polyMTEA, $(polyMTEA)_n$-polyDVB and $(polyMSEA)_n$-polyDVB and (b) static light scattering traces of $(polyMTEA)_n$-polyDVB and $(polyMSEA)_n$-polyDVB.

The $(polyMSEA)_n$-polyDVB star polymer was synthesized by post-oxidation of the $(polyMTEA)_n$-polyDVB star with hydrogen peroxide solution and purified by dialysis. The oxidization was complete and no further oxidation to sulfone occurred as shown in the ^{1}H NMR spectra, Figure 100.[41] The $(polyMSEA)_n$-polyDVB had $M_{n,GPC}$ = 15,450 and $M_{n,LS}$ = 33,450 and narrow molecular weight distribution. The GPC values, based on the hydrodynamic volume, are smaller due to the compact structure of star-like polymers. Thus, static light scattering method provides more accurate values. Post-oxidation approach was used here due to better initiating efficiency of a polyMTEA macroinitiator than a polyMSEA macoinitiator.

A polymer that will be used for biomedical applications, such as a drug delivery carrier, should be biodegradable to assure renal clearance after delivery. β-Cyclodextrin (β-CD) is a highly water soluble biocompatible biodegradable multifunctional molecule.[48] Moreover, the hydrophobic cavity of cyclodextrin and its unique host-guest effect make it a good platform for hydrophobic drug delivery.[49] In order to prepare a star polymer with β-CD as a core, a β-CD ATRP macroinitiator with 14 attached bromoisobutyrate sites was synthesized, Figure 101,[50] by esterification of accessible hydroxyl groups. MSEA was grafted directly from the macroinitiator in a "core-first" manner by ARGET ATRP. The $M_{n,GPC}$ =29,240 (M_w/M_n =1.06) of final polymer $(polyMSEA)_n$-(β-CD) at conversion of 38.5% was measured by GPC with PMMA standards and $M_{n,LS}$ =46,300 by static light scattering method (M_w/M_n 1.09), Figure 93 and Figure 94.

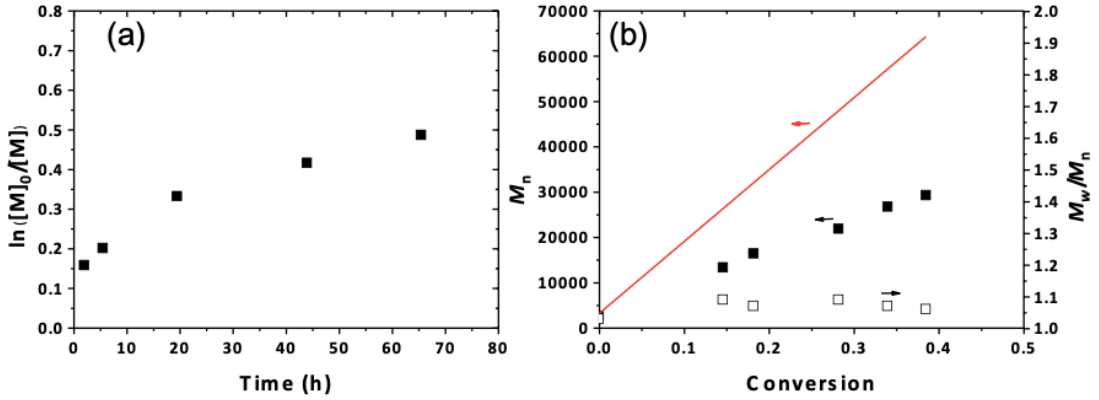

Figure 93. Synthesis of star polymer with β-cyclodextrin core. Kinetic plot of $\ln([M]_0/[M])$ vs time (a), plots of M_n and (b) M_w/M_n vs conversion. (Red curve: theoretical M_n, black square: M_n by GPC, open square: M_w/M_n by GPC.)

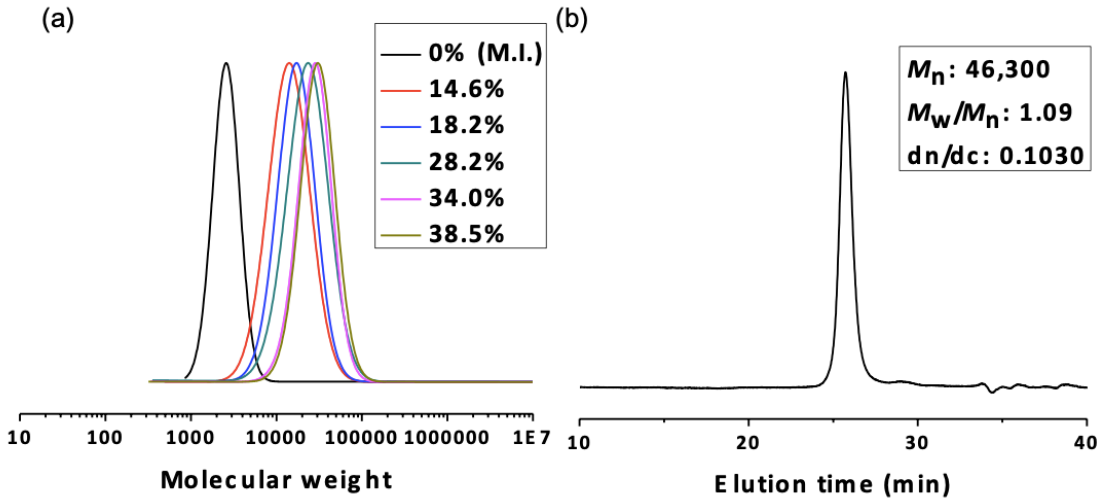

Figure 94. (a) GPC traces for ARGET ATRP of MSEA from β-CD macro-initiator and (b) static light scattering trace of the same sample at conversion of 38.5%.

As shown in Figure 102, the β-CD macroinitiator could be degraded in 5 wt% NaOH aqueous solution, 10 mg/mL, overnight. After degradation, molecular weight of sample at ~3,000 shifted to oligomer peaks at ~270. To demonstrate the biodegradability of the as synthesized star polymer $(polyMSEA)_n$-(β-CD), a polymer was prepared under the same conditions with conversion of 26.8%, $M_{n,GPC}$ = 23,800 and M_w/M_n = 1.05. The sample was treated with 5 wt% NaOH aqueous solution overnight (10 mg/mL). After degradation, the original star peak shifted to $M_{n,GPC}$ = 2,300 with dispersity M_w/M_n = 1.03, a size small enough for removal from the bloodstream, Figure 95.[51] Therefore, such a high molecular weight biodegradable star-like structure, with low molecular weight side-arms, can be tested for drug delivery applications, especially for delivery of small hydrophobic drugs.[49]

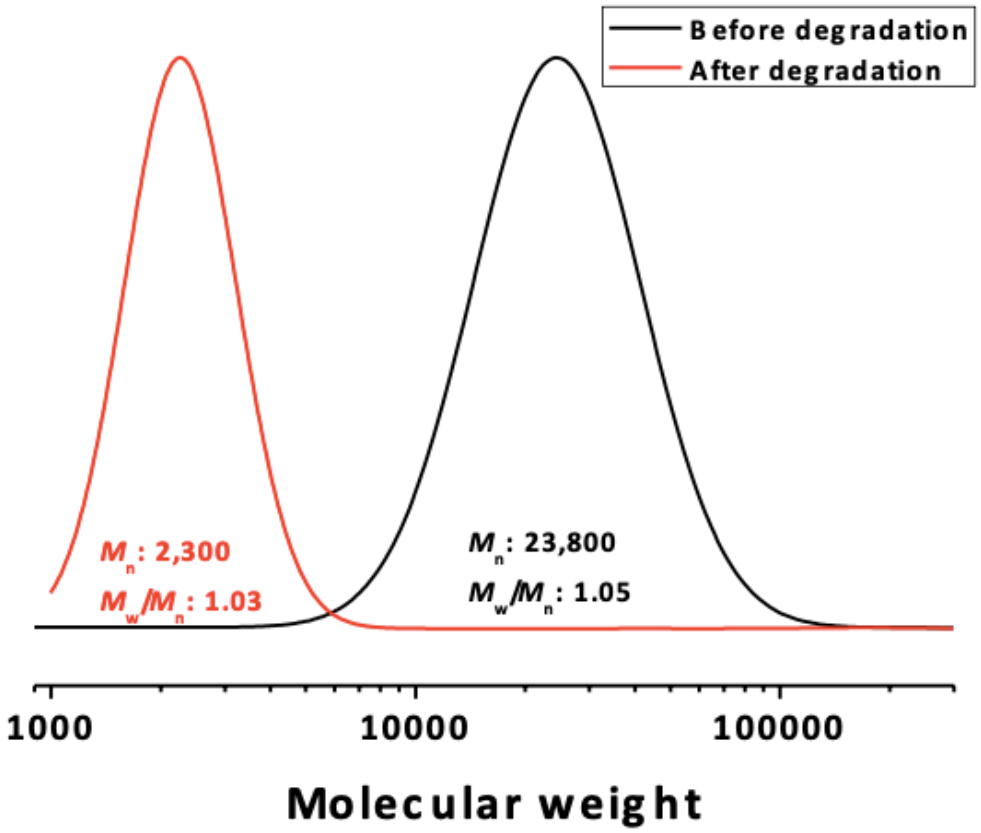

Figure 95. GPC traces of (polyMSEA)$_n$-(β-CD) before and after degradation by 5 wt% NaOH aqueous solution.

The glass transition temperature (T_g) was investigated by differential scanning calorimetry (DSC). The (polyMSEA)$_n$-polyDVB with M_n = 33,450 (M_w/M_n = 1.59) had a T_g = 31.5 °C while a linear polyMSEA with M_n = 5,200 (M_w/M_n = 1.18) had T_g = 15.7 °C, Figure 103.

Water-solubility and biocompatibility. Many biocompatible polymers, such as PEG, POZ, polyacrylamides, and polyOEGMA exhibit lower critical solution temperature (LCST) behavior. The LCST could be advantageous for drug delivery, but it may decrease solubility in water, especially at elevated temperature. A more hydrophobic polymer can be attached to opsonins, leading to early bloodstream removal. Therefore, to evaluate the water-solubility and

hydrophobicity of polyMSEA, its solution behavior was studied at different temperatures. Dynamic light scattering (DLS) was used in the temperature range of 25~92 °C. Since DLS analysis of pure polyMSEA showed no aggregation within the investigated temperature range, Figure 96a, the LCST of copolymers with variable composition were used and the LCST of polyMSEA was estimated via extrapolation to pure polyMSEA. Thus, free radical copolymerization of NIPAM and MSEA was carried out at different molar ratios of comonomers. DLS traces for polyMSEA-co-polyNIPAM copolymers with different fractions of MSEA are presented in Figure 104 ~ Figure 106.

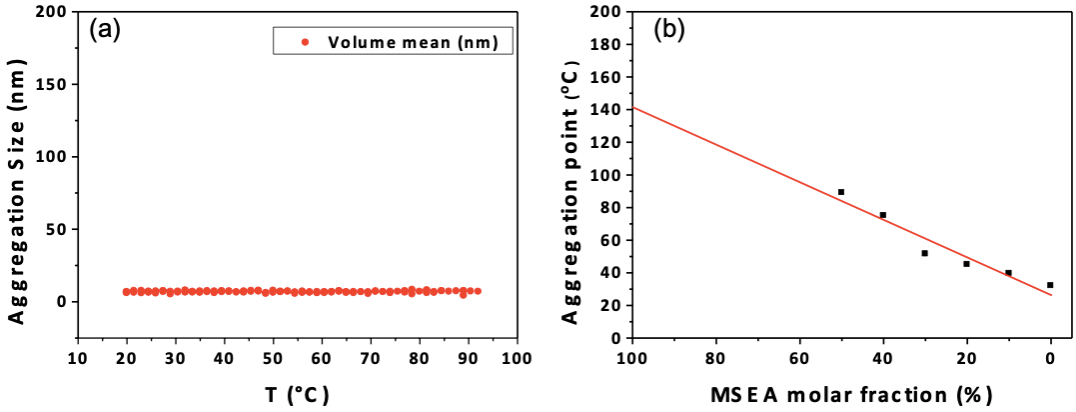

Figure 96. (a) DLS data of polyMSEA in water from 25 °C to 92 °C and (b) LCST of polyMSEA-co-polyNIPAM copolymers with different composition red curve: linear fitting with extrapolation to 100% polyMSEA.

As shown in Figure 96b, as the fraction of MSEA increased, the LCST of the copolymer also increased. By extrapolating the observed LCST of the copolymers to a composition of 100% polyMSEA, its LCST was estimated to be ~140 °C. This suggests that a neutral water-soluble polyMSEA should not have solubility limitations when utilized in bio-related applications. As an indication of direct solubility, 359 mg of polyMSEA with M_n of 14,400 was fully dissolved in 1 mL deionized water at room temperature, which equals the solubility of NaCl in water at the same temperature, Figure 107.

In addition, reactivity ratios of MSEA (monomer 1) vs NIPAM (monomer 2) were determined by Kelen-Tüdös method: r_1=1.24 and r_2=0.42,[52, 53] Figure 104 and Figure 105. Therefore, the samples prepared for LCST extrapolation are not pure random copolymers and can have some composition drift. The reactivity ratio of MSEA in copolymerization with three other acrylic monomers methyl acrylate, n-butyl acrylate and oligo(ethylene glycol) methyl ether acrylate ($OEGA_{480}$) were also calculated by the Kelen-Tüdös method with the values of r_1/r_2 as 0.49/1.01, 0.49/0.83, and 0.77/0.33, respectively, Figure 108 and Figure 109.

Finally, a cytotoxicity, of polyMSEA was examined by cell viability assessments using human embryonic kidney cells (HEK 293).[54] HEK 293 cells were grown in a 96 well tissue culture plate at a density of 10,000 cells/well for 24 hours. The monomer MSEA, linear polyMSEA (M_n= 14,400, M_w/M_n= 1.40) and star polymer $(polyMSEA)_n$-polyDVB (M_n = 33,450, M_w/M_n = 1.59) were dissolved in PBS at a concentration of 100 mg/mL and added to the tissue culture plate at different amounts. After 48 h, an ATP Cell Titer Glo® Assay was used and luminescence was measured and quantified as a percentage of the control wells. As shown in Figure 97, both linear polyMSEA and $(polyMSEA)_n$-polyDVB star showed no toxicity, even at concentrations up to 3 mg/mL in comparison to the control group, the only cell without extra addition of chemicals. This result proved that polymeric analogues of DMSO prepared by ATRP possess a low cytotoxicity, similar to their monomeric counterpart: DMSO. However, the cell viability decreased by 90% for the monomer MSEA at concentration of only 0.1 mg/mL. Such high toxicity of MSEA is expected and should be due to the presence of reactive acrylate groups that can react with amine groups or thiol groups in the cell environment.[55]

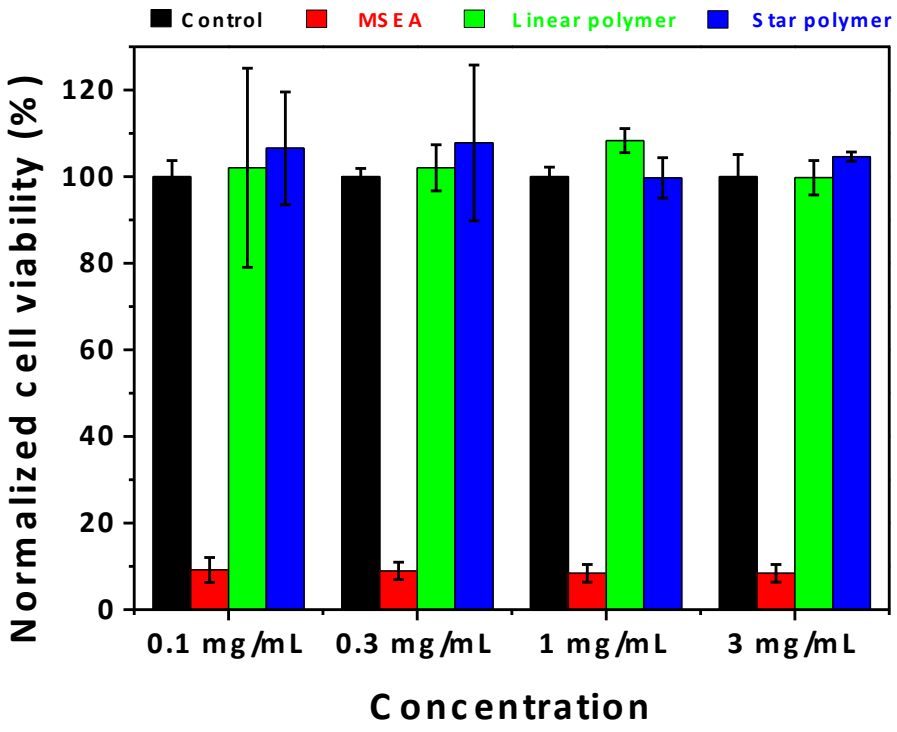

Figure 97. HEK 293 Cell toxicity of linear polyMSEA (M_n = 14,400, M_w/M_n = 1.40), star polymer $(polyMSEA)_n$-polyDVB (M_n = 33,450, M_w/M_n = 1.59) and monomer MSEA.

In future work, the polymer will be evaluated for preparation of therapeutic protein-polymer conjugates, use in gene knockdown therapy, and other applications requiring water-soluble biocompatible polymeric materials. The immunogenicity of the polyMSEA-based bio-hybrids will also be examined.

A.4. Conclusion

In conclusion, the well-defined biocompatible polymeric analogues of DMSO, based on a sulfoxide-containing monomer 2-(methylsulfinyl)ethyl acrylate (MSEA), was prepared by ATRP. Well-defined star polymers were synthesized by two approaches, an "arm-first" approach with DVB as crosslinker and a "core-first" approach with a biodegradable β-cyclodextrin core. LCST of polyMSEA ca. 140 °C was estimated from NIPAM copolymers by extrapolation to pure

polyMSEA. Both linear polyMSEAs and star polymers, (polyMSEA)$_n$-polyDVB, showed no cytotoxicity towards human embryonic kidney cells (HEK 293). Therefore, this polymer analogue of DMSO combines a set of following advantages: 1) straightforward synthesis from commercially available starting materials, 2) facile attachment onto a variety of biologically functional compounds/substrates, 3) low steric hindrance, high water-solubility and low cytotoxicity. This work represents a successful example of reinventing polymeric biomaterials from small molecule counterparts. We believe this new family of biomacromolecules could become highly important in the near future and potentially replace established polymers like PEG, polyOEGMA, polyNIPAM in a wide range of applications.

A.5. Experimental and supporting information

Materials. 2-(Methylthio)ethanol (≥99%) was purchased from Alfa Aesar. Hydrogen peroxide solution (30%) was purchased from Fisher Scientific. Acrylic acid (≥99%), tin(II) 2-ethylhexanoate ($Sn^{II}(EH)_2$, ≥95%), methyl acrylate (≥99%), n-butyl acrylate (≥99%), poly(ethylene glycol) methyl ether acrylate (OEGA, average M_n = 480), N-(3-dimethylaminopropyl)-N'-ethylcarbodiimide hydrochloride (EDC, ≥99%), N,N-dimethylamino pyridine (DMAP, ≥99%), copper bromide (≥99.99%), ascorbic acid, (AA, ≥99%), divinyl benzene (DVB, technical grade, 80%), ethyl α-bromoisobutyrate (EBiB, 98%) were purchased from Sigma Aldrich. Acrylic acid was distilled under vacuum before use. All acrylate monomers were passed through basic alumina columns before use. Tris(2-pyridylmethyl)amine (TPMA) was synthesized according to previous procedures.[56] All solvents and other chemicals are of reagent quality and were used as received unless special treatments discussed below were applied.

Instrumentation. ^{1}H nuclear magnetic resonance (^{1}H NMR) measurements were performed on a Bruker Avance 300 MHz spectrometer. Molecular weight and molecular weight distribution (M_w/M_n) were determined by a combination of gel permeation chromatography and multi-angle light scattering (GPC-MALS). The GPC-MALS used a Waters 515 HPLC pump, Wyatt Optilab refractive index detector, Wyatt DAWN HELEOS-II multi-angle light scattering detector and PSS columns (Styrogel 10^2, 10^3, and 10^5 Å) with either 40 °C pure THF or 50 °C 50 mM LiBr DMF solution as eluent phase at flow rate of 1 mL/min. Differential scanning calorimetry (DSC) was performed on a TA Instrument QA-2000 for three times each sample, involving the following steps: 1) hold at -80 °C for 2 min; 2) heat to 130 °C at rate of 10 °C/min, 3) hold for 2 min; 4) cool down to -80 °C. Temperature-dependent dynamic light scattering (DLS) was performed on a Malvern Zetasizer Nano ZS.

Synthesis of 2-(methylsulfinyl)ethyl acrylate (MSEA). 2-(Methylthio)ethyl acrylate (MTEA) was synthesized according to the previously reported procedure.[31] In a typical oxidation procedure, 5 g MTEA (1 equiv.) was added to a 25 mL round bottom flask sealed with rubber stopper. The flask was kept in an ice bath and purged with N_2 then 3.77 g hydrogen peroxide solution (1.1 equiv.) was slowly injected into the flask at rate of 50 μL/min. The reaction was allowed to stir for 24 h and was then stopped by adding 50 mL deionized water. The aqueous solution was washed 3 times with 100 mL dichloromethane. The organic phase was collected and dried over magnesium sulfate. Excess solvent was removed under vacuum to give 4.5 g pure product of MSEA (yield 81.2%). ^{1}H NMR (300 MHz, DMSO-d_6): δ (ppm) = 6.38 (1H, dd, CH*H*═CH), 6.19 (1H, q, CHH═C*H*), 5.98 (1H, dd, C*H*H═CH), 4.49 (2H, m, C═OOC*H*$_2$CH$_2$), 3.15 (1H, m, CH$_2$CH*H*S═O), 2.99 (1H, m, CH$_2$C*H*HS═O), 2.60 (3H, s, S═OC*H*$_3$).

Synthesis of linear polyMSEA. The polymerization of MSEA was carried out using A(R)GET ATRP. In a typical AGET procedure, 8.6 mg EBiB (1 equiv.), 0.5 g MTEA (70 equiv.) 0.69 mg copper (II) bromide (0.07 equiv.), 1.9 mg TPMA (0.15 equiv.), 0.1 mL DMF and 2.9 mL DMSO were mixed in a sealed 10 mL Schlenk flask equipped with a stirring bar. The Schlenk flask was degassed by three freeze-pump-thaw cycles. The flask was allowed to warm up to room temperature and placed in an oil bath thermostated at 35 °C. Deoxygenated ascorbic acid (AA) solution (5.4 mg in 0.1 mL DMSO) was injected into the flask under N_2 purge to trigger the polymerization, and an initial sample (t = 0) was collected by syringe. Samples were taken periodically to measure conversion via ^{1}H NMR and molecular weight via GPC. The polymer was precipitated in ether, purified by dialysis (MWCO = 100~500 Da) against water, and dried by lyophilization. In a typical ARGET procedure, 8.6 mg EBiB (1 equiv.), 0.5 g MTEA (70 equiv.) 0.04 mg copper (II) chloride (0.007 equiv.), 0.2 mg TPMA (0.015 equiv.), 0.1 mL DMF and 2.9 mL DMSO were mixed in a sealed 10 mL Schlenk flask equipped with a stirring bar. The Schlenk flask was degassed by three freeze-pump-thaw cycles. The flask was allowed to warm up to room temperature and placed in an oil bath thermostated at 35 °C. Deoxygenated ascorbic acid (AA) solution (1.1 mg in 0.1 mL DMSO) was injected into the flask under N_2 purge intermittently over 5 hr, and an initial sample (t = 0) was collected by syringe. Samples were taken periodically to measure conversion via ^{1}H NMR and molecular weight via GPC.

Measurement of reactivity ratios. The reactivity ratio measurements were carried out according to the Kelen-Tüdös approach.[52, 53] For the MSEA/MA pair (monomer 1: MSEA, monomer 2: MA), four ARGET ATRP reactions were conducted with the ratio of reagents $[MSEA]_0/[MA]_0/[EBiB]_0/[AA]_0/[Cu_2Br]_0/[TPMA]_0$ = x/(70-x)/1/0.7/0.07/0.15 in DMSO at the same concentration (1 M of all monomers), x = 60, 45, 25, 10. For the MSEA/*n*BA pair (monomer

1: MSEA, monomer 2: *n*BA), four ARGET ATRP reactions were conducted with $[MSEA]_0/[nBA]_0/[EBiB]_0/[AA]_0/[Cu_2Br]_0/[TPMA]_0$ = x/(70-x)/1/0.7/0.07/0.15 in DMSO at the same concentrations as the above example, x = 60, 45, 35, 10. For the MSEA/OEGA pair (monomer 1: MSEA, monomer 2: OEGA), four different ratios of $[MSEA]_0/[OEGA]_0/[EBiB]_0/[AA]_0/[Cu_2Br]_0/[TPMA]_0$ = x/(70-x)/1/0.7/0.07/0.15 in DMSO were carried out under the same concentrations as the above example, x = 60, 45, 35, 10. For the MSEA/NIPAM pair (monomer 1: MSEA, monomer 2: NIPAM), four different ratios of $[MSEA]_0/[NIPAM]_0/[EBiB]_0/[AA]_0/[Cu_2Br]_0/[TPMA]_0$ = x/(70-x)/1/0.7/0.07/0.15 in DMSO were carried out under the same concentrations as the above example, x = 60, 45, 35, 25). The conversion of monomers was measured by ^{1}H NMR. All reactions were stopped within 15 min to keep conversion low.

Synthesis of star polymer (polyMSEA)$_n$-polyDVB by "arm-first" approach.

The polyMTEA macroinitiators were synthesized by ARGET ATRP. In a typical procedure, 0.222 g EBiB (1 equiv.), 10 g MTEA (60 equiv.) 17.8 mg $CuBr_2$ (0.07 equiv.), 49.7 mg TPMA (0.15 equiv.) were mixed in a solution of 11 mL acetone and 0.5 mL DMF in a sealed 50 mL Schlenk flask equipped with a stirring bar. The Schlenk flask was degassed by three freeze-pump-thaw cycles. The flask was allowed to warm up to room temperature and placed in an oil bath thermostated at 35 °C. Deoxygenated ascorbic acid (AA) solution (140 mg in 0.5 mL DMF) was injected into the flask under a N_2 purge to activate the polymerization, and an initial sample (t = 0) was collected by syringe. Samples were taken periodically to measure conversion via ^{1}H NMR and molecular weight via GPC. The polymer with M_n = 3000 was isolated by precipitation in methanol and dried under vacuum.

The polysulfide star $(polyMTEA)_n$-polyDVB was synthesized by ARGET ATRP using the aforementioned polyMTEA-Br as macroinitiator. In a typical procedure, 470 mg polyMTEA-Br (1 equiv.), 222 mg DVB (14 equiv.), 0.16 mg $CuBr_2$ (0.01 equiv.) and 3.5 mg TPMA (0.1 equiv.) were mixed in a solution of 4.5 mL anisole and 0.1 mL DMF in a sealed 10 mL Schlenk flask equipped with a stirring bar. The Schlenk flask was degassed by three freeze-pump-thaw cycles. The flask was allowed to warm up to room temperature and then placed in an oil bath thermostated at 90 °C. A deoxygenated solution of 9.9 mg $Sn(EH)_2$ in 0.5 mL anisole was injected into the flask under N_2 purge to reduce the cupric complex and trigger the polymerization, and an initial sample (t = 0) was collected by syringe. Samples were taken periodically to measure conversion via ^1H NMR and molecular weight via GPC-MALS. The final polymer was isolated by precipitation in ether to remove non-polymerized DVB and purified by dialysis (MWCO = 10,000 Da) against THF and dried under vacuum.

The polysulfoxide star, $(polyMSEA)_n$-polyDVB, was synthesized by post-oxidation. In a typical procedure, 0.1514 g $(polyMTEA)_n$-polyDVB (1 equiv. per MSEA repeating unit) was dissolved in 1 mL deoxygenated THF in a sealed 10 mL round-bottom flask equipped with a stirring bar. 121.3 mg hydrogen peroxide solution (1.3 equiv.) was slowly injected at rate of 50 μL/min and allowed to react for 72 h then the product was precipitated by addition of the solution to 10 mL THF and purified by dialysis (MWCO = 10,000 Da) against deionized water and dried under vacuum to give pure $(polyMSEA)_n$-polyDVB. The molecular weight of star polymers was analyzed by GPC-MALS.

Synthesis of β-CD-14Br ATRP initiator. The synthesis of macroinitiator was synthesized according to previous report.[50] In a typical procedure, 10 g of β-cyclodextrin (β-CD, 8.81 mmol) was dried under vacuum overnight and placed in 250 mL round bottom flask. The β-CD was

dissolved in 100 mL of anhydrous 1-methyl-2-pyrrolidone (NMP) and the flask was placed in an ice bath. 2-Bromoisobutyryl bromide (BriBBr) (27 mL, 1.2 eq. to –OH) was dissolved in anhydrous NMP (50 mL) and slowly added to the β-CD solution. The solution temperature was allowed to warm up to room temperature and the reaction was stirred for 1 day. The dark brown solution was dialyzed against distilled water (MWCO = 500) for 1 week. The remaining product was concentrated at reduced pressure and crystallized in cold hexane to obtain a pale yellow solid product. The ^{1}H NMR spectrum of the macroinitiator in $CDCl_3$ is shown in Figure 102. The peak at ~ 2.0 ppm was from the solvent of NMP and the methyl groups on the bromo initiator sites. The functionality was calculated by equation: $\delta_{\text{ini.}}/(\delta_{\text{H1}} \times 3 \times 7)$. The functionality of the macroinitiator corresponded to 14 initiator sites per β-CD molecule with a purity of 95%.

Synthesis of star polymer (polyMSEA)$_n$-(β-CD) by "core-first" approach. The "grafting from" polymerization of MSEA was carried out using ARGET ATRP. In a typical procedure, 10 mg β-CD macro-initiator (1 equiv.), 0.5 g MSEA (70 equiv.) 1.38 mg copper (II) bromide (0.14 equiv.), 6.4 mg TPMA (0.5 equiv.), 3 mL DMF were mixed in a sealed 10 mL Schlenk flask equipped with a stirring bar. The Schlenk flask was degassed by three freeze-pump-thaw cycles. The flask was allowed to warm up to room temperature. Deoxygenated ascorbic acid (AA) solution (5.4 mg in 0.1 mL DMF) was injected into the flask under N_2 purge to trigger the polymerization, and an initial sample (t = 0) was collected by syringe. Samples were taken periodically to measure conversion via ^{1}H NMR and molecular weight via GPC MALS.

Determination of the LCST of polyMSEA. The polymers for LCST determination were prepared by copolymerizing different ratios of MSEA with N-isopropylacrylamide (NIPAM) by free radical polymerization (FRP). In a typical procedure, 100 mg MSEA (12 equiv.), 104.7 mg NIPAM (18 equiv.) and 8.53 mg AIBN (1 equiv.) were dissolved in 2 mL DMF in a 10 mL Schlenk

flask equipped with a stirring bar. The flask was sealed and degassed by three freeze-pump-thaw cycles. The flask was allowed to warm up to room temperature and placed in an oil bath thermostated at 70 °C. All reactions were allowed to reach ca. 99% conversion and the copolymers were precipitated by addition of the reaction mixture to ether. The final product was collected and dried in vacuum oven overnight. For DLS analysis, 30 mg of the as-dried copolymer was dissolved in 3 mL deionized water and passed through a 0.2 micron PTFE filter before tests.

Cytotoxicity test. Human Embryonic Kidney Cells (HEK 293) were grown in a 96 well tissue culture plate at a density of 10,000 cells/well for 24 hours. 100 mg/mL solutions of the linear polyMSEA and $(polyMSEA)_n$-polyDVB were prepared by mixing with 1x PBS which was then added to the tissue culture plate at concentrations of 10 μg, 30 μ, 100 μg, and 300 μg. All concentrations were tested in triplicate. The polymer was then incubated with the HEK 293 cells for 48 hours at 37°C in the presence of 5% CO_2. After 48 hours, ATP Cell Titer Glo® Assay was used and luminescence was measured and quantitated as a percentage of the control wells.

Synthesis of Star Polymer

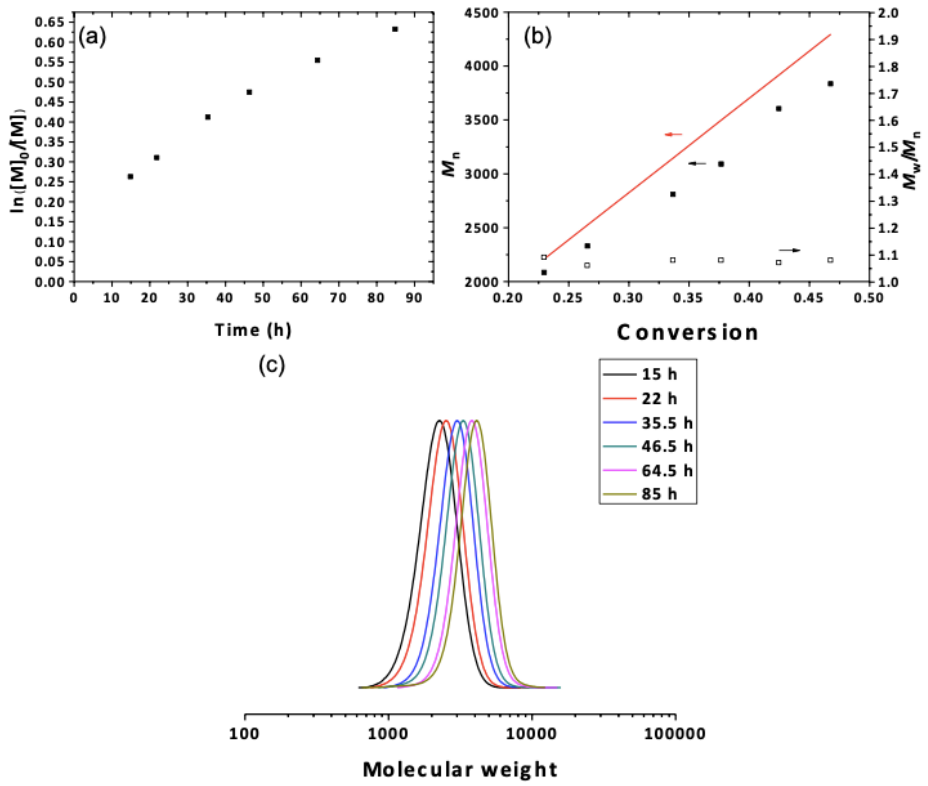

Figure 98. Kinetic plot of ln([M]$_0$/[M]) vs time (a), plots of M_n and M_w/M_n vs conversion. (Black filled square: M_n from GPC; Red curve: theoretical molecular weight) (b) and GPC traces (with 40 °C THF as eluent and PMMA as calibration standards) for ARGET ATRP of MTEA (c). Conditions: [MTEA]$_0$/[EBiB]$_0$/[$CuBr_2$]$_0$/[TPMA]$_0$/[AA]$_0$ = 60/1/0.07/0.15/0.7, 35 °C in acetone.

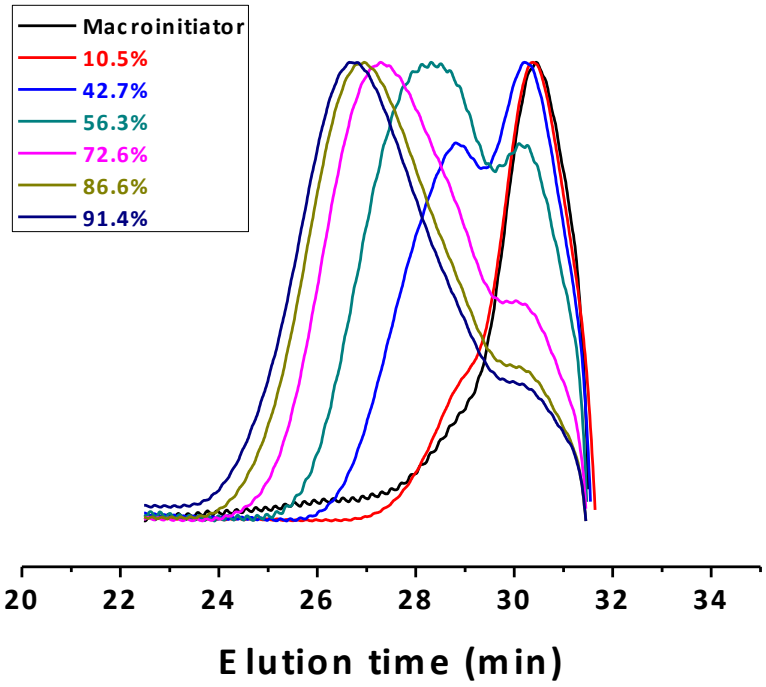

Figure 99. GPC traces of (polyMTEA)$_n$-polyDVB during ARGET ATRP. (The traces were cut off at ~32 min due to the presence of negative peak from dissolved air in DMF eluent phase)

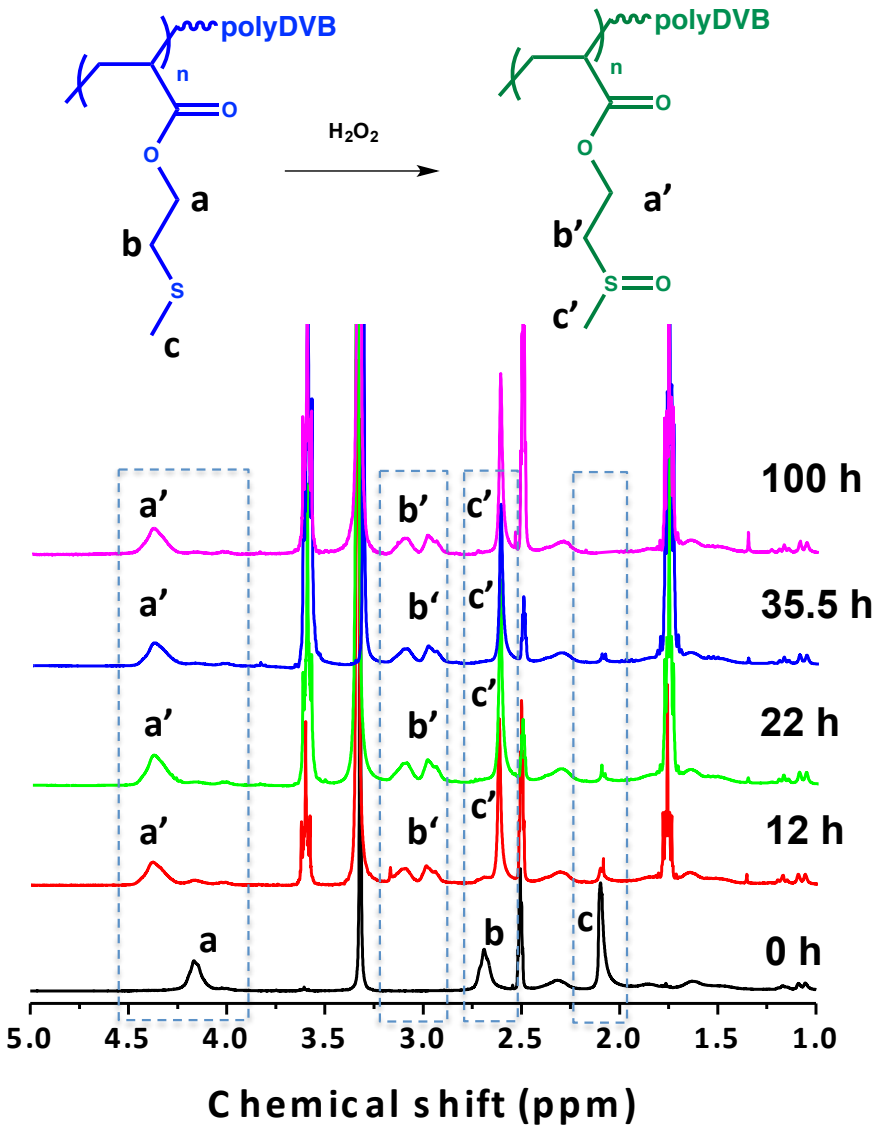

Figure 100. Oxidation of star polymer from (polyMTEA)$_n$-polyDVB to (polyMSEA)$_n$-polyDVB. As oxidation proceeded, methylene proton **a** (4.1 ppm) shifted to **a'** (4.3 ppm), methylene proton b (2.7 ppm) shifted to **b'** (2.8 ~ 3.0 ppm), methyl proton **c** (2.1 ppm) shifted to **c'** (2.6 ppm).

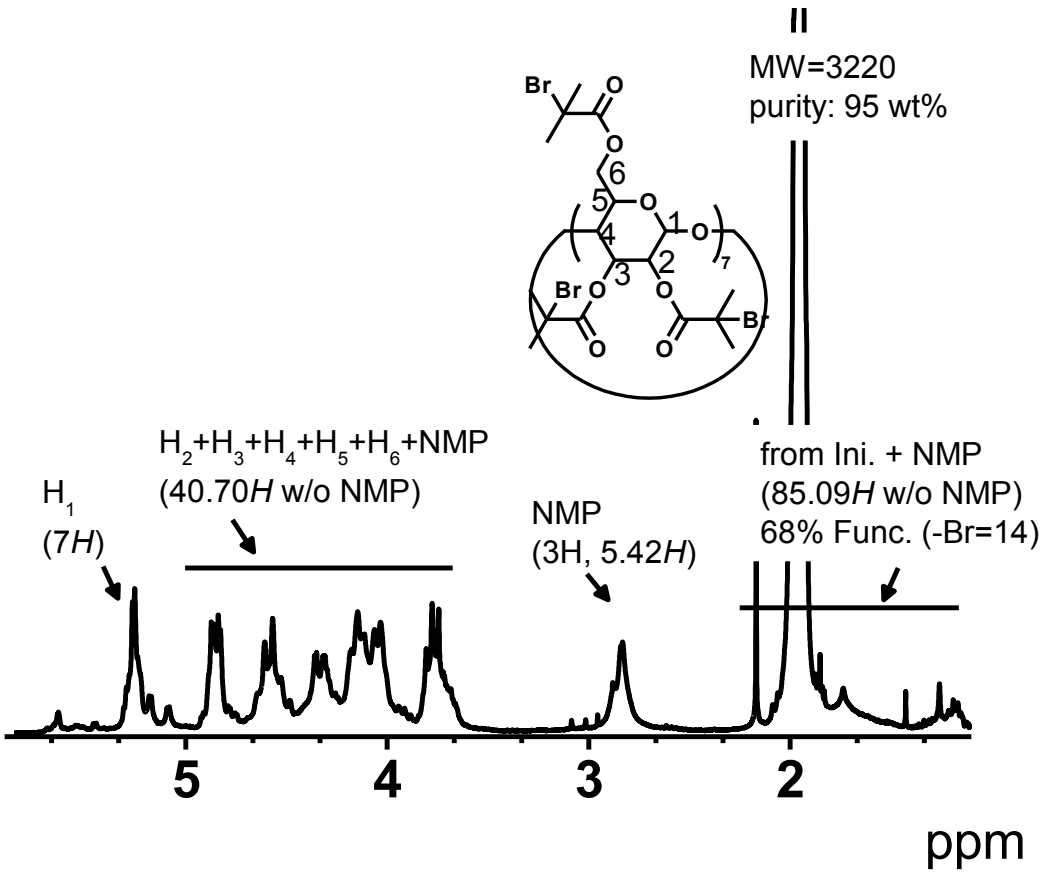

Figure 101. ^{1}H NMR spectrum of β-CD-14Br macroinitiator.

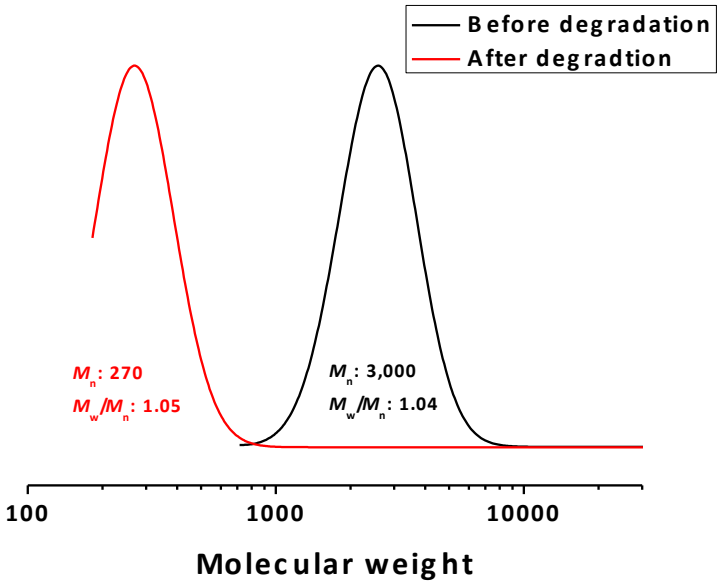

Figure 102. GPC traces of β-CD-14Br macroinitiator before and after degradation in 5 wt% NaOH aqueous solution for 12 hr. (50 °C DMF 50 mM LiBr DMF solution as eluent phase with PMMA standard, red curve were only partially shown because the peak overlapped with internal standard peak at low molecular weight range)

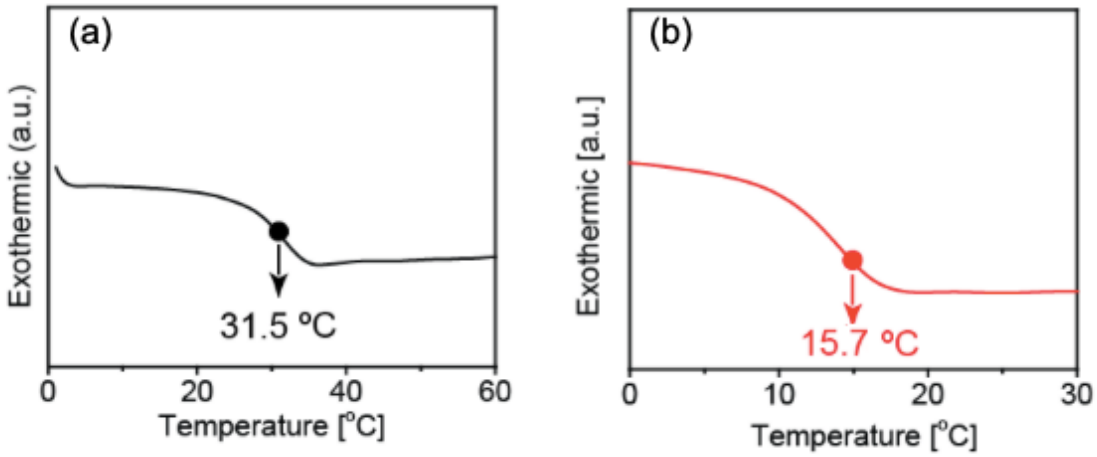

Figure 103. DSC analysis of star polymer $(polyMSEA)_n$-polyDVB with M_n = 30,500 (M_w/M_n =1.59) (a) and linear polyMSEA with M_n = 5,200 (M_w/M_n =1.18) (b).

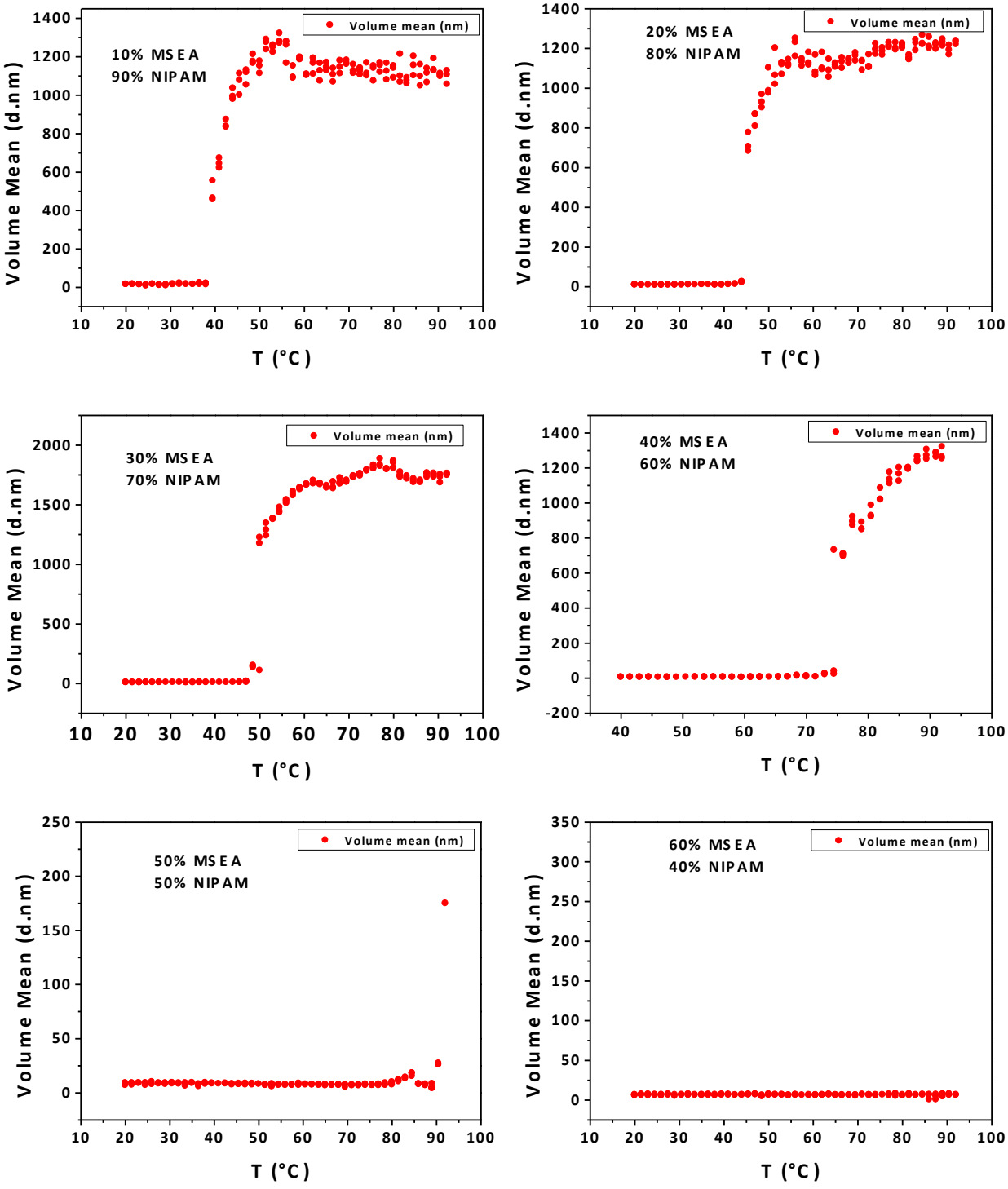

Figure 104. Volume-mean sizes of copolymers poly(MSEA-co-NIPAM)s with different compositions as a function of temperature in water.

2. LCST Study.

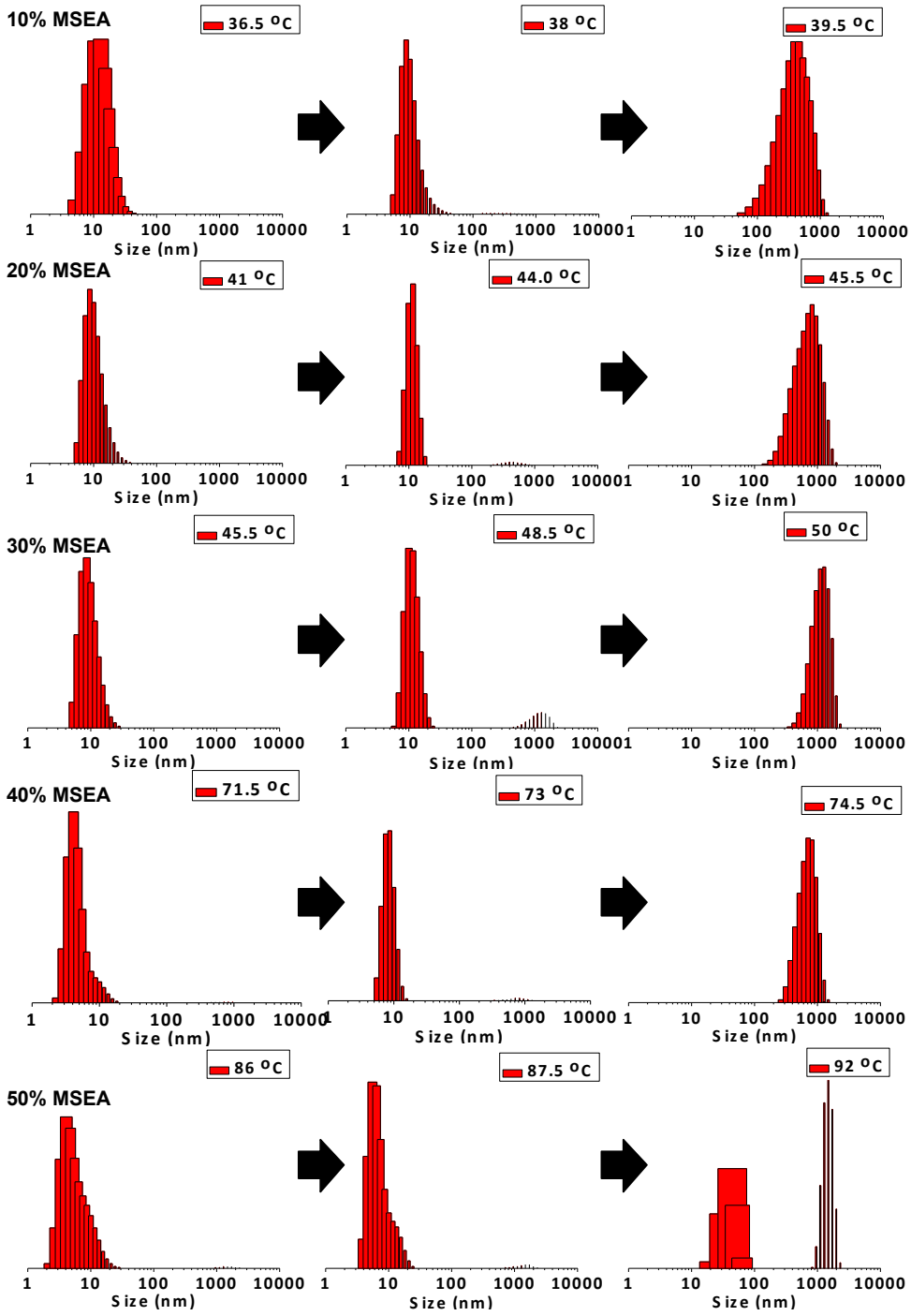

Figure 105. Onset point of dispersity change of poly(MSEA-co-NIPAM)s with different molar compositions (from 10% to 50%) in water.

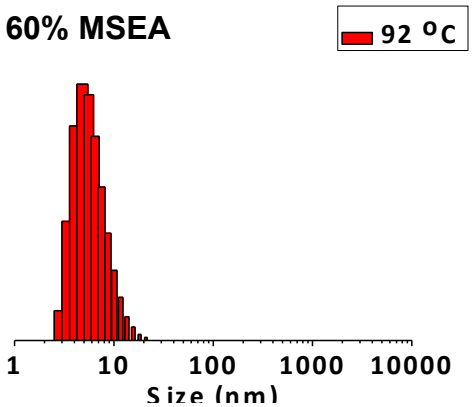

Figure 106. Size distribution of poly(MSEA-co-NIPAM)s with 60% molar fraction of MSEA in water at 92 ºC.

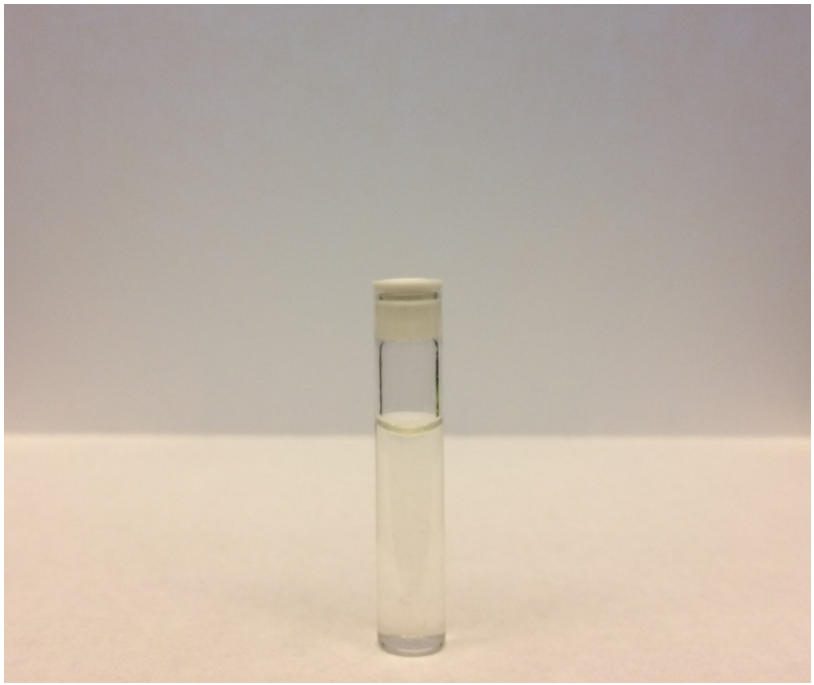

Figure 107. Transparent solution of polyMSEA (M_n = 14,400) in deionized water at r.t.. (Concentration = 359 mg/1 mL, same as solubility of NaCl in water at same temperature)

3. Determination of Reactivity Ratios

Kelen-Tüdös method. The ultimate composition of copolymers depends on the reactivity ratios of comonomers. Therefore, it was necessary to determine the reactivity ratios of the MSEA monomer with a range of other comonomers. The reactivity ratios of four different comonomer pairs were evaluated by the Kelen-Tüdös method. They were MSEA/MA, MSEA/*n*BA, MSEA/$OEGA_{500}$ and MSEA/NIPAM, respectively.[52, 53] The relationship of η^C vs. ξ^C was plotted according to Eq. S1.

$$\eta^C = \left(r_1 + \frac{r_2}{\alpha}\right)\xi^C - \frac{r_2}{\alpha} \qquad \text{(S1)}$$

$$\xi^C = \frac{\frac{m_1}{m_2}\left(\frac{\log(M_2/M_{20})}{\log(M_1/M_{10})}\right)^2}{\alpha + \frac{m_1}{m_2}\left(\frac{\log(M_2/M_{20})}{\log(M_1/M_{10})}\right)^2} \qquad \text{(S2)}$$

$$\eta^C = \frac{\frac{m_1 - m_2}{m_2}\left(\frac{\log(M_2/M_{20})}{\log(M_1/M_{10})}\right)}{\alpha + \frac{m_1}{m_2}\left(\frac{\log(M_2/M_{20})}{\log(M_1/M_{10})}\right)^2} \qquad \text{(S3)}$$

η^C and ξ^C were calculated according to Equation S2 and Equation S3 where m_i represent the concentration of polymerized repeating units of monomer *i*, M_{i0} and M_i represent the initial and final concentrations of monomer *i*. Values r_1 and r_2 and were calculated from slope and intercept of the fitted plot in Figure 104 and Equation S1. Parameter α is defined by Equation S4. Figure 105 shows the Mayo-Lewis plots, in which f_1 is the initial feed fraction of MSEA, F_1 is the ultimate polymer composition fraction of MSEA. For comonomer pair MSEA/MA, reactivity ratios r_1 = 0.49, r_2 = 1.01 were calculated. For comonomer pair MSEA/*n*BA, they were r_1 = 0.49, r_2 = 0.83; for comonomer pair MSEA/OEGA (MW 480), r_1 = 0.77, r_2 = 0.30 and for MSEA/NIPAM, r_1 = 1.24, r_2 = 0.42. In all four pairs, MSEA was defined as comonomer 1. These results indicated, the tendency to form statistical copolymers with a preference for alternation. The reactivity ratio was

also calculated by the Fineman-Ross approach, which showed good agreement with the Kelen-Tüdös method (Figure 106).

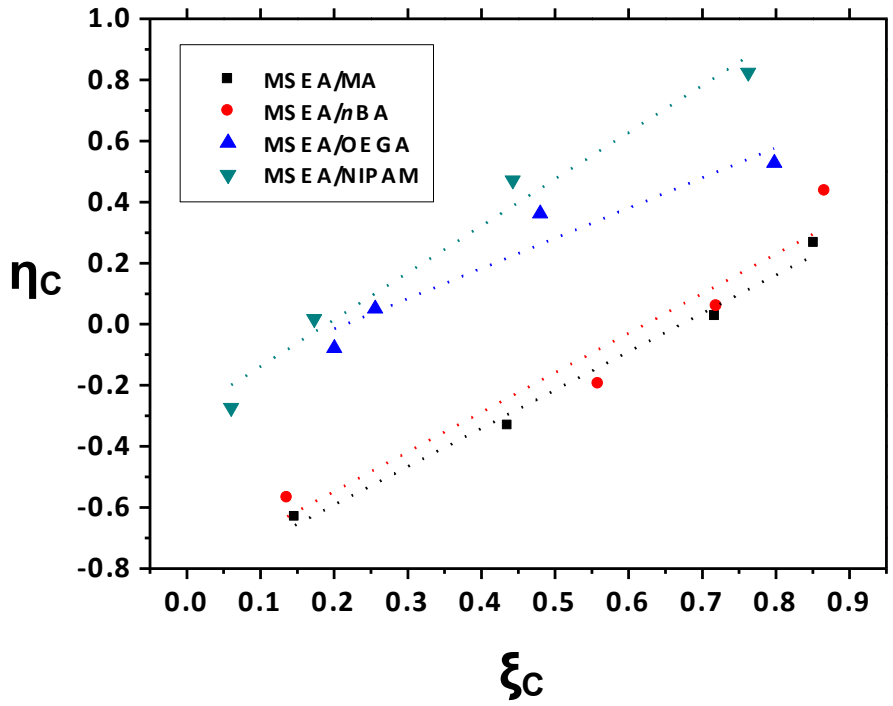

Figure 108. Kelen-Tüdös plots of four monomer pairs

$$\alpha = \sqrt{\left(\frac{M_{10}^2}{M_{20}^2}\frac{m_2}{m_1}\right)_{\mathrm{MIN}}\left(\frac{M_{10}^2}{M_{20}^2}\frac{m_2}{m_1}\right)_{\mathrm{MAX}}} \qquad \text{(S4)}$$

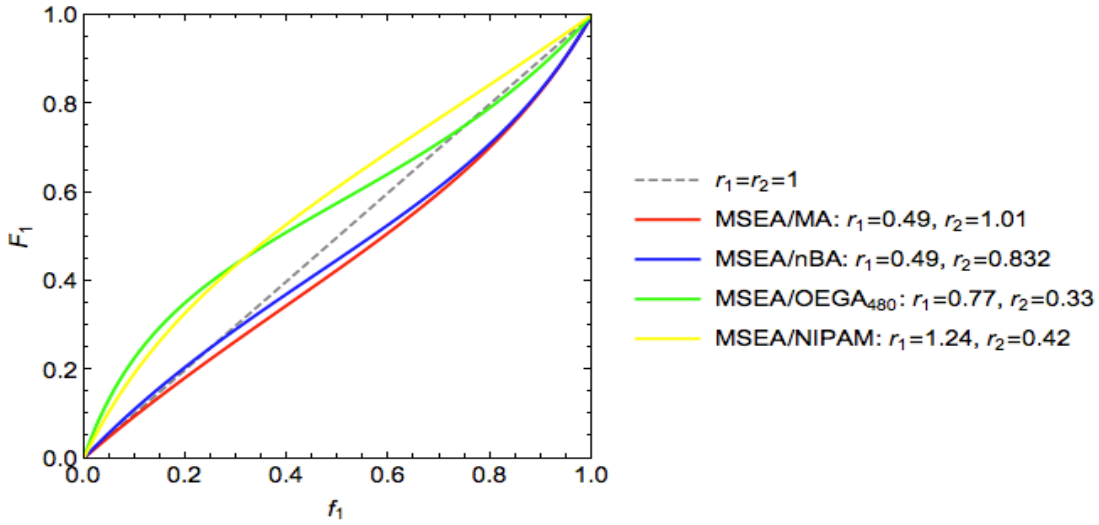

Figure 109. Mayo-Lewis plot of four monomer pairs based on reactivity ratio from Kelen-Tüdös apporach

Fineman-Ross method. The Fineman-Ross method is based on the equations S5-S7. f_1 is defined as the initial monomer concentration ratio (Equation S5). F_1 is defined as the polymer composition ratio (Equation S6). r_1 and r_2 were obtained by extrapolating Equation S7 as shown in Figure 106. As calculated by Fineman-Ross approach, for MSEA/MA pair, $r_1 = 0.5$ $r_2 = 1.2$. For MSEA/*n*BA pair, $r_1 = 0.66$, $r_2 = 1.14$. For MSEA/OEGA pair, $r_1 = 0.71$, $r_2 = 1.22$. For MSEA/NIPAM pair, $r_1 = 1.04$, $r_2 = 0.17$. The results were in agreement with the results from the Kelen-Tüdös approach.

$$f_1 = \frac{M_1}{M_2} \quad \text{(S5)}$$

$$F_1 = \frac{dM_1}{dM_2} \quad \text{(S6)}$$

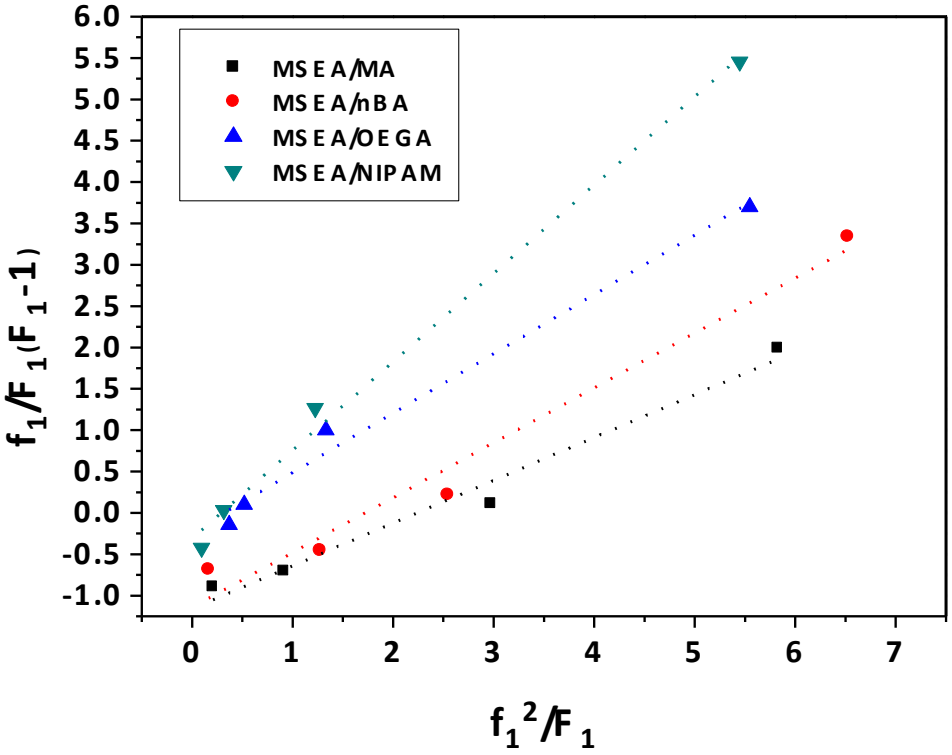

Figure 110. Fineman-Ross plots of four monomer pairs.

$$\frac{f_1}{F_1}(F_1 - 1) = r_1 \frac{f_1^2}{F_1} - r_2 \quad \text{(S7)}$$

A.6. References

[1] Kataoka, K.; Harada, A.; Nagasaki, Y., Block copolymer micelles for drug delivery: design, characterization and biological significance, *Advanced Drug Delivery Reviews* **2001,** 47, 113.

[2] Kanasty, R.; Dorkin, J. R.; Vegas, A.; Anderson, D., Delivery materials for siRNA therapeutics, *Nature materials* **2013,** 12, 967.

[3] Duncan, R. R., The dawning era of polymer therapeutics, *Nature reviews. Drug discovery* **2003,** 2, 347.

[4] DeMuth, P. C.; Min, Y.; Huang, B.; Kramer, J. A.; Miller, A. D., Polymer multilayer tattooing for enhanced DNA vaccination, *Nature materials* **2013,** 12, 367.

[5] Lutolf, M. P.; Hubbell, J. A., Synthetic biomaterials as instructive extracellular microenvironments for morphogenesis in tissue engineering, *Nature biotechnology* **2005,** 23, 47.

[6] Owens Iii, D. E.; Peppas, N. A., Opsonization, biodistribution, and pharmacokinetics of polymeric nanoparticles, *International Journal of Pharmaceutics* **2006,** 307, 93.

[7] Pelegri-O'Day, E. M.; Lin, E.-W.; Maynard, H. D., Therapeutic Protein–Polymer Conjugates: Advancing Beyond PEGylation, *Journal of the American Chemical Society* **2014,** 136, 14323.

[8] Hoogenboom, R., Poly(2 - oxazoline)s: A Polymer Class with Numerous Potential Applications, *Angewandte Chemie International Edition* **2009,** 48, 7978.

[9] Braunecker, W. A.; Matyjaszewski, K., Controlled/living radical polymerization: Features, developments, and perspectives, *Progress in Polymer Science* **2007,** 32, 93.

[10] Matyjaszewski, K., Atom Transfer Radical Polymerization (ATRP): Current Status and Future Perspectives, *Macromolecules* **2012,** 45, 4015.

[11] Moad, G.; Rizzardo, E.; Thang, S. H., Living Radical Polymerization by the RAFT Process, *Australian Journal of Chemistry* **2005,** 58, 379.

[12] Hawker, C. J.; Barclay, G. G.; Orellana, A.; Dao, J.; Devonport, W., Initiating Systems for Nitroxide-Mediated "Living" Free Radical Polymerizations: Synthesis and Evaluation, *Macromolecules* **1996,** 29, 5245.

[13] Oh, J. K.; Siegwart, D. J.; Lee, H.-i.; Sherwood, G.; Peteanu, L.; Hollinger, J. O.; Kataoka, K.; Matyjaszewski, K., Biodegradable Nanogels Prepared by Atom Transfer Radical

Polymerization as Potential Drug Delivery Carriers: Synthesis, Biodegradation, in Vitro Release, and Bioconjugation, *Journal of the American Chemical Society* **2007,** 129, 5939.

[14] Oh, J. K.; Tang, C.; Gao, H.; Tsarevsky, N. V.; Matyjaszewski, K., Inverse Miniemulsion ATRP: A New Method for Synthesis and Functionalization of Well-Defined Water-Soluble/Cross-Linked Polymeric Particles, *Journal of the American Chemical Society* **2006,** 128, 5578.

[15] Keefe, A. J.; Jiang, S., Poly(zwitterionic)protein conjugates offer increased stability without sacrificing binding affinity or bioactivity, *Nat Chem* **2012,** 4, 59.

[16] Durán-Lobato, M.; Martín-Banderas, L.; Gonçalves, L. M. D.; Fernández-Arévalo, M.; Almeida, A. J., Comparative study of chitosan- and PEG-coated lipid and PLGA nanoparticles as oral delivery systems for cannabinoids, *Journal of Nanoparticle Research* **2015,** 17, 1.

[17] Reader, P.; Pfukwa, R.; Jokonya, S.; Arnott, G. E.; Klumperman, B., Synthesis of [small alpha], [small omega]-heterotelechelic PVP for bioconjugation, via a one-pot orthogonal end-group modification procedure, *Polymer Chemistry* **2016**.

[18] Jakubowski, W.; Matyjaszewski, K., Activators regenerated by electron transfer for atom-transfer radical polymerization of (meth)acrylates and related block copolymers, *Angew Chem Int Ed Engl* **2006,** 45, 4482.

[19] Konkolewicz, D.; Wang, Y.; Zhong, M.; Krys, P.; Isse, A. A.; Gennaro, A.; Matyjaszewski, K., Reversible-Deactivation Radical Polymerization in the Presence of Metallic Copper. A Critical Assessment of the SARA ATRP and SET-LRP Mechanisms, *Macromolecules* **2013,** 46, 8749.

[20] Konkolewicz, D.; Wang, Y.; Krys, P.; Zhong, M.; Isse, A. A.; Gennaro, A.; Matyjaszewski, K., SARA ATRP or SET-LRP. End of controversy?, *Polym. Chem.* **2014,** 5, 4396.

[21] Matyjaszewski, K.; Jakubowski, W.; Min, K.; Tang, W.; Huang, J., Diminishing catalyst concentration in atom transfer radical polymerization with reducing agents, *Proceedings of the National Academy of Sciences - PNAS* **2006,** 103, 15309.

[22] Pan, X.; Lamson, M.; Yan, J.; Matyjaszewski, K., Photoinduced Metal-Free Atom Transfer Radical Polymerization of Acrylonitrile, *ACS Macro Letters* **2015,** 4, 192.

[23] Treat, N. J.; Sprafke, H.; Kramer, J. W.; Clark, P. G.; Barton, B. E.; Read de Alaniz, J.; Fors, B. P.; Hawker, C. J., Metal-Free Atom Transfer Radical Polymerization, *Journal of the American Chemical Society* **2014,** 136, 16096.

[24] Magenau, A. J. D.; Strandwitz, N. C.; Gennaro, A.; Matyjaszewski, K., Electrochemically mediated atom transfer radical polymerization, *Science (New York, N.Y.)* **2011,** 332, 81.

[25] Zheng, Y.; Li, S.; Weng, Z.; Gao, C., Hyperbranched polymers: advances from synthesis to applications, *Chemical Society Reviews* **2015,** 44, 4091.

[26] Matyjaszewski, K., The synthesis of functional star copolymers as an illustration of the importance of controlling polymer structures in the design of new materials, *Polymer international* **2003,** 52, 1559.

[27] Gao, H.; Matyjaszewski, K., Synthesis of functional polymers with controlled architecture by CRP of monomers in the presence of cross-linkers: From stars to gels, *Progress in polymer science* **2009,** 34, 317.

[28] Oh, J. K.; Drumright, R.; Siegwart, D. J.; Matyjaszewski, K., The development of microgels/nanogels for drug delivery applications, *Progress in polymer science* **2008,** 33, 448.

[29] Siegwart, D. J.; Oh, J. K.; Matyjaszewski, K., ATRP in the design of functional materials for biomedical applications, *Progress in Polymer Science* **2012,** 37, 18.

[30] Matyjaszewski, K.; Tsarevsky, N. V., Macromolecular Engineering by Atom Transfer Radical Polymerization, *J. Am. Chem. Soc.* **2014,** 136, 6513.

[31] Mackenzie, M. C.; Shrivats, A. R.; Konkolewicz, D.; Averick, S. E.; McDermott, M. C.; Hollinger, J. O.; Matyjaszewski, K., Synthesis of Poly(meth)acrylates with Thioether and Tertiary Sulfonium Groups by ARGET ATRP and Their Use as siRNA Delivery Agents, *Biomacromolecules* **2015,** 16, 236.

[32] Prausnitz, M. R.; Langer, R., Transdermal drug delivery, *Nature biotechnology* **2008,** 26, 1261.

[33] Kloesch, B.; Liszt, M.; Broell, J.; Steiner, G., Dimethyl sulphoxide and dimethyl sulphone are potent inhibitors of IL-6 and IL-8 expression in the human chondrocyte cell line C-28/I2, *Life sciences (1973)* **2011,** 89, 473.

[34] Fahy, G. M.; Lilley, T. H.; Linsdell, H.; Douglas, M. S.; Meryman, H. T., Cryoprotectant toxicity and cryoprotectant toxicity reduction: in search of molecular mechanisms, *Cryobiology* **1990,** 27, 247.

[35] Squires, E. L.; Carnevale, E. M.; McCue, P. M.; Bruemmer, J. E., Embryo technologies in the horse, *Theriogenology* **2003,** 59, 151.

[36] Wang, J.-S.; Matyjaszewski, K., Controlled/"Living" Radical Polymerization. Halogen Atom Transfer Radical Polymerization Promoted by a Cu(I)/Cu(II) Redox Process, *Macromolecules* **1995,** 28, 7901.

[37] Matyjaszewski, K.; Xia, J. H., Atom transfer radical polymerization, *Chemical reviews* **2001,** 101, 2921.

[38] Wang, J.-S.; Matyjaszewski, K., Controlled/"living" radical polymerization. atom transfer radical polymerization in the presence of transition-metal complexes, *Journal of the American Chemical Society* **1995,** 117, 5614.

[39] Ren, J. M.; McKenzie, T. G.; Fu, Q.; Wong, E. H. H.; Xu, J.; An, Z.; Shanmugam, S.; Davis, T. P.; Boyer, C.; Qiao, G. G., Star Polymers, *Chemical Reviews* **2016,** 116, 6743.

[40] Boyer, C.; Corrigan, N. A.; Jung, K.; Nguyen, D.; Nguyen, T.-K.; Adnan, N. N. M.; Oliver, S.; Shanmugam, S.; Yeow, J., Copper-Mediated Living Radical Polymerization (Atom Transfer Radical Polymerization and Copper(0) Mediated Polymerization): From Fundamentals to Bioapplications, *Chemical Reviews* **2016,** 116, 1803.

[41] Wei, J.; Zhang, Z.; Tseng, J.-K.; Treufeld, I.; Liu, X.; Litt, M. H.; Zhu, L., Achieving High Dielectric Constant and Low Loss Property in a Dipolar Glass Polymer Containing Strongly Dipolar and Small-Sized Sulfone Groups, *ACS Applied Materials & Interfaces* **2015,** 7, 5248.

[42] Jiang, D.; Wang, G.; Zheng, F.; Han, J.; Wu, X., Novel thermo-sensitive hydrogels containing polythioether dendrons: facile tuning of LCSTs, strong absorption of Ag ions, and embedment of smaller Ag nanocrystals, *Polymer Chemistry* **2015,** 6, 625.

[43] Batz, H. G.; Hofmann, V.; Ringsdorf, H., Pharmakologisch aktive polymere, 4. Monomere und polymere alkylsulfinyl‐alkylacrylate und ‐methacrylate als mögliche resorptionsvermittler, *Die Makromolekulare Chemie* **1973,** 169, 323.

[44] Konkolewicz, D.; Magenau, A. J. D.; Averick, S. E.; Simakova, A.; He, H.; Matyjaszewski, K., ICAR ATRP with ppm Cu Catalyst in Water, *Macromolecules* **2012,** 45, 4461.

[45] Min, K.; Gao, H.; Matyjaszewski, K., Preparation of Homopolymers and Block Copolymers in Miniemulsion by ATRP Using Activators Generated by Electron Transfer (AGET), *Journal of the American Chemical Society* **2005,** 127, 3825.

[46] Averick, S.; Simakova, A.; Park, S.; Konkolewicz, D.; Magenau, A. J. D.; Mehl, R. A.; Matyjaszewski, K., ATRP under Biologically Relevant Conditions: Grafting from a Protein, *ACS Macro Letters* **2012,** 1, 6.

[47] Ding, H.; Park, S.; Zhong, M.; Pan, X.; Pietrasik, J.; Bettinger, C. J.; Matyjaszewski, K., Facile Arm-First Synthesis of Star Block Copolymers via ARGET ATRP with ppm Amounts of Catalyst, *Macromolecules* **2016,** 49, 6752.

[48] Verstichel, S.; De Wilde, B.; Fenyvesi, E.; Szejtli, J., Investigation of the Aerobic Biodegradability of Several Types of Cyclodextrins in a Laboratory-Controlled Composting Test, *Journal of Polymers and the Environment* **2004,** 12, 47.

[49] Uekama, K., Design and Evaluation of Cyclodextrin-Based Drug Formulation, *Chemical and Pharmaceutical Bulletin* **2004,** 52, 900.

[50] Li, J.; Xiao, H., An efficient synthetic-route to prepare [2,3,6-tri-O-(2-bromo-2-methylpropionyl]-β-cyclodextrin), *Tetrahedron Letters* **2005,** 46, 2227.

[51] Alexis, F.; Pridgen, E.; Molnar, L. K.; Farokhzad, O. C., Factors Affecting the Clearance and Biodistribution of Polymeric Nanoparticles, *Molecular Pharmaceutics* **2008,** 5, 505.

[52] Rao, S. P.; Ponratnam, S.; Kapur, S. L.; Iyer, P. K., Kelen-tüdös method applied to the analysis of high-conversion copolymerization data, *Journal of Polymer Science: Polymer Letters Edition* **1976,** 14, 513.

[53] Kelen, T.; TÜds, F., Analysis of the Linear Methods for Determining Copolymerization Reactivity Ratios. I. A New Improved Linear Graphic Method, *J. Macromol. Sci., Part A: Chem.* **1975,** 9, 1.

[54] Cui, D.; Tian, F.; Ozkan, C. S.; Wang, M.; Gao, H., Effect of single wall carbon nanotubes on human HEK293 cells, *Toxicology Letters* **2005,** 155, 73.

[55] Yoshii, E., Cytotoxic effects of acrylates and methacrylates: Relationships of monomer structures and cytotoxicity, *Journal of Biomedical Materials Research* **1997,** 37, 517.

[56] Britovsek, G. J. P.; England, J.; White, A. J. P., Non-heme iron(II) complexes containing tripodal tetradentate nitrogen ligands and their application in alkane oxidation catalysis, *Inorg. Chem.* **2005,** 44, 8125.

Appendix B. Cationic Hyperbranched Polymers with Biocompatible Shells for siRNA Delivery

B.1. Preface

The polyDMSO described in Appendix A possesses the combined-advantage of low toxicity and low steric hindrance. In collaboration with Prof. Yuji Mishina from University of Michigan, I further explored the application of this type of polymer in siRNA delivery to knockdown Runt-related transcription factor 2 (Runx2) expression that is responsible for the development of heterotopic ossification (HO), an urgent clinical concern. This work resulted in a first author publication in *Biomacromolecules* - Sipei Li, Maiko Omi, Francis Cartieri, Dominik Konkolewicz, Gordon Mao, Haifeng Gao, Saadyah E. Averick, Yuji Mishina, and Krzysztof Matyjaszewski, "Cationic Hyperbranched Polymers with Biocompatible Shells for siRNA Delivery", *Biomacromolecules* **2018**, *19*, 3754-3765.

I would especially like to thank Prof. Saadyah Averick, Prof. Yuji Mishina and Maiko Omi for their contribution in experiment design and manuscript writing. I would also like to thank Prof. Dominik Konkolewicz and Prof. Haifeng Gao for their contribution in analysis of degree of branching. I would also like to thank Maiko Omi, Francis Cartieri and Gordon Mao for their contribution in bio-related characterizations.

This work is supported by National Institutes of Health R01DE020843 and the NSF DMR 1501324.

B.2. Introduction

RNA interference (RNAi) is the process of post-transcriptional silencing of gene expressions triggered by short interfering RNA (siRNA). The therapeutic potential of RNAi has been far-reaching since it can prevent the production of targeted proteins that could lead to diseases,

including inherited disorders, some types of cancers and certain viral infections.[1-9] For example, heterotopic ossification (HO) is of an urgent clinical concern, it may occur as a consequence of musculoskeletal trauma from blast and high-energy injuries, total joint arthroplasty (TJA), traumatic brain injury, or spinal cord injury.[10-12] Contemporary treatments of HO such as anti-inflammatory drugs and radiation therapy have adverse effects and are not inherently designed to correct the molecular mechanism of the etiology of HO. It was suggested the cause of HO may be due to dysregulated signals in the bone morphogenetic protein osteogenic cascade. siRNA delivery against Runt-related transcription factor 2 (*Runx2*) genes can potentially decrease messenger RNA expression, inhibit activity of the osteogenic marker alkaline phosphatase (ALP) and thus abrogate HO.[13] However, the selective delivery of siRNA into cells has been a challenge since unmodified siRNA that is unstable in bloodstream can be immunogenic and difficult to pass through cell membranes.[2, 14] There are two major types of siRNA carriers to facilitate the delivery, viral and nonviral systems.[15, 16] The viral system is risky due to potential virus replication and inflammation reactions. Therefore, development of efficient nonviral carriers based on cationic lipids or synthetic polymers has become a more promising option.[15, 17-28]

Positively charged polymers can generate polyplexes with negatively charged siRNA and thus improve the transfection of siRNA into cells via adsorptive endocytosis.[29, 30] Some cationic polymeric materials include chitosan,[24] cationic polypeptides,[31] cationic lipids,[32] polyethylenimine (PEI),[33, 34] quaternized or non-quaternized poly(2-(dimethylamino)ethyl methacrylate) (polyDMAEMA)[35, 36] poly(meth)acrylates with tertiary sulfonium groups,[37] etc. However, polymers with the "naked" positive charges on the surface can cause toxic effect to cell survival and non-specific gene suppression. Such surface charges can be "screened" by incorporating biocompatible segments of poly(ethylene glycol) (PEG) or poly(oligo(ethylene glycol)

methacrylate) (polyOEGMA) via "PEGylation".[38-41] These biocompatible segments can be introduced in a block copolymer structure that contains PEG or polyOEGMA as a second block, but can still interact with siRNA to form biocompatible micelles under heterogeneous conditions.[42, 43] Another approach is to use multicomponent cationic nanogels prepared from emulsion, which shows higher structural stability than micelles. As an example, a biocompatible nanogel made of quaternized DMAEMA, OEGMA and crosslinkers was previously synthesized in microemulsion.[44] It showed promise for both plasmid DNA (pDNA) and siRNA delivery.[44] However, the preparation of either micelles or multicomponent nanogels employs assembly or polymerization under heterogeneous conditions and requires extensive post-purifications.[45] Alternatively, biocompatible cationic polymeric carriers can be prepared under homogeneous conditions in the form of dendritic polymers, such as multi-arm polymers,[46] hyperbranched polymers (HBP),[47-50] and star-like polymers with a cationic crosslinked core.[17, 36]

Hyperbranched polymers (HBP) possess interesting properties such as abundance of intramolecular cavities, high surface functionality, high solubility and unique viscosity, compared to their linear analogues.[51-54] Because of these properties, HBP can have much higher transfection efficiency than their linear analogues with a similar molecular weight.[55 46, 56-59] Hyperbranched cationic polymers can be easily synthesized by self-condensing vinyl polymerization (SCVP) using controlled radical polymerization on a large scale.[60-65] However, due to combination of step-growth and chain-growth mechanisms, HBP with higher degree of branching (DB) can only be achieved at the cost of broad molecular weight distribution. Recently, it was demonstrated that synthesis of HBP in microemulsion provides polymers with much lower dispersity.[66] Yet, to prepare HBP with low dispersity under homogeneous conditions remained to be an unsolved problem.

Another challenge for successful siRNA delivery is the choice of biocompatible segments. Recent reports of immunogenicity issues of PEG-based polymers have come to light primarily due to the abundance of modern drugs and cosmetics which employ PEG or polyOEGMA as a part of their formulation.[67] Moreover, if OEGMA is densely grafted to the core, it may sterically hinder the complexation with siRNA and diminish the efficiency of gene silencing. Thus, development of new biocompatible polymers for siRNA delivery is welcomed.[67, 68] Recently, the synthesis of a highly biocompatible polymeric analogue of dimethyl sulfoxide (DMSO) (poly(2-(methylsulfinyl) ethyl acrylate)) by atom transfer radical polymerization (ATRP) was reported.[69] The polymer showed very high hydrophilicity and also much smaller steric hindrance than OEGMA.[70-72] Therefore, the efficiency of this new type of polymer as protective layers and comparison to polyOEGMA for siRNA complexation and delivery were investigated.

Herein, we report a direct synthesis of cationic HBP with low molecular weight dispersity via activator generated by electron transfer (AGET) ATRP.[61, 73-75] SCVP of a cationic inimer bearing a quaternary ammonium group was successfully conducted. The degree of branching (DB) was adjusted (16 %, 22 % and 34 %) by changing the ratio of activator to deactivator in an AGET ATRP process. Due to the use of charged inimers, the charge-charge repulsion between each growing chain reduced the oligomer coupling and generated HBPs with relatively low dispersity (<1.8) even at DB of 34 %. To increase the biocompatibility and decrease the toxic effect of the cationic HBP core, a biocompatible shell layer based on either polyOEGMA or poly(2-(methylsulfinyl) ethyl methacrylate) (abbreviated as polyDMSO) was introduced via surface initiation polymerization of the corresponding monomers from the cationic core using activator regenerated by electron transfer (ARGET) ATRP. Both of the core-shell structures had low cytotoxicity down to 1 mg/mL. Due to the lower steric hindrance, the polyDMSO-based HBP

showed higher complexing efficiency with siRNA. The long-term efficacy of cationic polymer-mediated RNAi attack on *Runx2* expression in wild-type osteoblasts cells was determined by using quantitative real-time polymerase chain reaction detection. The assessment of mineralized nodule formation in osteoblast cultures was conducted by the Alizarin Red S staining. While the naked HBP core showed non-specific gene suppression due to cytotoxicity, the biocompatible core-shell structures were crucial to minimizing undesired cytotoxicity and non-specific gene suppression. PolyDMSO-HBP showed higher efficacy of forming polyplexes with siRNA than polyOEGMA-HBP due to lower steric hindrance of the polyDMSO shell. Interestingly, the gene silencing efficacy of both polyOEGMA-HBP and polyDMSO-HBP was similar and comparable to *Lipofectamine*. The results indicated that the core-shell polymer strategy based on a cationic HBP core may have long-term potential for treatment of HO without any undesirable cytotoxic effects.

B.3. Results and discussion

Synthesis of cationic hyperbranched polymers (HBPs).

An ATRP inimer bearing a quaternary ammonium group was synthesized by Menshutkin reaction of 2-bromoethyl α-bromoisobutyrate with DMAEMA in dimethylformamide (DMF), a polar aprotic solvent, at 35 ^{o}C.[48, 62, 76] The reaction was completed within 2 hours; the inimer yield was 98% after purification. Hyperbranched polymers were prepared via SCVP using AGET ATRP of this inimer with $CuBr_2$/ tris(2-pyridylmethyl)amine (TPMA) complexes as the catalyst source and ascorbic acid as reducing agent to generate Cu^{I} species (Scheme 12).

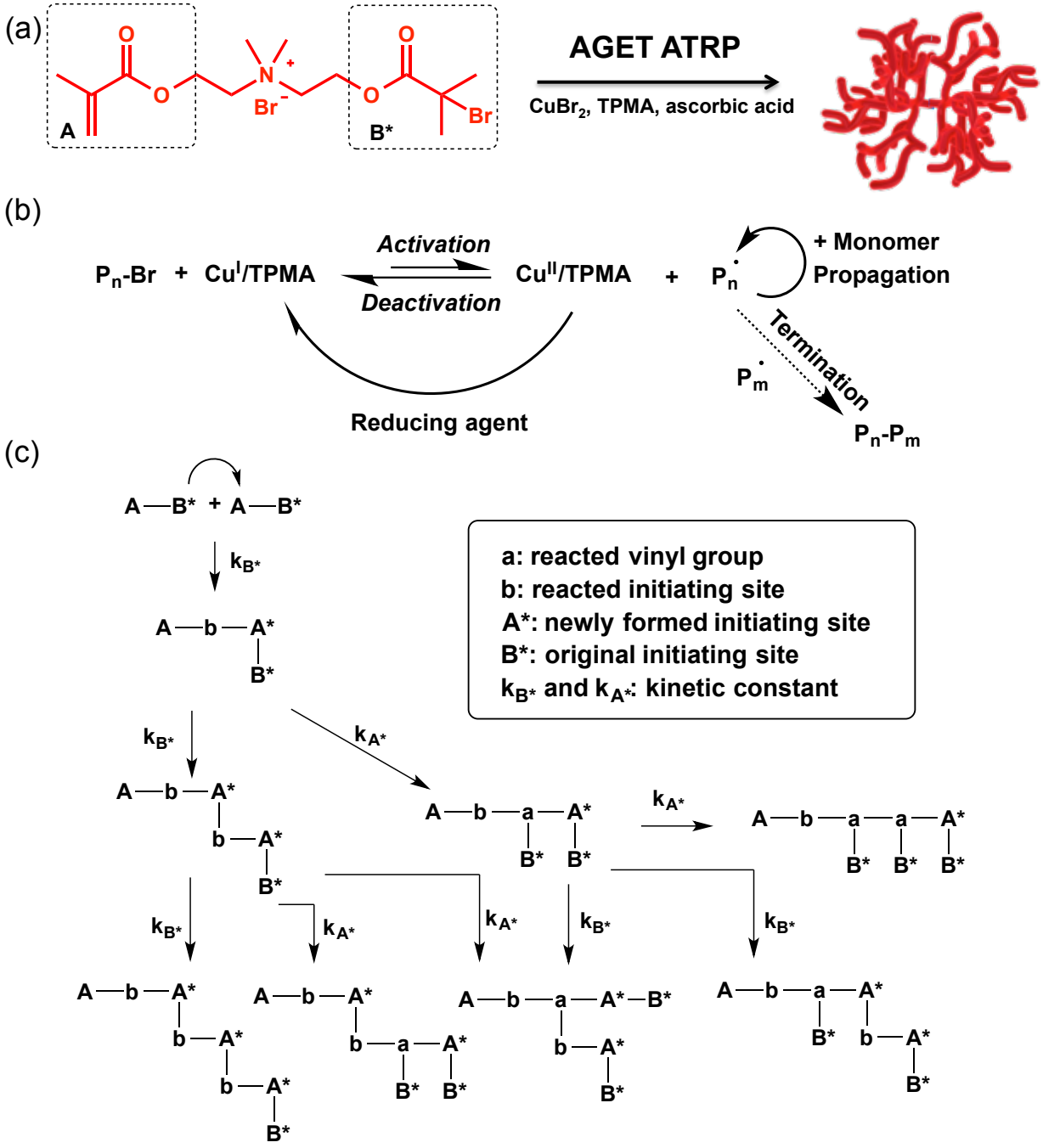

Scheme 12. (a) Synthesis of cationic hyperbranched polymers (HBP). Conditions: [inimer]/[ascorbic acid]/[$CuBr_2$]/[TPMA] =50/x/4/6 (35 °C, DMSO, 38 wt%, x = 0.3, 1.3 or 4.4). (b) Mechanism of AGET ATRP involving activation and deactivation. (c) Reaction mechanism of the first three steps in a SCVP process.

Three different amounts of reducing agents were used: [cationic inimer]/[ascorbic acid]/[$CuBr_2$]/[TPMA] =50/x/4/6, where x = 0.3, 1.3 or 4.4. SCVPs were conducted at 35 ºC in DMSO using 38 wt% of inimer, Table 10. After one hour, conversion exceeded 95 % in all polymerizations. By using different amount of reducing agent, the feed ratios of [Cu^{I}/TPMA] activator to [Cu^{II}/TPMA] deactivator was adjusted. By increasing the ratio of ascorbic acid to $CuBr_2$ from 0.3 to 4.4, the DB decreased from 34 % to 16 %. This is because at lower concentration of reducing agent, and consequently higher concentration of deactivator, the deactivation rate was faster to allow both types of initiating sites to be activated at statistical ratio, leading to higher DB. Meanwhile, a lower concentration of deactivator facilitated chain propagation, i.e., reaction of a radical with more vinyl groups, in one activation deactivation cycle, leading to low primary chain segment and low DB, **Error! Reference source not found.**. The details of calculation of DB are included in supplementary information.[66, 77]

Table 10. Molecular weight, dispersity (*Đ*) and degree of branching (DB) of cationic HBPs.

Reaction #	[Asc. A.]/[$CuBr_2$]	Conversion	M_n[b]	$Đ$[b]	DB
HBP-1	0.3/4	98.3 %	5,700	1.78	34 %
HBP-2	1.3/4	98.1 %	19,000	1.81	22 %
HBP-3	4.4/4	97.0 %	14,200	1.49	16 %

[a] Feed ratio of [ascorbic acid] to [$CuBr_2$]
b Number averaged molecular weight and MW dispersity determined by SEC-MALS in pure DMF

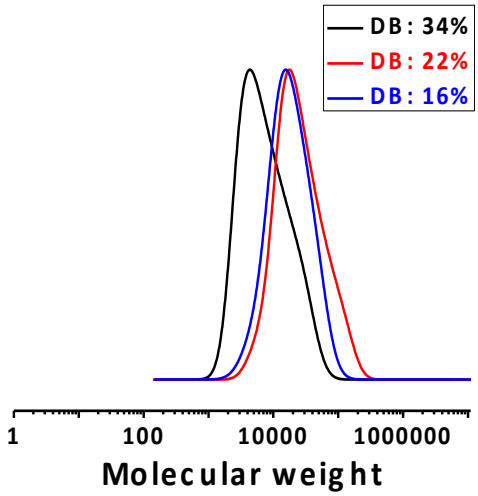

Figure 111. SEC traces of the cationic hyperbranched polymers with different DB.

Generally the formation of hyperbranched structures follows the step/chain-growth mechanism.[78] As a result, the polymerization is accompanied by random polymer-polymer coupling which leads to extremely broad molecular weight distribution.[66, 79] Recently, it was shown that confining growing polymers in droplets of microemulsions gives low molecular weight dispersity below 2. This is due to the fact that growing chain-end of radicals in separate droplets have diminished chance of random polymer-polymer coupling.[66] The molecular weights of the cationic HBPs were measured by SEC in pure DMF eluent phase without addition of any salt. SEC traces of all the polymers showed monomodal distribution, indicating relatively homogeneous structure. Interestingly, all the HBPs showed relatively narrow molecular weight distribution. Polymer with DB of 34% had molecular weight of 5700 and dispersity $Đ$ = 1.78, Figure 111. With lowered DB, the molecular weight increased, indicating larger fraction of linear structural units. Such low molecular weight dispersity could be due to the charge-charge repulsion between each growing chain, which reduces the chance of oligomer coupling and favors the reaction of inimers

with existing chains. With sufficient amount of Cu(II) species, the polymerization can still generate DB as high as 34 %.

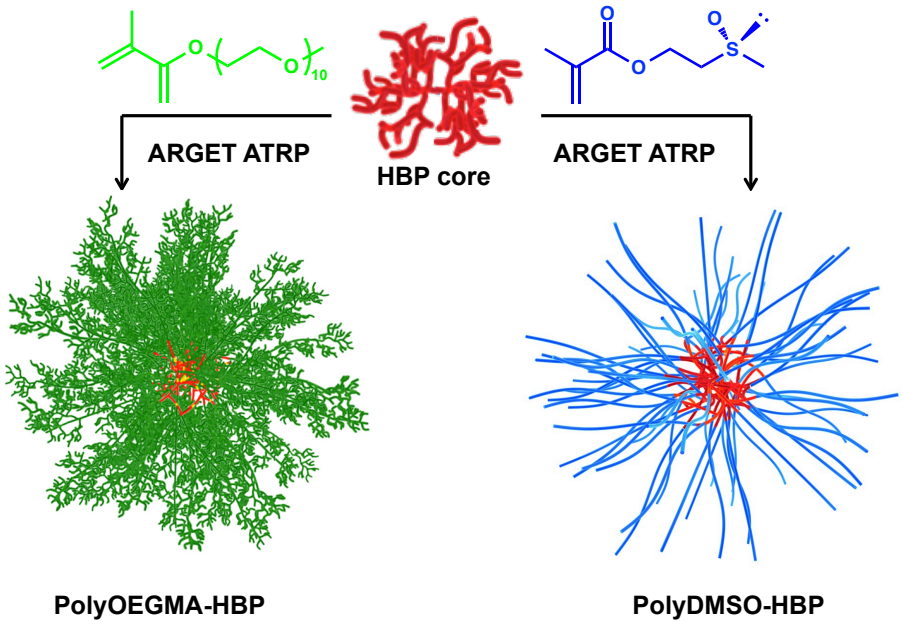

Scheme 13. Schematic representation of two types of core shell systems, polyOEGMA-HBP and polyDMSO-HBP.

Synthesis of biocompatible core-shell structures

As the surface of the HBPs contains abundant initiating bromine sites and cationic species, the cytotoxicity can be reduced by grafting biocompatible polymers from the surface of the HBP to form core-shell structures. In order to achieve high transfection efficiency,[55] HBP samples with the highest DB of 34 % were selected for the subsequent synthesis of core-shell structures, Scheme 13. OEGMA as a common "PEGylation" agent has been widely used to improve biocompatibility in biofunctional polymers synthesized by controlled radical polymerizations. On the other hand, a novel biocompatible polymeric analogue of DMSO, poly(2-(methylsulfinyl)ethyl acrylate), has been also developed. This polymeric analogue of DMSO possesses high biocompatibility, high

water-solubility and smaller steric hindrance compared to polyOEGMA. In this work, we introduce a methacrylate version of the polymer based on monomer of 2-(methylsulfinyl)ethyl methacrylate (MSEMA). OEGMA (MW=500) or MSEMA were grafted from the cationic HBP to form core-shell structures polyOEGMA-HBP and polyDMSO-HBP respectively, Scheme 13. The conditions for the synthesis of polyOEGMA-HBP are [OEGMA]/[per Br]/[Ascorbic Acid]/[$CuBr_2$]/[TPMA]=100/1/2/0.6/0.8 (m/v = ¼) in DMSO at 40 °C. Three samples with different sizes of shell were synthesized. As shown in Table 11, core-shell structures polyOEGMA-HBP with shell DP of 5, 48 and 95 were synthesized. SEC traces showed that the core shell structures had low molecular weight dispersity below 1.4, Figure 3a. With the shell DP increased from 5 to 95, the molecular weight analyzed by SEC MALS increased from 31,500 to 1,500,000, Figure 112. The synthesis conditions for polyDMSO-HBP are [MSEMA]/[per Br]/[Ascorbic Acid]/[$CuBr_2$]/[TPMA]=100/1/2/0.6/0.6 (m/v = 1/8) in DMSO at 40 °C. Three samples with different shell DPs, i.e., 5, 35 and 45 were synthesized at different conversions. The SEC curves showed that all the polymers have monomodal distribution. As the DP increased from 5 to 45, the molecular weight by SEC MALS increased from 15,900 to 62,100 with dispersity increased from 1.41 to 1.73, Figure 112.

Table 11. Two types of core-shell structures.[a]

#	Shell Type	Shell DP[b]	Core-Shell M_{nSEC}	Core-Shell $Đ$	Core-Shell M_{nLS}	Zeta[c] (mV)	Size[d] (nm)
A	PolyOEGMA	5	8500	1.37	31500	+10.1	10.6
B	PolyOEGMA	48	69300	1.21	95100	+1.3	14.0
C	PolyOEGMA	95	127000	1.33	1500000	+1.2	20.1
D	PolyDMSO	5	2800	1.41	15900	+12.7	7.7
E	PolyDMSO	35	20800	1.73	41300	+1.49	10.5
F	PolyDMSO	45	28600	1.73	62100	+1.38	12.6

[a] All structures were based on core with DB of 34 %.
[b] Degree of polymerization of each side chains.
[c] Surface charge of the core-shell structures

[d] Volume-mean size determined by DLS

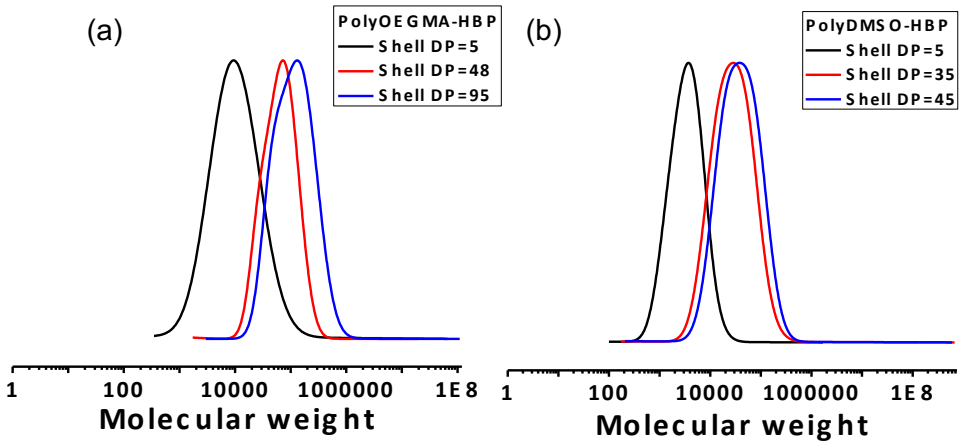

Figure 112. (a) SEC traces of polyOEGMA-HBP star polymers and (b) SEC traces of polyDMSO-HBP star polymers.

Biocompatibility and siRNA complexation

Since cell toxicity of siRNA delivery material is the major obstacle that limits the use of siRNA for therapeutic applications, cell toxicity of the polymers was first examined on SH-SY5Y epithelial neuroblastoma cells. To determine the siRNA complexation efficiency of the HBP and core-shell structures, agarose gel shift assays were conducted for the polymers. Negative control siRNA from IDT DNA was used in the experiment. The HBP with a DB of 34 % showed a hydrodynamic volume-mean size of 3.37 nm and a zeta potential of +38.1 mV indicating high concentration of positive charges on the surface of HBP, **Error! Reference source not found.**a. The HBP formed polyplexes with siRNA at a weight ratio of polymer/siRNA = 4/1, **Error! Reference source not found.**b. However, due to the surface charge, the HBP became highly toxic upon concentration of 0.33 mg/mL, **Error! Reference source not found.**c. By grafting a biocompatible shell from the cationic core, the hydrodynamic size of the core-shell structures

increased while the positive surface charge decreased as expected, Table 11. Core-shell structure polyOEGMA-HBP with a shell DP of 5 had a hydrodynamic size of 10.6 nm and a zeta potential of +10.1 mV. In comparison, polyDMSO-HBP with the same shell DP has a smaller size of 7.7 nm and a larger zeta potential of +12.7 mV. Crucially, both of the structures showed equally improved biocompatibility than the naked HBP core**,** Figure 113.

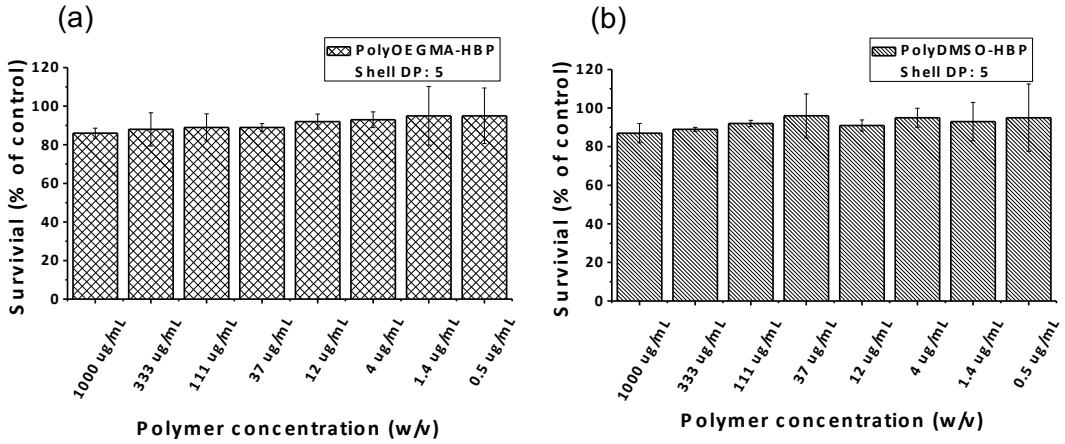

Figure 113. Cytotoxicity of SH-SY5Y epithelial neuroblastoma cells treated with (a) polyOEGMA-HBP with shell DP 5 and (b) polyDMSO-HBP with shell DP 5. HBP core with DB of 34 % were used for grafting shell.

In agarose gel experiment, polyOEGMA-HBP with a shell DP of 5 was observed to form complexes with negative control siRNA at polymer/siRNA weight ratio of 20/1 and formed complete complexes at weight ratio of 400/1, Figure 114a. When the shell DP was increased to 48, the polymers did not bind to siRNA at weight ratio of polymer/siRNA lower than 200/1 and no complexes were formed up to weight ratio of 400/1 for polyOEGMA-HBP with shell DP of 95, **Error! Reference source not found.**5. This observation indicated that lowering the steric hindrance of the biocompatible shell can increase the siRNA complexing efficiency. In comparison,

polyDMSO-HBP with shell DP of 5 was observed to start to form complex with negative control siRNA at a weight ratio of 10/1 and fully formed complexes at 200/1, Figure 114b. Moreover, for polyDMSO-HBP with shell DP of 45, complexes started to form at a weight ratio of 40/1 (5 times lower than polyOEGMA-HBP with same shell DP, **Error! Reference source not found.**. Such an observation indicated that due to the smaller steric hindrance and low cytotoxicity, polyDMSO can provide similar biocompatibility enhancement as polyOEGMA while with higher siRNA binding efficiency. Moreover, because the lower steric hindrance arises from the lower molecular weight of the polymer shell, the actual loading of cationic charges is also higher, which synergistically improved the complexing efficiency. The stability of siRNA polyplexes was assessed by agarose gel electrophoresis, **Error! Reference source not found.**. Interestingly, the results suggest that polyDMSO-HBP polyplexes are more stable than polyOEGMA polyplexes in culture media containing 10% FBS up to 2 days.

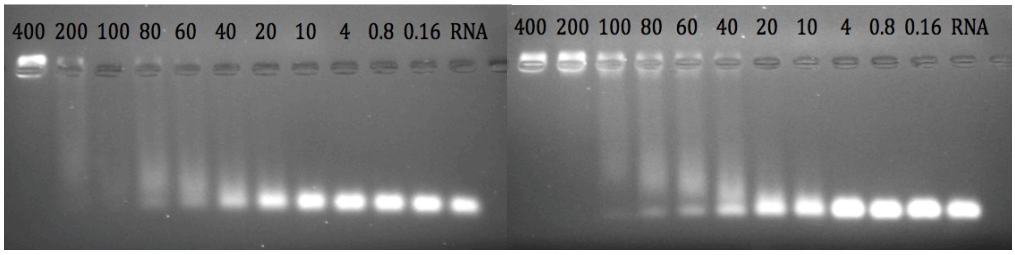

(a) (b)

Figure 114. Agarose gel of (a) core-shell structure polyOEGMA-HBP and (b) core-shell structure polyDMSO-HBP at weight ratios of polymer/siRNA from 0.16/1 to 400/1. Both polymers with shell DP = 5.

Effects of cationic polymers without siRNA on osteogenic differentiation

We then examined the cytotoxicity of a series of different concentrations of HBP core polymers and core-shell structures on primary osteoblasts by cell counting. Figure 115a shows that

cell proliferation was largely unaltered by 2.5 μg/mL of hyperbranched polymer treatments after 5 days in culture, while 10 μg/mL of the naked HBP core significantly decreased osteoblast number after 5 days, Figure 115b, suggesting the degree of cytotoxicity caused by the HBP core. To verify if cationic HBP core alone affect the gene expression in osteoblasts, cells were treated with each polymer without siRNA. Results indicated that all polymers at 2.5 μg/mL had no significant effect on *Runx2*, *Osx* and *Alp* expressions compared to untreated groups at 30 h, Figure 115c, and at 7 days, Figure 115e, after the treatment. However, HBP core at 10 μg/mL significantly reduced *Osx* expression at 30 h, Figure 115d and *Alp* expression at day 7, Figure 115f, indicating non-specific gene suppression by the HBP core treatment. Next, an assessment of mineralized nodule formation in osteoblast cultures was conducted by the Alizarin Red S staining. Cells were cultured with osteogenic differentiation medium for 14 days. Figure 5g shows that the delivery of polyOEGMA-HBP and polyDMSO-HBP alone had no impact on osteoblast mineralization after 14 days in culture, while HBP core both at 2.5 μg/mL and 10 μg/mL resulted in reduced alizarin red positive colonies, indicating a decrease in mineralization, Figure 115g and h. Although we have demonstrated that HBP core at low concentration does not show toxicity for cell survival, **Error! Reference source not found.**c, the long-term treatment with low doses of the HBP core shows negative impact on osteogenic ability of the primary osteoblasts. These results suggest that biocompatible shells such as polyOMEGA and polyDMSO are crucial to minimizing undesired cytotoxicity and non-specific gene suppression of the cationic HBP core.

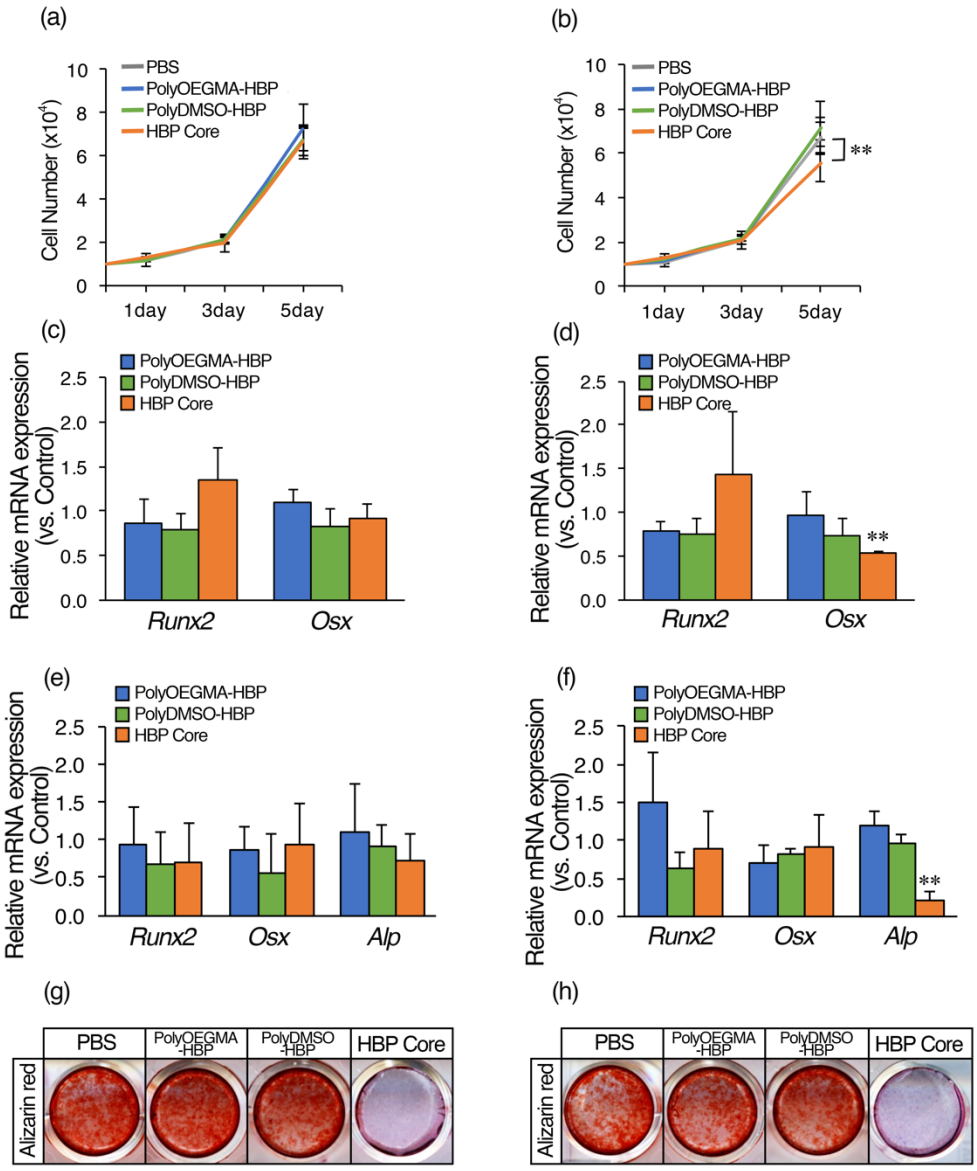

Figure 115. Effects of HBP polymers and core-shell structures on osteoblast proliferation and differentiation at 2.5 μg/mL (a, c, e and g) and 10 μg/mL (b, d, f and h). (a, b) The rate of cell growth by polymer treatments after 5 d in culture. (c, d) Effect of polymers on both *Runx2* and *Osx* gene expressions compared to untreated groups at 30 h. (e, f) The gene expression levels after polymer treatment at day seven. (g, h) The effect of treatment of polymers on osteoblast mineralization after 14 d in culture in alizarin red positive colonies. Data expressed as mean ± SD

of three replicate determinations. Significant differences between PBS-treated cells vs. polymer-treated cells. **p<0.01, *p<0.05.

Polymer-mediated RNAi attack on *Runx2* expression

The efficacy of cationic polymer-based RNAi against *Runx2* expression in osteoblasts was determined by using quantitative real-time PCR. Cells were treated with the siRNA polyplexes and incubated in media containing 10% serum for 24 h prior to rhBMP-2 delivery. Analysis of *Runx2* gene expressions was conducted after 6h of the rhBMP-2 treatment, Figure 116a. The commercially available lipid-based siRNA delivery reagent, *Lipofectamine*, was used as a reference for gene silencing. For transfection, the siRNA-*Lipofectamine* complexes were incubated in serum-free media for 6 h. The delivery of scramble siRNAs by cationic polymers was conducted to determine if the gene silencing capabilities of polymer-based RNAi were sequence specific. Results indicated that scramble siRNAs delivered by polyOEGMA-HBP and polyDMSO-HBP, with a polymer/siRNA weight ratio at 20/1, had no significant effect on *Runx2* expression compared to cells receiving rhBMP-2 treatments without siRNA, Figure 116b. The cells treated with the various siRNA polyplexes showed a significant decrease in *Runx2* expression compared to rhBMP-2 treated cells without siRNA, Figure 116c. For polyOEGMA-HBP, a polymer/siRNA weight ratio at 5/1 resulted in a significant reduction in *Runx2* expression of 59.2 ± 13.8% ($p < 0.05$), while a polymer/siRNA weight ratio at 20/1 resulted in Runx2 knockdown of 18.9 ± 27.5% ($p = 0.38$). For polyDMSO-HBP, polymer/siRNA weight ratios both at 5/1 to 20/1 exhibited significant Runx2 mRNA reductions of 77.2 ± 2.9% ($p < 0.01$) and 55.1 ± 8.7% ($p < 0.05$), respectively. Each polymer showed silencing efficiencies comparable to *Lipofectamine* (68.2 ± 11.9% gene suppression). It is notable that *Runx2* mRNA levels were knocked down by

polymer-based RNAi treatments to levels consistent with untreated cells. For HBP core, polymer/siRNA weight ratios ranging from 5/1 to 20/1 elicited significant reductions in *Runx2* expression of 53.6 ± 15.7% ($p < 0.05$) and 72.3 ± 15.3% ($p < 0.01$), respectively, **Error! Reference source not found.**. This is likely due to the toxic effects caused by HBP core based on the results shown in Figure 115, and thus non-specific reductions in gene expression. Additionally, *Runx2* siRNA delivery with core-shell structured polymers had no significant effect on *Osx* expression at 6h after the treatment, **Error! Reference source not found.**, indicating that RNAi using polymers developed here allows targeted gene-specific silencing.

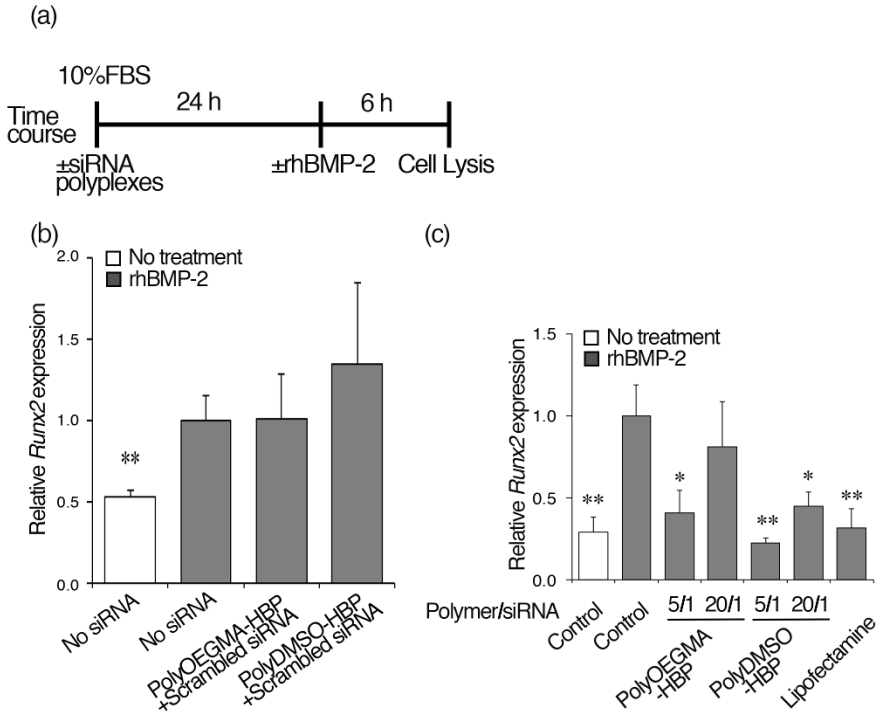

Figure 116. The cationic hyperbranched polymer-based RNAi against *Runx2* in primary osteoblasts by delivery of *Runx2* siRNAs at 20 pM doses. (a) Schematic of experimental time course. The siRNA polyplexes were delivered 24 h prior to delivery of recombinant human bone morphogenetic protein 2 (rhBMP-2, 100 ng/mL). Analysis of mRNA expression was conducted after 6 h of treatment by rhBMP-2. (b) Gene silencing effects on *Runx2* mRNA expressions by

polymer/scramble siRNAs polyplexes compared to rhBMP-2 treated cells without siRNA. (c) Gene silencing effects on *Runx2* mRNA expressions by polymer/siRNAs polyplexes. Data expressed as mean ± SD of three replicate determinations. $^{**}p<0.01$, $^{*}p<0.05$, vs rhBMP-2 treated cells without siRNA.

Effect of polymer-mediated *Runx2* knockdown on osteoblast differentiation

To address whether the polymer-based RNAi can alter biological function of osteoblasts, osteogenesis was induced with rhBMP-2 and cultures were treated with siRNA polyplexes against *Runx2* every 48 h cycle for 14 days, then deposition of mineral was assessed by Alizarin red S staining, **Error! Reference source not found.**a. Results indicated that scramble siRNAs delivered by polyOEGMA-HBP and polyDMSO-HBP, at a polymer/siRNA weight ratio at 20/1, or treatment of siRNA alone without polymers, **Error! Reference source not found.**, and had no significant effect on mineral deposition compared to rhBMP-2 treated cells without siRNA. RNAi treatments against *Runx2* with polyOEGMA-HBP and polyDMSO-HBP, with polymer/siRNA weight ratios at 20/1, resulted in significant reductions in mineral deposition in osteoblasts compared to cells receiving rhBMP-2 treatments without siRNA, **Error! Reference source not found.**b & c). Areas of nodules in the treatment groups were similar to those in rhBMP-2 untreated cells, and this level of reduction was comparable with that of *Lipofectamine* (all $p < 0.01$). These results suggest that repeating the polymer-based siRNA transfection several times on the same cells provides long-term silencing efficiency. Overall, the gene silencing efficacy of each core-shell structures was comparable to *Lipofectamine*. Further, there were no apparent cytotoxic effects by both polyOEGMA-HBP and polyDMSO-HBP treatment. Therefore, the hyperbranched core-

shell structures may have potential for efficient gene silencing without any undesirable cytotoxic effects.

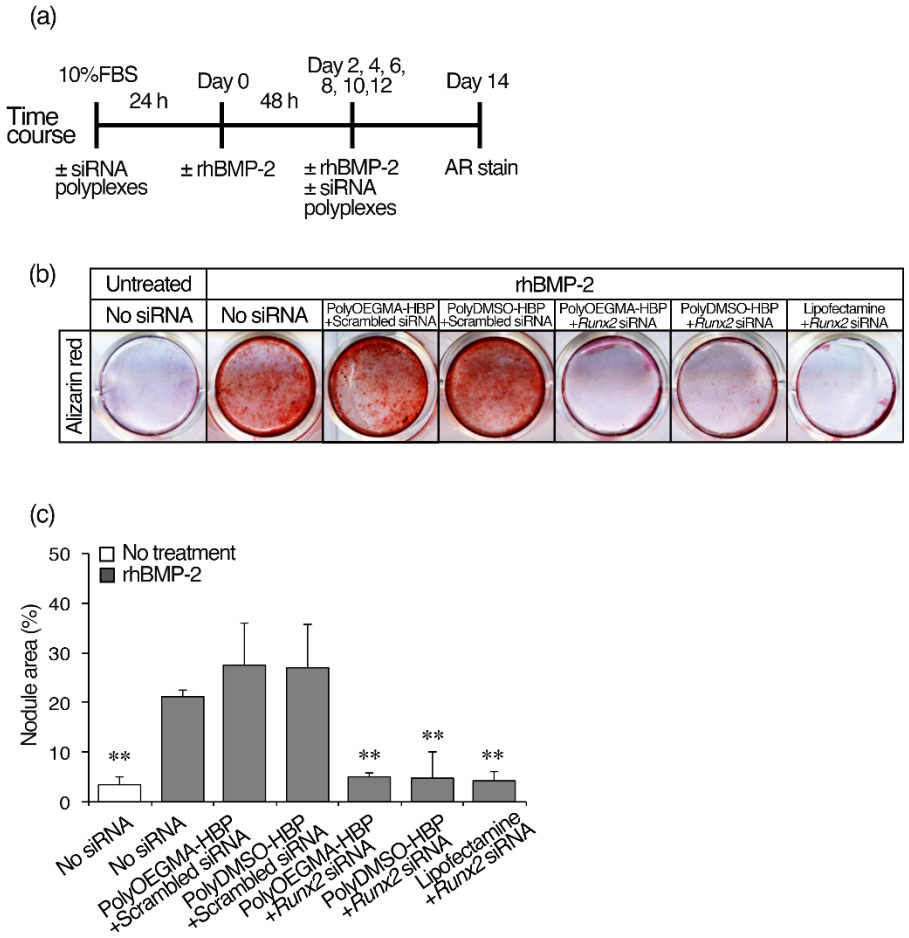

Figure 117. Alizarin red staining was performed after siRNA against *Runx2* transfections. (a) Schematic of experimental time course. RNAi treatments against *Runx2* were delivered 24 h prior to delivery of rhBMP-2. Cell culture media were refreshed in conjunction with RNAi treatments and rhBMP-2 every 2 days for the duration of the study. After 14 d in culture, mineral deposition in osteoblasts was assessed by Alizarin red staining. (b) The scramble siRNAs delivered by polyOEGMA-HBP and polyDMSO-HBP, a polymer、 siRNA weight ratio at 20/1, had no significant effect on mineral deposition compared to rhBMP-2 treated cells without siRNA. RNAi

treatments against *Runx2* with polyOEGMA-HBP and polyDMSO-HBP, a polymer/siRNA weight ratio at 20/1, resulted in significant reductions in mineral deposition in osteoblasts compared to cells receiving rhBMP-2 treatments without siRNA. (c) The percentage of nodule area was measured using ImageJ. Data expressed as mean ± SD of three replicate determinations. $^{**}p<0.01$, vs rhBMP-2 treated cells without siRNA.

B.4. Conclusion

In conclusion, cationic hyperbranched polymers (HBP) were synthesized by SCVP of an ATRP inimer containing a quaternary ammonium moiety with a cationic charge. By tuning the ratio of activator to deactivator, the degree of Branching (DB) of the HBP could be tuned from 16 % to 34 %. The cationic HBP showed efficient siRNA complexation but high cytotoxicity. In order to improve biocompatibility, two types of core-shell structures polyOEGMA-HBP and polyDMSO-HBP were synthesized from the cationic HBP core with DB of 34 %. Both type of core-shell structures displayed improved biocompatibility up to 1 mg/mL with SH-SY5Y epithelial neuroblastoma cells. Due to the lower steric hindrance of polyDMSO compared to polyOEGMA shell, the polyDMSO-HBP polymer showed much higher siRNA complexing efficiency than polyOEGMA-HBP. The efficacy of cationic polymer-based RNAi against *Runx2* expression in osteoblasts was determined by using quantitative real-time PCR and the osteoblast differentiation was determined using Alizarin red S staining. The analysis indicated that the HBP core showed non-specific gene suppression while both the core-shell structures showed long-term specific gene suppression against *Runx2* expression with efficacy comparable to the commercial agent *Lipofectamine*. This work is the first example of successful use of the new biocompatible polymer polyDMSO for gene knockdown and the use of HBP based core-shell structures showed promise for long-term treatment of HO.

B.5. Experimental sections and supporting information

Materials. 2-Bromoisobutyric acid (98 %), 2-bromoethanol (95 %), 2-(dimethylamino)ethyl methacrylate (DMAEMA, 98%), poly(ethylene glycol) methyl ether methacrylate (OEGMA, MW=500), methacrylic acid (99 %), *N*-(3-dimethylaminopropyl)-N'-ethylcarbodiimide hydrochloride (EDC, ≥99 %), *N,N*-dimethylamino pyridine (DMAP, ≥ 99%), copper bromide (≥ 99.99%), ascorbic acid, (AA, ≥99 %) were purchased from Sigma Aldrich. 2-(Methylthio)ethanol (≥ 99%) was purchased from Alfa Aesar. Hydrogen peroxide solution (30 %) was purchased from Fisher Scientific. All methacrylate monomers were passed through basic alumina columns before use. Tris(2-pyridylmethyl)amine (TPMA) was synthesized according to previous procedures.[80] All solvents and other chemicals are of reagent quality and were used as received unless special treatments discussed below were applied.

Instrumentation. ^{1}H NMR measurements were performed on a Bruker Avance 300 MHz spectrometer. Molecular weight and molecular weight distribution (dispersity, $Đ$) were determined by size exclusion chromatography (SEC) equipped with a Waters 515 HPLC pump, Wyatt Optilab refractive index detector, Wyatt DAWN HELEOS-II multi-angle light scattering detector and PSS GRAM columns containing polyester copolymer networks at 50 ^{o}C. The cationic hyperbranched polymers were analyzed in pure DMF phase at flow rate of 1 mL/min. The core-shell structures were analyzed in 50 mM LiBr DMF solution as eluent phase at flow rate of 1 mL/min.

Synthesis of cationic ATRP inimer. 2-Bromoethyl α-bromoisobutyrate was synthesized by esterification between 2-bromoethanol and 2-bromoisobutyric acid. In a typical procedure, 3.4 g 2-bromoethanol (1 equiv.), 5 g 2- bromoisobutyric acid (1.1 equiv.), 6.38 g EDC (1.5 equiv.) and 0.17 g DMAP (0.05 equiv.) were dissolved in 50 mL dichloromethane in a 100 mL round

bottom flask equipped with a stirring bar in an ice bath. The solution was purged with N_2 for 10 min and allowed to warm up to room temperature. After 24 h, the solution was washed with 50 mL 1M HCl solution, saturated $NaHCO_3$ solution and brine 3 times each. The organic phase was collected and dried over anhydrous $MgSO_4$. The solvent was removed under vacuum to yield yellow liquid product, yield 85%. ^{1}H NMR (300 MHz, $CDCl_3$): δ (ppm) = 4.48 (1H, t, COOC*H*$_2$CH$_2$Br), 3.55 (2H, t, COOCH$_2$C*H*$_2$Br), 1.98 (6H, s, Br(C*H*$_3$)$_2$CCOO). The cationic inimer was synthesized by a subsequent quaternization (Menschutkin reaction). In a typical procedure, 5 g 2-bromoethyl α-bromoisobutyrate (1.05 equiv.) and 2.73 g DMAEMA (1 equiv.) were dissolved in 25 mL DMF in a 50 mL round bottom flask equipped with a stirring bar at 35 ^{o}C. The reagents in the solution were allowed to react for 2 h. The solution was then precipitated in 500 mL diethyl ether. The precipitate was collected and dried under vacuum to give white solid, 98 % yield. ^{1}H NMR (300 MHz, DMSO-d_6): δ (ppm) = 6.09 (1H, s, CH*H*═CCH$_3$), 5.78 (1H, s, C*H*H═CCH$_3$), 4.58 (4H, m, COOC*H*$_2$CH$_2$N(CH$_3$)$_2$CH$_2$C*H*$_2$OCO), 3.84 (4H, m, COOCH$_2$C*H*$_2$N(CH$_3$)$_2$C*H*$_2$CH$_2$OCO), 3.20 (6H, s, COOCH$_2$CH$_2$N(C*H*$_3$)$_2$CH$_2$CH$_2$OCO), 1.93 (6H, s, Br(C*H*$_3$)$_2$CCOO), 1.91 (3H, s, CH$_2$═CC*H*$_3$).

Synthesis of sulfoxide containing monomer 2-(methylsulfinyl)ethyl methacrylate (MSEMA). 2-(Methylthio)ethyl methacrylate (MTEMA) was synthesized according to our previously reported procedure.[37] In a typical oxidation procedure, 25.5 g MTEMA was added to a 100 mL round bottom flask sealed with rubber stopper. The flask was kept in an ice bath and purged with N_2 then 18.3 g hydrogen peroxide solution (20 %) was slowly injected into the flask at rate of 50 μL/min. The reaction mixture was allowed to stir for 24 h and was then stopped by adding 50 mL deionized water. The aqueous solution was washed 3 times with 100 mL dichloromethane. The organic phase was collected and dried over magnesium sulfate. Solvent was

removed under vacuum to give white solid, yield 75 %. ^{1}H NMR (300 MHz, DMSO-d_6): δ (ppm) = 6.05 (1H, s, CH*H*═CCH$_3$), 5.71 (1H, s, C*H*H═CCH$_3$), 4.35~4.54 (2H, m, C═OOC*H*$_2$CH$_2$), 3.95~3.23 (2H, m, CH$_2$C*H*$_2$S═O), 2.60 (3H, s, S═OC*H*$_3$), 1.89 (3H, s, CH$_2$═CC*H*$_3$).

Synthesis of cationic hyperbranched polymers (HBP). The synthesis employed an AGET ATRP. In a typical procedure, 1 g cationic inimer (50 equiv.), 0.041 g CuBr$_2$ (4 equiv.) and 0.081 g TPMA (6 equiv.) were dissolved in 1.4 mL DMSO and 0.1 mL DMF in a 10 mL Schlenk flask equipped with a stirring bar. The solution was degassed by three cycles of freeze-pump-thaw and then filled with N_2. The flask was then placed in 35 ^{o}C oil bath then 0.011 g ascorbic acid (1.32 equiv.) in 0.1 mL DMSO was injected into the flask under N_2 purge. The reaction was stopped after 24 h. The hyperbranched polymer was purified by dialysis (MWCO = 100~500 Da) against water and dried under vacuum. The conversion was measured by ^{1}H NMR and the molecular weight and dispersity were measured by SEC-MALS. The calculation of degree of branching (DB) was elaborated in the supporting information. A similar approach compared to previous report was used.[66] In general, to determine the DB, polymers were purified by dialysis and analyzed by ^{1}H NMR. The DB was calculated under the assumption that there is minimal radical termination and intramolecular cycling. The number of newly formed initiating sites should equal to the reacted initiating sites and the number of original initiating sites in the inimer should equal to the combined amount of reacted and unreacted vinyl groups. (Scheme S1) These two equations, combined with the integration of NMR peaks (δ = 2.6−2.8, 0.7−2.2, and 5.7−6.3), allowed for the calculation of reactivity ratio r = k_{A*} / k_{B*} and the DB.

Synthesis of core-shell structure polyOEGMA-HBP. The synthesis employed an ARGET ATRP. In a typical procedure, 2 g OEGMA (100 equiv.), 17.2 mg cationic HBP (1 equiv. per Br), 5.3 mg CuBr$_2$ (0.6 equiv.), 9.3 mg TPMA (0.8 equiv.) were dissolved in 7.9 mL DMSO

and 0.25 mL DMF in a 25 mL Schlenk flask equipped with a stirring bar. The flask was degassed by three cycles of freeze-pump-thaw and filled with nitrogen after the last cycle. 14.1 mg ascorbic acid (2 equiv.) dissolved in 0.1 mL DMSO was injected into the solution under nitrogen purge. The mixture was allowed to react in a 40 ºC heating plate. An initial sample (t = 0) was collected by syringe. Samples were taken periodically to measure conversion via ^{1}H NMR and molecular weight via SEC-MALS. The polymer was purified by dialysis (MWCO = 100~500 Da) against water and dried by lyophilization.

Synthesis of core-shell structure polyDMSO-HBP. The synthesis employed an ARGET ATRP. In a typical procedure, 0.5 g 2-(methylsulfinyl)ethyl methacrylate (MSEMA) (100 equiv.), 12.2 mg cationic hyperbranched polymer (1 equiv. per Br), 3.8 mg $CuBr_2$ (0.6 equiv.), 4.9 mg TPMA (0.8 equiv.) were dissolved in 3.65 mL DMSO and 0.1 mL DMF in a 10 mL Schlenk flask equipped with a stirring bar. The flask was degassed by three cycles of freeze-pump-thaw and filled with nitrogen after the last cycle. 10 mg ascorbic acid (2 equiv.) dissolved in 0.1 mL DMSO was injected into the solution under nitrogen purge. The mixture was allowed to react in a 40 ºC heating plate. An initial sample (t = 0) was collected by syringe. Samples were taken periodically to measure conversion via ^{1}H NMR and molecular weight via SEC-MALS. The polymer was purified by dialysis (MWCO = 100~500 Da) against water and dried by lyophilization.

Cytotoxicity tests with SH-SY5Y cells. SH-SY5Y epithelial neuroblastoma cells (ATCC CRL-2266) were cultured in a base medium composed of a 1/1 ratio of Eagle's Minimum Essential Medium and F-12 growth medium. Fetal bovine serum (FBS) was added to base medium to reach 10% final concentration of FBS, as per cell line manufacturer's instructions (GenTarget Inc., cat# SC042). Before testing, cells were grown on above medium in Corning T-75 culture flasks at 37 °C and 5 % CO_2 in a humidified incubator. Prior to biocompatibility testing, each well of a 96-well

culture plate was seeded with ~10,000 cells in 150 μL growth medium. After 24 h incubation, tested polymers were added to wells in concentrations of 1000, 333, 111, 37, 12, 4, 1.4, and 0.5 μg/mL via serial dilutions repeated in triplicate. Untreated + control wells contained cells and media only, and – control wells were treated with 1% Triton X to kill all cells. After 48 h of exposure to test polymer, 100 uL was taken from each test well and combined with 100 μL ATP assay solution (CellTiter-Glo® Luminescent Cell Viability Assay from Promega) in a pre-warmed black 96-well reading plate, then incubated for 30 minutes at 23°C. Endpoint luminescence was measured for each well as an average of 5 readings per well, using a BioTek plate reader with Gen5.2.09 software. Percent survival was approximated as averaged triplicate luminance of treated vs. control wells; variance in luminance across experimental and control replicates reported as error.

siRNA complexation using negative control siRNA. To determine each polymer's efficiency of complexing with siRNA, agarose gel shift assays were conducted for the polymers. Negative control siRNA from IDT DNA was used in the experiment. Because unbounded siRNA and bounded siRNA possess opposite charge, the gel shift assay indicates the weight ratios at which siRNA is incorporated into a given complex. Polyplexes were prepared by incubating polymers of varying concentrations (diluted with nuclease-free ultrapure water) with 500 ng siRNA, to produce polymer/siRNA weight ratios of 400/1, 200/1, 100/1, 80/1, 60/1, 40/1, 20/1, 10/1, 4/1, 0.8/1, 0.16/1, and 0/1 (0/1 are control wells containing 500 ng siRNA and water alone). Upon addition of siRNA, polyplexes were incubated at 23 °C for 60 minutes, after which they were weighed with 5 uL nuclease-free glycerin for total loading volumes of 30 μL per well. Polyplexes were then loaded into 100 mL volume 2 % agarose gels prepared with Tris/Borate/EDTA (TBE) buffer and 7.5 μL Ethidium Bromide. After loading, electrophoresis was

conducted under 100 V current for 60 minutes. After electrophoresis, all gels were photographed with 500 ms exposures under ultra-violet illumination via Labnet's ENDURO GDS system. To determine the stability of siRNA polyplexes, negative control siRNA (naked siRNA) and siRNA polyplexes at polymer/siRNA weight ratio of 400/1 were incubated in alpha-minimum essential medium (αMEM) supplemented with 10 % FBS at 37 °C. The samples were collected at different time points (4, 12, 24, 36 and 48 h) and analyzed by agarose gel electrophoresis.

Wild-type osteoblasts cell proliferation assay. Wild-type osteoblasts were isolated from newborn mouse calvaria and cultured in alpha-minimum essential medium (αMEM) supplemented with 10 % fetal bovine serum (Denville Scientific) and 1 % penicillin/streptomycin (Invitrogen). All cells were used for experiments before passage 4. To determine cell counts, osteoblasts were seeded in 24-well plates (1.0×10^4 cells/well) and incubated with hyperbranched polymers. At day 1, 3 and 5, adherent cells were washed with PBS and incubated with trypsin at 37 ^{o}C for 5 min. After trypsinization, cell suspensions were transferred to a hemocytometer with Trypan Blue Solution and counted under the microscope.

Quantitative PCR. Cells were seeded at 2.0×1.0^4 cells/well in 24-well plates and RNA was isolated using TRIzol reagent (Life Technologies). For quantitative real-time PCR analyses, 100 ng of total RNA was reverse-transcribed using Superscript first-strand synthesis system (Invitrogen) with Oligo (dT) as a primer. The levels of gene expressions were measured by quantitative real-time PCR using ABI Prism 7500 (Applied Biosystems). Taqman probes for *Runx2* (Mm00501578_m1), *Osterix/Sp7 (Osx)* (Mm04209856_m1), *alkaline phosphatase* (*Alp)* (Mm00475831_m1) and *glyceraldehyde-3-phosphate dehydrogenase* (*Gapdh)* (Mm99999915_g1) were used for quantification. Data were normalized to *Gapdh* expression using the comparative Ct method.

Alizarin Red S Staining. Cells were seeded at 2.0 x 1.0^4 cells/well in 24-well plates and incubated with osteogenic differentiation medium containing 10mM β-glycerophosphate and 50 μg/mL L-ascorbic acid. After 14 days in culture, cells were fixed in 70 % ethanol for 15 min at room temperature. Cells were stained with 40mM alizarin red S (Sigma-Aldrich) for 10 min and then rinsed five times with DI water to minimize nonspecific staining. The stained area was digitally photographed and measured using of the ImageJ (National Institutes of Health, USA).

RNAi experiments. Silencer® select Pre-designed siRNA against mouse *Runx2* gene (5'-CAAGUGCGGUGCAAACUUUtt-3' and 5'-AAAGUUUGCACCGCACUUGtg-3') and scrambled siRNA (Silencer Negative Control #1 siRNA) were purchased from Ambion (Austin, TX). siRNA polyplexes were prepared by mixing hyperbranched polymers and siRNAs (20 pM) in polymer/siRNA weight ratios ranging from 5/1 to 20/1 in volumes up to 5 μL. For transfection, 2.0 x 10^4 cells/well were seeded in 24-well plates the day before transfection. The siRNA polyplexes were delivered 24 h prior to delivery of recombinant human bone morphogenetic protein 2 (rhBMP-2, R&D Systems, 100 ng/mL). Cell culture media were refreshed in conjunction with RNAi treatments and rhBMP-2 every 2 days for the duration of the study.

Statistical analysis. All results were expressed as means ± standard deviation of triplicate measurements with all experiments independently repeated at least three times. Unpaired Student's t-tests were used to evaluate statistical differences. Values of $p<0.05$ were considered significant.

Calculation of Degree of Branching (DB)

The calculation was based on previous reports.[66, 77, 81] **Error! Reference source not found.**shows the ^{1}H NMR of a hyperbranched polymer (HBP) with DB of 34 % purified with dialysis.

The HBP structure is composed of five different moieties (**Error! Reference source not found.**):

Structure A: unreacted vinyl group

Structure a: reacted vinyl group

Structure b: reacted initiating site

Structure A*: newly formed initiating site

Structure B*: original initiating site

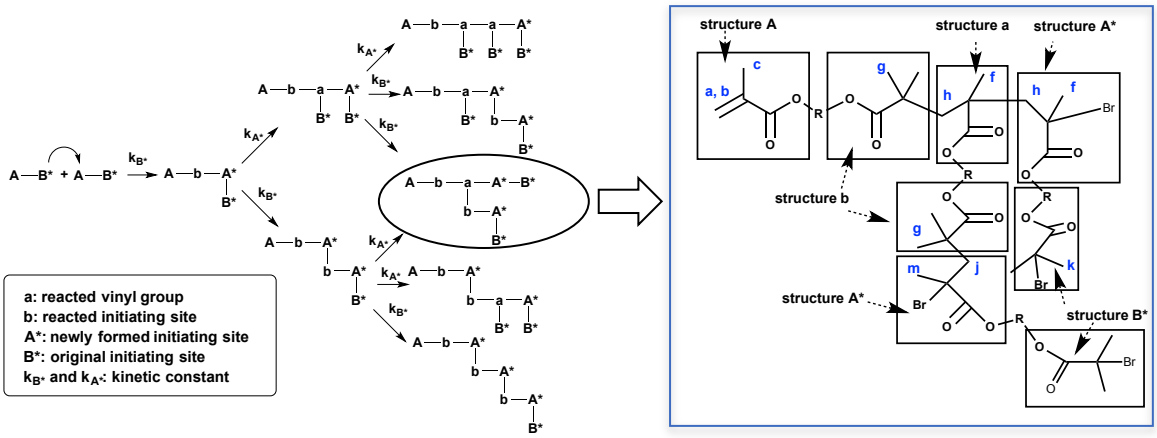

Scheme 14. Illustration of all moieties of the HBP with rate constants, k_{A*} and k_{B*} in the initial steps in the polymerization. ($r=k_{A*}/k_{B*}$)

Relative amounts of each moiety in the HBP structure was calculated by integration of NMR peaks shown in **Error! Reference source not found.**:

Area(**j**) = $2N_{A*}$;

Area(**c**+**f**+**g**+**h**+**k**+**m**)= $3N_a + 6N_b + 3N_{A*} + 6N_{B*} + 2N_a + 3N_A$;

Area(**a**+**b**)= $2N_A$;

$N_{A*} = N_b$;

$N_{B*} = N_a + N_A$;

With the above six equations, N_{B*} and N_B can be calculated. Since conversion of vinyl groups approached essentially 100 %, Conv. A was assumed as 1, to simplify the calculation.[66, 81] With the calculated results, DB can be calculated according to the following equations:

$$f_{B*} = \frac{N_{B*}}{N_{B*} + N_B}$$

$$r = \frac{Conv.A + f_{B*} - 1}{-lnf_{B*} + f_{B*} - 1} = \frac{e^{-z}}{e^{-z} + z - 1}$$

$$DB = 2e^{-z}(1 - e^{-z})$$

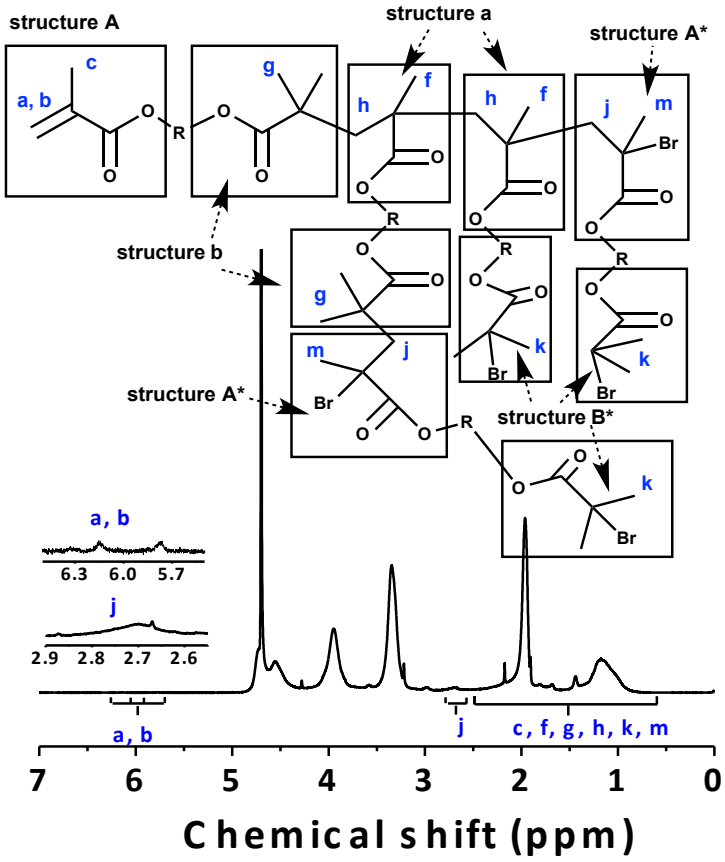

Figure 118. [1]H NMR spectrum of HBP (DB=34 %) with assigned NMR peaks.

The relative NMR integrations of Area(**j**), Area(**c**+**f**+**g**+**h**+**k**+**m**) and Area(**a**+**b**) for HBP with different DB are listed below in **Error! Reference source not found.**.

Table 12. Relative NMR integration areas and calculated DB.

Polymers	Area(**j**)	Area(**c**+**f**+**g**+**h**+**k**+**m**)	Area(**a**+**b**)	DB
HBP-1	1	27.0	0.026	34 %
HBP-2	1	43.4	0.151	22 %
HBP-3	1	67.1	0.099	16 %

Characterization of cationic hyperbranched polymers (HBP).

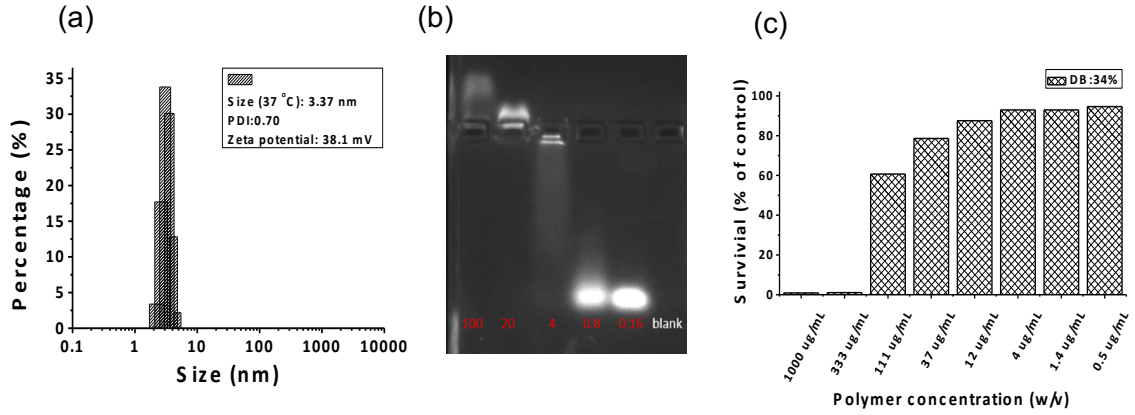

Figure 119. (a) Volume-mean size distribution by DLS of cationic HBP with DB 34%. (b) Agarose gel analysis of cationic HBP/siRNA complexes (weight ratio of polymer/siRNA from left to right: 100/1, 20/1, 4/1, 0.5/1, 0.16/1 and blank) (c) Cytotoxicity data of cationic HBP with SH-SY5Y cell. The polymer became toxic at concentration over 333 μg/mL, indicating that a biocompatible corona is needed to reduce the toxicity of the naked cationic core.

3. Characterization of core-shell structures.

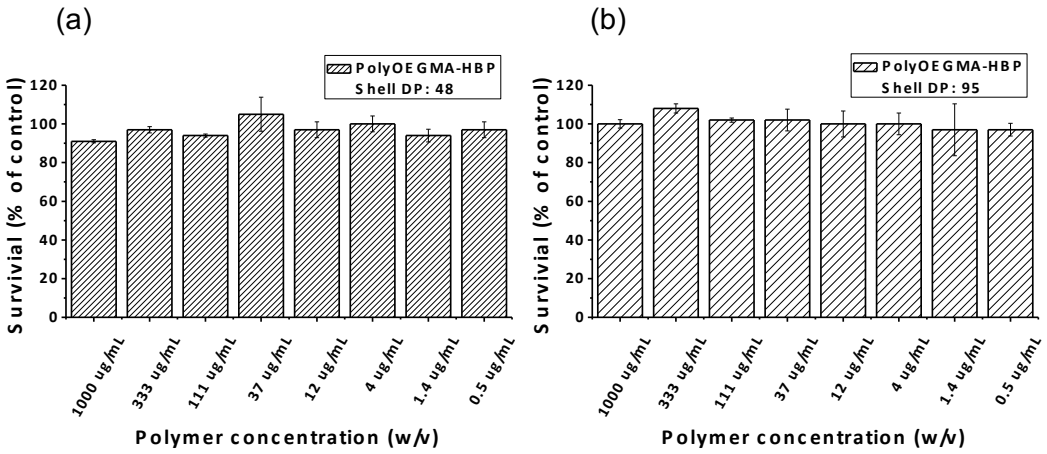

Figure 120. Cytotoxicity of the polyOEGMA-HBP polymers with different shell DPs grafted from a cationic core with DB of 34 %. (cells tested: SH-SY5Y) (a) Shell DP=48, (b) shell DP=95.

Core-shell structure polyOEGMA-HBP with thicker corona (shell DP = 48 or 95) also showed low cytotoxicity towards cell SH-SY5Y with concentration up to 1 mg/mL.

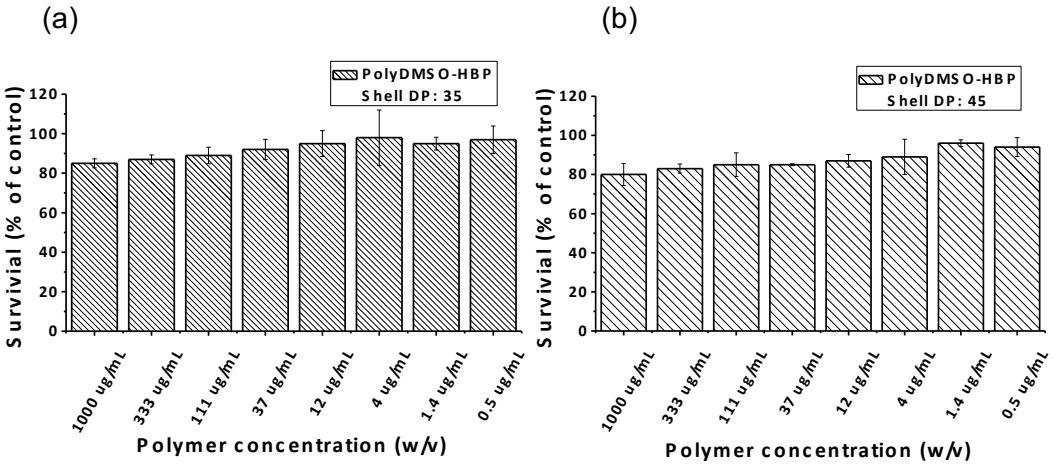

Figure 121. Cytotoxicity of the polyDMSO-HBP polymers with different shell DPs grafted from a cationic core with DB of 34 %. (cells tested: SH-SY5Y) (a) Shell DP=35, (b) shell DP=45.

Similarly, core-shell structure polyDMSO-HBP with thicker corona (shell DP = 35 or 45) also showed low cytotoxicity towards cell SH-SY5Y with concentration up to 1 mg/mL. These results suggest that polyDMSO provides biocompatible systems.

The siRNA complexing ability of polyOEGMA-HBP and polyDMSO-HBP with thicker corona was examined using agarose gel, **Error! Reference source not found.**. PolyOEGMA-HBP with a shell DP of 48 did not show complexation with siRNA at weight ratio of polymer/siRNA lower than 200/1 and no complexes was formed even at a weight ratio of 400/1 for polyOEGMA-HBP with shell DP of 95. In comparison, polyDMSO-HBP with shell DP of 45 started to form complexes at a weight ratio of 40/1 (5 times lower than polyOEGMA-HBP with similar shell DP). This result indicated that due to the lower steric hindrance of polyDMSO the core-shell structured polyDMSO-HBP was more efficient than polyOEGMA-HBP for complexing siRNA.

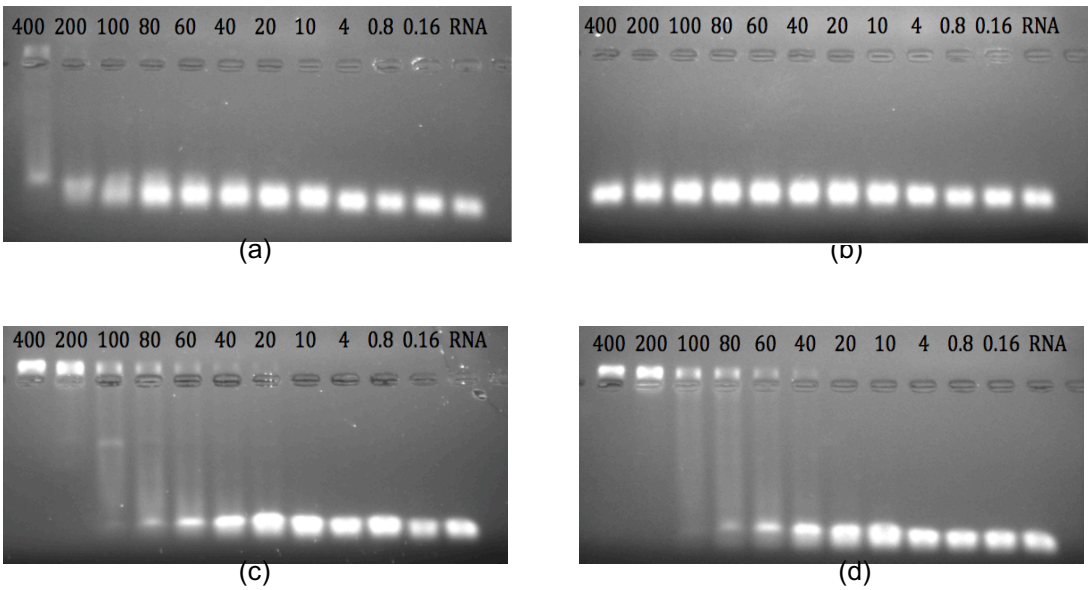

Figure 122. Agarose gel analysis of core-shell structure polyOEGMA-HBP with shell DP 48 (a) and 95(b); agarose gel of core-shell structure polyDMSO-HBP with shell DP 35 (c) and 48(d). Weight ratios of polymer/siRNA range from 0.16/1 to 400/1.

Stability of siRNA complexes

The stability of siRNA polyplexes was assessed by agarose gel electrophoresis. The result showed that the incubation of naked siRNA with culture media containing 10% FBS resulted in clear bands for 4h, and after 12 h, blurred bands were observed up to 48 h, **Error! Reference source not found.**a. For polyOEGMA-HBP, siRNA complexes were stuck in the wells and prevented the internalization of siRNA into agarose gel, but the bands became blurred after 12 h, **Error! Reference source not found.**b. By contrast, polyDMSO-HBP/siRNA polyplexes showed slightly blurred bands after 12 h, but the formation of polyplexes remained detectable up to 48 h, **Error! Reference source not found.**c. No free siRNA was observed in either the polyOEGMA-

HBP or polyDMSO-HBP polyplexes up to 48 h. These results suggest that polyDMSO-HBP polyplexes are more stable than polyOEGMA polyplexes in culture media containing 10% FBS.

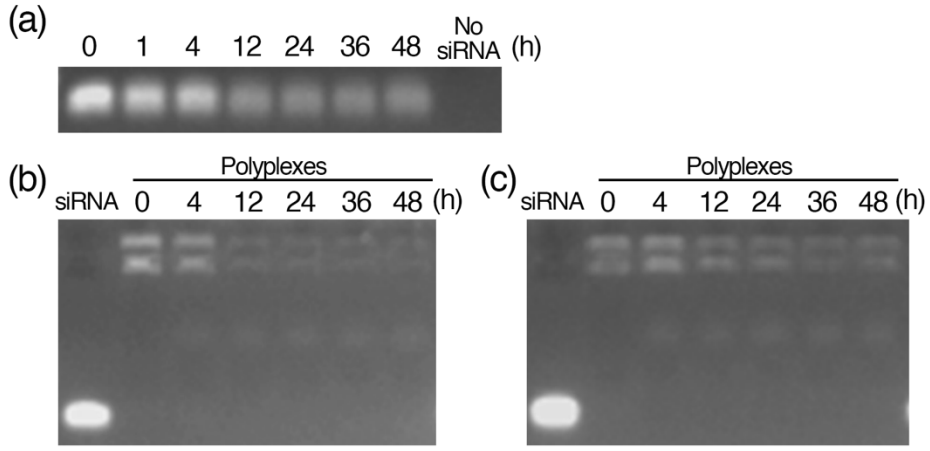

Figure 123. The stability of siRNA polyplexes in culture media containing 10% FBS up to 2 days. (a) Naked siRNA, (b) polyOEGMA-HBP and (c) polyDMSO-HBP at polymer/siRNA weight ratio of 400/1 were incubated for 4, 12, 24, 36 and 48 h at 37 °C. The stability of complexes was analyzed by electrophoresis on agarose gel stained with ethidium bromide. For better comparison, each gel was put in the same image.

siRNA delivery for gene knockdown

As shown in **Error! Reference source not found.**, for HBP core, polymer/siRNA weight ratios ranging from 5/1 to 20/1 caused significant reductions in *Runx2* expression of 53.6 ± 15.7 % ($p < 0.05$) and 72.3 ± 15.3 % ($p < 0.01$), respectively. This is likely due to the toxic effects caused by HBP core, based on the results shown in Figure 5, and thus non-specific reductions in gene expression.

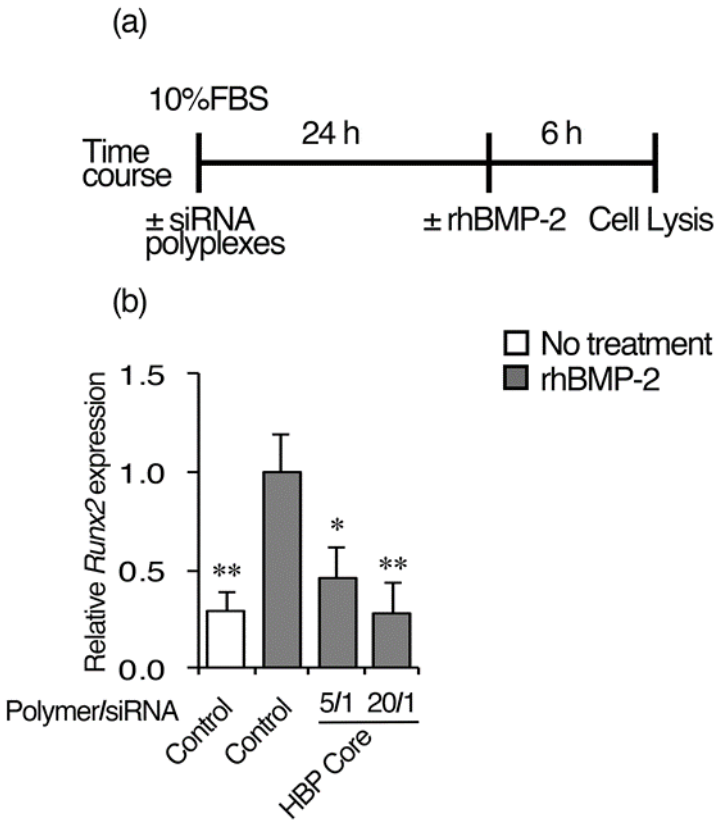

Figure 124. The HBP core-based RNAi against *Runx2* in primary osteoblasts by delivery of *Runx2* siRNAs at 20 pM doses. (a) Schematic of experimental time course. The siRNA polyplexes were delivered 24 h prior to delivery of recombinant human bone morphogenetic protein 2 (rhBMP-2, 100 ng/mL). Analysis of mRNA expression was conducted after 6 h of treatment by rhBMP-2. (b) The effects on *Runx2* mRNA expressions by HBP Core/siRNAs polyplexes. The polymer/siRNA weight ratios ranging from 5/1 to 20/1 elicited significant reductions in *Runx2* expression. Data expressed as mean ± SD of three replicate determinations. $^{**}p<0.01$, $^{*}p<0.05$, vs rhBMP-2 treated cells without siRNA.

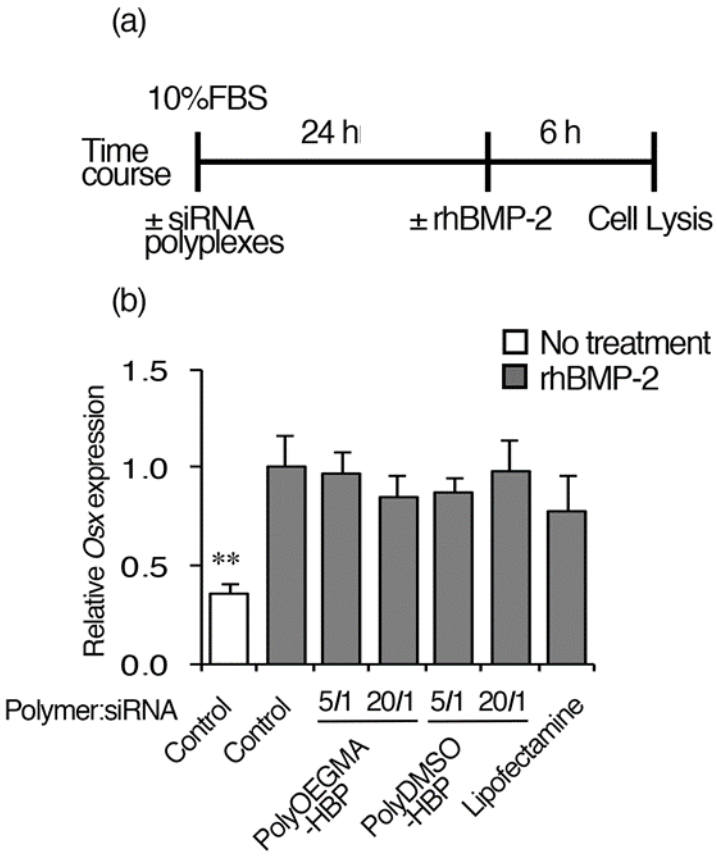

Figure 125. Delivery of *Runx2* siRNAs with core-shell structured polymers had no significant effect on *Osx* expression at 6 h after the treatment. (a) Schematic of experimental time course. The siRNA polyplexes were delivered 24 h prior to delivery of rhBMP-2. (b) Gene silencing effects on *Osx* mRNA expressions as a consequence of RNAi targeting *Runx2*. This result indicated that RNAi using core-shell structured polymers allows targeted gene-specific silencing. Data expressed as mean ± SD of three replicate determinations. $^{**}p<0.01$, vs rhBMP-2 treated cells without siRNA.

The *Runx2* siRNA delivery with core-shell structured polymers had no significant effect on *Osx* expression at 6 h after the treatment (**Error! Reference source not found.**), indicating that RNAi using polymers developed here allows targeted gene-specific silencing.

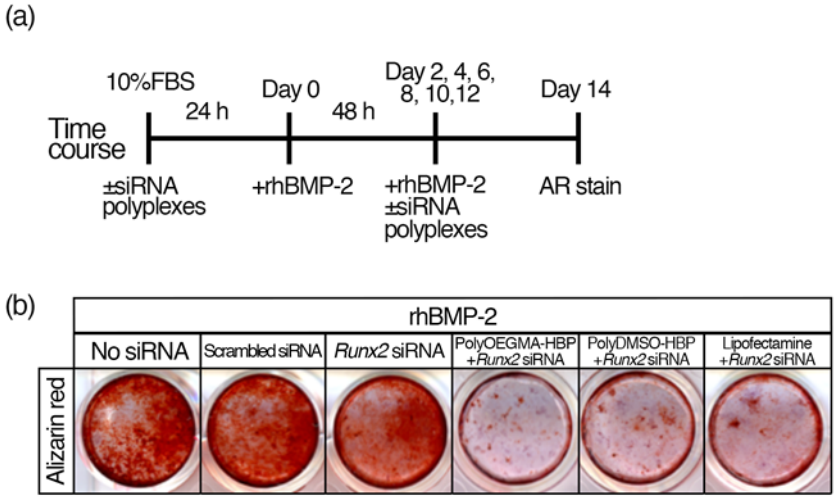

Figure 126. Alizarin red staining was performed after siRNA against *Runx2* transfections. (a) Schematic of experimental time course. RNAi treatments against *Runx2* were delivered 24 h prior to delivery of rhBMP-2. Cell culture media were refreshed in conjunction with RNAi treatments and rhBMP-2 every 2 days for the duration of the study. After 14 d in culture, mineral deposition in osteoblasts was assessed by Alizarin red staining. (b) The cells receiving rhBMP-2 treatments with *Runx2* siRNA alone had no significant effect on mineral deposition compared to rhBMP-2 treated cells without siRNAs. RNAi treatments against *Runx2* with PolyOEGMA-HBP and PolyDMSO-HBP, a polymer/siRNA weight ratio at 5/1, resulted in significant reductions in mineral deposition in osteoblasts compared to cells receiving rhBMP-2 treatments without siRNA.

As shown above, cells treated with *Runx2* siRNA alone had no significant effect on mineral deposition compared to cell not treated with siRNAs, indicating the knockdown process requires the co-delivery of cationic polymers.

B.6. References

[1] Lu, Q. L.; Bou-Gharios, G.; Partridge, T. A., Non-viral gene delivery in skeletal muscle: a protein factory, *Gene Ther.* **2003,** 10, 131.

[2] Li, Z.; Rana, T. M., Molecular Mechanisms of RNA-Triggered Gene Silencing Machineries, *Acc. Chem. Res.* **2012,** 45, 1122.

[3] Dykxhoorn, D. M.; Lieberman, J., The silent revolution: RNA interference as basic biology, research tool, and therapeutic, *Annu. Rev. Med.* **2005**, 401.

[4] Hamilton, A. J.; Baulcombe, D. C., A Species of Small Antisense RNA in Posttranscriptional Gene Silencing in Plants, *Science* **1999,** 286, 950.

[5] Fire, A.; Xu, S.; Montgomery, M. K.; Kostas, S. A.; Driver, S. E.; Mello, C. C., Potent and specific genetic interference by double-stranded RNA in Caenorhabditis elegans, *Nature* **1998,** 391, 806.

[6] Verma, I. M.; Somia, N., Gene therapy - promises, problems and prospects, *Nature* **1997,** 389, 239.

[7] Lin, E.-W.; Maynard, H. D., Grafting from Small Interfering Ribonucleic Acid (siRNA) as an Alternative Synthesis Route to siRNA–Polymer Conjugates, *Macromolecules* **2015,** 48, 5640.

[8] Lin, Z.; Liu, T.; Ai, X.; Liang, C., Aligning academia and industry for unified battery performance metrics, *Nature Communications* **2018,** 9, 5262.

[9] Lee, J. B.; Hong, J.; Bonner, D. K.; Poon, Z.; Hammond, P. T., Self-assembled RNA interference microsponges for efficient siRNA delivery, *Nat. Mater.* **2012,** 11, 316.

[10] Alfieri, K. A.; Forsberg, J. A.; Potter, B. K., Blast injuries and heterotopic ossification, *Bone Joint Res.* **2012,** 1, 174.

[11] Ahrengart, L., Periarticular Heterotopic Ossification After Total Hip Arthroplasty: Risk Factors and Consequences, *Clin. Orthop. Relat. Res.* **1991,** 263.

[12] Aubut, J.-A. L.; Mehta, S.; Cullen, N.; Teasell, R. W.; Group, E.; Team, S. R., A Comparison of Heterotopic Ossification Treatment within the Traumatic Brain and Spinal Cord Injured Population: An Evidence Based Systematic Review, *NeuroRehabilitation* **2011,** 28, 151.

[13] Shrivats, A. R.; Hsu, E.; Averick, S.; Klimak, M.; Watt, A. C. S.; DeMaio, M.; Matyjaszewski, K.; Hollinger, J. O., Cationic Nanogel-mediated Runx2 and Osterix siRNA Delivery Decreases Mineralization in MC3T3 Cells, *Clin. Orthop. Relat. Res.* **2015,** 473, 2139.

[14] Aagaard, L.; Rossi, J. J., RNAi therapeutics: Principles, prospects and challenges, *Advanced Drug Delivery Reviews* **2007,** 59, 75.

[15] Akhtar, S.; Benter, I. F., Nonviral delivery of synthetic siRNAs in vivo, *J. Clin. Invest.* **2007,** 117, 3623.

[16] Barquinero, J.; Eixarch, H.; Pérez-Melgosa, M., Retroviral vectors: new applications for an old tool, *Gene Ther.* **2004,** 11, S3.

[17] Cho, H. Y.; Srinivasan, A.; Hong, J.; Hsu, E.; Liu, S.; Shrivats, A.; Kwak, D.; Bohaty, A. K.; Paik, H.-j.; Hollinger, J. O.; Matyjaszewski, K., Synthesis of Biocompatible PEG-Based Star Polymers with Cationic and Degradable Core for siRNA Delivery, *Biomacromolecules* **2011,** 12, 3478.

[18] Cho, H. Y.; Gao, H.; Srinivasan, A.; Hong, J.; Bencherif, S. A.; Siegwart, D. J.; Paik, H.-j.; Hollinger, J. O.; Matyjaszewski, K., Rapid Cellular Internalization of Multifunctional Star Polymers Prepared by Atom Transfer Radical Polymerization, *Biomacromolecules* **2010,** 11, 2199.

[19] Duncan, R.; Ringsdorf, H.; Satchi-Fainaro, R., Polymer Therapeutics: Polymers as Drugs, Drug and Protein Conjugates and Gene Delivery Systems: Past, Present and Future Opportunities.

In *Polymer Therapeutics I*, Satchi-Fainaro, R.; Duncan, R., Eds. Springer Berlin Heidelberg: Berlin, Heidelberg, 2006; pp 1.

[20] Heath, W. H.; Senyurt, A. F.; Layman, J.; Long, T. E., Charged Polymers via Controlled Radical Polymerization and their Implications for Gene Delivery, *Macromol. Chem. Phys.* **2007,** 208, 1243.

[21] Siegwart, D. J.; Whitehead, K. A.; Nuhn, L.; Sahay, G.; Cheng, H.; Jiang, S.; Ma, M.; Lytton-Jean, A.; Vegas, A.; Fenton, P.; Levins, C. G.; Love, K. T.; Lee, H.; Cortez, C.; Collins, S. P.; Li, Y. F.; Jang, J.; Querbes, W.; Zurenko, C.; Novobrantseva, T.; Langer, R.; Anderson, D. G., Combinatorial synthesis of chemically diverse core-shell nanoparticles for intracellular delivery, *Proc. Nat. Acad. Sci.* **2011,** 108, 12996.

[22] Li, S.; Rizzo, M. A.; Bhattacharya, S.; Huang, L., Characterization of cationic lipid-protamine-DNA (LPD) complexes for intravenous gene delivery, *Gene Ther.* **1998,** 5, 930.

[23] Whitehead, K. A.; Langer, R.; Anderson, D. G., Knocking down barriers: advances in siRNA delivery, *Nature reviews. Drug discovery* **2009,** 8, 129.

[24] Mao, S.; Sun, W.; Kissel, T., Chitosan-based formulations for delivery of DNA and siRNA, *Advanced drug delivery reviews* **2010,** 62, 12.

[25] Wang, Y.; Gao, S.; Ye, W.-H.; Yoon, H. S.; Yang, Y.-Y., Co-delivery of drugs and DNA from cationic core–shell nanoparticles self-assembled from a biodegradable copolymer, *Nat. Mater.* **2006,** 5, 791.

[26] Gary, D. J.; Puri, N.; Won, Y.-Y., Polymer-based siRNA delivery: Perspectives on the fundamental and phenomenological distinctions from polymer-based DNA delivery, *J. Controlled Release* **2007,** 121, 64.

[27] Guo, X.; Huang, L., Recent Advances in Nonviral Vectors for Gene Delivery, *Acc. Chem. Res.* **2012,** 45, 971.

[28] Heath William, H.; Senyurt Askim, F.; Layman, J.; Long Timothy, E., Charged Polymers via Controlled Radical Polymerization and their Implications for Gene Delivery, *Macromol. Chem. Phys.* **2007,** 208, 1243.

[29] Han, S.-o.; Mahato, R. I.; Sung, Y. K.; Kim, S. W., Development of Biomaterials for Gene Therapy, *Mol. Ther.* **2000,** 2, 302.

[30] Fischer, P. M., Cellular uptake mechanisms and potential therapeutic utility of peptidic cell delivery vectors: Progress 2001–2006, *Medicinal Research Reviews* **2007,** 27, 755.

[31] Zheng, C.; Zheng, M.; Gong, P.; Deng, J.; Yi, H., Polypeptide cationic micelles mediated co-delivery of docetaxel and siRNA for synergistic tumor therapy, *Biomaterials* **2013,** 34, 3431.

[32] Rehman, Z. u.; Zuhorn, I. S.; Hoekstra, D., How cationic lipids transfer nucleic acids into cells and across cellular membranes: Recent advances, *J. Controlled Release* **2013,** 166, 46.

[33] Zintchenko, A.; Philipp, A.; Dehshahri, A.; Wagner, E., Simple modifications of branched PEI lead to highly efficient siRNA carriers with low toxicity, *Bioconjugate Chem.* **2008,** 19, 1448.

[34] Zhang, S.; Zhao, B.; Jiang, H.; Wang, B.; Ma, B., Cationic lipids and polymers mediated vectors for delivery of siRNA, *J. Controlled Release* **2007,** 123, 1.

[35] Zhu, C.; Jung, S.; Luo, S.; Meng, F.; Zhu, X.; Park, T. G.; Zhong, Z., Co-delivery of siRNA and paclitaxel into cancer cells by biodegradable cationic micelles based on PDMAEMA–PCL–PDMAEMA triblock copolymers, *Biomaterials* **2010,** 31, 2408.

[36] Cho, H. Y.; Averick, S. E.; Paredes, E.; Wegner, K.; Averick, A.; Jurga, S.; Das, S. R.; Matyjaszewski, K., Star Polymers with a Cationic Core Prepared by ATRP for Cellular Nucleic Acids Delivery, *Biomacromolecules* **2013,** 14, 1262.

[37] Mackenzie, M. C.; Shrivats, A. R.; Konkolewicz, D.; Averick, S. E.; McDermott, M. C.; Hollinger, J. O.; Matyjaszewski, K., Synthesis of Poly(meth)acrylates with Thioether and Tertiary Sulfonium Groups by ARGET ATRP and Their Use as siRNA Delivery Agents, *Biomacromolecules* **2015,** 16, 236.

[38] Ping, Y.; Liu, C.; Zhang, Z.; Liu, K. L.; Chen, J.; Li, J., Chitosan-graft-(PEI-β-cyclodextrin) copolymers and their supramolecular PEGylation for DNA and siRNA delivery, *Biomaterials* **2011,** 32, 8328.

[39] Frère, A.; Baroni, A.; Hendrick, E.; Delvigne, A.-S.; Orange, F.; Peulen, O.; Dakwar, G. R.; Diricq, J.; Dubois, P.; Evrard, B.; Remaut, K.; Braeckmans, K.; De Smedt, S. C.; Laloy, J.; Dogné, J.-M.; Feller, G.; Mespouille, L.; Mottet, D.; Piel, G., PEGylated and Functionalized Aliphatic Polycarbonate Polyplex Nanoparticles for Intravenous Administration of HDAC5 siRNA in Cancer Therapy, *ACS Appl. Mater. Interfaces* **2017,** 9, 2181.

[40] Xu, X.; Saw, P. E.; Tao, W.; Li, Y.; Ji, X.; Yu, M.; Mahmoudi, M.; Rasmussen, J.; Ayyash, D.; Zhou, Y.; Farokhzad, O. C.; Shi, J., Tumor Microenvironment-Responsive Multistaged Nanoplatform for Systemic RNAi and Cancer Therapy, *Nano Lett.* **2017,** 17, 4427.

[41] Hutnick, M. A.; Ahsanuddin, S.; Guan, L.; Lam, M.; Baron, E. D.; Pokorski, J. K., PEGylated Dendrimers as Drug Delivery Vehicles for the Photosensitizer Silicon Phthalocyanine Pc 4 for Candidal Infections, *Biomacromolecules* **2017,** 18, 379.

[42] Cabral, H.; Kataoka, K., Progress of drug-loaded polymeric micelles into clinical studies, *J. Controlled Release* **2014,** 190, 465.

[43] Nishiyama, N.; Kataoka, K., Current state, achievements, and future prospects of polymeric micelles as nanocarriers for drug and gene delivery, *Pharmacology & therapeutics (Oxford)* **2006,** 112, 630.

[44] Averick, S. E.; Paredes, E.; Irastorza, A.; Shrivats, A. R.; Srinivasan, A.; Siegwart, D. J.; Magenau, A. J.; Cho, H. Y.; Hsu, E.; Averick, A. A.; Kim, J.; Liu, S.; Hollinger, J. O.; Das, S. R.; Matyjaszewski, K., Preparation of Cationic Nanogels for Nucleic Acid Delivery, *Biomacromolecules* **2012,** 13, 3445.

[45] Leroux, J. C., Editorial: Drug Delivery: Too Much Complexity, Not Enough Reproducibility?, *Angew. Chem. Int. Ed.* **2017,** 56, 15170.

[46] Nakayama, Y., Hyperbranched Polymeric "Star Vectors" for Effective DNA or siRNA Delivery, *Acc. Chem. Res.* **2012,** 45, 994.

[47] Zheng, Y.; Li, S.; Weng, Z.; Gao, C., Hyperbranched polymers: advances from synthesis to applications, *Chemical Society Reviews* **2015,** 44, 4091.

[48] Han, J.; Li, S.; Tang, A.; Gao, C., Water-Soluble and Clickable Segmented Hyperbranched Polymers for Multifunctionalization and Novel Architecture Construction, *Macromolecules* **2012,** 45, 4966.

[49] Li, S.; Han, J.; Gao, C., High-density and hetero-functional group engineering of segmented hyperbranched polymers via click chemistry, *Polym. Chem.* **2013,** 4, 1774.

[50] Li, S.; Gao, C., Dendritic molecular brushes: synthesis via sequential RAFT polymerization and cage effect for fluorophores, *Polym. Chem.* **2013,** 4, 4450.

[51] Konkolewicz, D.; Gilbert, R. G.; Gray-Weale, A., Randomly Hyperbranched Polymers, *Phys. Rev. Lett.* **2007,** 98, 238301.

[52] Konkolewicz, D.; Thorn-Seshold, O.; Gray-Weale, A., Models for randomly hyperbranched polymers: Theory and simulation, *J. Chem. Phys.* **2008,** 129, 054901.

[53] Konkolewicz, D.; Gray‐Weale, A.; Perrier, S., Describing the Structure of a Randomly Hyperbranched Polymer, *Macromol. Theory Simul.* **2010,** 19, 219.

[54] Konkolewicz, D.; Perrier, S.; Stapleton, D.; Gray‐Weale, A., Modeling highly branched structures: Description of the solution structures of dendrimers, polyglycerol, and glycogen, *J. Polym. Sci., Part B: Polym. Phys.* **2011,** 49, 1525.

[55] Yamagata, M.; Kawano, T.; Shiba, K.; Mori, T.; Katayama, Y.; Niidome, T., Structural advantage of dendritic poly(l-lysine) for gene delivery into cells, *Biorg. Med. Chem.* **2007,** 15, 526.

[56] Smith, D.; Holley, A. C.; McCormick, C. L., RAFT-synthesized copolymers and conjugates designed for therapeutic delivery of siRNA, *Polym. Chem.* **2011,** 2, 1428.

[57] Zhang, Q.-F.; Yu, Q.-Y.; Geng, Y.; Zhang, J.; Wu, W.-X., Ring-opening polymerization for hyperbranched polycationic gene delivery vectors with excellent serum tolerance, *ACS Appl. Mater. Interfaces* **2014,** 6, 15733.

[58] Fischer, W.; Quadir, M. A.; Barnard, A.; Smith, D. K.; Haag, R., Controlled release of DNA from photoresponsive hyperbranched polyglycerols with oligoamine shells, *Macromol. Biosci.* **2011,** 11, 1736.

[59] Höbel, S.; Loos, A.; Appelhans, D.; Schwarz, S.; Seidel, J., Maltose- and maltotriose-modified, hyperbranched poly(ethylene imine)s (OM-PEIs): Physicochemical and biological properties of DNA and siRNA complexes, *J. Controlled Release* **2011,** 149, 146.

[60] Gao, C.; Yan, D., Hyperbranched polymers: from synthesis to applications, *Prog. Polym. Sci.* **2004,** 29, 183.

[61] Fréchet, J. M.; Henmi, M.; Gitsov, I.; Aoshima, S.; Leduc, M. R., Self-condensing vinyl polymerization: an approach to dendritic materials, *Science (New York, N.Y.)* **1995,** 269, 1080.

[62] Gao, J.; Zhai, G.; Song, Y.; Jiang, B., Synthesis and characterization of hyperbranched cationic polyelectrolytes via aqueous self‐condensing atom transfer radical polymerization, *J. Appl. Polym. Sci.* **2009,** 112, 2522.

[63] Matyjaszewski, K.; Gaynor, S. G., Preparation of Hyperbranched Polyacrylates by Atom Transfer Radical Polymerization. 3. Effect of Reaction Conditions on the Self-Condensing Vinyl Polymerization of 2-((2-Bromopropionyl)oxy)ethyl Acrylate, *Macromolecules* **1997,** 30, 7042.

[64] Matyjaszewski, K.; Gaynor, S. G.; Kulfan, A.; Podwika, M., Preparation of Hyperbranched Polyacrylates by Atom Transfer Radical Polymerization. 1. Acrylic AB* Monomers in "Living" Radical Polymerizations, *Macromolecules* **1997,** 30, 5192.

[65] Gaynor, S. G.; Edelman, S.; Matyjaszewski, K., Synthesis of Branched and Hyperbranched Polystyrenes, *Macromolecules* **1996,** 29, 1079.

[66] Min, K.; Gao, H., New Method To Access Hyperbranched Polymers with Uniform Structure via One-Pot Polymerization of Inimer in Microemulsion, *J. Am. Chem. Soc.* **2012,** 134, 15680.

[67] Pelegri-O'Day, E. M.; Lin, E.-W.; Maynard, H. D., Therapeutic Protein–Polymer Conjugates: Advancing Beyond PEGylation, *J. Am. Chem. Soc.* **2014,** 136, 14323.

[68] Cobo, I.; Li, M.; Sumerlin, B. S.; Perrier, S., Smart hybrid materials by conjugation of responsive polymers to biomacromolecules, *Nat. Mater.* **2014,** 14, 143.

[69] Li, S.; Chung, H. S.; Simakova, A.; Wang, Z.; Park, S.; Fu, L.; Cohen-Karni, D.; Averick, S.; Matyjaszewski, K., Biocompatible Polymeric Analogues of DMSO Prepared by Atom Transfer Radical Polymerization, *Biomacromolecules* **2017,** 18, 475.

[70] Garnier, S.; Laschewsky, A., Synthesis of New Amphiphilic Diblock Copolymers and Their Self-Assembly in Aqueous Solution, *Macromolecules* **2005,** 38, 7580.

[71] Hennaux, P.; Laschewsky, A., Novel nonionic surfactants based on sulfoxides. 2. Homo- and copolymers, *Colloid. Polym. Sci.* **2003,** 281, 807.

[72] Hofmann, V.; Ringsdorf, H.; Muacevic, G., Pharmakologisch aktive polymere, 8.Poly[2-(methylsulfinyl)äthylacrylat]e und ihre vermittelnde wirkung auf die transkutane resorption von pharmaka, *Die Makromolekulare Chemie* **1975,** 176, 1929.

[73] Matyjaszewski, K.; Xia, J. H., Atom transfer radical polymerization, *Chem. Rev.* **2001,** 101, 2921.

[74] Yan, D.; Muller, A. H. E.; Matyjaszewski, K., Molecular Parameters of Hyperbranched Polymers Made by Self-Condensing Vinyl Polymerization. 2. Degree of Branching, *Macromolecules* **1997,** 30, 7024.

[75] Müller, A. H. E.; Yan, D. Y.; Wulkow, M., Molecular Parameters of Hyperbranched Polymers Made by Self-Condensing Vinyl Polymerization. 1. Molecular Weight Distribution, *Macromolecules* **1997,** 30, 7015.

[76] Reinheimer, J. D.; Harley, J. D.; Meyers, W. W., Solvent Effects in the Menschutkin Reaction, *J. Org. Chem.* **1963,** 28, 1575.

[77] Graff, R. W.; Wang, X.; Gao, H., Exploring Self-Condensing Vinyl Polymerization of Inimers in Microemulsion To Regulate the Structures of Hyperbranched Polymers, *Macromolecules* **2015,** 48, 2118.

[78] Voit, B. I.; Lederer, A., Hyperbranched and Highly Branched Polymer Architectures—Synthetic Strategies and Major Characterization Aspects, *Chem. Rev.* **2009,** 109, 5924.

[79] Müller, A. H. E.; Yan, D.; Wulkow, M., Molecular Parameters of Hyperbranched Polymers Made by Self-Condensing Vinyl Polymerization. 1. Molecular Weight Distribution, *Macromolecules* **1997,** 30, 7015.

[80] Xia, J.; Matyjaszewski, K., Controlled/"Living" Radical Polymerization. Atom Transfer Radical Polymerization Catalyzed by Copper(I) and Picolylamine Complexes, *Macromolecules* **1999,** 32, 2434.

[81] Yan, D.; Müller, A. H. E.; Matyjaszewski, K., Molecular Parameters of Hyperbranched Polymers Made by Self-Condensing Vinyl Polymerization. 2. Degree of Branching, *Macromolecules* **1997,** 30, 7024.